# An Isotopic Study of the Fluid Flow and Thermal History of the 2.8 Ma Chegem Ash-flow Caldera and Related Intrusive Rocks (Caucasus Mountains, Russia)

Thesis by
Carey Alice Gazis

In Partial Fulfillment of the Requirements
for the Degree of
Doctor of Philosophy

California Institute of Technology
Pasadena, California
1995

(Defended October 31, 1994)

*haba na haba hujaza kibaba*

Kiswahili saying

*(little by little, fills the whole)*

# ACKNOWLEDGMENTS

I have interacted with many people during my stay at Caltech and the time has come to thank all those who helped me in one way or another. First of all, I thank my thesis advisor, Hugh P. Taylor, Jr. He has an admirably clear view of geology and has taught me much about isotope geology and about communicating science. I also appreciate the fact that he gave me his full attention when I needed it, and left me to work on my own the rest of the time. I thank Jason Saleeby for introducing me to a spectacular field area and for letting me work in his laboratory. Lee Silver has been an important mentor to me at Caltech, and I am grateful that I had the opportunity to learn from him. Caltech has been a very stimulating intellectual environment and I have benefited from discussions with many of the faculty in the Division, particularly Tom Ahrens, Don Burnett, Sam Epstein, Ed Stolper, and George Rossman, and visiting professors Page Chamberlain, Peter Kokelaar, and Mordeckai Magaritz.

During the course of my thesis work, I have had the privilege of working with two excellent volcanologists from the U.S. Geological Survey, Peter Lipman and Ken Hon. It was indeed a treat to enter my field area with two personal volcanology tutors, and I appreciate all of the input they have given me as I wrote this dissertation. Through the U.S. Geological Survey, I also had the opportunity to work with Marvin Lanphere, who kindly allowed me to work in his laboratory and was always willing to answer my questions. None of this work would have been possible without the efforts of our Russian counterparts, particularly Andrei Tsvetkov, Anatoly Gurbanov and Valentine Beus. Nikolai Koronovsky, Egana Latifova, Igor Nikolaev, and Masha Bogina are also thanked for their collaborations and assistance in field work.

I am grateful to the many people who have helped me out in the various labs at Caltech, especially Rosemary Capo, Mahmood Chaudry, Eleanor Dent, Joop Goris, Phil Ihinger, Diane Clemens Knott, Laurie Leshin, Sally Newman, Mike Palin and Brian Stewart. And a special thanks goes to Xiahong Feng, who was often around to advise me and to blow glass that I had broken. In addition, Mary Mellon has been a perpetual source of good cheer and a valuable resource in the office.

I have enjoyed my interactions with the other students at Caltech, particularly my officemate Doug Yule, my labmate Greg Holk, and my housemate Elizabeth Nagy. Thanks also to Jen Blank, Joel Blum, Eme Burt, Mihai Ducea, Liz Holt, Jean Hsieh, Tom LaTourette, Wohjer Lee, Charlie Rubin, and DJ Wood.

Outside of work, I have remained happy by running, swimming and playing with many friends, especially Becky McGrew, Carolyn Beck and the Homechicks. And of course Jeff Hashimoto has been an important running companion and friend in the last year. I thank my family for making me who I am. My mother, who went through graduate school with seven children, has always been an inspiration to me. I thank my father for his constant support and belief in me. My grandmother, Frances Beckwith, has also been an important influence on me, and my siblings Paul, Jean, Lynn, Andrew, Jessie and Ace will continue to mold me. I dedicate this thesis to my grandfather Sterling Beckwith, who died two years ago. He was a great scientific thinker.

# ABSTRACT

The 2.8 Ma Chegem caldera, an 11x15 km ash-flow caldera located in the Caucasus Mountains, presents a unique opportunity to study silicic magma systems because of its combination of youth, exposure and simplicity. Rapid uplift and erosion in the region has exposed over 2 km of flatlying caldera fill, consisting of densely welded tuff (rhyolitic to dacitic), overlain by glacial deposits and andesite flows and cut by a granodiorite porphyry intrusion. The Eldjurta Granite, whose age and composition are similar to the Chegem volcanics, is exposed in an adjacent river valley 10 km to the northeast. Major Mo-W deposits located in nearby skarns have prompted mineral-exploration drillholes (to 4 km depth) in the granite. An isotopic study of the rocks of the Chegem caldera and the Eldjurta Granite has been performed to examine their petrogenesis, fluid flow and thermal histories.

Biotite and sanidine $^{40}Ar/^{39}Ar$ ages for 8 Chegem Tuff samples and the granodiorite intrusion are analytically indistinguishable at 2.82 ± 0.02 Ma. Thus, the Chegem Tuff was erupted, cooled and intruded by the granodiorite within < 50,000 yrs. In the nearby Eldjurta Granite, biotite and K-feldspar $^{40}Ar/^{39}Ar$ ages for 11 samples, including 8 from the deep drillhole (to 3970m depth) yield ages between 0.83 ± 0.29 Ma and 2.78 ± 0.09 Ma. A decrease in biotite ages from 1.90 ± 0.24 Ma near the roof of the granite to 0.83 ± 0.29 Ma at 3970m depth, apparently records the uplift and cooling history of this pluton. The ages of the upper 10 samples imply an isotherm migration rate of 13 mm/yr, probably due to a combination of downward migration of isotherms and regional uplift.

Oxygen isotope studies of the intracaldera tuff, including 38 samples from a continuous 1405m-stratigraphic section, reveal a striking caldera-wide stratigraphic horizon of $^{18}O$-depleted rocks in which there is extreme

disequilibrium between phenocrysts and groundmass (sometimes still glassy). All quartz and feldspar phenocrysts have "normal" igneous $\delta^{18}O$ values of ≈8.5 and ≈7.0, respectively. Whole-rock and groundmass $\delta^{18}O$ values are as low as –4.0 and –7.7, respectively. Infrared spectroscopic analyses of glassy pumices reveal that they contain 3.3 to 4.8 wt% water. The δD and water speciation of these glasses reflects low-temperature hydration by meteoric water, whereas some of their $\delta^{18}O$ values require higher temperature water-glass interaction.

Pronounced disequilibrium between coexisting feldspar and groundmass or glass has never been observed before on this scale. It requires a hydrothermal event involving large amounts of low-$^{18}O$ $H_2O$ at sufficiently high temperatures and short enough time that glass exchanges thoroughly but feldspar does not. The most likely process responsible for the $^{18}O$ depletions at Chegem is a high-temperature (500-600°C), short-lived (10-25 years), vigorous meteoric-hydrothermal event similar to that which occurred at the Valley of Ten Thousand Smokes, Alaska. Mass balance calculations indicate fluid fluxes of ≈$6x10^{-6}$ mol/$cm^2$-sec over that time period. Sr isotopic studies reveal that this hydrothermal event caused increases in whole-rock $^{87}Sr/^{86}Sr$, possibly because the hydrothermal waters attained radiogenic Sr from crystalline rocks which were incorporated in the caldera fill during caldera collapse.

$^{87}Sr/^{86}Sr_i$ ratios of unaltered Chegem volcanic and intrusive rocks range from 0.7044 to 0.7060, significantly lower than values for surrounding country rock (0.7070 to 0.7319). Thus, the Chegem magmas were probably derived from the mantle or lower crust. The $^{87}Sr/^{86}Sr_i$ ratios correlate with major- and trace-element trends, indicating that the Chegem magma chamber was both isotopically and compositionally zoned. Compared to the Chegem rocks, the Eldjurta Granite has higher $^{87}Sr/^{86}Sr_i$ (0.7069), $\delta^{18}O_{quartz}$ (≈10.0) and $\delta^{18}O_{feldspar}$ (≈8.8), and so must have evolved separately at some time.

# TABLE OF CONTENTS

# LIST OF FIGURES

## Chapter 1



## Chapter 2



## Chapter 3



## Chapter 4

# LIST OF TABLES

## Chapter 3



## Chapter 4



## Chapter 5



## Chapter 6



## Appendices

# Chapter 1. Introduction

## 1.1 Ash-flow Calderas

### *1.1.1 The Importance of Studying Ash-Flow Calderas*

Large-volume silicic ash-flow eruptions are some of the most catastrophic geologic events that occur at the earth's surface. Pyroclastic flows are hot, gaseous, particulate-rich density currents produced during these giant explosive volcanic eruptions, which take place in a matter of hours. In most if not all cases when erupted volumes are greater that 25 to 50 $km^3$, a roughly circular caldera collapse structure surrounded by ring fractures develops to compensate for the removal of the erupted volume of magma. These calderas can be as large as 60 kilometers in diameter while volumes of erupted ash-flow can be greater than 3000 $km^3$.

The erupted deposits provide a unique geochemical "snap-shot" in the evolution of the sub-volcanic magma chamber, and studies of the caldera structure provide clues to the eruption process itself. Frequently, the shallow

intrusions associated with resurgent doming or ring fracturing of these structures provide a heat source which drives hydrothermal circulation. These hydrothermal fluids are a source of geothermal energy, and they also serve to transport metals that may form economically important ore deposits.

### *1.1.2 Occurrence*

Ash-flow calderas occur in a variety of tectonic settings. In general, silicic magmas are generated at convergent plate margins in regions of island arcs and active continental margins and in areas of extensional tectonics within continental plates.

Probably the most extensively studied ash-flow calderas are the Cenozoic calderas of western North America (e.g., Lipman, 1984). These calderas are scattered across the western U.S.A. from Mexico to Canada, with concentrated clusters in three major Tertiary volcanic fields on the boundaries of the Colorado Plateau (Fig. 1.1): Marysvale (Utah), San Juan (Colorado), and Mogollan Datil (New Mexico). Because most of these calderas are older that 11 million years, they are exposed by erosion to deep levels, so that both volcanic rocks and the upper parts of the cogenetic intrusion are exposed (Lipman, 1984). Some well-known and relatively well-studied examples of mid- to late-Tertiary calderas (Fig. 1.1), which will be referred to in this thesis, are: Creede (Colorado; Steven and Ratte, 1965); Grizzly Peak (Colorado; Fridrich and Mahood, 1984); Lake City, San Juan, Silverton, and Uncompaghre (Colorado; Lipman et al., 1973); Questa (New Mexico; Lipman, 1983); and Timber Mountain (Arizona; Byers et al., 1976). Other examples are listed in Lipman (1984). Several younger caldera structures, less than 1.5 million years old, are also found in the western U.S.A., exposed in their uppermost levels. Examples which have been extensively studied are: Valles (New Mexico, the type example of a resurgent caldera; Smith

and Bailey, 1966); Long Valley (California; Bailey et al., 1976); Yellowstone (Wyoming; Christiansen and Blank, 1972); and Crater Lake (Oregon; Williams, 1942; Bacon, 1983).

Large volume silicic magmas, often associated with volcanic eruptions, are common around the circum-Pacific region. Ash-flow calderas commonly occur in active volcanic arcs (e.g., the Kurile and Aleutian Islands, Kamchatka, Alaska, Japan, Indonesia and the South American Andes). Well-known large volume ash-flow deposits are found in Indonesia (Toba Tuff; Bemmelen, 1949), New Zealand (Taupo volcanic field; Healy, 1964) and Japan (Nohi rhyolites; Kawada, 1971).

### *1.1.3 Historical Perspective*

For many years, ash-flow tuffs, particularly welded deposits, were misinterpreted, in part because they resemble both lava flows and pyroclastic rocks. Our understanding of their origin and depositional environment developed over a long period of time through a series of observations and events. The present conceptions of ash-flow calderas have been strongly influenced by the work of R.L. Smith and his colleagues (Smith, 1960a, b, 1979; Smith and Bailey, 1968; Smith and Shaw, 1975). In a now classic paper, Smith and Bailey (1968) outlined a generalized model of caldera formation and its relationship to ash-flow deposits. This model (Fig. 1.2) includes seven stages of volcanic, structural and sedimentary events: regional tumescence and generation of ring fractures; caldera-forming eruptions; caldera collapse; preresurgence volcanism and sedimentation; resurgent doming; major ring volcanism; and terminal fumarolic and hot spring activity. More recently, Lipman (1984) reviewed the current knowledge of ash-flow calderas, emphasizing variations in eruptive history, volcanic structures, petrologic evolution and tectonic settings. The

general caldera cycle described by Lipman (1984; Fig. 1.3) combines the stages of Smith and Bailey (1968) into three major divisions: premonitory activity; culminating eruptions and collapse; and postcollapse activity. This caldera cycle is similar to the seven-stage cycle of Smith and Bailey (1968) but it emphasizes possible time overlaps between stages, such as eruption and caldera collapse.

## 1.2 The Role of Aqueous Fluids in Caldera Evolution

As in many crustal processes, aqueous fluids play an important role in caldera formation, evolution and cooling. They transport heat, creating hydrothermal systems around cooling sub-volcanic plutons, and chemicals, often being responsible for mineral and ore deposition in and near calderas. Water can also interact directly with magma, as is the case in phreatic and phreatomagmatic eruptions.

### *1.2.1 Hydrothermal Activity*

Caldera formation is commonly accompanied by hydrothermal activity, because a shallow magma chamber is usually present to provide the heat to drive hydrothermal circulation. Hydrothermal activity is most common late in the caldera cycle and thus was considered by Smith and Bailey (1968) to be the final stage in the caldera cycle . Several presently active volcanic fields that have undergone caldera collapse, such as Long Valley (Bailey et al., 1976), Yellowstone (Christiansen and Blank, 1972), and Valles (Smith and Bailey, 1966), are now going through a hydrothermal stage. However, hydrothermal activity can occur at any time during a caldera's evolution provided that the shallow subvolcanic magma chamber is large enough and has risen to a level where the country rocks are sufficiently permeable to ground waters that a hydrothermal circulation system can be established. Some calderas show little or no evidence for

hydrothermal activity and associated mineralization (e.g., Mount Hope caldera, Colorado; Steven et al., 1974), possibly because they have relatively simple structural histories and are not extensively fractured.

The hydrothermal systems associated with calderas are frequently sources of geothermal energy. Consequently, some active hydrothermal systems have been extensively studied. Examples of well-studied geothermal areas are: Valles Caldera, New Mexico (e.g., Hulen and Nielson, 1986; White, 1986; Vuataz and Goff, 1986; Truesdell and Janik, 1986); volcanic fields in Italy (reviewed in Wohletz and Heiken, 1992); and the Taupo Volcanic Zone of New Zealand (reviewed in Wohletz and Heiken, 1992). The hydrothermal system around the Long Valley caldera (California), though it is not a major source of geothermal energy, has also been the subject of much research (Goff et al., 1991; Smith and Suemnicht, 1991; White and Peterson, 1991; Sorey et al, 1978, 1991; Flexser, 1991).

### *1.2.2 Mineralization*

Ore deposits are commonly associated with caldera structures. There are a broad range of types of mineralization, and the ores are deposited in a variety of styles. This point is best illustrated by considering calderas of the western United States where the ore deposits have been studied extensively and where considerable effort has been made to date these ore deposits as well as the calderas. Examples of such ore deposits are: gold and other metals at the Goldfield, Round Mountain and Jefferson calderas in central Nevada (Rytuba and Glanzman, 1979); gold, silver and base metals at the Silverton, Creede and Summitville calderas in the San Juan Mountains of Colorado (Steven et al., 1974); molybdenum at the Questa caldera in northern New Mexico (Lipman, 1983); uranium near calderas of the Marysvale volcanic field in Utah (Cunningham and

Steven, 1979); and major porphyry copper deposits associated with Late Cretaceous to early Tertiary calderas in southern Arizona (Lipman and Sawyer, 1985).

The frequent association of ash-flow calderas with ore deposits is due to the structural controls provided by the calderas (Steven et al., 1974; McKee, 1972; Rytuba, 1981; Lipman, 1992). Caldera-related faults serve as channels for circulating hydrothermal waters, while the shallow magma chamber provides the heat to drive such circulation. The ore potential of this environment is further enhanced by an extended history of igneous and structural activity after caldera subsidence (Steven et al., 1974). In fact, mineralization which is not genetically related to the subcaldera magma chamber can occur in a caldera setting long after caldera collapse (Steven et al., 1974).

### *1.2.3 Water-Magma Interaction*

The study of hydrovolcanism, or the natural phenomena produced by the interaction of magma and/or magmatic heat with an external source of water, is reviewed by Sheridan and Wohletz (1983). The most obvious settings for direct interaction between magma and external water are subaqueous environments, such as submarine, lacustrine or littoral environments. Many studies have documented the deposits and landforms resulting from magma-water interaction in these environments (e.g., Bonatti, 1967; Sigvaldason, 1968; Honnorez and Kirst, 1975; Moore, 1975).

The extent to which external water interacts with magmas during explosive caldera-forming eruptions is not well understood, as it is difficult to observe. Historical caldera-forming ash-flow eruptions are rare, and it is hazardous to monitor them up close. The question of water-magma interaction

during ash-flow eruptions is usually addressed by examining their deposits (e.g., Heiken, 1972; Wohletz, 1983; Heiken and Wohletz, 1985; Cioni et al., 1992).

In some cases, water-magma interaction has actually triggered volcanic eruptions, as is certainly the case for phreatic and phreatomagmatic eruptions. Phreatic eruptions are steam explosions, which occur entirely within the country rock above a magmatic heat source. Examples are crater-producing steam eruptions in Yellowstone (Muffler et al., 1971), Long Valley (Mastin, 1991) and New Zealand (Nairn and Wirdadiradja, 1980). Phreatomagmatic eruptions also involve the conversion of groundwater to steam by a subvolcanic magma, but, by definition, deposits from these eruptions must include clasts derived from the magma. Well-known phreatomagmatic eruptions are the 1888-90 eruptions of Vulcano, Italy (Mercalli and Silvestri, 1891) and those of Surtsey, Iceland in 1963-1964 (Kokelaar, 1983). Large scale infiltration of fluids into a magma chamber during eruption is a more controversial topic (see below and Chapter 4, where the problems associated with low-$^{18}O$ magmas are discussed in some detail).

### *1.2.4 Studying Aqueous Fluids Associated with Calderas*

In regions of active silicic volcanism, aqueous fluids at shallow depths can be monitored directly by sampling on the surface and from drillholes (e.g., White, 1986; Sorey et al., 1991). Deeper fluids can be sensed remotely by geophysical means, such as studies of heat flow (e.g., Ingebretson et al., 1992). In ancient calderas, the hydrothermal fluids involved are not recovered except perhaps in inclusions (e.g., Browne et al., 1976). Evidence for the timing, amounts and transport properties of these fluids is usually indirect, through studies of timing of mineralization, veining and stable isotopes.

## 1.3 Previous Geochemical Studies of Calderas

I have used a variety of geochemical techniques to study the Chegem ash-flow caldera. Previous geochemical studies of rocks associated with ash-flow calderas are too numerous to list here. Many will be mentioned in the chapters of this thesis, which are arranged according to the technique used. Here, I briefly review some important observations and conclusions of previous studies.

### *1.3.1 Major and Trace Elements*

Major and trace element studies of numerous ash-flow sheets have revealed compositional zoning, from silicic at the bottom to more mafic at the top (e.g., Smith, 1979; Hildreth, 1979, 1981; Fridrich and Mahood, 1984). This zonation is believed to represent an inverted view of the compositional zonation at the top of the silicic magma chamber. That is, the ash-flow eruption taps a magma chamber to progressively lower levels as the eruption progresses. There is currently much debate over how this zonation forms. Mechanisms which have been proposed for zonation in rhyolitic magmas are assimilation and/or fractional crystallization (e.g., Noble and Hedge, 1969; Michael, 1983; Johnson, 1989), and liquid state thermodiffusion (Hildreth, 1981).

### *1.3.2 Radiogenic Isotope Studies*

Radiogenic isotope studies of ash-flow calderas are frequently aimed at deciphering the petrogenesis of those magmas. Many of these studies have found that ash-flow tuffs have isotopic signatures which are closer to mantle rocks than to the radiogenic crustal rocks which surround them (e.g., Halliday et al., 1984; Johnson and Fridrich, 1990; Johnson et al., 1990). As a result, it is generally believed that large-volume silicic magma chambers which erupt ash flows originate in the mantle or lower crust. A common scenario (e.g., Johnson et

al., 1990) is one in which silicic magmas are generated by fractional crystallization of substantial volumes of mantle-derived magmas, which have assimilated country rock from the lower, middle and upper crust during their ascent. Isotopic zonations have been observed in various individual ash-flow sheets (e.g., Noble and Hedge, 1969; Stuckless and O'Neil, 1973; Farmer et al., 1991; Johnson and Fridrich, 1990), and are most easily explained by some amount of assimilation.

### *1.3.3 Stable Isotope Studies*

Stable isotope studies of calderas have been useful for deciphering the history of water-rock interaction, especially when meteoric waters are involved. As described above, hydrothermal activity involving meteoric waters is commonly associated with calderas. Several stable isotope studies have been performed to determine the flow pathways and extent of water-rock interaction in these environments (e.g., Lambert and Epstein, 1980; Larson and Taylor, 1986a,b; Smith and Suemnicht, 1991).

Stable isotope studies have also revealed an intriguing phenomenon: the low-$^{18}O$ magma. In a few cases, it has been shown that erupted magmas are significantly depleted in $^{18}O$ relative to "normal" igneous compositions (e.g., Lipman and Friedman, 1975; Hildreth et al., 1984). The origin of these magmas is a subject of controversy. The two main theories are: (1) they are the result of direct interaction between meteoric water and magma (e.g., Lipman and Friedman, 1975; Hildreth et al., 1984); or (2) they are the result of assimilation or melting of large amounts of hydrothermally altered country rock (e.g., Taylor, 1987; Bacon et al., 1989). This debate will be discussed in more detail in Chapter 4.

## 1.4 Description of Thesis Project and Chapters

### *1.4.1 Chegem Caldera Research*

My thesis research has involved an isotopic and petrologic study of the Chegem ash-flow caldera in the north-central Caucasus Mountains of Russia. This research project grew from a co-operative exchange program on "Geological Processes in the History of the Earth" between the U.S. and Russian Academies of Sciences, involving field trips in the Caucasus Mountains of Russia and the Sierra Nevada of the western United States. During the first field season in the summer of 1989, the scientists recognized the great potential of the Chegem caldera as a site for studying processes affecting silicic magmatism. This caldera is unique in the world for its combination of young age, vertical exposure and simple eruptive history.

The following two summers (1990 and 1991) a team of American scientists consisting of Peter Lipman and Ken Hon of the U.S. Geological Survey and myself returned to the Caucasus Mountains together with our Russian counterparts, led by Andrei Tsvetkov and Anatoly Gurbanov. The aim of this research group was to study and sample the Chegem caldera, its outflow sheets and the nearby Eldjurta Granite. My part in this project was to study the fluid flow and related thermal history of this shallow magma system by using various isotopic techniques. The questions I was concerned with were: What was the timing of the eruptive and intrusive events associated with the Chegem caldera? How closely are the Chegem caldera and the Eldjurta Granite related? How quickly did these bodies of rock cool? How were aqueous fluids involved? Did they play a role in the eruption process? Was there any interaction between water and magma before eruption? Was there an active hydrothermal system at any time? Might this caldera lend any insight into the general question of the origin of low-$^{18}O$ magmas?

### *1.4.2 Description of Thesis Chapters*

The chapters in this thesis describe some of my attempts to answer the above questions. Chapter 2 is an overview of the tectonic and geologic setting of the Chegem caldera, including descriptions of the various rock units and their field relationships. Chapter 3 presents an $^{40}Ar/^{39}Ar$ geochronological study of the Chegem volcanic rocks as well as total fusion $^{40}Ar/^{39}Ar$ ages and mineral oxygen isotope data for samples from a four-kilometer drillhole in the Eldjurta Granite. This chapter has been submitted to *Earth and Planetary Science Letters* with co-authors, Marvin Lanphere, Hugh P. Taylor, Jr. and Anatoly Gurbanov. In Chapter 4, the oxygen isotope and major- and trace-element geochemical data are presented for the rocks of the Chegem caldera. This chapter will be submitted to *Journal of Volcanology and Geothermal Research* with co-authors Ken Hon, Hugh P. Taylor, Jr. and Andrei Tsvetkov. Chapter 5 presents a study of the hydrogen isotopic composition and water speciation in glasses from the intracaldera Chegem Tuff. These studies were carried out in collaboration with Sally Newman and Philip Ihinger. Chapter 6 presents strontium isotopic data for the various lithologies in the field area. The strontium isotopic studies were performed in the laboratory of Jason Saleeby. Finally, because all of these data sets are truly intertwined, Chapter 7 summarizes the results of the previous chapters in terms of the overall picture of fluid flow and heat transport in the Chegem system and poses some concluding questions and recommendations for future research.

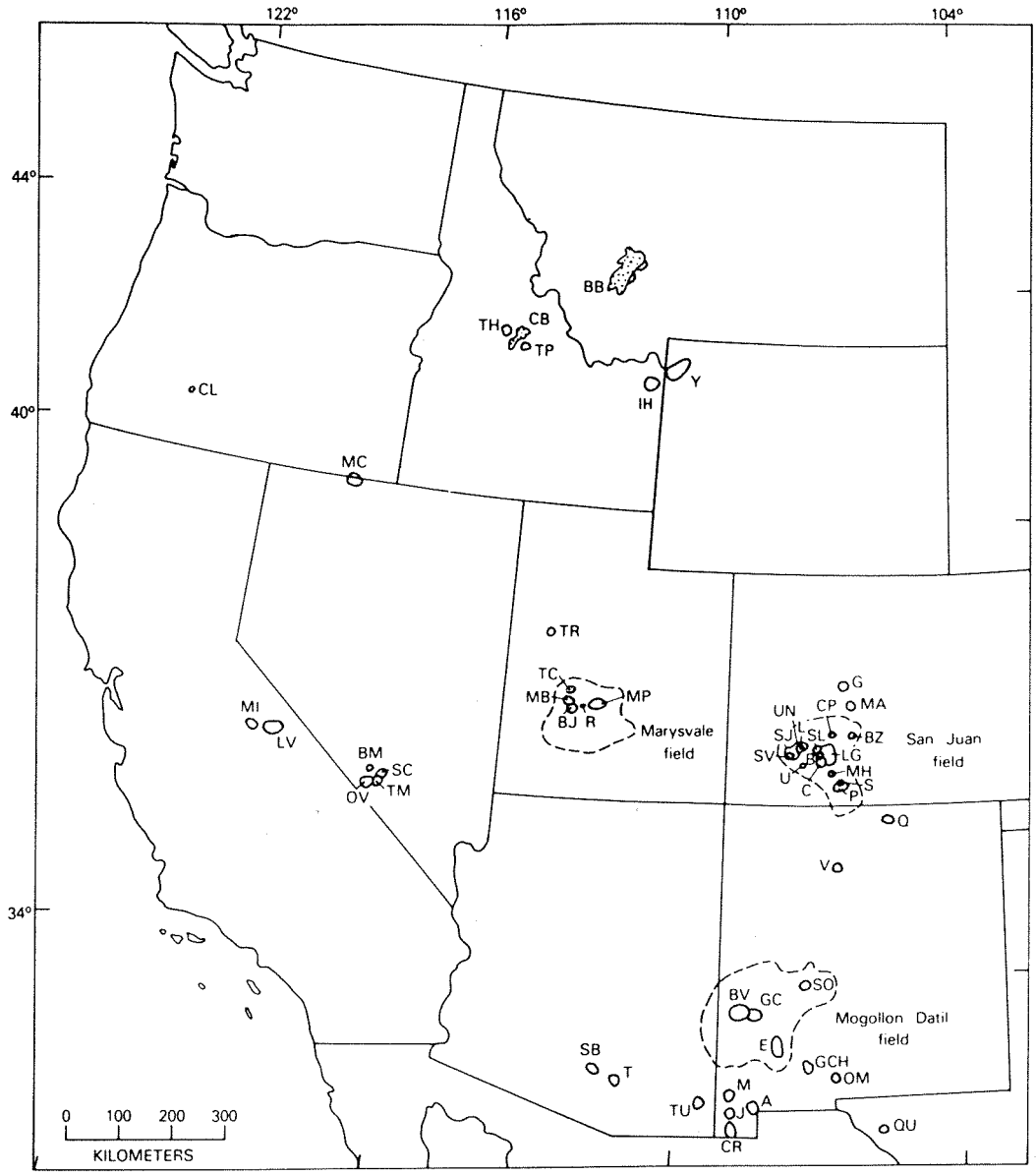


**Figure 1.1** -- Locations of Cenozoic calderas (circles), selected batholiths (coarse stipple), and major Tertiary volcanic fields (dashed lines) in the western U.S. (Fig. 1 from Lipman, 1984). A, Apache; B, Bachelor; BB, Boulder Batholith; BM, Black Mountain; BJ, Big John; BZ, Bonanza; BU, Bursom; C, Creede; CB, Casto Batholith; CH, Chinati; CL, Crater Lake; CP, Cochetopa Park; CR, Cowboy Rim; E, Emory; G, Grizzly Peak; GC, Gila Cliff Dwellings; GCH, Goodsight-Cedar Hills; I, Infiernito; H, Henrys Fork; J, Juniper; L, Lake City; LG, La Garita; LV, Long Valley; M, Muir; MA, Mount Aetna; MB, Mount Belknap; MC, McDermit Complex; MH, Mount Hope; MI, Minarets; MP, Monroe Peak; OM, Organ Mountain; OV, Oasis Valley; P, Platoro; Q, Questa; QU, Quitman; R, Red Hills; S, Summitville; SB, Silver Bell; SC, Silent Canyon; SJ, San Juan; SL, San Luis Peak; SO, Socorro; SV, Silverton; T, Tucson Mountains; TC, Three Creeks; TM, Timber Mountain; TP, Twin Peaks; TH, Thunder Mountain; TR, Thomas Range; TU, Turkey Creek; U, Ute Creek; UN, Uncompahgre; V, Valles; Y, Yellowstone.

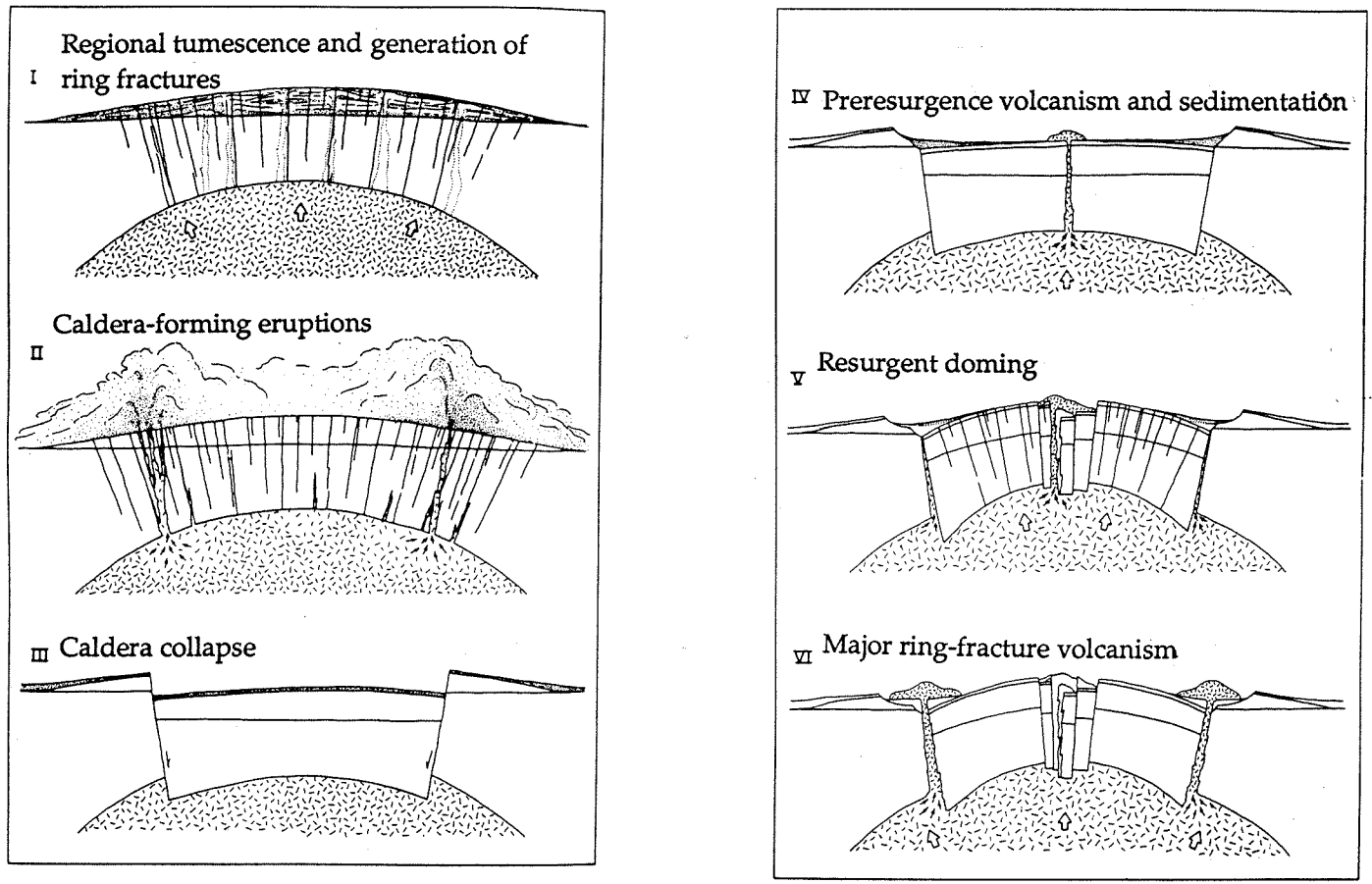


**Figure 1.2** -- Stages in the resurgent cauldron cycle based on the Valles caldera (modified from Smith and Bailey, 1968). Six of the seven stages are shown here: regional tumescence and generation of ring fractures; caldera-forming eruption; caldera collapse; preresurgence volcanism and sedimentation; resurgent doming; major ring-fracture volcanism. The seventh stage, terminal fumarolic and hot spring activity, is not shown.

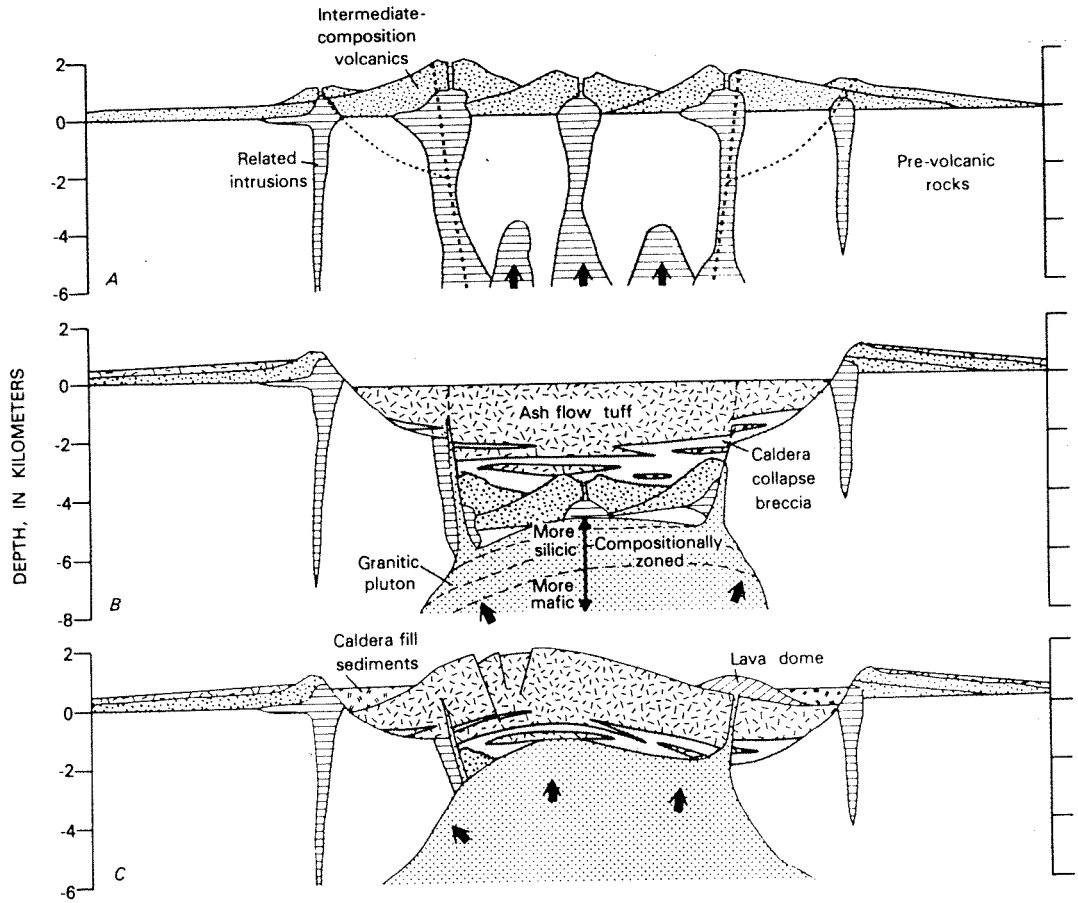


**Figure 1.3** -- A generalized ash-flow caldera cycle (Fig. 3 from Lipman, 1984). (a) Precollapse volcanism. Clustered intermediate-composition stratovolcanoes grow over isolated small high-level plutons that mark beginning of accumulation of batholithic size silicic magma body that will feed ash flow eruptions. Uplift related to emplacement of plutons leads to development of arcuate ring fractures: site of subsequent caldera collapse indicated by dotted lines. Heavy arrows indicate upward movement of magma. (b) Caldera geometry just after ash flow eruptions and concurrent caldera collapse. Central area of clustered earlier volcanoes caves into collapsed area. Intracaldera tuff ponds during subsidence and is an order of magnitude thicker than cogenetic outflow ash flow sheet. Initial collapse along ring faults is followed by slumping of oversteepened caldera walls and accumulation of voluminous collapse breccias that interfinger with ash flow tuff in the caldera fill sequence. Caldera floor subsides asymmetrically and is tilted to the left side of diagram. Main magma body underlies entire caldera area and is compositionally zoned (or was prior to eruptions), becoming more mafic downward. (c) Resurgence and post-caldera deposition. Resurgence is asymmetrical, with greatest uplift in area of greatest prior collapse. Extensional graben faults form over crest of the dome. Some resurgent uplift is accompanied by movement along the ring faults in the sense opposite that during caldera subsidence. Magma body has risen into volcanic pile and intrudes cogenetic intracaldera welded tuff. Original caldera floor has been almost entirely obliterated by rise of the magma chamber to near the level of prevolcanic land surface. Caldera moat is partly filled by lava domes and volcaniclastic sediments. Hydrothermal activity and mineralization become dominant late in cycle.

# Chapter 2. Geologic Background

## 2.1 Tectonic Setting

The Greater Caucasus Mountain Range, a rapidly rising collisional orogenic belt located in southwestern Russia between the Black Sea and the Caspian Sea (Fig. 2.1), is one of the largest mountain belts in Eurasia, rising as high as 5648 m at Mount Elbrus, the tallest mountain in Europe. It represents a central section of the active Alpine-Himalayan system and is presently in the early stages of continental collision. Philip et al. (1989) describe three principle phases in the evolution of this mountain range (Fig. 2.2a-c): (1) From Jurassic to Paleogene times, the Tethys ocean was subducted northward under the Turkish, Lesser Caucasus and Iranian continental blocks. A calc-alkaline volcanic arc was active with a back-arc basin in the position of the present-day Greater Caucasus (Fig. 2.2a). When the Red Sea began to open in the middle-late Miocene, the Arabian Plate began to migrate northward, thus closing the Tethys Sea. (2) The Tethys was closed at about 20 Ma, at which time subduction shifted to the

northern boundary of the back-arc basin. A new episode of calc-alkaline volcanism developed north of the new subduction zone as the back-arc basin rapidly closed (Fig. 2.2b). By Middle Pliocene time, the basin was closed at the northern border of the Lesser Caucasus and the present stage of continental collision began, with oceanic crust remaining on either side of the collision zone (the Black Sea and the Caspian Sea). (3) The present tectonic setting (Fig. 2.2c) is characterized by the on-going collision of the northward-moving Arabian plate with the Russian craton, accompanied by lateral ejection of the Turkish Plate to the west and of the Iranian Plate to the east. Uplift in the Greater Caucasus Mountains began in Middle Pliocene time and volcanic arc activity has continued into the present, represented by Kazbek and Elbrus volcanoes.

The present stage of uplift in the Caucasus Mountains has given rise to a west-northwest trending regional anticlinoral structure. On the north flank of the range, the limb of this structure is a northward-dipping monoclinal section of Jurassic through Plio-Pleistocene strata. The basement is well-exposed in the core of the anticlinoria. The basement rocks to the south are thrust southward over Jurassic through Cretaceous marine strata.

The anticlinoral structure is complicated by thrust and reverse faults, especially on the southern flank, and is intersected and segmented longitudinally by a major north-northeast trending transverse structural zone known as the Trans-Caucasus Rise. Two alternative explanations for the Trans-Caucasus Rise have been proposed: (1) that it represents a wrench system related to the impact of the promontory against the northern edge of the Arabian Plate (Philip et al., 1989); or (2) that it is a northward-propagating extension of the Red Sea rift system (Tsvetkov, 1989).

## 2.2 Regional Geology

The Chegem caldera is located in the intersection zone of the Trans-Caucasus Rise and the long axis of the range. Plate 1 is a geologic map of the central section of the Caucasus Mountains in the vicinity of this zone. The central Caucasus can be divided into four zones from north to south: (1) the Bechasin zone in the north contains mostly northeast-dipping Jurassic-Cretaceous Russian platform strata with local windows into the basement; (2) the Fore Range zone contains crystalline basement rocks, interfolded with Paleozoic marine and volcanic strata. Locally, Jurassic strata overlap these rocks; (3) the Main Range zone comprises the core of the range, consisting almost entirely of crystalline basement. Topographically, it is the highest of the four zones; (4) the Southern Slope zone consists of Jurassic volcanic and marine strata which are in thrust contact with the crystalline rocks of the Main Range zone.

The structural configuration of the core of the Caucasus is the result of several episodes of compressional and extensional tectonics. There is a complicated record of magmatism, sedimentation and tectonic activity from Hercynian time to the late Mesozoic. Then, because of the Alpine and modern uplift and consequent extensive erosion of the Caucasus Mountains, there is a large gap in the preserved geologic history in the core of the range. The only post-Jurassic rocks exposed in the core region are Plio-Pleistocene and Recent volcanic and plutonic associations.

## 2.3 Plio-Pleistocene and Recent Volcanic and Intrusive Rocks

Pliocene to Recent volcanic rocks extend for over 1200 km from Armenia to the Russian craton, trending roughly north-south, in the general vicinity of the Trans-Caucasus Rise (Fig. 2.2c). It appears that this structure, rather than

subduction-related structures, may be controlling the locations of these magma chambers.

Along the axis of the Greater Caucasus, rapid uplift and erosion have exposed extremely young plutonic rocks, usually 1-2 Ma, in the core zone. These so-called "neointrusions" (Gurbanov and Favorskaya, 1977) are exposed where deeply-incised river drainages cut into the high mountains; they are often associated with metallogenic ore deposits. The Eldjurta Granite and the Chegem intracaldera intrusion are members of this belt and thus are probably related to this significant, but volumetrically small pulse of silicic magmatism.

The 2.8 Ma Chegem caldera represents a major episode of Pliocene silicic ignimbrite activity. Remarkably, it is the only known ash-flow caldera in the entire Greater Caucasus Mountains. The Chegem caldera is perched between two active andesitic stratocones, Mount Elbrus (the highest mountain in the range, 5648m) and Mount Kazbek (5043m), and is itself overlain by Pliocene post-caldera andesites.

## 2.4 Rocks of the Chegem Caldera

### *2.4.1 Previous Studies*

The geology around the region of the upper Chegem Valley was first described by Abich (1874) and Levinson-Lessing (1913), and later in more detail by Soloviev (1938) and Masurenkov (1957, 1961). In the middle 1950s, the area was mapped by Sedenko and Rzhevinsky, members of the Northern Caucasus Territorial Geological Survey (SKTGU) from the USSR Ministry of Geology. From the late 1950s to the 1970s, the Pliocene volcanic rocks of the Chegem caldera were studied by E. Milanovsky and his student N. Koronovsky (Milanovsky and Koronovsky, 1961, 1973; Milanovsky et al., 1962). Koronovsky continued this mapping, later joined by Molyavko and Ostafiychuk of Kiev

University (Koronovsky, 1975, 1976a, b, 1983a,b; Koronvsky et al., 1982). Koronovsky and his co-workers described the rocks of the Chegem caldera as rhyolite (liparite) lava flows with tuffaceous horizons. They interpreted the volcanic rocks of the lower Chegem Valley as ash-flow tuff erupted from local vents. Recently, the present research group reinterpreted both upper and lower Chegem volcanic rocks as ash-flow from a single eruption at the Chegem caldera (Bogatikov et al., 1992; Lipman et al., 1993). The difference in thicknesses and resultant welding styles are responsible for the different appearance of the intracaldera tuff and its earlier interpretation as lava. Lipman et al. (1993) provide a description in English of our present knowledge of the Chegem caldera.

### *2.4.2 Field Relationships and Structure*

The Chegem caldera (Fig. 2.3) formed during a single eruptive event 2.8 million years ago. The 11x15 km structure collapsed along arcuate ring faults and was filled with a thick sequence of ash-flow tuff, locally interlayered with breccia of the surrounding country rock which fell into the caldera along the over-steepened ring faults. Recent rapid uplift and erosion in the Caucasus Mountains has exposed over two kilometers of stratigraphic thickness in the caldera fill, but no pre-caldera floor is exposed. The welded tuff within the caldera is resistant to erosion, and so the caldera fill stands out as a topographic high beside the Chegem River. Bedding within the caldera fill, defined by the orientation of flattened pumices, is subhorizontal; this indicates that there has been little, if any, caldera-wide resurgent doming.

In the northeast quarter of the caldera, a granodiorite porphyry has intruded along the caldera ring fault, pushing up a block of intracaldera tuff in piston-fashion along high angle faults (Fig. 2.3). A foundered block of Chegem

Tuff is present in the northeast section of this intrusion. In the southern and western sides of the caldera, the intracaldera tuff is capped by post-caldera andesite flows. Generally, these flows are stratigraphically above an erosional horizon which contains glacial deposits. Thus a glaciation event occurred between the time of deposition of the tuff and the eruption of the andesites; locally, however, the andesites appear to rest directly on poorly-welded intracaldera tuff.

Outside the caldera structure, the Chegem Tuff is more poorly welded and thus less resistant to weathering. Nevertheless, it is preserved as small erosional outliers in the vicinity of the caldera and as larger outflow remnants in the lower Chegem Valley. These are found up to 50 km away from the margin of the caldera, where they dip below more recent deposits on the stable craton. These outflow tuff sheets are exposed on both sides of the Chegem and Baksan River valleys, where they filled broad, shallowly sloping (2-5°) paleovalleys. Exposed thicknesses of outflow tuff range from a few tens to several hundred meters. The original top of the outflow sheet is not preserved, and the base is usually covered by talus.

The country rock around the Chegem caldera can be classified in two groups: Paleozoic and Proterozoic crystalline rocks of the Main Range Zone to the southwest of the caldera, and Jurassic marine strata of the Bechasin Zone to the northeast (Fig. 2.3). The contact between the two rock groups is a regional unconformity which is locally faulted along transverse fault structures. The Jurassic strata are openly folded, as well as being tilted along the outer ring faults of the caldera.

### *2.4.3 Intracaldera Chegem Tuff*

The intracaldera Chegem Tuff is compositionally-zoned, ranging from silicic rhyolite (76 wt% $SiO_2$) at the lowest exposure to silicic dacite (69 wt% $SiO_2$) at the top of the section. Phenocrysts of quartz, sanidine, plagioclase, biotite, and pyroxene with minor magnetite and ilmenite constitute approximately 20% of the rock. These phenocrysts vary in abundance with the compositional zoning; the rhyolite contains predominantly quartz and sanidine, whereas in the dacite, the phenocrysts are predominantly plagioclase, biotite and pyroxene. Intracaldera tuff is typically moderately to densely welded with ubiquitous flattened pumices, usually about 1-5 cm in length with compaction ratios of 3:1 to 5:1. The lower 1000 m of exposed caldera fill is fairly massive with cooling joints passing through the section, indicating that the bulk of the intracaldera tuff cooled as a single unit. However, there are welding variations, including one distinct horizon of poorly-welded tuff toward the middle of the section (at 3160m elevation), which suggests that there were brief interruptions in the caldera-forming eruption.

The upper dacitic section of tuff has at least two, and possibly three, distinct cooling subunits that are 30-50 m thick. Cooling breaks are defined by 2-3 m zones of flattened vitrophyric pumice at the base of each subunit. The uppermost dacitic subunit is capped by 20m of tan, nonwelded tuff that marks the top of the intracaldera ash-flow sequence. Emissions were apparently more sporadic in the waning stages of eruption. However, there are no erosional horizons anywhere in the intracaldera tuff stratigraphy, implying that there were no major interruptions to the caldera-forming eruption. Thus, the intracaldera Chegem Tuff is considered to be a complex cooling unit with discernible cooling subunits (such as the dacitic horizons).

Vitrophyric horizons are preserved at and near the marginal contacts between tuff and wallrock, occurring as discrete layers, as dikelike structures or as more complexly-shaped zones where the cooling of the tuff has been controlled by irregularities (such as water content?) in the adjacent wallrocks. Glassy pumices, up to 15 cm in length, are preserved in the upper 100-200m of dacitic tuff.

### *2.4.4 Outflow Chegem Tuff*

The outflow tuff of the lower Chegem Valley is predictably much less densely welded than the intracaldera tuff. At distal sites, where the thickness of outflow tuff is 50 m or less, the tuff is only partly welded and displays strong vapor-phase crystallization, whereas in the thicker sections, the tuff is densely welded in the interior with well-developed columnar jointing.

A nearly complete section of outflow tuff is located near the town of Lechnikai, exposed for ≈100-200 m in natural and quarry outcrops. There, the outflow tuff is rhyolitic in composition, ranging from 73 to 75% $SiO_2$. Large black glassy pumices (fiamme, up to 5 cm) are preserved toward the top of this section. At least two other pumice types are present in the upper interior exposures. Phenocryst content, biotite content, and pumice diversity increase upward in the outflow tuff. At the top of this outflow remnant, there is a large quarry, the Lechnikai Quarry, which contains tuff with a light brown, devitrified matrix and black glassy rhyolitic pumices.

### *2.4.5 Granodiorite Intrusion*

The intracaldera granodiorite intrusion, exposed for 1100m vertically in the northeast part of the caldera, is locally steep-walled with a gently dipping roof zone. The intruded tuff was probably not completely cooled when the

pluton intruded, but it was brittle enough to fracture along faults as the pluton pushed a block of tuff upward.

The granodiorite is porphyritic, with phenocrysts of plagioclase, quartz, biotite, rare sanidine and locally magnetite in a groundmass of fine-grained quartz and feldspar. The groundmass constitutes up to 60% of the rock and displays both aplitic and felsitic (near contacts) textures. Compositionally, the granodiorite is similar to late-erupted tuff with 70-72 wt% $SiO_2$. The margins of the intrusion tend to be more granitic (quartz-rich) with local zones of miarolitic cavities.

Within the intrusion, sparse inclusions of porphyritic andesite were found. These inclusions are rounded and embayed with locally finer-grained borders; they are thought to represent more mafic magma that was incompletely mixed with the granodiorite (Lipman et al., 1993). Lipman et al. (1993) suggest that the granodiorite may represent the core of a post-caldera volcano that has now been removed by erosion.

### *2.4.6 Andesites*

The andesitic lava flows which cap the intracaldera tuff sequence are chiefly found at the tops of three peaks: Bolshaya (Big) Kum Tyube and Malaya (Little) Kum Tyube in the southeast; and Mt. Kyugenkaya in the west. The flows are up to 200-300 m thick with an unknown thickness eroded from above. On Mt. Kyugenkaya, as many as eight separate flows 10-50 m thick are discernible.

On Bolshaya and Malaya Kum Tyube, eruption of the andesites was preceded by erosion and deposition of glacial deposits. Because of this glacial erosion, the andesite flows do not necessarily lie entirely at the highest stratigraphic level of tuff; some of the flows also fill paleovalleys which cut into

the intracaldera tuff sequence. In contrast, the andesite flows on Mt. Kyugenkaya lie directly on intracaldera tuff with no obvious erosional breaks.

The andesites contain 10-40 volume% phenocrysts of plagioclase (andesine-labradorite), pyroxene, amphibole and biotite. The groundmass is usually crystalline and fine-grained, although at the base of some flows glasses are still preserved in the groundmass. Microdiorite inclusions (2-5cm) are common in the andesites. They may represent chilled margins ripped from dike walls during eruption (Lipman et al., 1993). A single altered basaltic inclusion, in an andesite flow near Mt. Kyugenkaya, is the most mafic sample found among the intracaldera rocks.

### .2.4.7 *Basaltic Andesite*

One important difference between the Chegem caldera and most other ash-flow calderas is that its formation was not preceded by significant precaldera volcanism. However, a single basaltic andesite flow, located beside and topographically below one of the outflow tuff remnants, is a notable exception. This flow has a typical basaltic texture with a finer-grained, quenched base and a highly vesicular top. The basaltic andesite contains olivine phenocrysts in a dark, aphanitic matrix. In addition, distinctive quartz xenocrysts rimmed with augite are present in the rock.

## 2.5 Eldjurta Granite

The Eldjurta Granite (Fig. 2.4; also called the Eldzhurtinskiy Granite) is exposed in the valley of the Baksan River, the next river to the north of the Chegem River. The surface exposure covers an area of 8 $km^2$ and 1150 m of vertical relief. In addition, mineral-exploration drillholes have been placed in the granite, the deepest of which extends to a depth of 4 km. The granite is similar in

age and composition to the Chegem volcanic rocks, and thus it has been suggested that they constitute a single, physically continuous magma system (Lipman et al., 1993).

Throughout its entire sampled thickness, the Eldjurta Granite is texturally and compositionally remarkably uniform. It is porphyritic with large phenocrysts of K-feldspar and a fine- to medium-grained matrix of quartz, K-feldspar, plagioclase (An 16-37) and biotite with trace amounts of apatite, sphene and zircon. The margins of the granite are finer-grained, more equigranular and often more mafic than the interior of the intrusion. Sparse mafic inclusions are also present in the granite.

### *2.5.1 Rhyolite Necks*

Three large porphyritic rhyolite necks cut through the Eldjurta Granite, on its northwest side. The necks are about 500 m in diameter and dip steeply. The rhyolites are similar in bulk composition to the Eldjurta Granite and contain phenocrysts of quartz, K-feldspar and some plagioclase. Smaller dikes of andesite and non-porphyritic rhyolite are associated with the rhyolites.

### *2.5.2 Tirniauz Ore Deposit*

The Eldjurta Granite has been the subject of much research because it is located adjacent to the Tirniauz ore deposit, Russia's largest source of tungsten and a major source of molybdenum. The Tirniauz deposit, whose geology has been described in detail, especially in the Russian literature (e.g., Khruschev, 1958; Pek, 1962; Semochkin, 1969; Liakhovich, 1976; summary in English by Smirnov, 1977), is located at the upper contact of the Eldjurta Granite. The mineralization is associated with amphibole-biotite hornfels and pyroxene-garnet skarn zones which, like the granite, lie in a block between two WNW-

trending regional faults. Though the deposits are adjacent to the Eldjurta Granite, the molybdenum mineralization appears to be genetically related to two small (<1 km) leucogranite bodies.

The relationship of the ore deposit to the Eldjurta Granite is an on-going topic of debate. Many researchers have assumed the Eldjurta Granite, leucogranites and Tirniauz deposits are genetically related because of they appear to be closely associated in time and space (Smirnov, 1977). The recent study of Zhuravlev and Negrey (1993, 1994), who found that Rb/Sr isochron ages for the Eldjurta Granite and an ore metasomatite are identical, supports this view.

On the other hand, several arguments have developed against this theory. Theoretical calculations suggest that the Eldjurta Granite could not have generated enough heat to produce the large hornfels and skarn zone associated with the mineralization (Lyakhovich, 1953, 1976; Rodzyanko, 1969; Rodzyanko et al., 1973). However, this argument was developed before the deep drillhole revealed that the Eldjurta Granite is actually a very large body, possibly of batholithic dimensions. Another argument against a genetic relationship between the Eldjurta Granite and the Tirniauz deposits is that the leucogranites with which the deposits are most closely associated have yielded K-Ar ages of 20 Ma (Borsuk, 1979) and data of Arakelyants et al. (1988) suggests that this may in fact represent a resetting age. Nonetheless, even those who argue against a direct genetic relationship between the Eldjurta Granite and the Tirniauz deposit acknowledge that there may be an indirect relationship. The Eldjurta Granite may have initiated a hydrothermal convection cell which remobilized the Mo-W concentrates and deposited them in their present location.

## 2.6 Sampling for This Study

Given the excellent 3-dimensional exposure in this young silicic magma system, our research group made an effort to sample the various lithologies at a range of stratigraphic and structural levels, with an emphasis on sampling the Chegem caldera stratigraphy in detail and attaining samples from the 4-km deep drillhole in the Eldjurta Granite. The surface exposures of the Chegem caldera span over 2 km, while the Eldjurta Granite is exposed for over 1 km above the Baksan River valley where the deep drillhole is sited. Thus, the combined structural thickness which we sampled was over seven kilometers. In two summers of fieldwork, we collected (and transported to the U.S.) over 250 samples. Field descriptions of these samples are given in Appendix A. Locations of the Chegem caldera samples are shown on Plate 2.

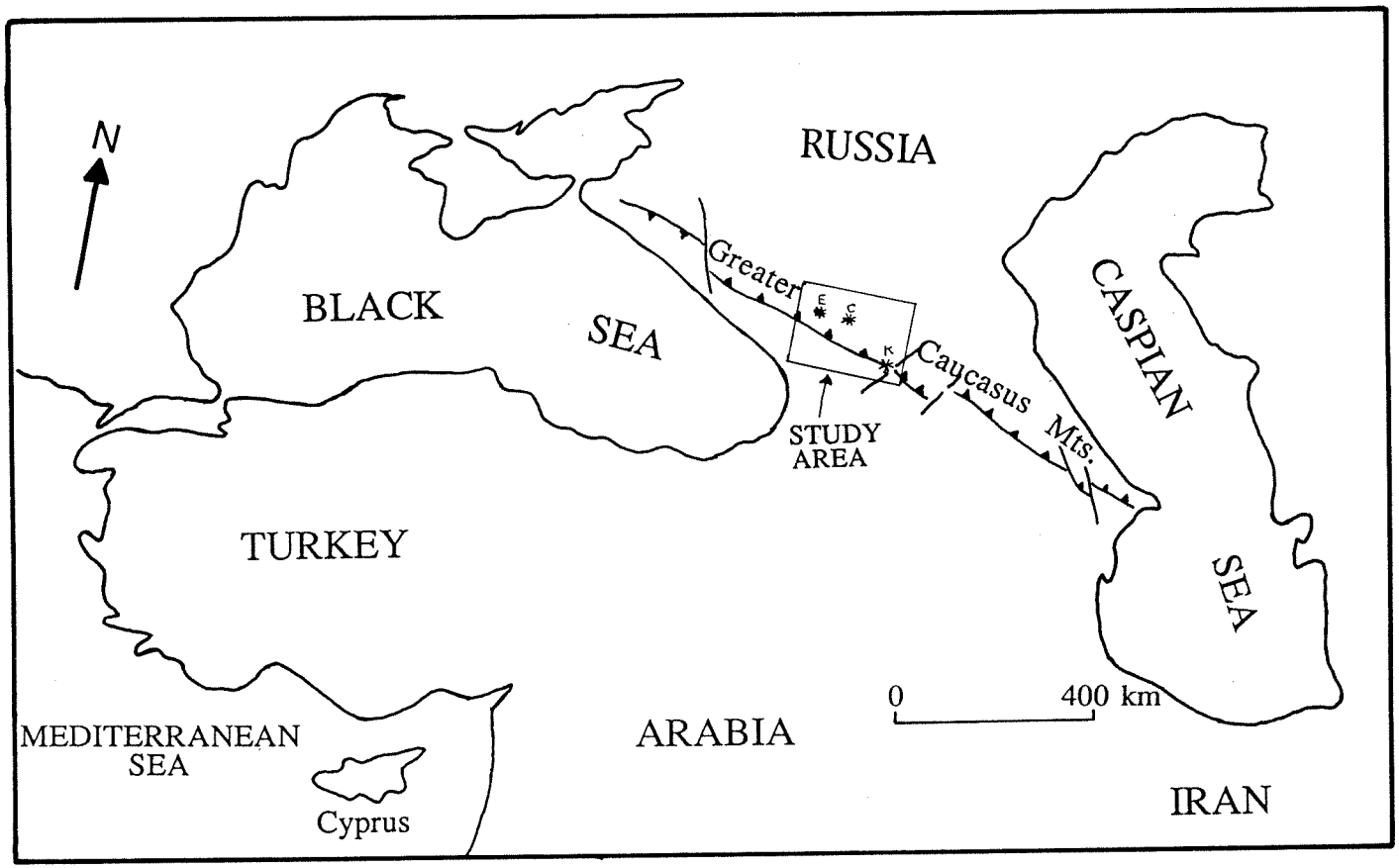


**Figure 2.1** -- Location map for Greater Caucasus Mountains. The box outlines the area of Plate 1. E = Elbrus volcano; C = Chegem caldera; K = Kazbek volcano

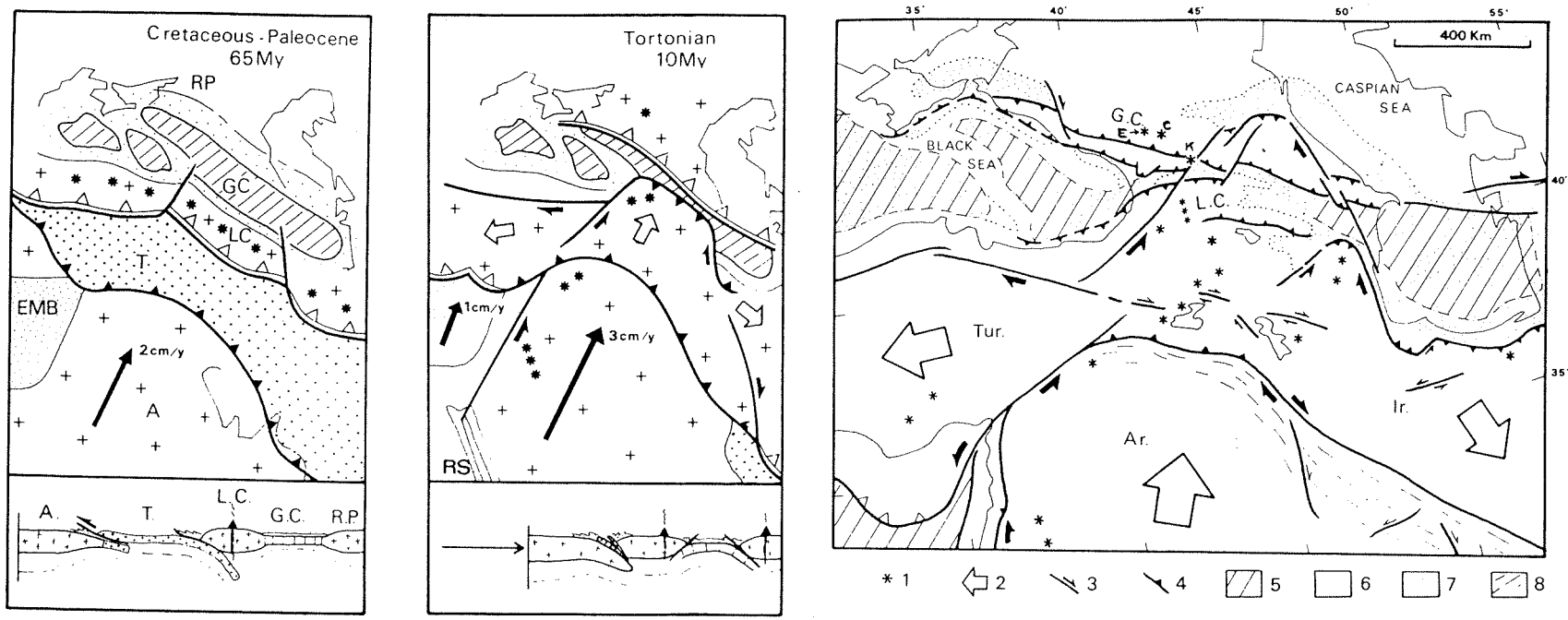


**Figure 2.2 --** Tectonic setting of the Caucasus Region (modified from Philip et al., 1989). (a) 65 million years ago - map (present-day coastline of Black Sea and Caspian Sea given for reference) and N-S cross section. A = Arabian Plate; T = Tethys Ocean; LC = Lesser Caucasus; GC = Greater Caucasus; RP = Russian Platform; EMB = East Mediterranean Basin; RS = Red Sea; large arrows indicate motion relative to Eurasia; open triangles show sense of subduction; closed triangles show obduction or thrusts; stars are volcanoes. (b) 10 million years ago - map (present -day coastline of Black Sea and Caspian Sea given for reference) and N-S cross section. (c) Present-day tectonic setting. 1 = recent volcanoes; 2 = relative motion with respect to Eurasia; 3 = major strike-slip fault; 4 = major thrust fault; 5 = oceanic or intermediate crust; 6 = continental crust; 7 = main sedimentary basin; 8 = recent folding at the border of the Arabian plate; E = Elbrus volcano; C = Chegem caldera; K = Kazbek volcano; Tur. = Turkish block; Ir. = Iranian block

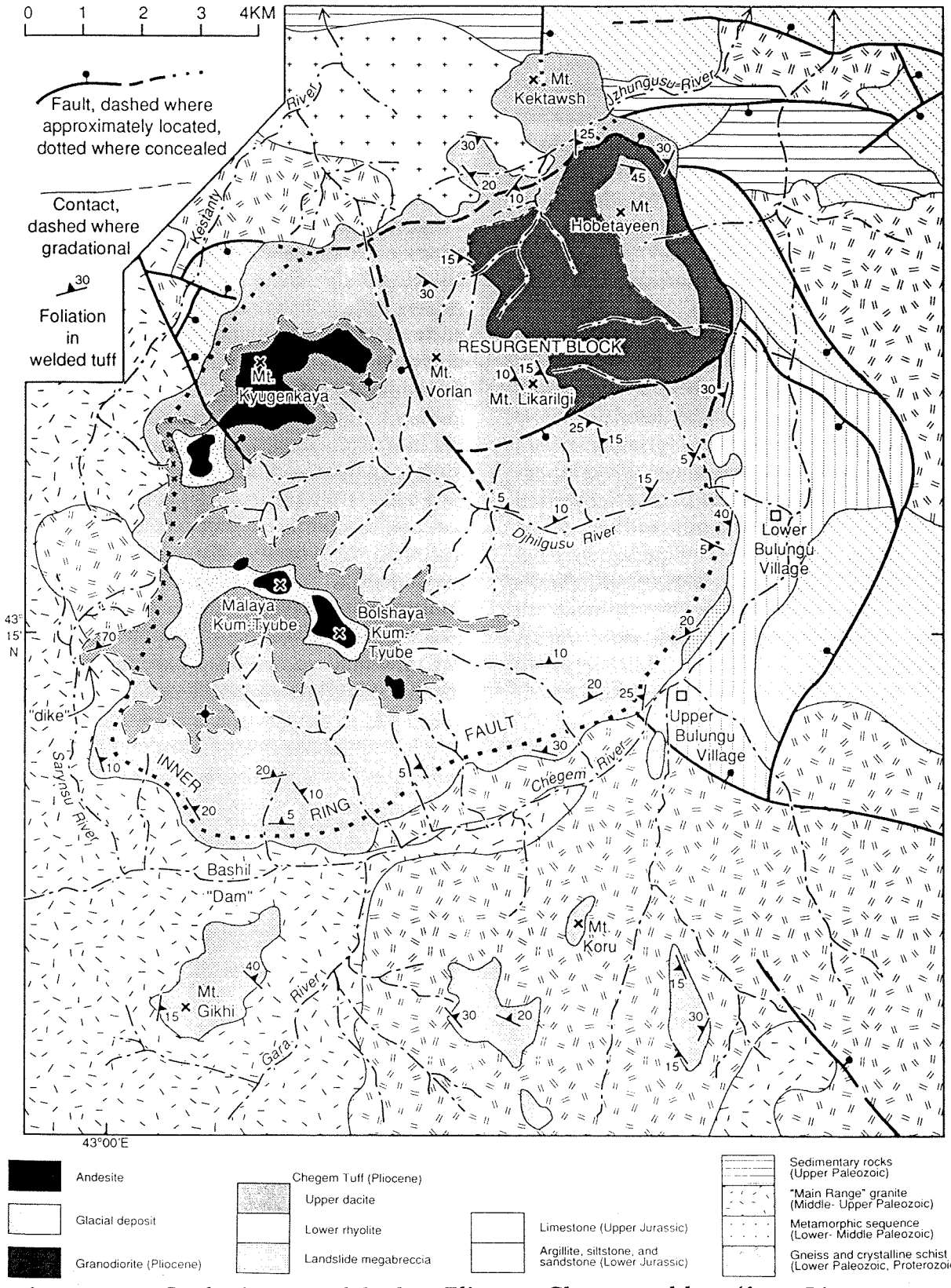


**Figure 2.3** -- Geologic map of the late Pliocene Chegem caldera (from Lipman et al., 1993). Precaldera geology modified from Milanovsky and Koronovsky (1961) and Koronovsky (1976).

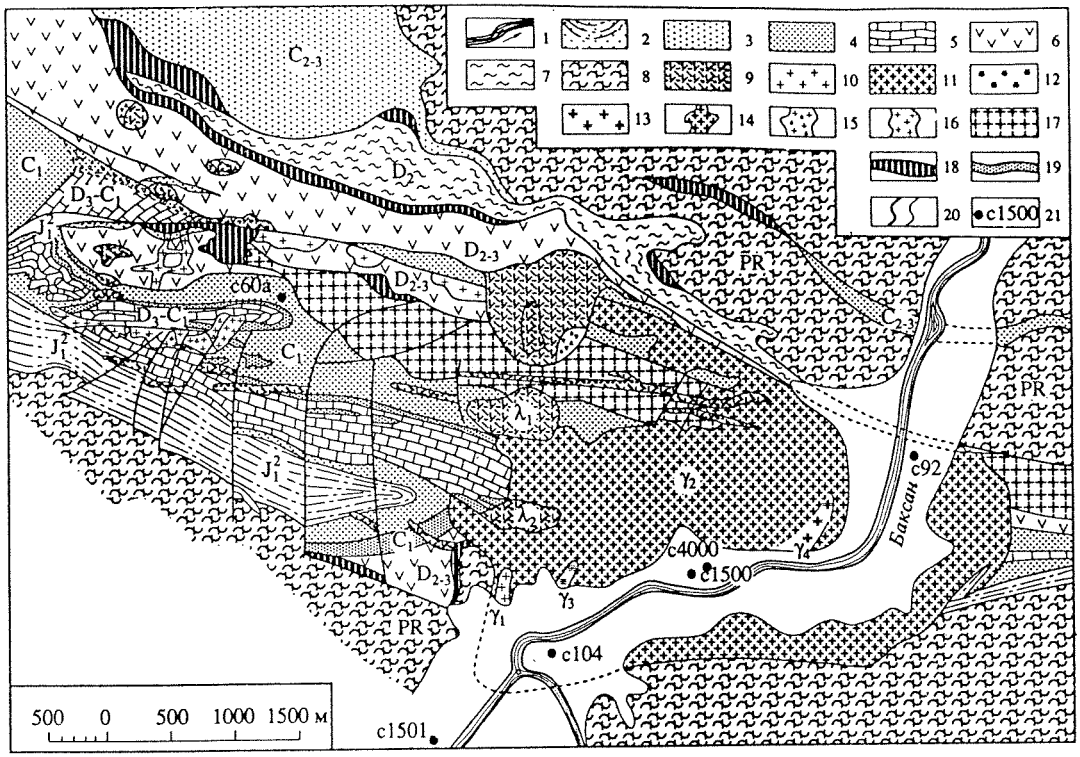


1 - alluvial deposits and rivers. 2 - Lower Jurassic argillites, sands and conglomerates. 3 - Upper Carboniferous molasse. 4 - Lower Carboniferous carbonates. 5 - Upper Devonian-Lower Carboniferous carbonates. 6 - Upper Devonian volcanogenic rocks. 7 - Middle Devolian phyllite. 8 - Proterozoic metamorphic rocks (schist, gneiss, migmatite). 9 - liparites. 10-13 - Eldjurta Granite (10 - Phase 1; 11 - Phase 2; 12 - Phase 3; 13 - Phase 4). 14-16 - leucocratic granitoids (14 - two-feldspar granite; 15 - intrusive breccia; 16 - granite prophyry). 17 - tonalite and plagiogranite. 18 - ultrabasite. 19 - skarn. 20 - contacts and faults. 21 - number of drillhole.

**Figure 2.4 --** Geologic map of the Eldjurta Granite and the surrounding country rocks (from Sobolev and Kononov, 1993). The Eldjurta Granite is represented by patterns 10-13. The 4-km deep drillhole is number c1500.

# Chapter 3. An $^{40}Ar/^{39}Ar$ Study of the Chegem Ash-flow Caldera Including $^{18}O/^{16}O$ and $^{40}Ar/^{39}Ar$ Analyses from a 4-km Deep Drillhole in the Eldjurta Granite (Caucasus, Russia)

*(Submitted to Earth and Planetary Science Letters, coauthors are Marvin Lanphere, Hugh P. Taylor, Jr. and Anatoly Gurbanov)*

## 3.1 Introduction

Because of their combination of youth, exposure and simplicity, the Chegem caldera and the related Eldjurta Granite in the northern Caucasus Mountains of Russia offer a unique opportunity to study high-level silicic magmatic systems. The Chegem caldera rocks are late Pliocene in age, but because of the rapid uplift of the Caucasus Mountains, a 2-km thick section of caldera fill is exposed in deeply incised river drainages. Several drillholes, originally intended for mineral exploration, but later used for scientific research, have been sited in the Eldjurta Granite, which is exposed in an adjacent river valley. These drillholes extend as deep as 4 km below the river valley, whereas

the roof of the granite is 1150 m above the river valley. Accordingly, an overall structural thickness of at least 7 km can be sampled in this young magmatic system. The Chegem caldera is structurally simple, containing a single cooling unit of caldera-filling welded tuff and little evidence for precaldera volcanism. A small resurgent pluton in the northeast region of the caldera has faulted the caldera fill and pushed up a block of tuff, somewhat analogous to resurgent structures in calderas elsewhere (e.g., Grizzly Peak, Colorado; Fridrich et al., 1991). However, this resurgence has not significantly domed the intracaldera tuff as is commonly observed (e.g., Yellowstone, Wyoming, Christiansen, 1990; Long Valley, California, Bailey et al., 1976). Petrographically, the Chegem caldera rocks and the Eldjurta Granite typically show only minor amounts of hydrothermal alteration.

The $^{40}Ar/^{39}Ar$ method of K/Ar dating has allowed us to decipher the chronology of igneous processes, particularly volcanic processes, with high resolution. Incremental-heating experiments are useful in eliciting information about the cooling history of plutonic and metamorphic rocks. Previous conventional K-Ar age measurements on minerals from Chegem caldera rocks and some of the related intrusives gave ages ranging from 1.2 to 3.0 Ma (Borsuk, 1979 - discussed in detail below). The uncertainties on these age estimates are as high as 0.2 Ma, about 10% of the age estimate itself. Our $^{40}Ar/^{39}Ar$ studies were undertaken to refine these earlier age estimates for the Chegem volcanic rocks, as well as to address some basic questions about caldera formation: Can $^{40}Ar/^{39}Ar$ ages resolve the time difference between cooling of the deep interior and the outer edge of a single thick cooling unit of welded tuff? How closely after the eruption of the ash flow were the intracaldera intrusion and the post-caldera andesites emplaced? What is the temporal relationship between the Eldjurta Granite and the Chegem volcanic and intrusive rocks?

The Eldjurta Granite has recently been studied in detail by Hess et al. (1993), who obtained $^{40}Ar/^{39}Ar$ ages for biotites from 7 samples, taken from a horizontal and vertical profile through the granite body. Two of these samples were from the deepest drillhole (4 km deep). Hess et al. (1993) also compared ages of different grain-size fractions of biotite and found a rough correlation between biotite age and grain-size. Our study of the Eldjurta Granite expands on the Hess et al. (1993) study: 8 of our samples are from the 4-km drillhole, providing a much more extensive vertical profile than has heretofore been sampled. In addition to biotite total-fusion ages for these drillhole samples, we measured K-feldspar total fusion ages and two plagioclase incremental-heating age spectra. Our data can be compared to the data of Hess et al. (1993) and combined with those data to further constrain the uplift and cooling history of the granite pluton. These two data sets are the first $^{40}Ar/^{39}Ar$ data which span such an extensive vertical profile in a single young pluton.

In this chapter, we present $^{40}Ar/^{39}Ar$ results for 3 whole rocks and 32 mineral separates (biotite, K-feldspar and plagioclase) from 20 samples. Argon was extracted from irradiated samples by two methods: total fusion of biotite and K-feldspar using a continuous Ar laser; and incremental heating of plagioclase and whole rock using a resistance-heated furnace. We also present oxygen isotope data for mineral separates from the Eldjurta Granite; the oxygen data can be combined with the argon data to determine the role of hydrothermal fluids in the granite's cooling history.

### 3.2 Previous Geochronology

The most complete geochronologic analysis of the Chegem volcanic and intrusive rocks prior to the present work was a K-Ar study by Borsuk (1979), whose results are listed in Table 3.1 and described below. The most complete

thermochronologic study of the Eldjurta Granite was performed by Hess et al. (1993). Some of their results are shown in Fig. 3.8 and described below.

### *3.2.1 Chegem Volcanic Rocks and Porphyry Intrusion*

At the time of Borsuk's work, the rhyolite of the Chegem highland was not recognized as tuff, as fill within a caldera structure, or as correlative with the outflow tuff to the north. Within the caldera fill, sanidine from a gray tuff near the base of the caldera fill sequence gave an age of 3.0 ± 0.2 Ma and sanidine from a black vitrophyric rhyolite, presumably from the margin of the caldera, yielded an age of 2.8 ± 0.2 Ma (Borsuk, 1979). Biotite from an outflow tuff sample on the Jungusu plateau, 15km NNE of the caldera gave an age of 2.5 ± 0.2 Ma (Borsuk, 1979).

Of the post-caldera rocks, biotite from the cross-cutting granodiorite porphyry was dated at 2.6 ± 0.2 Ma (Borsuk, 1979). The caldera-capping andesite was not dated, but an andesite dike in the Baksan River valley yielded a biotite age of 1.2 ± 0.2 Ma (Borsuk, 1979).

### *3.2.2 Eldjurta Granite*

Borsuk (1979) obtained K/Ar biotite and K-feldspar ages for surface samples of the Eldjurta Granite of 1.8-1.9 ± 0.15 Ma, while an associated rhyolite dike within the granite yielded an age of 1.8 ± 0.25 Ma. More recently, Hess et al. (1993) completed an $^{40}Ar/^{39}Ar$ study of biotite from 7 samples of Eldjurta Granite, including 4 drillhole samples. Their biotite ages range from 2.48 ± 0.03 Ma at the roof to 1.26 ± 0.03 Ma at a depth of 3825 m in the deepest drillhole. They note that $^{40}Ar/^{39}Ar$ ages for biotites of different sieve fractions from the same sample are discordant, that there is a general correlation between grain size and age, and that for a given sieve fraction there is a steady decrease in age with

depth. However, the smallest sieve fractions (50-100 μm) do not follow this trend.

Recently, Zhuravlev and Negrey (1993, 1994) determined Rb-Sr isochron ages of 1.98 ± 0.01 Ma for a surface Eldjurta Granite sample and 1.96 ± 0.02 Ma for an ore-bearing metasomatite from the Tirniauz Mo-W deposit. These isochron ages were based on density separates of 3 minerals (biotite, K-feldspar and plagioclase) for the granite and two minerals (amphibole and biotite) for the metasomatite.

## 3.3 Samples Studied

Twenty-three samples were examined in this study: 5 intracaldera Chegem Tuff samples, 3 outflow Chegem Tuff samples, one intracaldera granodiorite porphyry, 3 andesites and 11 Eldjurta Granite samples. The sample locations are shown on Fig. 3.1 (the geologic map of the area) and Figs. 3.2 and 3.3 (cross sections through the Chegem caldera and the Eldjurta Granite). The units and samples are described below.

### *3.3.1 Chegem Tuff*

The intracaldera tuff, exposed over a vertical distance of 2 km on the northeast side of the Chegem River, ranges from silicic rhyolite (76% $SiO_2$) at river level to silicic dacite (69% $SiO_2$) high in the section. This entire section appears to be a single cooling unit with no evidence for significant interruptions during deposition. Black vitrophyre zones (5-20 m thick) are well developed at the margins of the intracaldera tuff, and black glassy pumices (fiamme) up to 15 cm in length are abundant in the upper 200-300 m of section.

The Chegem Tuff contains approximately 20% phenocrysts of quartz, plagioclase (An32-47), sanidine, biotite and pyroxene. Quartz and sanidine are

more abundant low in the section; pyroxene only occurs in the upper, dacitic tuff. Generally, phenocrysts are fresh with little evidence for hydrothermal alteration. However, biotite deep in the caldera fill and near the granodiorite porphyry intrusion has been extensively altered to magnetite + feldspar.

Five samples were collected from the intracaldera tuff (Fig. 3.2): one marginal vitrophyre (MV), representing early-cooled tuff; two densely-welded, devitrified tuffs from deep in the interior of the caldera (DI), presumably the most slowly-cooled samples available; and two glassy dacitic pumice lenses (DP) collected high on the southwest side of the caldera.

### 3.3.2 *Granodiorite Porphyry*

Across a 4x5 km area in the northeast quadrant of the Chegem caldera, a porphyritic granodiorite intrusion has uplifted in piston-fashion a block of rhyolitic tuff at least 300 m to the level of silicic dacites in the south and west. The intrusion, exposed for 1100 m vertically, is locally steep-sided with a gently dipping roof zone on its south side.

Compositionally, the granodiorite is similar to late-erupted dacitic Chegem Tuff, although locally at its margins the porphyry is granitic and more fine-grained with zones of miarolitic cavities. The granodiorite consists of plagioclase (An38-61), biotite and K-feldspar (sanidine?) phenocrysts in a groundmass of fine-grained quartz and feldspar. As in the deeper part of the intracaldera welded tuff, biotite is extensively altered to magnetite + feldspar while feldspar is largely unaltered. A single granodiorite (GD) sample was collected several meters from the southeastern margin of the intrusion.

### *3.3.3 Andesite*

Andesite flows cap the southern and western parts of the Chegem caldera. In the west, as many as 8 separate flows (10-50m thick) can be discerned on Kyugenkaya Peak, where flows appear to overlie intracaldera tuff directly. In the southeast, on Kum Tyube Peak, andesite flows were preceded by variable erosion and overlie glacial deposits above Chegem Tuff. Thus, there is the possibility of two or more generations of andesite flows. The two andesite samples of this study were collected from Kyugenkaya (A-KY) and Kum Tyube (A-KT) Peaks (Fig. 3.1).

### *3.3.4 Outflow Tuff*

Erosional remnants of outflow Chegem Tuff are exposed up to 50 km to the north of the caldera in the lower Chegem and Baksan River valleys. The outflow tuff filled paleovalleys and was later dissected by these modern rivers. The outflow facies ranges from tens to hundreds of meters in thickness and is compositionally similar to the lower to middle section of the Chegem caldera fill. There are several quarries in the outflow tuff; the three outflow tuff samples in this study were collected from Lechnikai quarry (Fig. 3.1), the largest of these quarries. Two are pumice samples (OP) and one is a whole-rock tuff sample (O).

### *3.3.5 Basalt*

A single small basaltic andesite flow is located on the flank of one of the outflow tuff erosional remnants, Teraclan Hill (Fig. 3.1). Because of its topographic position below the tuff, this flow has been interpreted as part of a precaldera eruption (Koronvsky, oral communication); however, an alternative interpretation (Lipman et al., 1993) is that it fills a paleovalley, created after the

tuff was deposited. A sample of basalt (B) was collected in order to try to resolve this question with whole-rock $^{40}Ar/^{39}Ar$ dating.

### *3.3.6 Eldjurta Granite*

The Eldjurta Granite is exposed 10 km NW of the Chegem caldera, in the adjacent Baksan River valley, over an area of 6 $km^2$ and a vertical distance of 1150 m. The granite is of particular economic interest because the Tirniauz mine, Russia's largest tungsten mine and a major source of molybdenum, is located along the upper contact of this intrusion. The relationship of this mineralization to the Eldjurta Granite is uncertain and has stimulated much research, including the drilling of three cored drillholes; the deepest of these extends to 4 km depth below the Baksan River valley. This hole was drilled to that depth in the hopes that the Mo-W deposits would be encountered below the granite, but it was discontinued when the granite body turned out to be bigger than expected.

Fig. 3.3 is a simplified cross section of the Eldjurta Granite with several details of the deep drillhole. The temperature at the base of the drillhole is 223°C, and the geothermal gradient is fairly constant at 43°C/km. At ≈900 m depth the granite is cut by dikes, and at 3850 meters depth, a sheared contact separates the more typical Eldjurta Granite from a finer grained, more leucocratic granite below. Hess et al. (1993) state that this is probably a younger intrusion of Pliocene or Quaternary age.

Over nearly the entire vertical range sampled (over 5 km), the Eldjurta Granite is remarkably homogeneous, both compositionally and texturally. It is porphyritic with megacrysts of K-feldspar in a matrix of quartz (26 ± 2%), plagioclase (32 ± 2%, An16-37), K-feldspar (34 ± 2%) and biotite (8 ± 2%) with accessory apatite, zircon, monazite and sphene (Umsonst, 1991). Muscovite is present in trace amounts in all samples below 2340m depth. The lowermost

sample contains slightly more muscovite (1-2%), slightly less biotite (4-5%) and has plagioclases with much lower Ca content (An3). Petrographic evidence, such as concentric and oscillatory zoning in plagioclase and microperthitic textures in K-feldspar, records a complex history of crystallization and exsolution but there is little evidence for substantial hydrothermal alteration. Biotites contain minor amounts of chlorite (<3%) but are otherwise quite fresh and inclusion-free.

Eleven Eldjurta Granite samples have been analyzed in this study (Fig. 3.3): one (CG-C2-58B) was collected one meter from an upper contact, 670 m above the Baksan River valley; two were collected from 70-100 m above the Baksan River valley, near the center of the exposed granite; and 8 samples were collected at approximately 500-m intervals in the 4-km drillhole in the center of the exposure. Hess et al. (1993) collected two of their samples from this same drillhole. Two of their surface samples are from river level at the top of that drillhole.

## 3.4 Analytical Techniques

### *3.4.1 Sample Preparation*

The nine Chegem samples selected for mineral separation were crushed and sieved. Biotite and sanidine separates were obtained from the 165-335μm size fraction by conventional heavy-liquid and magnetic techniques. Sanidines were usually etched in 5-10% HF to remove glass fragments and other impurities. As a final step, separates were hand-picked to ensure >98% purity. Plagioclase, K-feldspar and biotite separates from the Eldjurta Granite, provided by Anatoly Gurbanov, were prepared by similar techniques at the mineral separation laboratory of the Russian Academy of Sciences. Whole-rock andesite and basalt powders were ground with a mortar and pestle, and the 350-590μm size fraction was analyzed.

### *3.4.2 $^{40}Argon/^{39}Argon$ Analysis*

Purified mineral separates were encapsulated in commercial grade Al foil (for laser fusion) or 99.995% pure Cu foil (for incremental heating) and sealed in three fused silica vials. The vials were wrapped in Cd foil to reduce the neutron-induced $^{40}Ar$ production. Sixteen flux monitor packets of sanidine from the Taylor Creek Rhyolite, which has an age of 27.92 Ma (Duffield and Dalrymple, 1990), were interspersed among the samples. The samples were irradiated for 2 hours in the core of the U.S. Geological Survey TRIGA reactor (Dalrymple et al., 1981).

The two extraction systems used in this study are attached to the ultraclean, ultrasensitive mass spectrometer (Mass Analyser Products model 216) at the U.S. Geological Survey in Menlo Park, California. The GLM continuous laser extraction system described in Dalrymple (1989) was used on biotite and K-feldspar separates. A low-blank, resistance-heated furnace attached to the same mass spectrometer and extraction system was used for analyses of whole-rock samples and plagioclase separates. For the Eldjurta Granite samples, the laser extraction system was chosen for analysis of biotite and K-feldspar to minimize the amount of sample consumed; plagioclase was analyzed by the incremental-heating method because the laser extraction method would require unacceptably long fusion times.

The spatial distribution of the neutron flux parameter, J, was calculated by analyzing the sanidine monitors using the laser extraction system. Five or six separate analyses were made on each packet of monitor mineral, using three or four grains of sanidine were used in each analysis.

For analyses of K-feldspar from the Chegem and Eldjurta samples on the laser extraction system, 30-40 grains were fused and degassed in one step. To aid

total fusion to a single glass ball without bubbles, synthetic basalt glass was fused with the feldspars. For biotites, 30-150 grains were fused, depending on the apparent age of the sample. A defocused beam was used to minimize the mobility of biotite grains under the laser beam.

For whole-rock samples and the two Eldjurta Granite plagioclase separates, argon was extracted using a resistance-heated furnace for periods of 5 minutes at successively higher temperatures followed by clean-up for 8 minutes on non-evaporable getters. Temperatures were measured with an optical-fiber thermometer and are probably accurate to within ±2%.

### *3.4.3 Age Uncertainty Estimates*

***Laser Total Fusion*** - When the laser extraction system was used, 5 replicate measurements were made on the same irradiated sample. Each measurement has an associated corrected $^{40}Ar/^{39}Ar$ ratio and error that can be converted to an age and error if the neutron flux is known. These instrumental errors are calculated using formulae given by (Dalrymple et al., 1981). Two methods are commonly used to get an apparent age and error from these 5 measurements and errors: one is to disregard the error estimates and calculate a mean and standard deviation for the five values; the second is to weight the age estimates according to their errors as described in (Taylor, 1982) using the formulas:

$$\bar{x}_{weighted} = \frac{\sum_i \left( x_i / \sigma_i^2 \right)}{\sum_i \left( 1 / \sigma_i^2 \right)}; \qquad \bar{\sigma}^2_{weighted} = \frac{1}{\sum_i \left( 1 / \sigma_i^2 \right)}$$

The error estimate associated with this second method is essentially a standard error of means because it sums the standard deviations for the five measurements. In this study, since the individual machine errors are similar in

size, the weighted mean and the unweighted mean are essentially the same. In order not to overestimate our precision, we report here the more conservative error estimate, the standard deviation ($\sigma$) for the five measurements.

***Incremental Heating*** - For the incremental heating experiments, the analytical uncertainty for ages of the argon extracted at each temperature step were also calculated as described by Dalrymple et al. (1981). When a series of gas fractions released contiguously had the same age within analytical uncertainty, a "plateau age" could be calculated as described in Dalrymple and Lanphere (1974). A mean and uncertainty were assigned to this "plateau age" by weighting the age estimates according to their uncertainties (Taylor, 1982). This method is warranted here because the extracted gases all clearly come from the same minerals. However, in cases where the ages were not within analytical uncertainty, an unweighted mean age and standard deviation were determined.

### *3.4.4 Oxygen Isotope Analysis*

Oxygen isotope analyses were performed on quartz, K-feldspar, plagioclase and biotite separates from the Eldjurta Granite samples. The fluorination technique used is essentially that described by Taylor and Epstein (1962). Oxygen isotope ratios are reported in the familiar $\delta$-notation as per mil difference from standard mean ocean water (SMOW). Raw $\delta$-values were corrected to the SMOW scale by comparison with the Caltech Rose Quartz standard whose $\delta$-value is +8.45. NBS-28 has a $\delta$-value of +9.60 on this scale. Analytical precision is better than $\pm 0.15$ per mil ($1\sigma$).

## 3.5 Results

### *3.5.1 Chegem Tuff and Postcaldera Granodiorite*

Calculated $^{40}Ar/^{39}Ar$ ages and their associated errors for the 7 Chegem Tuff samples and the Chegem granodiorite sample are listed in Table 3.2. Ages for the tuff samples, both intracaldera samples and outflow samples are analytically indistinguishable with a (weighted) mean and standard deviation of 2.82 ± 0.02 Ma. Sanidine from the post-caldera granodiorite intrusion yielded an age of 2.84 ± 0.03 Ma.

### *3.5.2 Andesite Flows*

The results of incremental heating experiments for the two andesite samples are shown as age spectra in Fig. 3.4. The age spectrum for sample KH91-16 is flat and yields a plateau age of 2.81 ± 0.02 Ma, with ≈80% of the argon released between temperatures of 600° and 770°C. Incremental heating of sample CG-C-44P yields a more disturbed age spectrum: Ages fluctuate between 2.71 Ma and 6.82 Ma, the bulk of the gas yielding an unweighted mean age of 3.07 ± 0.22 Ma. Approximately 50% of the $^{39}Ar$ in this sample was released between the temperatures of 800° and 875°C.

### *3.5.3 Basalt*

Incremental heating ages from the single basaltic andesite flow located adjacent to the outflow tuff of Teraclan Hill (Fig. 3.5a) range from 3.1 to 3.8 Ma (except for the 1400°C step). Total fusion and plateau ages are 3.51 ± 0.25 Ma, while the isochron ages (Figs. 3.5b and 3.5c) are 3.7-3.8 Ma.

### *3.5.4 Eldjurta Granite*

***$^{40}Ar/^{39}Ar$ Laser Total Fusion-*** $^{40}Ar/^{39}Ar$ total fusion ages for biotites and K-feldspars from the 11 Eldjurta Granite samples are listed in Table 3.3 and plotted against depth in Fig. 3.6a. The biotite ages decrease from 1.90 ± 0.24 Ma at the roof-zone contact with country rock 670 m above river level to 0.83 ± 0.26 Ma at 3970 meters depth in the drillhole. By contrast, K-feldspar ages range from 2.09 ± 0.09 Ma to 2.78 ± 0.09 Ma and show no clear trend with depth.

***$^{40}Ar/^{39}Ar$ Incremental Heating-*** Incremental heating ages were determined for plagioclase separates from two drillhole samples (Fig. 3.7), one at 800m depth (5-2/90) and the other at 3700m depth (59/90). Sample 5-2/90 (Fig. 3.7a) has a saddle-shaped spectrum, indicative of excess $^{40}Ar$ in the low and high temperature steps, and a roughly flat plateau from 825° to 1150°C with an unweighted mean age of 2.18 ± 0.21 Ma. The deeper sample, 59/90 (Fig. 3.7b), also shows signs of excess $^{40}Ar$ in its low temperature steps but does not have a distinct plateau. From 550° to 750°C, ages steadily decrease from 1.58 to 0.98 Ma. At temperatures of 800° to 1500°C, ages are much higher (5.59 to 7.49 Ma).

***Oxygen*** - The oxygen isotopic compositions of quartz, K-feldspar, plagioclase and biotite (Table 3.3, Fig. 3.6b) remain relatively constant with depth in the drillhole with several exceptions. One clear exception is the shallowest drillhole sample 5-2/90 from 800m depth, whose mineral $\delta^{18}O$ values (particularly the two feldspars and the biotite) are markedly lower than those of other samples. The sample 525m below that (10-4/90) contains minerals with relatively high $\delta^{18}O$ values, including the most $^{18}O$-rich quartz and feldspar analyzed in the entire drillhole. Nevertheless, the mineral isotopic compositions of the bottom

7 drillhole samples are remarkably uniform with means (1σ std. dev.) of: $\delta^{18}O_{quartz} = +10.1 \pm 0.3$; $\delta^{18}O_{kspar} = +9.1 \pm 0.4$; $\delta^{18}O_{plagioclase} = +8.6 \pm 0.3$; $\delta^{18}O_{biotite} = +5.6 \pm 0.5$. The two surface samples have biotite and plagioclase oxygen isotopic compositions comparable to the drillhole samples, but the K-feldspar $\delta^{18}O$ values of +7.9 and +7.2 are more than one per mil lighter than the mean in the drillhole; thus the surface samples are more comparable to the shallowest drillhole sample at 800m depth.

## 3.6 Discussion

### *3.6.1 Chegem Tuff and Postcaldera Granodiorite*

Interpreting geochronologic data for the Chegem igneous rocks requires evaluation of the processes of eruption and emplacement that have modified magmatic thermal conditions and influenced subsequent cooling rates of the igneous bodies. The formation of phenocrysts and eruption of the ash-flow occurred at temperatures well above the range of argon closure temperatures in biotite and sanidine (≈115-400°C; Berger and York, 1981; Harrison et al., 1985). Typical rhyolite eruption temperatures are 700-900°C (Cas and Wright, 1988). After eruption, the vitrophyric margins of the tuff were quenched. Meanwhile, the tuffs remained hot after they came to rest, and welding was initiated at temperatures of about 600-750°C (Cas and Wright, 1988). Then, because porous glassy tuffs are poor conductors of heat, the mass of welded tuff cooled slowly. At some time during the course of this cooling, when the tuff was cool enough to undergo brittle fracture along faults, the granodiorite porphyry intruded in the northeast quadrant of the caldera. Estimated timescales of resurgence are $10^3$-$10^5$ years (Smith and Bailey, 1968; Christiansen, 1984). Marsh (1984) infers that these timescales of resurgence are inversely proportional to the size of the caldera. If

this were the case, the time between the quenching of the marginal vitrophyre and the cooling of the granodiorite porphyry below the range of argon closure temperatures for this medium-sized caldera would probably be less than 0.1 Ma. In fact, the ages of the caldera fill, both quenched margin and deep interior, and the age of the granodiorite porphyry are analytically indistinguishable, suggesting, based on the uncertainties of our age measurements, that the time between eruption and resurgence was less than 50,000 years.

### *3.6.2 Andesite Flows*

The two andesite samples may represent two temporally different post-caldera flows. KH91-16 lies directly on top of poorly-welded tuff without any discernible erosional break. CG-C-44P sits stratigraphically above glacial till that has in turn been deposited on poorly-welded tuff. Petrographically, KH91-16 has a microcrystalline groundmass with 15-20% phenocrysts, whereas CG-C-44P has a partly glassy groundmass with ≈30% phenocrysts. The two andesite samples yielded different incremental heating age spectra: KH91-16 has a flat age spectrum. The weighted mean plateau age of 2.82 ± 0.02 Ma is consistent with the stratigraphic relationships, which require that this andesite is younger, but probably only slightly younger, than the Chegem Tuff. In contrast, sample CG-C-44P has an irregular age spectrum and its total fusion and "plateau" ages are inconsistent with the stratigraphic relationships: this andesite is younger than the Chegem Tuff, yet it has an apparent age of 3.07 ± 0.22 Ma, marginally distinguishably older than the tuff. Inasmuch as this is the only whole-rock sample with a partly glassy groundmass, a possible explanation for the stratigraphically inconsistent age is the loss of $^{39}Ar$ by recoil, a well-known problem in fine-grained samples and glasses (Harrison and McDougall, 1989).

### *3.6.3 Basalt*

The single basaltic andesite flow, exposed adjacent to and topographically below an outflow tuff remnant, is the only candidate for precaldera volcanism in the region. Alternatively, it might be a postcaldera flow which filled a paleovalley (Lipman et al., 1993). $^{40}Ar/^{39}Ar$ age determinations provide a simple means of resolving this question. The age spectrum (Fig. 3.5a) is fairly flat, and all heating steps (except 1400°C) yielded gas ages between 3.1 and 3.8 Ma with a mean age of 3.51 ± 0.25 Ma. Isochron diagrams (Figs. 3.5b and 3.5c) yield ages of 3.7-3.8 ± 0.1 Ma with a "trapped argon" isotopic composition ($^{40}Ar/^{36}Ar$) of 285±4, slightly below the atmospheric value of 295.5 (Nier, 1950). The incremental heating ages assume an atmospheric trapped component. A lower $^{40}Ar/^{36}Ar$ ratio in the trapped component will produce older ages, so the approximate plateau age of 3.51 ± 0.25 Ma should be a *minimum* age. Thus, it appears that this basalt is indeed older than the Chegem Tuff and represents a precaldera flow.

### *3.6.4 Eldjurta Granite*

***Biotite****- Comparison with Data from Hess et al. (1993)* - Our biotite ages are plotted against depth on Fig. 3.8 together with the ages reported by Hess et al. (1993). Hess et al. (1993) concluded that it is important to compare ages for biotite populations of the same grain size. Our samples have variable grain size from 50 to 400μm but the majority of the grains are 200-300μm. Though the age data of Hess et al. (1993) for all grain sizes span our age-depth curve, their data for grains 200-315μm define a distinctly different slope than our curve. However, the uncertainties reported by Hess et al. (1993) are instrumental errors based on single analyses which only account for errors in the $^{40}Ar/^{39}Ar$ ratio measurements and uncertainties in irradiation monitors and gradient corrections,

whereas we report standard deviations for 5 replicate analyses of each sample. Our errors also account for uncertainties due to incomplete fusion, impurities in the sample, problems in cleaning the sample gas, etc. If Hess et al. (1993) had performed multiple analyses, their 200-315μm data points with 2σ error bars would probably overlap our curve. Furthermore, only two of their samples (HP 201 and 63/90) were collected from the same drillhole sampled in this study. The slope of the line defined by the ages of these two samples is actually quite similar to the slope of the line through our data. The surface sample ages of Hess et al. (1993) are much more variable than the drillhole ages, perhaps because of mobility of K during surface weathering. The slope of their age/depth line is largely controlled by one surface sample collected 800m above the Baksan River.

*Uplift and Cooling History* - The regular decrease in biotite ages with depth, together with the observation of Hess et al. (1993) that biotites produce flat age spectra indicate that these ages reflect the uplift and cooling history of this young granite. The discussion which follows assumes that the observed biotite ages represent the time at which each sample passed through the "closure temperature" for argon diffusion in biotite, and that this "closure temperature" is approximately 350°C and does not vary significantly within the Eldjurta Granite body. We will discuss three possible explanations of the observed biotite age/depth profile (Fig. 3.9): (1) simple uplift through stationary isotherms; (2) simple cooling with no uplift; and (3) a combination of uplift and cooling.

The simplest calculations of uplift rate are made assuming that the geothermal gradient has remained constant (i.e., isotherms are horizontal and have not moved relative to the earth's surface, Fig. 3.9a) from the time that the roof of Eldjurta Granite cooled through the range of closure temperatures of argon diffusion in biotite to the present. Justification of this assumption is that

by the time the body had cooled to ≈400°C, a pluton of this size would be almost entirely thermally equilibrated with its wall rocks (Hess et al., 1993). For this stationary isotherm assumption, the uplift rate is equal to the slope of the age-depth curve. Excluding the lowermost point, which is discussed below, the slope of our age-depth curve suggests an uplift rate of approximately 13 mm/yr. This is significantly higher than previous estimates, which range from 3 to 6 mm/yr (Hess et al., 1993; Philip et al., 1989; Lewis, 1993); however, this rate is not implausible for this dynamic tectonic setting.

Nevertheless, several lines of reasoning argue against an uplift of 13 mm/yr rate being maintained for over 0.5 million years. Arakelyants et al. (1988) observed that K-Ar mica ages outside the aureole of this pluton have not been reset since Permian times. Based on this observation, Hess et al. (1993) estimate a depth of emplacement of 10 km or less, which would imply a net uplift rate of ≤5.5 mm/yr. Thus, the uplift rate of 13 mm/yr could not have remained constant throughout the cooling history of the pluton. In fact, the ages which constrain this rate only range from 1.90 to 1.56 Ma. Secondly, for the stationary isotherm assumption, uplift rates of 13 mm/yr are equivalent to cooling rates of 500°C/Ma, over three times the 180°C/Ma rate estimated by Hess et al. (1993). Not only is this an extremely high cooling rate, but it is highly unlikely that isotherms would remain stationary when a pluton was being cooled so rapidly.

The stationary isotherm assumption will tend to overestimate uplift rates if there has been any cooling (isotherms moving down, Figs. 10b and 10c) after the argon ages are set. In fact, regional tectonic uplift with no movement of isotherms relative to the Earth's surface is unlikely, especially in cases of recent rapid uplift (Parrish, 1983, 1984). If the isotherms are not stationary, then the slope of the age/depth line represents the *isotherm migration rate* through the

pluton. The isotherm migration rate is equal to the uplift rate plus the rate of isotherm movement away from the earth's surface (particularly the critical isotherm which represents the "closure temperature" of biotite).

The next question to be addressed regards the second scenario, simple cooling (Fig. 3.9b): How quickly can an isotherm move through a stationary pluton? This depends on the method of heat transport, the thermal properties and heat production of the pluton and its surroundings, and the initial conditions. In the case of the Eldjurta Granite, heat transport within the pluton was apparently mainly by conduction as there is no stable isotopic evidence for influx of any substantial amounts of $H_2O$- or $CO_2$-rich fluids (see below). Outside the pluton, the presence of deposits of Mo and W at Tirniauz suggests that there was an external hydrothermal system associated with this pluton though some researchers (Gurbanov et al., 1987; Rhekharskii et al., 1987) believe that these ore deposits predate the Eldjurta Granite.

The size of a pluton, its temperature and emplacement depth are important variables which control the rate of movement of the 350°C isotherm. A large or hot pluton, or one emplaced at greater depth, will tend to cool more slowly and it will take longer for the 350°C isotherm to enter the pluton. The longer it takes an isotherm to enter a cooling pluton, the more slowly it will be moving, because the heat of the pluton is more dissipated and isotherms are further apart later in the pluton's cooling history. A smaller, colder or shallower pluton will tend to cool more quickly and it is likely that the 350°C isotherm will also move more quickly into the pluton.

Norton and Knight (1977) present numerical simulations of heat and mass transport in a shallow plutonic environment for a variety of permeability regimes. In these simulations, the thermal properties and intrusion temperatures (870-920°C) of the pluton are similar to those predicted for the Eldjurta Granite

composition. The model pluton is 3 km wide and is emplaced at 5 km depth. These simulations examine the thermal regime in the first 160,000 years after pluton emplacement. In general, isotherms will tend to move more rapidly during these initial stages of cooling. In most of these simulations, the 200°C isotherm moves away from the pluton as heat is conducted away from the hot body. Meanwhile, the 400°C isotherm either remains stationary above the roof of the hot pluton, or it moves slowly down into the cooling pluton. The fastest rate of movement of the 400°C isotherm in these simulations is 10 mm/yr in the case of purely conductive transport of heat from a relatively cool magma (870°C). The 350°C isotherm should move at about half this rate. Thus, for a pluton like the Eldjurta Granite, a large proportion of the isotherm migration rate can be explained simply by downward relaxation of isotherms (i.e. simple cooling, Fig. 3.9b). Most likely, the observed isotherm migration rate of 13 mm/yr is due to a combination of uplift and cooling (Fig. 3.9c) focused between 1.90 and 1.56 Ma.

In order to determine the relative contributions of uplift and cooling to the isotherm migration rate, it is critical to know the emplacement age (≈crystallization age) of the pluton. The measured $^{40}Ar/^{39}Ar$ ages represent cooling ages. The greater the time interval between the emplacement age and the these measured cooling ages, the more likely it is that the isotherms were moving slowly through the cooling pluton; thus, the contribution of cooling to the isotherm migration rate would be relatively small. At present, the emplacement age of the Eldjurta Granite is not known. It is possible that it was emplaced 2.8 million years ago when the nearby Chegem volcanics were erupting.

Though the exact proportion of uplift relative to downward migration of isotherms is difficult to discern, both will serve to cool a hot pluton. The net cooling rate of the pluton can be estimated given the modern temperature profile and assuming that a biotite $^{40}Ar/^{39}Ar$ age represents the time at which a given

sample was at 350°C. This would imply net cooling rates of 100 to 150°C/Ma, much lower than the cooling rates derived from the stationary isotherm assumption. However, if for some period of time, the pluton cooled very slowly, then the net cooling rates may be considerably lower than the maximum cooling rate. Again, the most likely scenario is that during the time of rapid isotherm migration (1.5-1.9 Ma), the cooling rates were also at a maximum, probably between 200 and 500°C/Ma.

*Sheared Contact at 3850m Depth* - The significantly younger age of the lowermost sample (as well as sample 63/90 of Hess et al., 1993) is probably due at least in part to the sheared contact at 3850m depth. Several possibilities exist: (1) The sheared contact is a fault which caused comminution of grain size which enhanced argon loss. The samples below the contact are finer-grained, which would help to account for some of the argon loss. However, additional heating would still be needed to explain the magnitude of the argon loss. (2) Heat was introduced along the shear zone, either by friction or by hot fluids traveling within the zone. Hess et al. (1993) note that their deepest sample (63/90), which is also near the sheared contact, has cooled more quickly than the shallower samples; this is based on the flatter correlation line on the age-log($a^2$) plot, where a is the mean grain radius. They suggest that fluids within the shear zone facilitated this cooling. The sample at 3970m depth does contain relatively low-$^{18}O$ biotite. However, the rest of the oxygen isotope data, including the fact that the bulk-rock $\delta^{18}O$ remains fairly constant across the contact, argue against infiltration of any appreciable external fluid in this zone. Frictional heating on a shear zone of such small dimensions (less than 5 m) would probably not have an effect on rocks 120 m away. (3) the sheared contact is simply a reactivated intrusive contact separating younger, hotter rocks below from older ones above.

Our preferred interpretation is possibility (3), namely that this contact is a sheared intrusive contact between the main body of the Eldjurta Granite and a slightly younger granite. Because of the mineralogical and isotopic similarities between the two units, the younger intrusion may be a later pulse from the same magma chamber, intruded into the overlying rocks after they had cooled significantly, thereby explaining the finer grain size. A break in the slope of the temperature-depth curve at this level (Fig. 3.3) supports this interpretation. Oxygen isotopic evidence (below) also indicates that rocks near this contact have experienced different thermal histories.

***Potassium Feldspar*** - K-feldspars from intrusive rocks have been known to yield unreliable K-Ar and $^{40}Ar/^{39}Ar$ ages (Zeitler and FitzGerald, 1986). The fact that the oldest K-feldspar total-fusion ages are in some of the deeper samples indicates that these ages do not have any significance in terms of the cooling history of the granite. Stepped heating experiments on K-feldspars from the deep drillhole have in fact identified "excess Ar" (Gazis, Grove and Harrison, unpublished data) which would explain the older K-feldspar ages. Possibly, we can gain further knowledge about excess Ar from this sample suite. Two observations about our data, though probably not statistically significant, are worth noting: (1) Though there is no clear trend of K-feldspar age with depth, the four deepest samples have the four oldest ages, and thus the K-feldspar age-depth curve crudely moves in the opposite direction of the biotite age-depth curve. (2) The two oldest K-feldspar samples correspond to the biotite ages with the greatest error, that is the biotites with the greatest range of ages when 5 replicate analyses were performed. One of these samples (37/90, 2800m) also contains slightly more chlorite (5-10% of biotite) than the other samples.

*Plagioclase* - The two Eldjurta Granite plagioclase (An37 and An22) separates, collected from 800 and 3700 m depth in the drillhole, both show evidence for excess $^{40}Ar$, especially at the low temperature heating steps. In other aspects, the age spectra for the two samples are quite different. The difference can be explained in part by the measured drillhole temperatures of these samples, 73 and 192°C, along with argon diffusion theory. The deeper sample is still within the range of closure temperatures for argon diffusion in plagioclase (170-270°C; Berger and York, 1981) and, because it is farther from the margin of the pluton, it probably had more time to develop the microstructures which allow for diffusion at these low temperatures. As a result, the deeper sample is less retentive of argon; that is, most of its $^{39}Ar$ is released at lower temperatures and the apparent age of this aliquot is younger, between 1.6 and 1.0 Ma. The shallower sample is presently closed to argon diffusion in plagioclase and displays an age spectrum more typical of samples which have cooled relatively quickly. The approximate plateau age of the shallower sample, 2.18 ± 0.21 Ma, is 0.3 million years older than the corresponding biotite ages, a puzzling result considering that the closure temperatures for plagioclase are thought to be lower than those of biotite (Berger and York, 1981). However, Lanphere and Dalrymple (1976) found that the minima of "saddle-shaped" age spectra approach but rarely reach the known crystallization age of a rock or mineral, and when excess $^{40}Ar$ is present, it may be present at all temperature steps.

*Oxygen Isotopes* - With the exception of the surface samples and the sample at 800m depth (5-2/90), the oxygen isotopic compositions of the Eldjurta Granite minerals are relatively constant with depth and appear to reflect "magmatic" values, essentially unaffected by hydrothermal isotope exchange. These mineral $\delta^{18}O$-values are distinctly higher than the phenocryst $\delta^{18}O$-values of Chegem

caldera rocks ($\delta^{18}O_{quartz}$ = +8.2 to +8.5, $\delta^{18}O_{feldspar}$ = +7.0 to +7.9 ; Gazis et al., 1991). Similarly, the calculated bulk magma $\delta^{18}O$-values for the two systems are different ($\delta^{18}O_{Chegem\ magma}$ = +7.5 to +8.0, $\delta^{18}O_{Eldjurta\ magma}$ = +8.7 to +9.2). Thus, the Eldjurta Granite and the Chegem caldera rocks have evolved as separate magma batches: either they were formed from different source rocks or they underwent different paths of assimilation and fractional crystallization.

Assuming equilibrium, measured fractionations for quartz - K-feldspar, quartz-plagioclase and quartz-biotite mineral pairs can be used to calculate temperatures (Table 3.4; Clayton and Kieffer, 1991; Bottinga and Javoy, 1975). Though the mineral isotopic compositions appear to be magmatic, they have clearly not all equilibrated at a uniform temperature. Most notably, K-feldspars, which have the most variable isotopic compositions, tend to record distinctly higher temperatures. Excluding samples 5-2/90 and 67/90, which we discuss below, quartz-plagioclase and quartz-biotite fractionations define temperatures between 550 and 680°C, while quartz-K-feldspar temperatures range between 610 and 1290°C. Possibly this discrepancy can be explained by the existence of K-feldspar megacrysts as well as the K-feldspars in the matrix. Petrographically, the megacrysts display a complex history of crystallization and exsolution. Perhaps the two populations of K-feldspar equilibrated isotopically at different temperatures.

Alternatively, the observed oxygen isotope fractionations can be explained utilizing the concept of Giletti (1986) that different minerals in a slowly cooling pluton become closed to diffusional isotopic exchange at different temperatures (the so-called "blocking" temperature). The simplest model of this concept assumes that all minerals begin with the $\delta^{18}O$ values appropriate for crystallization from the bulk magma at high temperature. As they slowly cool, each mineral is assumed to maintain instantaneous isotopic equilibrium until it

reaches its temperature of closure to oxygen diffusion (which is dependent on the cooling rate and the grain size). At this point, the isotopic composition of that mineral is "frozen" and the system can be treated as a new rock (with a different bulk isotopic composition and modal abundances) consisting of the minerals that are still open to $^{18}O/^{16}O$ exchange. As the cooling process continues, minerals continue to close to oxygen diffusion at different temperatures until the last two minerals are "frozen" at the temperature which corresponds to the isotopic fractionation between them. Given the modal abundances of minerals in a rock and their isotopic compositions, closure temperatures for all the minerals in that rock can be calculated by this method (Farquhar et al., 1993). The model closure temperatures for minerals from all drillhole samples except 5-2/90 (800m) are listed in Table 3.4, and Fig. 3.10 shows mineral isotope exchange trajectories for a typical sample (26-1-90). According to this model, in most of the samples (1325 m to 3300 m), quartz closed first to oxygen diffusion (630-750°C), followed by biotite (510-640°C) and the two feldspars (110-370°C). Note that the feldspar "temperatures" are much less reliable than those for quartz and biotite (Table 3.4). The two deepest samples are notably different: quartz closed at a substantially lower temperature (430-590°C) while the feldspars apparently closed at higher temperatures (430-470°C). Thus their range of closure temperatures is smaller, perhaps indicative of faster cooling, as might be expected around a finer-grained granite.

The sample at 800m depth has mineral $\delta^{18}O$ values considerably lower than the other drillhole samples, and this sample is also the one that is closest to the veins and dikes at ≈900 meters. Thus, the lower $\delta^{18}O$ values are best explained by exchange with low-$^{18}O$ meteoric-hydrothermal fluids associated with the veins. Such meteoric-hydrothermal fluids are known to have been abundantly present in the nearby Chegem caldera system (Gazis et al., 1992).

Mineral pair isotope fractionation temperatures for this sample are 240-560°C, 100 to 200 degrees lower than the other samples. In both this sample and surface sample 1-4/85, the K-feldspars are markedly lower in $^{18}O$ than coexisting plagioclase, clearly indicating that the K-feldspars continued to exchange $^{18}O$ in an open system down to lower temperatures than did the quartz and plagioclase. The quartz-plagioclase and quartz-biotite pairs yield temperatures of approximately 510°C and it is likely that the fluid infiltration and isotopic exchange occurred near this temperature, above the closure temperature for argon diffusion in minerals. As there is no anomaly in apparent $^{40}Ar/^{39}Ar$ age at this depth, this high-temperature hydrothermal exchange probably occurred shortly after the Eldjurta Granite was emplaced, before it had cooled to 350°C.

The deepest sample, 67/90, also displays mineral pair oxygen isotope fractionations indicative of lower temperatures (420-520°C) than the other rocks. However, here, in contrast to sample 5-2/90, the bulk $\delta^{18}O$ value of the rock has not been lowered significantly. Thus, closed-system isotopic exchange is more likely than open-system fluid infiltration. Infiltration of a fluid with a similar bulk $^{18}O$ content to the rock (a magmatic water) is possible but would seem fortuitous. Inasmuch as this sample is from a finer-grained granite lying beneath a sheared contact with the normal facies of the Eldjurta Granite, a simpler explanation, which is also consistent with the $^{40}Ar/^{39}Ar$ data, is that the rocks below this contact had a different thermal history than the rocks above. It appears that this sample has cooled relatively quickly through the temperatures of 420-530°C and that biotite was closed to oxygen diffusion first.

### 3.7 Conclusions

1. The rhyolitic and dacitic tuff of the Chegem caldera was erupted, deposited, cooled and intruded by granodiorite at 2.8 Ma, within a period of less than 50,000

years. Shortly thereafter, andesite flows were emplaced above the partially cooled tuff. A single basaltic andesite flow north of the Chegem caldera probably represents a remnant of precaldera volcanism between 3.5 and 3.8 Ma.

2. $^{40}Ar/^{39}Ar$ total fusion ages of biotite from 11 samples of Eldjurta Granite, including 8 extending to 4 km depth in a drillhole, record information on the uplift and cooling history of this pluton. The upper 7 samples in the drillhole document isotherm migration rates of 13 mm/yr between 1.90 and 1.56 Ma. As this was also a time of rapid cooling, it is likely that these isotherm migration rates are due to significant amounts of both uplift and downward relaxation of isotherms. Cooling rates over this time period were also quite high, probably between 200 and 500°C/Ma. Sometime after 1.56 Ma, uplift and cooling must have slowed down to below the net rates of <5.5 mm/yr and 130°C/Ma.

3. K-feldspar $^{40}Ar/^{39}Ar$ total fusion ages from the same 11 Eldjurta Granite samples cannot be interpreted in terms of uplift and cooling because they contain excess $^{40}Ar$. Deeper samples may contain greater amounts of excess $^{40}Ar$.

4. Stepped heating experiments on plagioclase from Eldjurta Granite samples at 800 and 3700 m depth confirm the presence of excess $^{40}Ar$ in feldspars. The different cooling histories and present-day temperatures for the two samples are reflected in their age spectra.

5. A sheared contact at 3850m depth in the Eldjurta drillhole superimposes rocks with different thermal histories. The sample below the sheared contact records lower oxygen isotope equilibration temperatures and a younger $^{40}Ar/^{39}Ar$ biotite age than the samples above the sheared contact. The simplest explanation

for this data is that the contact is a sheared intrusive contact between two similar granites of different ages.

6. The whole-rock $\delta^{18}O$ of the original Eldjurta Granite magma was distinctly higher than that of the chemically similar magma that formed the Chegem caldera system, 10 km to the southeast. These magmas were either derived from different source rocks, or they underwent distinctive paths of assimilation-fractional crystallization.

7. Oxygen isotope analyses of the 11 Eldjurta Granite samples show little evidence for open-system hydrothermal activity within the pluton body except in a sample collected near some cross-cutting veins at ≈900m depth and possibly in two surface outcrop samples. The whole rock and feldspar $\delta^{18}O$-values of these 3 samples were apparently lowered by 1 to 2 per mil by meteoric-hydrothermal fluids. Oxygen isotope compositions of quartz, K-feldspar, plagioclase and biotite separates record equilibration temperatures of 550-680°C for samples above the sheared contact and 430-530°C for the sample directly below the sheared contact.

**Table 3.1** Previous K-Ar dating of Plio-pleistocene volcanics and intrusives in the Chegem and Baksan River valleys

| Rock type | location | mineral | age(Ma) | Reference |
|---|---|---|---|---|
| *Chegem River valley:* | | | | |
| gray rhyolite tuff | caldera fill, low in sequence | sanidine<br>biotite | 3.0 ± 0.2<br>3.05 ± 0.2 | Borsuk (1979) |
| black vitrophyre | caldera fill, margin | sanidine | 2.8 ± 0.2 | Borsuk (1979) |
| outflow rhyolite tuff | Jungusu plateau, 15 km NNE of caldera | biotite | 2.5 ± 0.2 | Borsuk (1979) |
| granodiorite porhyry | intracaldera, collected along Jungusu River | biotite | 2.6 ± 0.2 | Borsuk (1979) |
| *Baksan River valley:* | | | | |
| andesite | dike in Baksan River valley | biotite | 1.2 ± 0.2 | Borsuk (1979) |
| Eldjurta granite | Baksan River valley | biotite<br>K-feldspar | 1.8 ± 0.15<br>1.9 ± 0.15 | Borsuk (1979) |
| granite-porphyry (leucocratic, facies of Eldjurta granite) | Baksan River valley | whole rock | 2.1 ± 0.2 | Borsuk (1979) |
| rhyolite | dike within Eldjurta Granite, near Tirniauz mine | biotite | 1.80 ± 0.25 | Borsuk (1979) |
| Eldjurta granite | 750 m above Baksan river valley to 3825 m below | biotite* | 1.26 ± 0.03 to 2.65 ± 0.08 | Hess et al. (1993) |

*variable grain size and depth within pluton

**Table 3.2** Chegem volcanic and intrusive rocks: $^{40}Ar/^{39}Ar$ total fusion ages

| Sample# | Description/Location† | Biotite Age* | Sanidine Age* |
|---|---|---|---|
| *Intracaldera tuff:* | | | |
| 90L-109 | marginal vitrophyre, east side of caldera | | 2.84 ± 0.06 Ma |
| 90L-115 | welded tuff, deep interior | | 2.85 ± 0.03 Ma |
| 90L-116 | welded tuff, deep interior | | 2.83 ± 0.07 Ma |
| KH91-11P1 | dacitic pumice, top SW side of caldera | 2.92 ± 0.13 Ma | |
| KH91-11P2 | dacitic pumice, same location as KH91-11P1 | 2.85 ± 0.08 Ma | |
| *Outflow tuff:* | | | |
| 90L-119A | outflow tuff, Lechnikai quarry | 2.72 ± 0.27 Ma | 2.81 ± 0.03 Ma |
| 90L-119P4 | pumice in outflow, Lechnikai quarry | | 2.77 ± 0.11 Ma |
| 90L-120P7 | pumice in outflow, Lechnikai quarry | | 2.79 ± 0.07 Ma |
| *Post-caldera rocks:* | | | |
| 90L-125A | granodiorite intrusion, intracaldera, near contact with tuff | | 2.84 ± 0.03 Ma |

†locations are shown on Fig. 3.1
*uncertainties are one standard deviation on five replicate analyses

**Table 3.3** Eldjurta Granite samples: Total fusion $^{40}Ar/^{39}Ar$ ages and oxygen isotope data

| | | $^{40}Ar/^{39}Ar$ ages** | | $\delta^{18}O$* | | | | | |
|---|---|---|---|---|---|---|---|---|---|
| Sample # | Location/Depth | biotite | kspar | bio | ksp | plag | qtz | bulk | Comments |
| CG-C2-58B | surface, 1 m from roof contact, 670 m above river | 1.90 ± 0.24 | 2.26 ± 0.02 | 5.6 | 7.9 | | | | near Tirniauz Mo-W mine |
| 1-1-85 | surface, 70 m above river, 700 m from margin | | 2.10 ± 0.04 | | 7.2 | 8.3 | | | |
| 1-4-85 | surface, 100 m above river, 100 m from margin | 1.79 ± 0.04 | | | | | | | |
| 5-2-90 | 800 m | 1.84 ± 0.05 | 2.15 ± 0.10 | 3.1 | 6.1 | 7.5 | 9.4 | 7.3 | |
| 10-4-90 | 1325 m | 1.80 ± 0.04 | 2.36 ± 0.09 | 5.6 | 9.6 | 9.2 | 10.5 | 9.5 | zoned plag w/calcic core An 21-45, calcite |
| 17-1-90 | 1850 m | 1.76 ± 0.05 | 2.09 ± 0.09 | 6.3 | 9.3 | 8.6 | 10.0 | 9.1 | |
| 26-1-90 | 2340 m | 1.67 ± 0.05 | 2.18 ± 0.08 | 5.2 | 8.9 | 8.3 | 9.8 | 8.7 | zoned plag, An 9-20 |
| 37-90 | 2800 m | 1.50 ± 0.20 | 2.78 ± 0.09 | 5.5 | 9.5 | 8.6 | 9.9 | 9.1 | trace muscovite, microcline |
| 49-90 | 3300 m | 1.65 ± 0.02 | 2.38 ± 0.16 | 6.0 | 9.3 | 8.9 | 10.2 | 9.2 | trace musc, more chl than other samples (5-10% of bio) |
| 59-90 | 3700 m | 1.56 ± 0.03 | 2.38 ± 0.08 | 5.6 | 8.8 | 8.4 | 10.0 | 8.8 | musc, microperthite |
| 67-90 | 3970 m | 0.83 ± 0.29 | 2.72 ± 0.14 | 4.9 | 8.5 | 8.5 | 10.4 | 8.9 | finer grained, larger bio associated w/musc (1-2%) plag=An 3 |

**age in Ma, uncertainties are one standard deviation for 5 replicate analyses
* per mil vs. SMOW; qtz = quartz, ksp = K-feldspar, plag = plagioclase, bio = biotite, bulk = calculated bulk rock assuming 26% qtz, 34% ksp, 32% plag and 8% bio; uncertainty in $\delta^{18}O$ is ± 0.15 per mil (1σ)

**Table 3.4** Eldjurta drillhole oxygen isotope fractionations and calculated temperatures

| | | mineral pair oxygen isotope temperatures | | | | | | | model closure temperatures | | | |
|---|---|---|---|---|---|---|---|---|---|---|---|---|
| Sample | depth (m) | $\Delta_{q-k}$ ‰ | $T_{q-k}$[a] (°C) | $\Delta_{q-p}$ ‰ | An[b] % | $T_{q-p}$[a] (°C) | $\Delta_{q-b}$ ‰ | $T_{q-b}$[c] (°C) | $T_c(q)$[d] (°C) | $T_c(b)$[d] (°C) | $T_c(k)$[d] (°C) | $T_c(p)$[d] (°C) |
| 5-2/90 | 800 | 3.3 | 240 | 1.9 | 37 | 560 | 6.3 | 460 | | | | |
| 10-4/90 | 1325 | 0.9 | 760 | 1.3 | 16 | 650 | 4.9 | 550 | 650 | 510 | 370 | 370 |
| 17-1/90 | 1850 | 0.7 | 900 | 1.4 | 16 | 620 | 3.7 | 650 | 700 | 640 | 170 | 170 |
| 26-1/90 | 2340 | 0.9 | 760 | 1.5 | 16 | 580 | 4.6 | 570 | 630 | 550 | 210 | 210 |
| 37/90 | 2800 | 0.4 | 1290 | 1.3 | 16 | 650 | 4.4 | 590 | 750 | 530 | 110 | 110 |
| 49/90 | 3300 | 0.9 | 760 | 1.3 | 16 | 650 | 4.2 | 600 | 670 | 580 | 340 | 340 |
| 59/90 | 3700 | 1.2 | 610 | 1.6 | 22 | 580 | 4.4 | 590 | 590 | 590 | 470 | 470 |
| 67/90 | 3970 | 1.9 | 420 | 1.9 | 3 | 430 | 5.5 | 510 | 430 | 530 | 430 | 430 |
| averages† | | 0.8 ± 0.3 | 850 ± 240 | 1.4 ± 0.1 | 17 ± 2.4 | 620 ± 40 | 4.4 ± 0.4 | 590 ± 30 | 670 ± 60 | 570 ± 50 | 280 ± 140 | 280 ± 140 |

[a] isotope equilibrium temperature calculated from expressions given in Clayton and Kieffer (1991), uncertainties in T due to ± 0.3‰ uncertainties in $\delta^{18}O$ measurements are ± 220°C for $T_{q-k}$ and ± 90°C for $T_{q-p}$

[b] anorthite content of plagioclase, based on unpublished microprobe data (measured by C. J. Lewis at UC Berkeley)

[c] isotope equilibrium temperatures calculated from expressions given in Bottinga and Javoy (1975), uncertainty in $T_{q-b}$ due to ± 0.3‰ uncertainties in $\delta^{18}O$ measurements is ± 25°C

[d] model "closure temperature" for mineral in slowly cooling pluton, calculated following strategies in Farquhar et al. (1993); typical uncertainties calculated by propagating uncertainties in modal abundances (2%), fractionation factors (0.1‰ ) and isotopic compositions (0.15‰ ) are: $\sigma T_c(q) = \pm 120°C$; $\sigma T_c(b) = \pm 30°C$; $\sigma T_c(p) = 180°C$; and $\sigma T_c(k) = \pm 260°C$

† excluding samples 5-2/90 and 67/90, mean and 1σ standard deviation

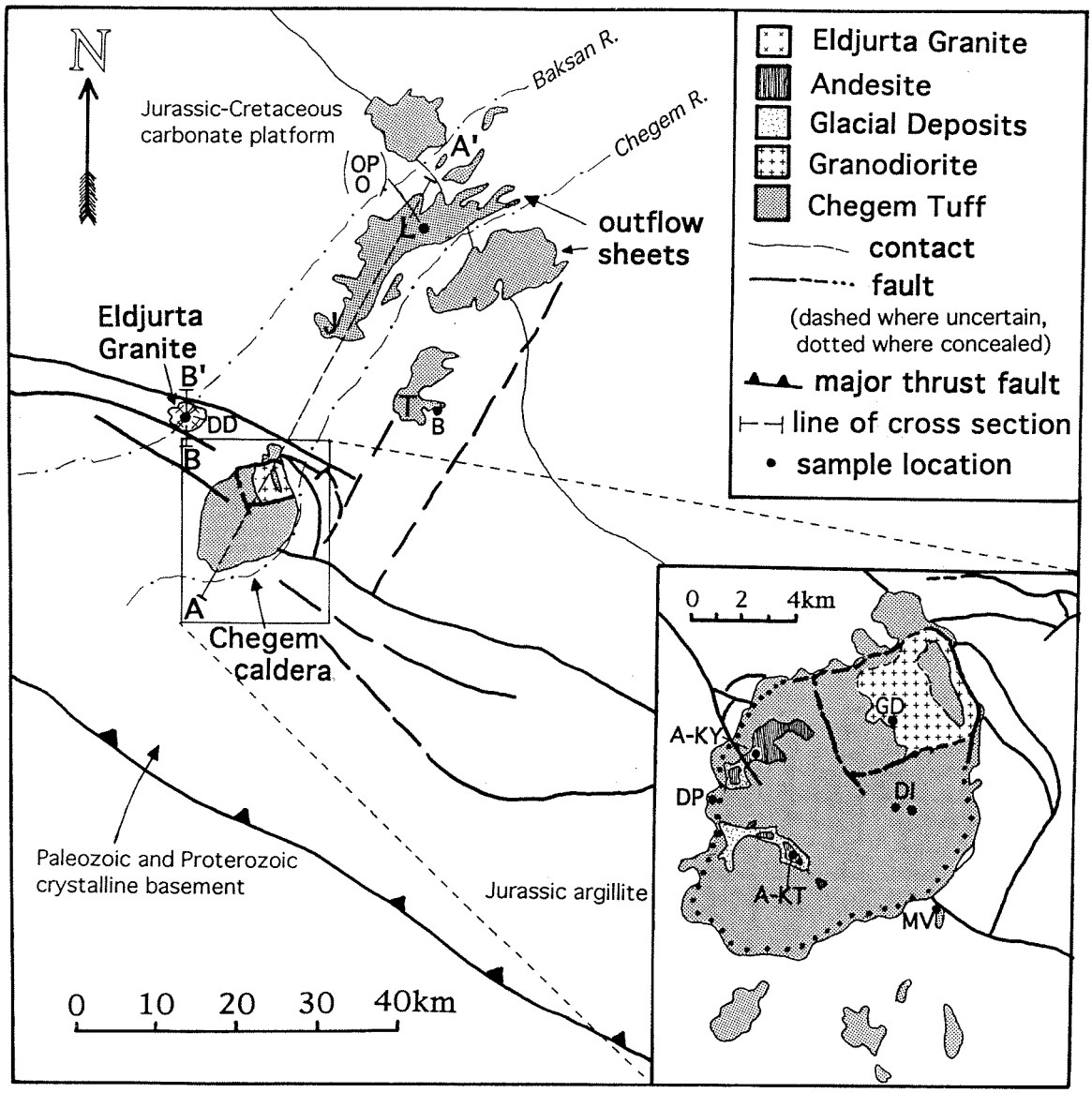


**Figure 3.1** -- Generalized geologic map of the central Greater Caucasus Mountain Range (modified from Lipman et al., 1993), emphasizing the Chegem caldera and the Eldjurta Granite. Sample locations are shown: MV=marginal vitrophyre; DP=dacitic pumice; A-KT=andesite at Kum Tyube; A-KY=andesite at Kyugenkaya; DI=deep interior welded tuff; GD=granodiorite porphyry; O=outflow tuff; OP=outflow pumice; B=Basalt; DD=deep drillhole in Eldjurta Granite; L=Lechnikai quarry; T=Tereclan hill; J=Jungusu plateau. Sections A-A' and B-B' are shown in Fig. 3.2 and Fig. 3.3, respectively.

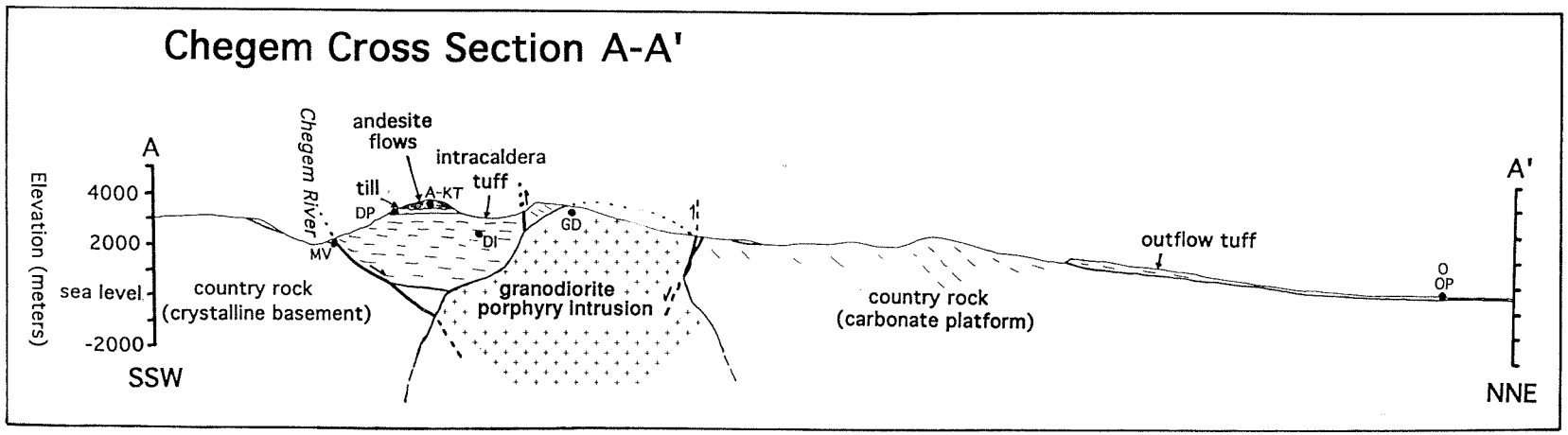


**Figure 3.2 --** Simplified cross section of the Chegem caldera and outflow facies. $^{40}Ar/^{39}Ar$ sample locations are projected onto the section. Location of section is shown in Fig 3.1. MV=marginal vitrophyre; DP=dacitic pumice; A-KT=andesite at Kum Tyube; DI=deep interior welded tuff; GD=granodiorite porphyry; O=outflow tuff; OP=outflow pumice.

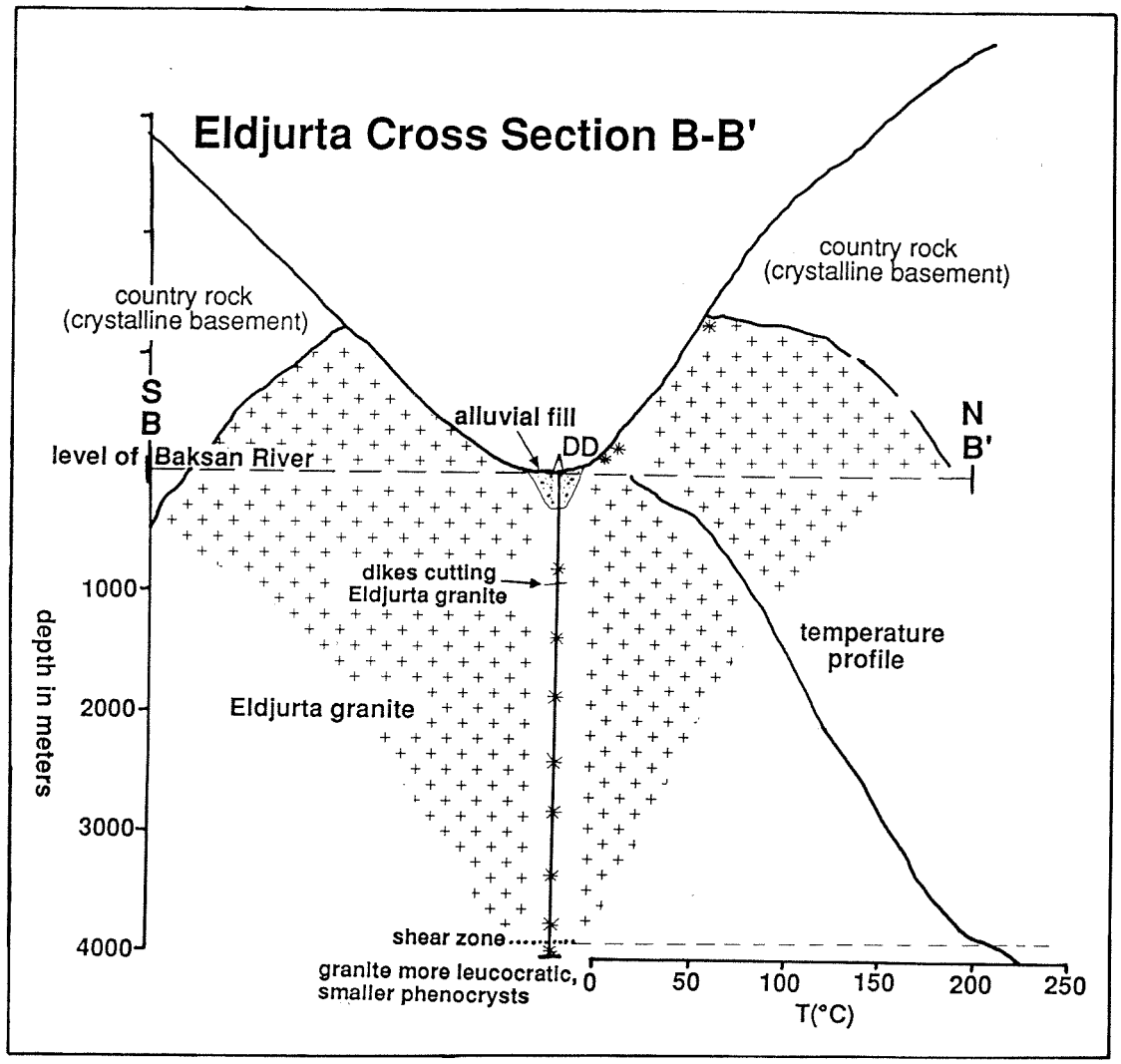


**Figure 3.3** -- Diagrammatic cross section of the Eldjurta Granite showing surface exposure and deep drillhole sampling profile. Samples are marked by *'s. Location of cross section is shown in Fig. 5.1.

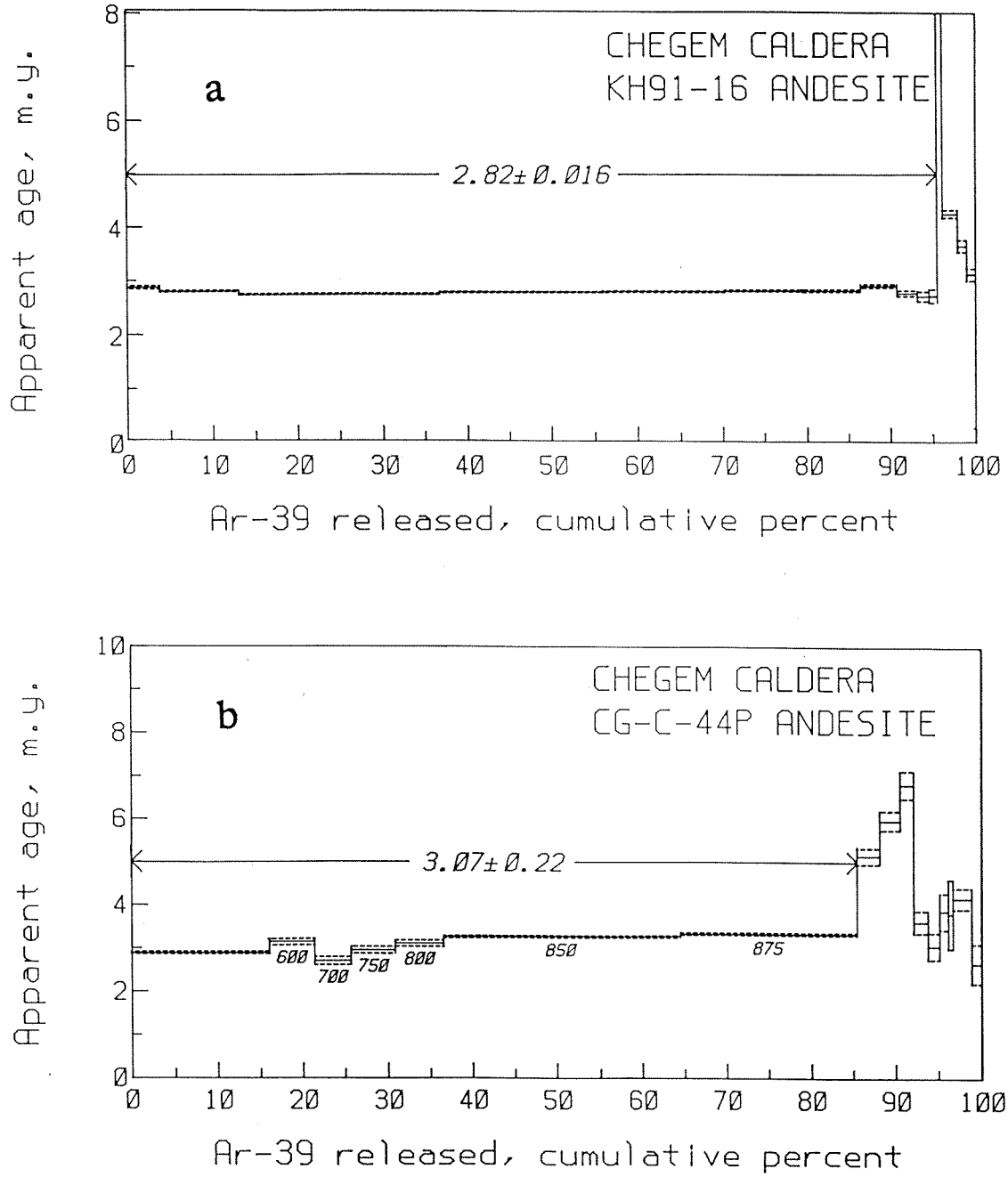


**Figure 3.4** -- Age spectra for andesites. (a) Sample KH91-16, which lies directly above poorly welded tuff, collected near Kyugenkaya Peak. Plateau age is weighted as described in text; (b) Sample CG-C-44P, partly glassy andesite which lies above glacial till above poorly welded tuff, collected near Kum Tyube Peak. Approximate plateau age given (unweighted mean and standard deviation).

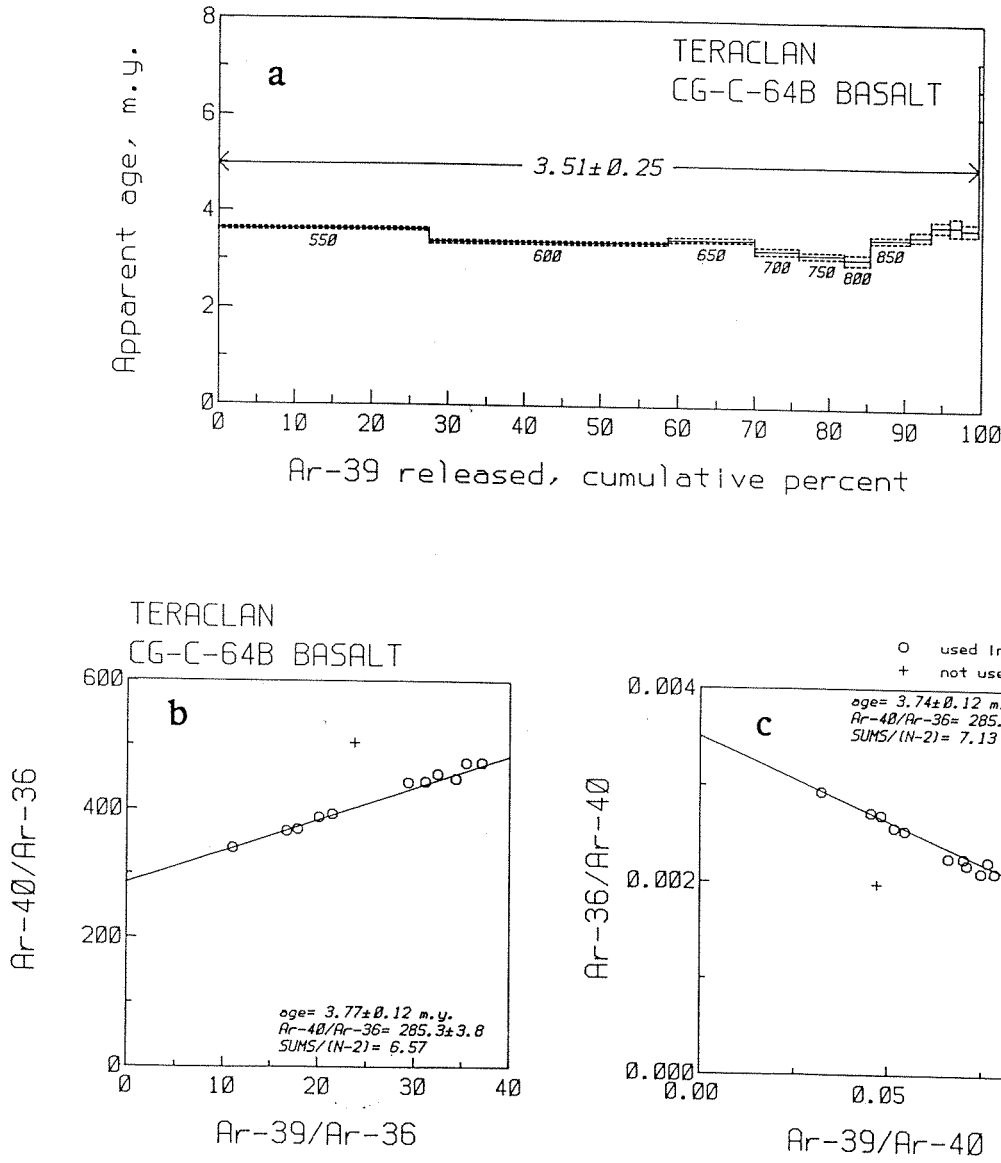


**Figure 3.5 --** Age spectrum and isochrons for basaltic andesite collected near Teraclan Hill in the lower Chegem River valley. (a) age spectrum with approximate plateau age (unweighted mean and standard deviation); (b) $^{40}Ar/^{36}Ar$ - $^{39}Ar/^{36}Ar$ isochron diagram; (c) $^{36}Ar/^{40}Ar$ - $^{39}Ar/^{40}Ar$ inverse isochron diagram.

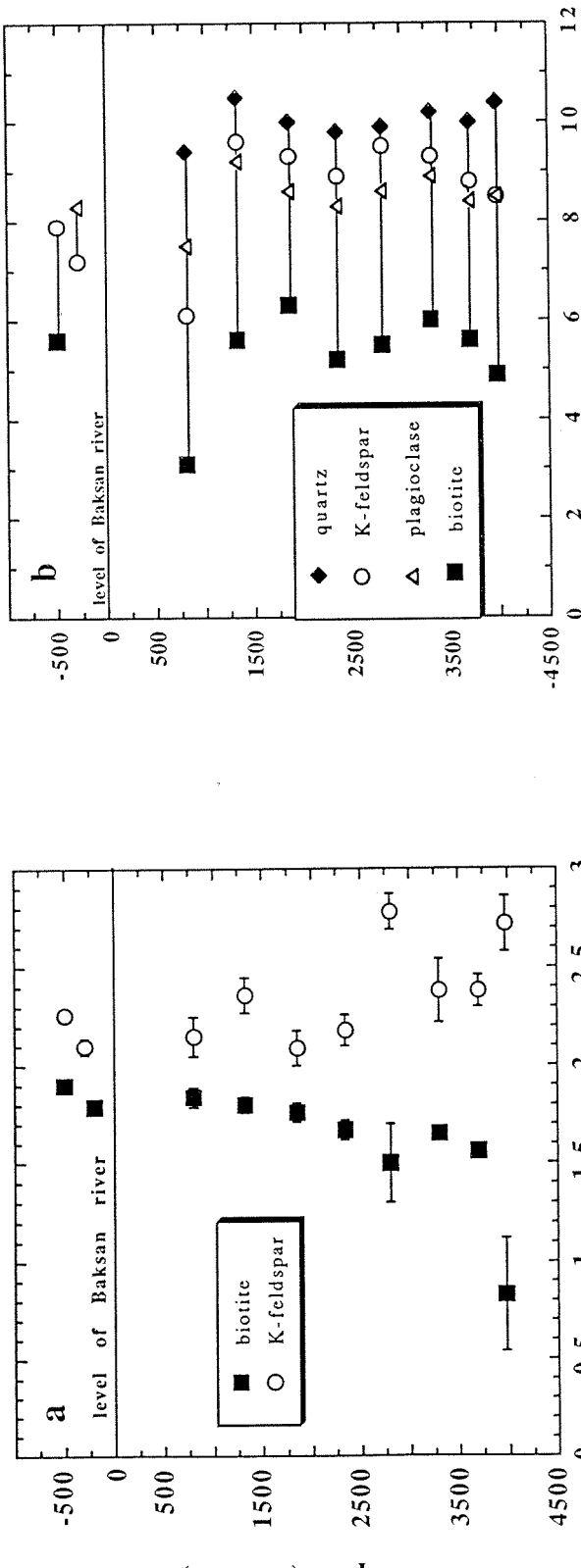


**Figure 3.6 --** $^{40}Ar/^{39}Ar$ total fusion ages and oxygen isotopic compositions of Eldjurta Granite samples plotted vs. depth below Baksan river. (a) $^{40}Ar/^{39}Ar$ total fusion ages of biotite (filled squares) and K-feldspar (open circles). Error bars are one standard deviation for five separate analyses; (b) $\delta^{18}O$ for biotite (squares), k-feldspar (circles), plagioclase (diamonds) and quartz (triangles). Estimated error is $\pm$ 0.15‰ (1$\sigma$).

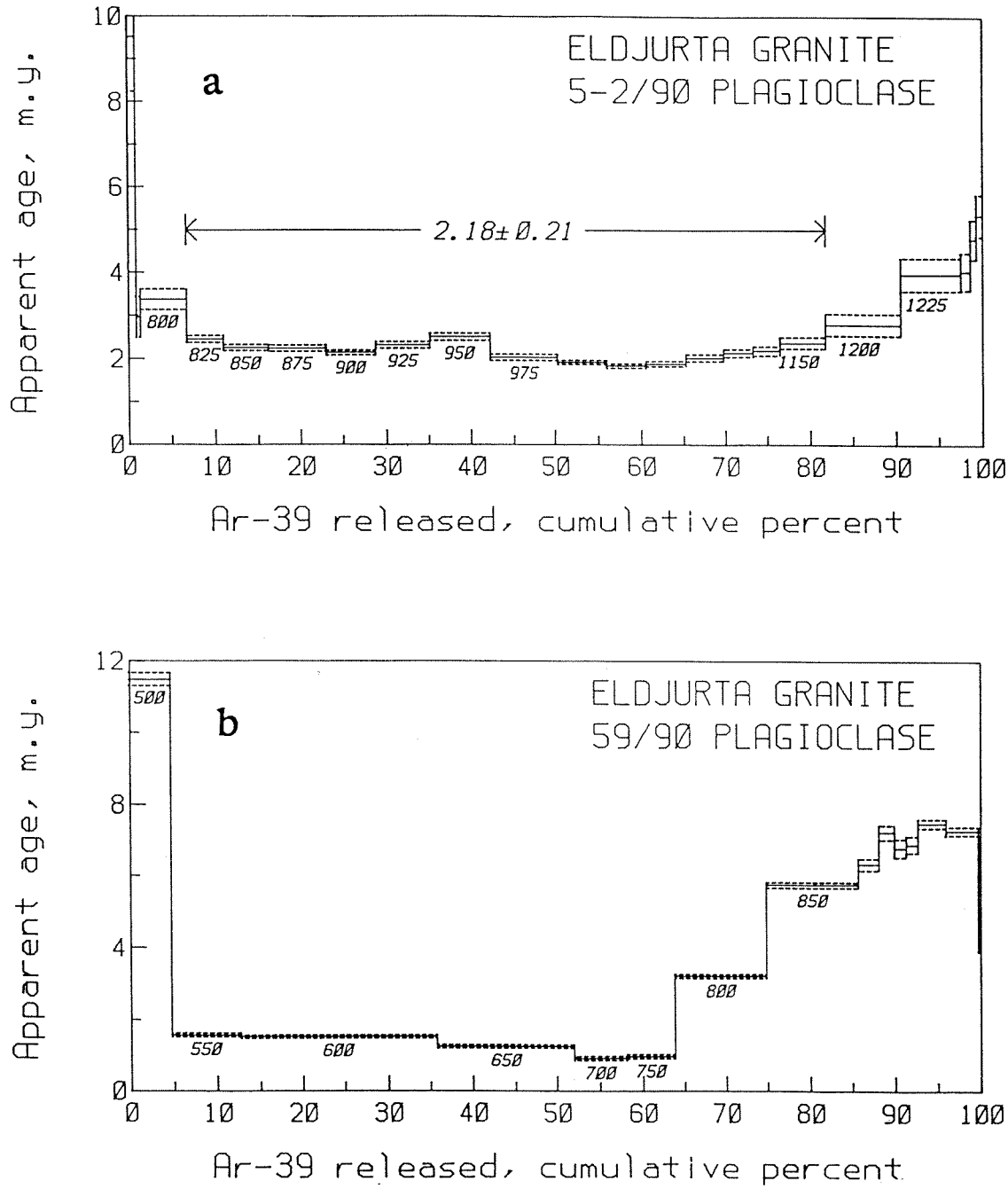


**Figure 3.7 --** Age spectra for Eldjurta Granite plagioclase. (a) Sample 5-2-90, collected at 800m depth below the Baksan River in the deep drillhole. Approximate plateau age given (unweighted mean and standard deviation); (b) Sample 59/90, collected from 3700m depth below the Baksan River in the deep drilhole.

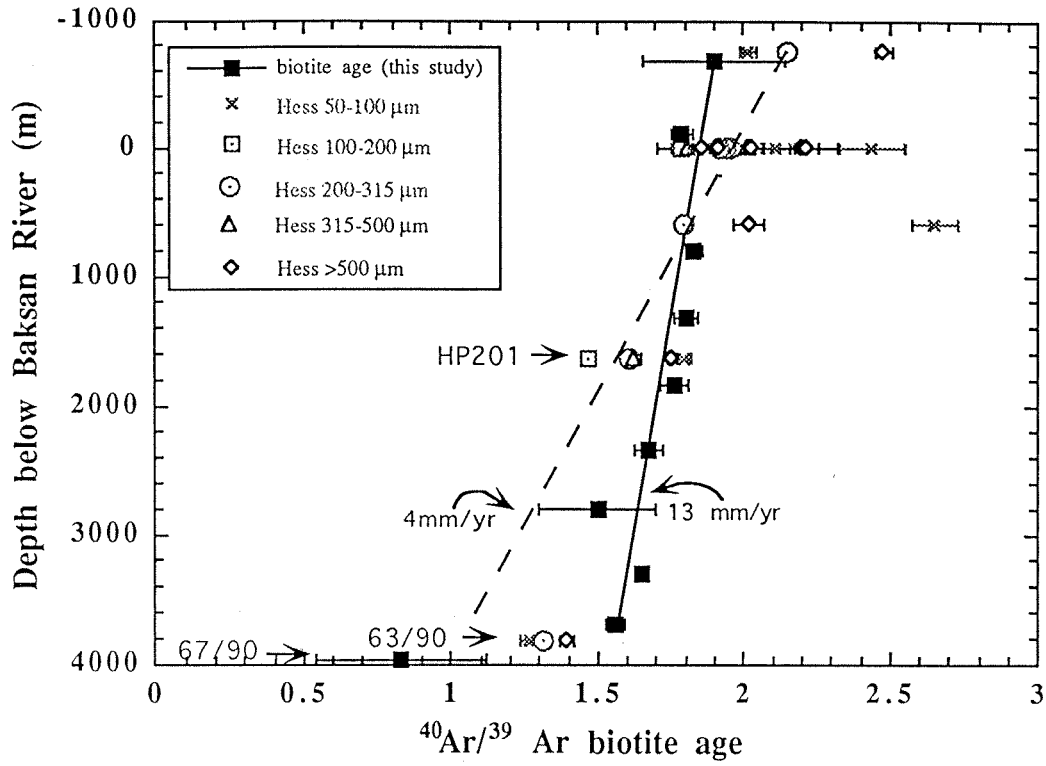


**Figure 3.8** -- Biotite $^{40}Ar/^{39}Ar$ ages from this study (solid squares) plotted together with the $^{40}Ar/^{39}Ar$ age data of Hess et al., 1993 for various sieve fractions of biotite. Samples HP201 and 63/90 are the samples of Hess et al. (1993) from the same drillhole as our samples. Sample 67/90 is our deepest sample, from below the shear zone. Solid line is linear fit to data (excluding sample 67/90) which represents an uplift rate of 13 mm/yr assuming isotherms have remained stationary and horizontal. Dotted line is fit to Hess et al. (1993) 200-315 mm age data and represents uplift rate of 4 mm/yr based on same assumption.

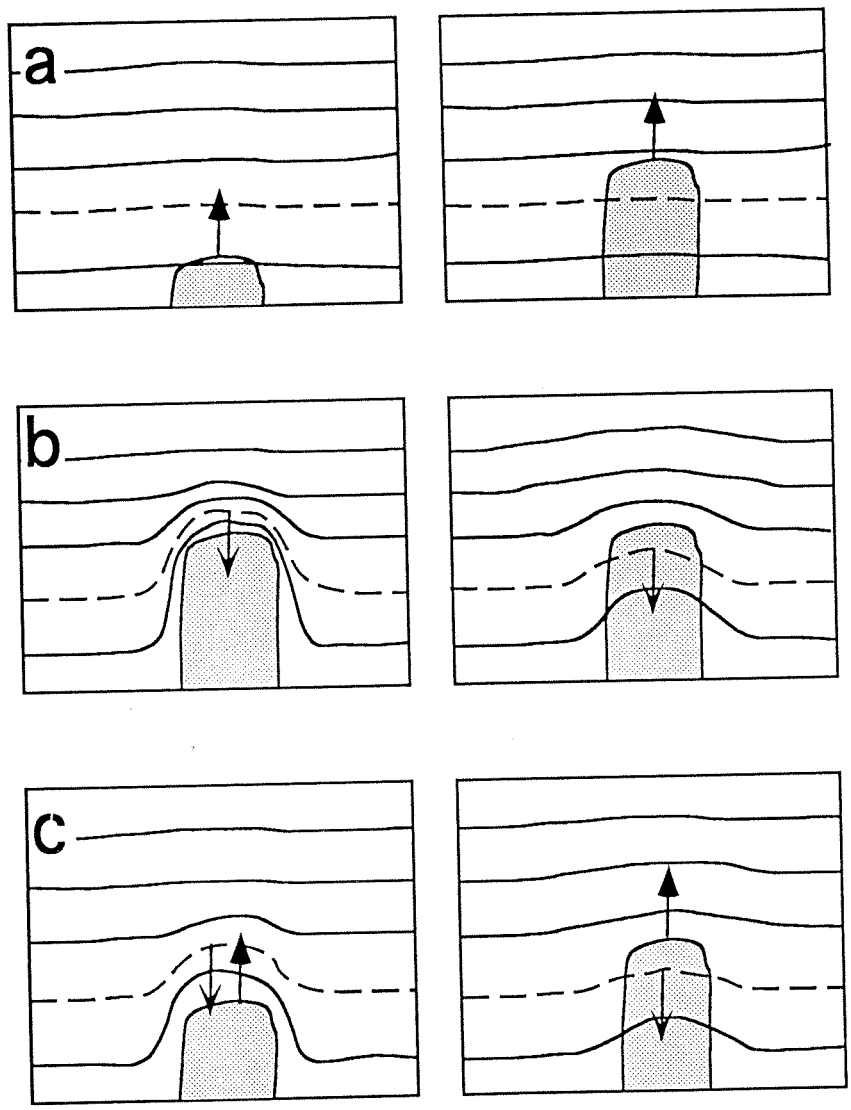


**Figure 3.9** -- Sketch diagrams of 3 possible explanations for isotherm migration in a pluton: (a) ***simple uplift*** -- stationary isotherm assumption, pluton has already cooled off and thermally equilibrated with country rock; (b) ***simple cooling*** -- isotherms move down into pluton as it cools, no uplift; (c) ***uplift + cooling*** -- pluton is moving up relative to the surface as it cools, isotherms move down. Lines = isotherms; dashed line = isotherm of interest ("closure temperature" for given mineral); stippled area = pluton; closed arrow tip=uplift; open arrow tip=cooling.

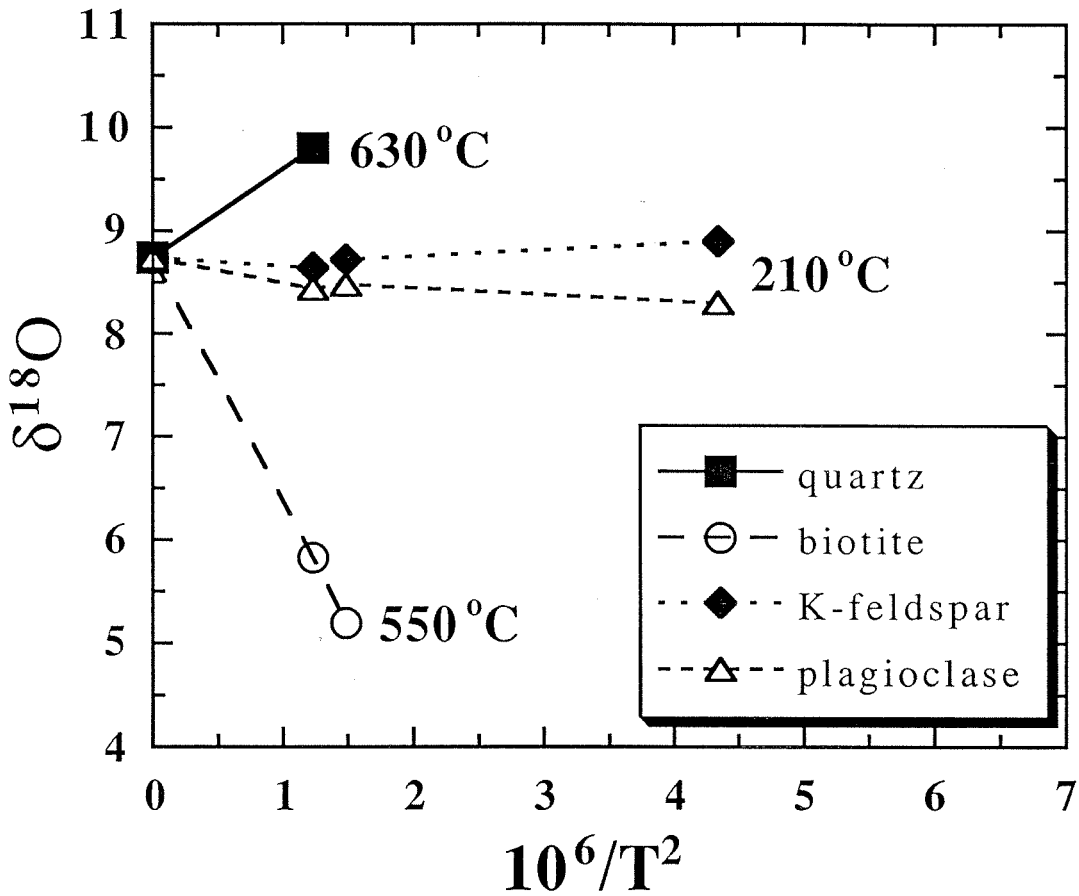


**Figure 3.10** -- Mineral isotope exchange trajectories for Eldjurta Granite sample 26-1/90, calculated following strategy in Farquhar et al. (1993), assuming modal abundances of quartz (26%); K-feldspar (34%); plagioclase (32%) and biotite (8%). Fractionation factors calculated from expressions in Clayton and Kieffer (1991) for quartz, K-feldspar and plagioclase, and in Bottinga and Javoy (1975) for biotite.

# Chapter 4. Oxygen Isotope, Major-element, and Trace-element Geochemistry of the Chegem Caldera

## 4.1 Introduction

Because they represent a massive, rapid emptying of the upper parts of a large magma chamber, thereby producing an "upside-down" version of the original magma system (e.g., Smith, 1979; Hildreth, 1979, 1981), ash-flow tuffs and other pyroclastic deposits erupted from major calderas provide a "snap-shot" of a specific stage in the evolution of silicic crustal magma chambers. Although many geochemical studies of such caldera systems have been made over the past three decades, most of these studies have concentrated on outflow sheets rather than the thick intracaldera deposits (which are more susceptible to post-depositional alteration). Fridrich et al. (1991) demonstrated that intracaldera tuffs can provide useful information about magma chamber evolution, even in mid-Tertiary calderas. Here, we present results of a geochemical study of a much younger and better preserved caldera, the Chegem ash-flow caldera, located in the northern Caucasus Mountains (Russia).

Principally because of its combination of youth, exposure, and simplicity, the Chegem caldera presents a unique research opportunity. Although it is only 2.8 million years old (Chapter 3), more than a 2-km thick section of caldera fill is now exposed as a result of recent rapid uplift and deep erosion in the Caucasus Mountains. In addition, the Chegem caldera has a relatively simple structural and eruptive history: the caldera fill consists of a single cooling unit of welded tuff with sub-horizontal bedding; there is no evidence for pre-caldera volcanism, nor has there been extensive post-caldera hydrothermal alteration. In other words, this particular "snap-shot" of the upper part of an inverted magma chamber is exceptionally well-exposed and well-preserved.

Oxygen isotope studies are useful for determining both the petrogenesis of an igneous rock and the extent of its interaction with water. Whole-rock $\delta^{18}O$ values for unaltered igneous rocks are normally between +6 and +10 (Taylor, 1968). Interaction and exchange with water can either lower (e.g., at high temperatures) or raise (e.g., at low temperatures) these $\delta^{18}O$ values, depending on the degree of equilibration, the temperature of exchange, and the isotopic composition of the water. Assimilation of country rock by a magma or exchange of isotopes with the country rock (usually mediated by an aqueous fluid) can also raise or lower the primary oxygen isotopic composition of a body of magma.

Previous oxygen isotope studies of ash-flow calderas (e.g. Lipman and Friedman, 1975; Lambert and Epstein, 1980; Hildreth et al., 1984; Larson and Taylor, 1986a,b; Johnson et al., 1990; Smith and Suemnicht, 1991) have documented a variety of interactions with water. For example, the Yellowstone volcanic plateau in Wyoming is a large caldera complex which has undergone an extended history of reactivation and eruption accompanied by hydrothermal activity. Hildreth et al. (1984) observed $^{18}O$-depletions in quartz and feldspar from several generations of post-collapse lavas at Yellowstone. Because the

measured oxygen isotopic fractionations between coexisting quartz and feldspar in these lavas recorded equilibration at magmatic temperatures, Hildreth et al. (1984) concluded that these rocks crystallized from low-$^{18}O$ magmas and that the $^{18}O$-depletions were caused by direct interaction between the magma and meteoric water. However, Taylor (1987) proposed that these $^{18}O$ depletions were the result of assimilation or melting of low-$^{18}O$ country rocks that had previously exchanged oxygen with meteoric-hydrothermal fluids (Taylor, 1987).

Bacon et al. (1989) present direct evidence that, prior to ash-flow eruption, there was a lowering of $\delta^{18}O$ in the magma at Crater Lake, Oregon, by assimilation of low-$^{18}O$ country rocks. They observed partially-fused low-$^{18}O$ granitoid blocks that were ejected during the climactic eruption. Lipman and Friedman (1975), in their study of the Timber Mountain caldera in the Southwest Nevada caldera complex, also demonstrated that $^{18}O$ depletions of very large-sized batches of ash-flow tuff magma had occurred just prior to eruption.

However, oxygen isotopic studies of a number of other calderas have revealed no evidence for pre-eruptive $^{18}O$-lowering. For example, the Questa, New Mexico and Grizzly Peak, Colorado calderas (Johnson et al., 1990), the Central Nevada caldera complex and numerous systems in the San Juan Mountains, Colorado (Larson and Taylor, 1986b), and the Superstition-Superior volcanic area, Arizona (Stuckless and O'Neil, 1973) all have erupted ash-flows and lavas with essentially unaltered igneous isotopic signatures. Others, like Lake City, Colorado (Larson and Taylor, 1986a), Long Valley, California (Smith and Suemnicht, 1991) and Valles, New Mexico (Lambert and Epstein, 1980) have experienced extensive post-collapse, sub-solidus hydrothermal alteration and oxygen isotopic exchange.

Thus, examination of oxygen isotope systematics provides basically three end-member types of situations that are associated with ash-flow tuff calderas:

(1) development of low-$^{18}O$ magmas; (2) extensive subsolidus hydrothermal $^{18}O$ exchange, particularly along ring fractures and adjacent resurgent intrusions; and (3) essentially "dry" systems where the primary magma $\delta^{18}O$ values are all largely preserved (except where they have been locally modified by low-temperature hydration or devitrification of volcanic glass).

In this chapter, we present results of oxygen isotope analyses of 134 samples from within and around the Chegem caldera, including 38 samples collected from a 1405-meter stratigraphic section of intracaldera tuff. Within this section we identified a zone of low-$^{18}O$ rocks which display extreme isotopic disequilibrium between phenocrysts and coexisting groundmass. As will be discussed below, we now believe that this represents a fourth end-member type that should be added to the above list. We shall also discuss why this fourth type may be very difficult to recognize in nature, except in historical eruptions or in very well-preserved caldera complexes.

Major and trace elements are useful for understanding the stratigraphy and eruption history of a set of ash-flow deposits. Inasmuch as most (if not all) large-volume silicic magma chambers become compositionally zoned in major and trace elements prior to eruption, the composition of the pyroclastic products can in principle be used to infer their original position within the magma chamber; this is most successfully done if pumices rather than whole rocks are studied (e.g., Lipman, 1967). The commonly observed mafic-upward zoning in tuff sequences (e.g., Long Valley, California, Hildreth, 1979; Grizzly Peak, Colorado, Fridrich et al., 1991) is believed to represent progressive downward tapping of a compositionally-layered magma chamber in which the top was the most silicic part of the system. In addition to the $^{18}O/^{16}O$ data, we also present major- and trace-element compositions for the Chegem stratigraphic section. Other intracaldera tuffs, outflow tuffs, post-caldera intrusives and lavas, and

older country rocks have also been analyzed for $^{18}O/^{16}O$ and for major and trace elements.

## 4.2 Geologic Setting

Here we briefly review the geologic setting of the Chegem caldera, which is described more fully in Chapter 2, as well as by Lipman et al. (1993). The Chegem caldera, located in the north-central Caucasus Mountains, consists of a single complex cooling unit of densely-welded tuff which ranges in composition from rhyolitic at the lowermost exposure to dacitic at the top. There are no erosional breaks in this unit, but there are welding variations, including horizons of more poorly-welded tuff and vitrophyres, especially in the upper part of the sequence. These probably represent short hiatuses in the caldera-forming eruption. However, cooling joints pass across most horizons, indicating that the bulk of intracaldera tuff cooled as an intact unit.

Flat-lying intracaldera tuff is unconformably overlain by glacial till capped by andesitic lava flows in the southern and western parts of the caldera. In the northeast quarter of the caldera, a fault-bounded block of gently dipping tuff has been pushed up in piston-fashion by a resurgent granitic to granodioritic porphyry intrusion. Outflow remnants of Chegem Tuff are found up to 50 km to the north on the stable craton, where they dip underneath more recent deposits.

$^{40}Ar/^{39}Ar$ total fusion ages of biotite and sanidine from the base, top and interior of the intracaldera tuff, as well as from the outflow tuff, are analytically indistinguishable at 2.82 ± 0.02 Ma (Chapter 3). Sanidine from the cross-cutting resurgent intrusion yielded a similar age (2.84 ± 0.03 Ma) as did an incrementally-heated whole-rock andesite (2.82 ± 0.02 Ma), indicating that the Chegem Tuff was erupted, resurgently intruded, and capped by post-collapse

andesite flows in a relatively short time period, probably less than 50,000 years (Chapter 3).

### 4.3 Analytical Methods

Unweathered samples, approximately 1 kg in size, were collected from within and around the Chegem caldera (Fig. 4.1). As the terrain is rather rugged, sampling was mainly confined to the more accessible parts of the caldera (i.e., along the Chegem River). Efforts were made to sample a complete stratigraphic section of caldera fill, as well as to collect samples from all identifiable lithologies and near all major structural features.

The main stratigraphic section discussed in this paper (Section 1, Fig. 4.1) is located on the southeast side of the caldera near Mt. Kum Tyube, and spans a vertical range of 1405 meters of rhyolitic to dacitic zoned tuff, locally overlain by 310 meters of andesitic flows. The sampled section traverses radially inward from the margin of the caldera, and as the traverse extends toward the center of the caldera, it samples progressively upward in the stratigraphic column. Thus, the stratigraphically higher samples are also more distant from the caldera margin, and this bias needs to be kept in mind in interpreting all of the geochemical data. Two other partial stratigraphic sections were sampled, one on the east side of the caldera (Section 2, Fig. 4.1) up a side drainage of the main Dzhilgusu drainage, and one in the upper dacitic tuff horizons southwest of Kum Tyube Peak (Section 3, Fig. 4.1).

Whole-rock samples selected for oxygen isotope analysis were crushed in a mortar and pestle. Mineral separates were obtained by hand-picking ≈50 mg of the given mineral from a 35-50 mesh fraction of the ground sample. The fluorination technique used for oxygen isotope analyses is essentially that described in Taylor and Epstein (1962). Modifications to that technique and to

the extraction line are described in Appendix B. Sample gases were analyzed with either a McKinney-Nier mass spectrometer or a Finnegan MAT 252 mass spectrometer and compared to the laboratory Rose Quartz standard. The results of the Rose Quartz standard analyses are also given in Appendix B. Oxygen isotope ratios are reported in the familiar δ-notation as per mil difference from SMOW (standard mean ocean water):

$$\delta^{18}O_{sample} = 1000 * \left( \frac{\left(^{18}O/^{16}O\right)_{sample} - \left(^{18}O/^{16}O\right)_{SMOW}}{\left(^{18}O/^{16}O\right)_{SMOW}} \right)$$

δ-values on this scale for NBS-28 and the Caltech Rose Quartz standard are +9.60 and +8.45, respectively. Analytical precision is better than ±0.15 per mil (1σ).

After removal of lithic fragments, whole-rock samples for major- and trace-element analysis were pulverized to ≈200 mesh in a ceramic shatterbox. The powders were fused into glass disks for major-element analysis and pressed into pellets for trace-element analysis. Major-element oxides were analyzed using wavelength X-ray fluorescence spectrometry, as described by Taggart et al. (1987). Accuracy for most of the major-elements in concentrations found in the Chegem rocks is ±1%. The trace-elements (Sr, Rb, Zr) were determined by energy dispersive X-ray fluorescence with an accuracy of ±5% for Rb and Sr and better than 10% for Zr (Yager and Quick, 1992).

## 4.4 Results

### 4.4.1 Mineralogy and Major- and Trace-Element Compositions

***Intracaldera Stratigraphy-*** The intracaldera Chegem Tuff is best characterized by the vertical sampled section on the east side of Mt. Kum Tyube (Stratigraphic Section 1, Fig. 4.1) that ranges from 2080m to 3485m in elevation. This section

spans over 1400m without exposing the base of the intracaldera tuff; a composite section through the caldera suggests the tuff is greater than 2 km thick. The intracaldera ash-flow sequence consists mainly of densely-welded, devitrified tuff that is zoned upwards from rhyolite to dacite. Crude, massive layers are defined by flattened pumices that also grade upwards from rhyolitic to dacitic. Densely-welded, vitrophyric rhyolite tuff occurs along the margins of the caldera fill, usually exposed low in the caldera-fill stratigraphic sequence. The upper dacitic section of tuff contains at least two, and possibly three, distinct cooling sub-units that are 30-50 m thick. Cooling breaks are defined by 2-3 m zones of flattened vitrophyric pumice at the base of each sub-unit.

The Chegem Tuff generally contains ≈20% phenocrysts which range from predominantly quartz and sanidine in the rhyolites at the base of the exposed section to predominantly biotite, pyroxene (augite), and plagioclase in the upper dacitic horizons. Corresponding to this systematic variation in phenocryst content, there are distinct trends in major- and trace-element composition.

Major-element compositions of the whole-rock samples in Section 1 are shown in Fig. 4.2: $SiO_2$ ranges from 76.1 wt% at the base to 69.9 wt% just below the andesite flows, decreasing upward in a generally monatonic and systematic fashion. There is a corresponding upward decrease in $K_2O$ and increase in $Al_2O_3$, $Na_2O$, CaO, and MgO. Total $Fe_2O_3$ also increases upward, but in a very erratic fashion. The $Na_2O$ content drops abruptly in the uppermost dacitic sub-unit.

Trace elements display the same overall stratigraphic trend (Fig. 4.3): Sr ranges from 30 ppm (base of section) to 275 ppm (top); Zr ranges from 74 ppm (base) to 185 ppm (top); Rb displays a more subtle upwards decrease from 177 ppm (base) to 109 ppm (top) that is partially obscured by minor fluctuations.

Aside from this general trend of increasing mafic constituents upward, there are two significant reversals; the smaller of the two is at 2870m (sample CG-C2-4B) and the more pronounced reversal occurs at 3225m (CG-C2-4F). These reversals are best seen as anomalous spikes in the trends of $SiO_2$, $K_2O$, CaO, $Al_2O_3$, $TiO_2$, Sr, and Rb. Although principally defined by the samples at 2870 and 3225m, a sample taken at 3280m (CG-C-44G) also displays intermediate compositions that lie between the normal trend and those of the anomalous sample at 3225m. Note, however, that the Rb anomalies document a more gradual change between the normal trends and the reversals. The lack of more supporting data points is probably an artifact of the sampling interval; vertical distance between samples (≈50m) is roughly the size of the anomalous zone.

A second partial stratigraphic section (Section 2, Fig. 4.1) spans a vertical range from 1775m to 3124m and also varies from high-silica rhyolite at the base to dacite (69.8% $SiO_2$) at the top. The base of the dacite unit in Section 2 is at 3080m, some 250-300 m lower that the base of the dacitic tuffs in Section 1. However, the distinctive cooling sub-units, and their partial vitrophyres, that mark the upper part of the dacitic tuffs in Section 1 have been removed by erosion at this locality. Rb decreases slightly upward in Section 2, whereas Sr and Zr contents increase upwards. One sample defines a slight spike in Sr and Zr, but the anomaly is not corroborated by the Rb data and is of opposite sense to the anomalies observed in Section 1.

*Outflow Stratigraphy* - The outflow tuff sheet, whose remnants are exposed ten to fifty kilometers away from the Chegem caldera, contains only a part of the sequence observed in the intracaldera stratigraphic section. Lower parts of the outflow sheets are typically covered by talus and poorly exposed, and the top of the outflow tuff remnants are invariably eroded. As with the intracaldera

Chegem Tuff, phenocrysts consist of quartz, feldspar, and biotite. The outflow tuff becomes more crystal-rich and more biotite-rich upward; the general geochemical trend of increasing mafic content upward is also present in the outflow tuff. The two most complete sections of outflow tuff are about 200 m thick and correlate with the lower part of the intracaldera stratigraphic section in their major- and trace-element contents ($SiO_2$ = 73.0-76.6 wt%; Sr = 12-161 ppm; Zr = 66-132 ppm; Fig. 4.4). These ranges of trace- and major-element compositions correspond most closely with the lower 600m of caldera fill (zone A, described below) although some of the anomalous spikes in the central part of Section 1 also have comparable major- and trace-element compositions.

***Resurgent Intrusion and Post-collapse Lavas*** - The porphyry intrusion in the northeastern quadrant of the Chegem caldera contains 30-40% phenocrysts of plagioclase (andesine), with lesser amounts of resorbed quartz, sanidine, biotite, pyroxene, and magnetite in a microcrystalline, granophyric groundmass of quartz and feldspar. It ranges in composition from fine-grained granite at its borders to coarser-grained granodiorite in its interior. The granodiorite is similar in both major- and trace-element composition to the late-erupted dacitic tuff units ($SiO_2$ = 70.3-71.9 wt%, Sr = 193-239 ppm and Zr = 141-188 ppm; Fig. 4.4).

The post-collapse lavas which cap the intracaldera Chegem Tuff are andesites to mafic dacites with 10-40% phenocrysts of plagioclase (andesine-labradorite), pyroxene (mainly hypersthene), amphibole, and rare biotite. Major and trace elements of the andesites indicate that they are much more mafic than any of the ash-flow tuffs of the Chegem volcanic suite, with $SiO_2$ = 63.0-64.4 wt%, Sr = 221-350 ppm and Zr = 149-221 ppm (Fig. 4.4).

### 4.4.2 Oxygen Isotopes

Oxygen isotopic compositions for the igneous rocks of the Chegem caldera as well as some of the nearby country rocks are presented in Table 4.1.

*Intracaldera Stratigraphy* - Measured whole-rock, quartz, feldspar, glass, and groundmass $\delta^{18}O$ values for the 1405 m of Stratigraphic Section 1 (Fig. 4.5) define an elevation profile in which the lower half and top have relatively high $\delta^{18}O$ values, whereas the intermediate portion contains some very low whole-rock and groundmass $\delta^{18}O$ values. Quartz and feldspar phenocrysts throughout this section and elsewhere in the caldera have relatively constant $\delta^{18}O$ values of $+8.5 \pm 0.2$ and $+7.4 \pm 0.9$, respectively (mean, std. dev.). In contrast, whole rock $\delta^{18}O$ values range from –4.0 to +12.1, while measured $\delta^{18}O$ values of separated groundmass and glass span an even wider range (–7.0 to +12.3). Also shown are the calculated material-balance $\delta^{18}O$ values for the groundmass based on the measured whole-rock values, assuming that these rocks consist of 80% groundmass and 20% phenocrysts; the phenocrysts (quartz + feldspar) are assumed to have a combined $\delta^{18}O$ of +7.9. The shaded zone represents the range of $\delta^{18}O$ values for a silicate melt in equilibrium with the quartz and feldspar phenocrysts, utilizing the empirical observation (e.g., Taylor, 1968) that granitic melts are typically 0.2 to 0.4 per mil higher in $^{18}O$ than their coexisting feldspars.

In order to determine whether the low-$^{18}O$ zone in Fig. 4.5 represents a caldera-wide, low-$^{18}O$ stratigraphic horizon or simply a local anomaly on the southeast side of the caldera, two partial stratigraphic sections (Sections 2 and 3; Fig. 4.1) were also studied. The whole-rock $\delta^{18}O$ results for Sections 2 and 3, shown in Fig. 4.6, clearly indicate that this is indeed a caldera-wide phenomenon.

For purposes of description, we have divided the ash-flow tuff stratigraphy into three zones on the basis of oxygen isotopic composition and

petrology. Zone A (from 1775 to 2700 m in Section 1) is a zone of "normal" $\delta^{18}O$, where the measured whole-rock $\delta^{18}O$ values are also in agreement with the calculated range for magmas in equilibrium with the analyzed phenocrysts. The rhyolite tuff within this interval shows a relatively smooth upward transition to more mafic compositions. Zone B (2700-3300 m) is a zone of low $\delta^{18}O$: whole-rock $\delta^{18}O$ values are as low as –4.0 while the measured groundmass for the lowest $^{18}O$ sample is –7.0. The measured whole-rock $\delta^{18}O$ values do not at all agree with the magma $\delta^{18}O$ values calculated from the phenocrysts. This interval also contains both of the anomalous compositional reversals defined by samples from Section 1 (Fig. 4.7). Zone C (3300-3465 m) is the upper dacitic part of the stratigraphic section. This part of the section shows very large whole-rock $\delta^{18}O$ variations over a very small stratigraphic interval, extending to some extremely high $\delta^{18}O$ values (+12.3). This zone is visually distinct from the lower two zones because of the partial vitrophyre horizons (containing black glassy pumices) that define welding breaks between cooling sub-units.

***Resurgent Block*** - Oxygen isotope compositions were measured for samples collected along the ridges which traverse the resurgent block of tuff in the northeast quadrant of the caldera (Fig. 4.8). Whole-rock $\delta^{18}O$ values tend to be higher (+6 to +8) on the northeast side of the resurgent block, near the intrusion. The $\delta^{18}O$ values decrease to 0 to +2 in the southwest, near the fault that bounds this block. Two anomalously $^{18}O$-depleted samples, CG-C2-17A and CG-C2-17B, were collected at a single location in the middle of this block. Sample CG-C2-17A is typical grey devitrified tuff, whereas CG-C2-17B is from a large dark grey devitrified pumice block found in float; in thin section this sample is entirely crystalline and lacks the pyroclastic texture of the rest of the tuff in the resurgent block.

*Vitrophyres and Glassy Pumices-* All intracaldera vitrophyres consisting entirely of black glass have whole-rock $\delta^{18}O$ of +8.1 or higher; many of the values are slightly enriched in $^{18}O$ relative to the range of calculated values for magma in equilibrium with the coexisting phenocrysts. A single outflow vitrophyre, collected as float but considered to come from the base of the outflow sheet, has the lowest whole-rock $\delta^{18}O$ value of the vitrophyres, +6.5. Glass from glassy pumices exhibits a range of $\delta^{18}O$ values, from +1.4 to +9.1. All of these glasses are hydrated, with ≈3 to 4 wt% $H_2O$ (Chapter 6).

*Outflow Tuff* - The oxygen isotope compositions of the outflow tuff, for whole rock, quartz, feldspar, groundmass, and glass separates (Table 4.1, Fig. 4.9) are similar to the caldera fill in that quartz and feldspar phenocrysts have very uniform $\delta^{18}O$ values of +8.4 ± 0.2 and +7.5 ± 0.5, respectively. Groundmass and glass separates are commonly lower in $^{18}O$, pulling the whole-rock compositions below the values for magmas in equilibrium with the phenocrysts. In contrast to the major and trace elements, these whole-rock oxygen isotopic compositions correlate best with either the lower part of Zone B or the interface between Zones B and C.

*Granodiorite Porphyry Intrusion* - The granodiorite intrusion also displays the same kinds of oxygen isotope disequilibrium phenomena as are observed in the middle section of Chegem Tuff, though the isotopic variations are considerably less pronounced (Table 4.1, Fig. 4.9). Again, the quartz and feldspar phenocrysts have $\delta^{18}O$ = +8.4 ± 0.2 and +7.0 ± 0.3, respectively, similar to all other Chegem samples. Groundmass $\delta^{18}O$ values range from +2.7 to +6.0, and corresponding whole-rock $\delta^{18}O$ values range from +3.7 to +7.3.

*Andesite*- All measured andesites have whole-rock $\delta^{18}O$ values between +7.2 and +7.9. These values are all within the range of calculated values for magmas in equilibrium with the analyzed phenocrysts from the andesites.

*Country Rock* - The Chegem caldera is surrounded by two different types of country rock: Proterozoic to Paleozoic crystalline rocks and Jurassic limestones. Measured whole-rock $\delta^{18}O$ values are +8.1 to +8.7 for the crystalline rocks and +27.4 to +30.2 for the limestones.

## 4.5 Discussion

### 4.5.1 Contrast with Other Caldera Complexes

It is useful to contrast the Chegem caldera with a couple of other caldera complexes where oxygen isotope trends have been well-documented, and where meteoric hydrothermal phenomena have been well documented. Two such settings are the Yellowstone volcanic field (Wyoming) and Lake City caldera (Colorado).

*Yellowstone Plateau Volcanic Field* - The Yellowstone volcanic field has produced ≈6000 $km^3$ of rhyolite tuffs and lavas which cover an area of ≈17000 $km^2$. These magmas were associated with three successive caldera cycles which spanned a period of 2.2 million years. Hildreth et al. (1984) analyzed oxygen isotopic compositions of quartz and feldspar phenocrysts from silicic eruptive units in the Yellowstone Plateau volcanic field. They found evidence for repeated eruptions of $^{18}O$-depleted rhyolitic magma following caldera collapse. While ash-flow phenocrysts typically had nearly "normal" igneous $\delta^{18}O$ values, post-collapse lava phenocrysts were up to 6 per mil lighter. Oxygen isotope

fractionations among coexisting quartz, feldspar, and other minerals all recorded magmatic temperatures, indicating that the $^{18}O$ depletions were present in the magma at the time of eruption, and were not the result of subsolidus hydrothermal alteration. Hildreth et al. (1984) explained these $^{18}O$ depletions as the result of influx of large volumes of low-$^{18}O$ meteoric waters into the magmas, whereas Taylor (1987) suggested that they were probably caused either by assimilation of hydrothermally altered rhyolitic roof rocks, or by partial melting of such low-$^{18}O$ rocks within the volcanic edifice.

Unlike the Yellowstone caldera complex, the Chegem caldera represents a single caldera-forming eruption with little if any pre-caldera volcanism. The zone of low-$^{18}O$ rocks at Chegem occurs late in the ash-flow sequence itself and not in the post-collapse lavas as in Yellowstone. Another important difference between the two settings is that in the low-$^{18}O$ rocks at Chegem, the groundmass is far out of equilibrium with the quartz and feldspar phenocrysts, which have nearly "normal" igneous $\delta^{18}O$ values, indicating that the $^{18}O$-lowering process at Chegem was short-lived. At Yellowstone, both quartz and feldspar $\delta^{18}O$ values have been lowered, indicating a process which occurred over a significantly longer time period and/or at a much higher temperature.

***Lake City Caldera*** - In contrast to the enormous area covered by the Yellowstone caldera complex, the 23 Ma Lake City caldera is 11x14 km, similar in size to the Chegem caldera. However, unlike the Chegem caldera, the Lake City caldera has undergone an extended period of resurgence accompanied by significant subsolidus hydrothermal activity and alteration. Larson and Taylor (1986a) observed systematic $\delta^{18}O$ variations throughout the Lake City caldera, with values as low as –2 per mil. Permeable zones of mineralogically altered (sericitized and chloritized) rocks typically were found to exhibit the greatest $^{18}O$

depletions, and thus Larson and Taylor (1986a) concluded that these depletions were caused by a caldera-wide hydrothermal system driven by the heat of the central resurgent intrusion and several ring intrusions.

In contrast, Chegem caldera rocks are remarkably fresh mineralogically. Fig. 4.10 shows photomicrographs of feldspars in $^{18}O$-depleted rocks from the two settings: the Chegem sample CG-C2-4H (Fig. 4.10a, $\delta^{18}O = -4.0$) has fresh feldspar and biotite phenocrysts with no trace of calcite, chlorite or other hydrothermal minerals; the Lake City sample (SC-71; Fig. 4.10b, $\delta^{18}O = +0.4$) displays extensive mineralogic alteration: feldspars are turbid and altered to calcite in their cores, and biotites are almost completely transformed to sericite + quartz.

### 4.5.2 Major- and Trace-Element Compositions

Major- and trace-element compositions at Chegem display mafic-upward zoning typical of ash-flow tuffs elsewhere in the world. We interpret these trends to represent downward tapping of the upper levels of a compositionally layered magma chamber during eruption, as has been inferred for other compositionally-zoned tuffs (e.g., Smith and Bailey, 1966; Smith, 1979; Hildreth, 1979, 1981; Fridrich et al., 1991). However, note that the whole-rock major- and trace- element compositions discussed here are bulk-tuff values that represent the average mixtures of erupted pumice compositions.

Analyses of 20 pumices collected from throughout the sections of intracaldera and outflow tuff show the same range of variation (69.0-76.6 wt% $SiO_2$) as the whole-rock tuff samples. Pumice fragments in the high-silica rhyolites are typically extremely small and difficult to collect; nevertheless, two such pumices showed a range from 76.6 to 74.5 wt% $SiO_2$, although part of the variation may be error related to the small sample sizes. The low-silica rhyolite

tuffs contain the complete spectrum of pumice compositions from 75.4 to 69.0 wt% $SiO_2$. In contrast, the dacitic tuffs have a restricted range of lower silica pumices (69.2-72.9 wt% $SiO_2$) and must be largely composed of 69-70 wt% $SiO_2$ pumice compositions to account for the observed whole-rock compositions. Both the lowermost high-silica rhyolite tuffs and the uppermost dacitic tuffs are composed of nearly pure end-member pumice compositions, whereas the low-silica rhyolite tuffs in the middle of the section are a mixture of all the pumice types. The anomalous compositional reversals found in the low-silica rhyolites in Section 1 appear to reflect changes in the mixture of erupted pumices, probably related to eruptions from separate vents and/or to fluctuations in the level of tapping of the sub-caldera magma chamber.

A comparison of the trace elements in Stratigraphic Sections 1 and 2 demonstrates that the fit between the two sections, especially at the top and bottom, is better when the Section 2 values are arbitrarily moved up in elevation 300m (Fig. 4.11a-c). This offset could be due to lateral variation of silicic/mafic pumice ratios within the caldera fill or to post-eruption vertical offsets along faults or folds. If Section 2 has indeed been moved down 300m vertically relative to Section 1, then restoring it to its original position improves the Sr and Zr correlations, but virtually destroys any correlation in oxygen isotope compositions (Fig. 4.11d). In fact, the fit between the oxygen profiles is best if Section 2 is moved *down* about 200m (Fig. 4.11e). Assuming that the major and trace element trends are magmatic, these offsets imply that the oxygen isotope trends are not magmatic. One could construct a multi-stage scenario in which Section 2 moved down 500m relative to Section 1 immediately following the ash-flow deposition, followed by a hydrothermal event which caused caldera-wide $^{18}O$ depletions along a horizontal zone about 600m thick; afterwards, further tectonic movements such as resurgence caused Section 2 to be displaced upward

about 200m relative to Section 1. An analogous type of late-stage collapse, followed by piston-like uplift, has been well documented at the Grizzly Peak caldera by Fridrich et al. (1991). The curved section of the Dzhilgusu River immediately south of the resurgent block is a likely candidate for the inner ring fracture zone in the Chegem caldera. If this multi-stage scenario is correct, then it implies that the hydrothermal event which caused the observed $^{18}O$ depletions occurred after the deposition of the tuff but prior to the resurgence of the granodiorite intrusion.

### 4.5.3 Cooling, Hydration and Devitrification

The cooling history of the Chegem Tuff, including the devitrification and hydration of glasses, is reviewed here because it undoubtedly has significant bearing on the observed oxygen isotope profile. Typical rhyolite eruption temperatures lie in the range of 700-900°C (Cas and Wright, 1988). Quartz-feldspar oxygen isotope fractionations in the Chegem Tuff correspond to temperatures within this range (≈825°C for $\Delta_{q\text{-}f} = 1.1‰$, feld = An35). During eruption, pyroclasts will cool variably before final emplacement. Most large ash-flows form during collapse of an eruption column, where emplacement temperatures are largely dependent on the initial gas content and gas velocities in the column (e.g., Sparks et al., 1978). Entrainment of additional air during collapse can result in emplacement temperatures up to 350 degrees lower than eruption temperatures. Eruption columns which have lower gas contents and gas velocities generally have emplacement temperatures closer to the eruption temperatures. Because there is no evidence for abnormally high gas contents or velocities in the Chegem eruption column, we estimate that the emplacement temperatures were probably about 650-800°C.

After emplacement, a pile of ash-flow tuff will undergo compaction and welding, and will cool slowly by conduction, advection-convection of aqueous fluids, and radiation of heat. Riehle (1973) developed an analytical model for heat flow from simple and complex cooling units of ash-flow tuff with a surface temperature of 25°C emplaced on cool substratum. In this model, the component of radiative heat transfer is incorporated in the coefficient of thermal conduction and convective heat transfer by volatiles is assumed to be negligible. Scaling this model to the 2-km thickness of intracaldera Chegem Tuff (Fig. 4.12), one discovers that it takes approximately 1300 years to cool the top 100 m of tuff to below 300°C and over 66,000 years to cool the entire thickness to less than 300°C. Any large-scale convection of aqueous fluids will accelerate this cooling process considerably.

The uppermost section of intracaldera Chegem Tuff was obviously the most quickly cooled, as evidenced by the 20 m of nonwelded tuff at the top of this unit. The dacitic tuff horizons also have well-preserved cooling sub-units with pristine glassy pumices at their boundaries. The presence of these partial vitrophyres within the dacitic tuff section suggests that there may have been short pauses or pulsations near the end of the eruption. The margins of the intracaldera tuff mass also cooled quickly against the caldera walls, quenching to form marginal vitrophyres a few meters thick. The densely welded nature of these marginal vitrophyres, deep within the caldera, suggests that welding was very rapid. At temperatures of 650°C, a 1-km thick tuff sheet probably requires less than 1 year to produce dense welding , but this time can be reduced to less than one week if at least 0.5% $H_2O$ is present (Bierwith, 1982).

The initially glassy tuffs also underwent high-temperature devitrification and hydration as they cooled within the interior of the caldera. Subsolidus crystallization of thermodynamically metastable glass produces a variety of

devitrification products, depending on the cooling rates (Lofgren, 1970). Rapid cooling produces fibrous crystals of quartz and sanidine that rapidly nucleate to form spherulites and axiolites (Ross and Smith, 1960). Slower cooling rates produce more equigranular granophyric textures. Experimental studies predict devitrification times for a 3mm glass shard of <3 years at 750°C to about 3000 years at 300°C (Lofgren, 1970).

All of the analyzed glassy pumices from the intracaldera Chegem Tuff have undergone hydration, typically attaining water contents of 3-4 wt% (Chapter 6). Glasses are rapidly hydrated, even at surface temperatures, when water diffuses into and through the glass structure. As water enters, spheroidal cracks are formed and the glass becomes perlitic. Hydration rate experiments (Friedman et al., 1966; Friedman and Smith, 1960) predict that a 3 mm shard will be hydrated in <3 hrs at 750°C or in about 3 years at 300°C. These rates are roughly 3-4 orders of magnitude faster than the time required to devitrify the same shard.

### 4.5.4 Significance of Low-$^{18}O$ Glasses

The presence of pristine glasses with $\delta^{18}O$ as low as +1.4 presents an interesting dilemma. Inasmuch as glasses are essentially silicate melts which have been quenched to subsolidus temperatures, they should originally have had exactly the same $\delta^{18}O$ value as the magma itself. These $\delta^{18}O$ values will usually lie in the normal "magmatic" range of about +6 to +10. The low temperature alteration and hydration that is commonly observed in older volcanic glasses in nature is known to cause an upward shift of the glass $\delta^{18}O$ value (Taylor, 1968; Cerling et al., 1985). This upward shift in $\delta^{18}O$ is a result of the intimate and pervasive exchange that occurs between Earth-surface waters and such glasses over the course of several thousand years, together with the fact that very large

oxygen isotope equilibrium fractionations exist between water and silicate minerals or glass at low temperature (e.g. at 25°C, $\Delta_{water\text{-}glass} \approx 20$ per mil: Taylor, 1968; Cerling et al., 1985). Thus, only extremely light meteoric waters in very cold climatic regions ($\delta^{18}O < -20$ at 25°C) could substantially lower the $\delta^{18}O$ value of a volcanic glass. On the other hand, water-glass oxygen isotope fractionations at higher temperatures (e.g., greater than 200°C) are sufficiently small that, even in temperate or subtropical climates, all meteoric water-glass interactions will lower the $^{18}O$-content of the glass; however, such high temperature alteration would also be expected to devitrify and recrystallize the inherently metastable glass. For example, experiments by Lofgren (1970) and Marshall (1961) predict that at 200°C, a 1mm (radius) glass shard will be devitrified by pure water in ≈3000 years. At higher temperatures or with saline waters, these times should be orders of magnitude shorter.

If low-$^{18}O$ glasses are indeed formed, and if they subsequently interact with additional water at low temperature, this high-$^{18}O$ overprint will in general obscure their original low-$^{18}O$ signature. This is very likely the main reason why low-$^{18}O$ glasses have rarely been observed, except in very young volcanic rocks in unique geological environments (e.g., in Iceland, Muehlenbachs et al., 1974). Smith and Suemnicht (1991) found two frothy glassy pumices on the surface of Long Valley caldera with $\delta^{18}O$ values of +0.3 and +0.4. Many other low-$^{18}O$ rocks exist at Long Valley but all such samples are argillically altered or fractured and silicified. Hildreth et al. (1984) found that glasses in the non-hydrated cores of some vitrophyres at Yellowstone volcanic field have $\delta^{18}O$ values as low as +0.5, but, as described above, the phenocrysts in those vitrophyres had equilibrated with low-$^{18}O$ silicate melts.

### 4.5.5 Lack of Hydrothermally Altered Country Rocks

The oxygen isotopic compositions of the country rocks surrounding the Chegem caldera, like the field and petrographic observations of the tuff itself, argue against the development of any substantial "normal" (i.e., 200-300°C) hydrothermal system after caldera collapse. In particular, samples CG-C-60A to 60C, which are limestones collected at distances of 4, 18, and 30 meters from the main caldera ring fault, have normal sedimentary $\delta^{18}O$ values of +29.0 to +29.9. If a significant hydrothermal system had developed after caldera collapse, as, for example, in the Lake City caldera (Larson and Taylor, 1986a), one would expect that abundant fluids would have moved along this ring fault, a zone of higher permeability. Limestones are sensitive indicators of the passage of meteoric-hydrothermal fluids in the brittle-fracture regime of the Earth's crust, because under such conditions they exchange rapidly and they can be very permeable; also, because they start out with such high $\delta^{18}O$ values, even a small amount of $^{18}O/^{16}O$ exchange can be readily observed.

### 4.5.6 Constraints on the Process Responsible for $^{18}O$ Depletion

The dramatic $^{18}O$ depletion and disequilibrium described in this paper has not to our knowledge been observed previously anywhere in the world, and certainly not on this scale. It is possible that these types of $^{18}O$ depletions in fact occur much more frequently than we realize, but are overlooked because they are usually overprinted and obscured by the ubiquitous hydrothermal alteration or low-temperature hydration that is so characteristic of volcanic centers, particularly calderas. The Chegem caldera may have uniquely preserved the effects of this $^{18}O$ depletion event because of its youth, and because the rapid uplift and associated deep erosion in the Caucasus Mountains may have short-circuited the possibility of any long-lived hydrothermal stage.

Based on our data, we can place certain constraints on the process which caused the $^{18}O$ depletion at Chegem. In quantifying these constraints in the following discussion, assumptions must be made regarding temperatures of equilibration, the isotopic compositions of meteoric waters and unaltered Chegem Tuff, and diffusion mechanisms and coefficients for oxygen exchange between $H_2O$ and feldspar or glass. Where these parameters are uncertain (as for temperature), a range of values is used or the most conservative estimate is made (i.e., the values which would minimize the amount of water necessary to produce the observed effects).

*Necessity for Involvement of High-Temperature Meteoric Waters* - Whatever the $^{18}O$-lowering process was, it *must* have involved meteoric waters at relatively high temperatures (>300°C). Earth-surface waters are the only waters isotopically light enough to cause the observed $^{18}O$ depletions, and high temperatures are necessary to produce sufficiently favorable equilibrium $^{18}O$-fractionations between silicates and $H_2O$.

It is possible that some of the less extreme $^{18}O$ depletions (such as those in the outflow sheets) were caused by isotopically light waters at temperatures below 300°C, and therefore we should perhaps consider two-stage (or multi-stage) processes, or processes involving a range of temperatures. In fact, the $^{18}O$ *enrichments* of up to 4 per mil present at the top of the intracaldera tuff section, if they were caused by meteoric waters (as seems likely), *must* have occurred at low temperatures (<100°C). Only at such low temperatures are oxygen isotope fractionations between silicates and $H_2O$ large enough to raise the $^{18}O$ contents of the rocks. Also, the simple cooling model (Fig. 4.12) indicates that the upper 100 m of tuff was cooled rapidly to <100°C.

In addition, mineralogical evidence provides an important constraint on the temperature of the water-rock interaction. Feldspars in the Chegem Tuff are entirely unaltered (Fig. 4.10a) and there is no sign of chloritization of biotites. Feldspars and biotites are known to be rapidly altered in a "low-temperature" (200-400°C) hydrothermal environment. For example, Cole et al. (1992) performed hydrothermal experiments with pure water on granites at temperatures of 170° to 300°C, and observed that chlorite formed in biotites in all cases after only 160 hours. The presence of salts (NaCl + KCl) in the water increased the alteration rate. This lack of "typical" hydrothermal alteration minerals, such as chlorite and sericite, implies that the hydrothermal $^{18}O$ exchange that produced the $^{18}O$ depletions at Chegem had to take place at very high temperatures (≈500-600°C), within the stability fields of the high-temperature minerals. Biotite is practically the only OH-bearing mineral likely to be stable under such conditions in this kind of volcanic environment.

The exact isotopic compositions of the waters that caused the observed $^{18}O$-lowering are difficult to ascertain, because these waters are no longer present, except possibly in fluid inclusions. The present-day Chegem River water, a combination of glacial meltwater and rain water, has a $\delta D$ value of –89 (Chapter 6) which corresponds to a $\delta^{18}O$ value of –12, assuming that it lies on the meteoric water line (Craig, 1961). Modern precipitation at the highest point in the Chegem caldera is expected to be several per mil lower in $^{18}O$ than this river water. However, estimates of recent uplift in the Greater Caucasus are quite high (up to 12mm/yr; Philip et al., 1989) and it is likely that erosion did not keep pace with uplift. Thus, the overall elevation of the central Caucasus Mountains was lower and topography was probably less pronounced 2.8 million years ago than at present. In such a scenario, all else being the same, one would expect that 2.8 Ma meteoric water in the Chegem area would have been slightly enriched in $^{18}O$

compared to modern meteoric water. For the purposes of our discussions, we will consider a range of meteoric water isotopic compositions from $\delta^{18}O = -12$ to $-16$. The lighter value will tend to minimize the amount of meteoric water needed.

***Mass-Balance W/R Ratios*** - Mass balance calculations can be used to estimate the amounts and fluxes of water necessary to cause the observed $^{18}O$ depletions. We will consider a range of temperatures, and the following assumptions will be used in the mass-balance calculations: (1) The original isotopic composition of the magma and erupted rock was $\delta^{18}O = +8$, which is an approximate value representing a close approach to equilibrium with the average phenocrysts. (2) The ≈700m-thick $^{18}O$-depleted zone observed in the stratigraphic section on the southeast side of the caldera was present throughout the 11x15 km caldera and is equally intense throughout, giving a flattened cylindrical volume of low-$^{18}O$ rock equal to $1.16 \times 10^{11}$ $m^3$. With a density of 2.4 $g/cm^3$, this translates into about $2.8 \times 10^{17}$g of $^{18}O$-depleted tuff. (3) The groundmass in each sample has exchanged thoroughly with (and attained isotopic equilibrium with) the interacting meteoric waters. This assumption will tend to minimize the amount of water needed to produce the observed $^{18}O$ depletions. (4) The groundmass $\delta^{18}O$ value can be accurately estimated by a simple material-balance calculation from the measured whole-rock $\delta^{18}O$ value, assuming that all of the samples contain 20% phenocrysts with a bulk $\delta^{18}O$ of +7.9. (5) The oxygen isotope fractionation between water and glass (or groundmass) is approximately the average between the measured equilibrium fractionations for quartz-$H_2O$ and albite-$H_2O$ (Clayton and Kieffer, 1991). (6) We assume that the interacting fluid is $H_2O$ and we will consider two cases, one with the isotopic composition of the

interacting water equal to the present day Chegem River water value ($\delta^{18}O = -12$) and one with a lighter meteoric water ($\delta^{18}O = -16$).

With the above assumptions, zero-dimensional box models such as those described by Taylor (1977) are useful for estimating the amounts of water required to produce observed oxygen isotopic shifts. Material-balance model water/rock (W/R) ratios can be calculated and converted to integrated fluxes when appropriate length scales and flow directions are known. An advantage of such models is that the details of the hydrothermal "plumbing" system or flow paths need not be known. On the other hand, a disadvantage of such models is that the actual W/R ratios in such systems in nature can only be calculated if the position of the rock in the flow path and the conditions of flow and exchange are taken into account (Norton and Taylor, 1979; Bowman et al., 1994). Also, although the actual W/R ratios are dimensionless, they depend on the size of the rock parcel (box) which is considered. The material-balance and actual water/rock ratios only become identical if the size of the rock parcel is increased to essentially encompass the entire hydrothermal system. Nevertheless, since neither the nature nor the direction of fluid flow in the Chegem caldera system is known, whereas the size of the $^{18}O$-depleted zone is well-defined, zero-dimensional models are appropriate in this case.

To minimize the amount of water needed to produce the observed $^{18}O$ depletions, we consider an open-system model, where a tiny parcel of water exchanges isotopes with the rocks and then passes out of the rock system forever. The material-balance model water/rock ratio (i.e., the amount of water oxygen/amount of rock oxygen) for an open system where rocks have reached equilibrium with the interacting water, integrated over the lifetime of the hydrothermal system, is given by (Taylor, 1977):

$$\frac{W}{R} = \ln\left[\frac{\delta^i_{H_2O} + \Delta - \delta^i_{rock}}{\delta^i_{H_2O} - \left(\delta^f_{rock} - \Delta\right)}\right]$$

where i is the initial value and f is the final value after exchange, and $\Delta = \delta^f_{rock} - \delta^f_{H_2O}$ is the equilibrium fractionation between water and rock at the given temperature.

Because we do not *a priori* know the temperature of exchange, we probably must consider a range of temperatures, from 25°C to 850°C. However, in applying the above expression one quickly discovers that the elevated $\delta^{18}O$ values in the upper 40 meters of the stratigraphic section can *only* be produced at temperatures below 100°C from waters with $\delta^i_{H_2O} > -13$. The lowest groundmass value (sample CG-C2-4H, calculated $\delta^{18}O_{gm} = -7$) requires temperatures of at least 350°C if $\delta^i_{H_2O} = -12$ and at least 250°C if $\delta^i_{H_2O} = -16$. Fig. 4.13 shows the calculated W/R ratios vs. elevation for temperatures of 850°C and 400°C (or 300°C) and for $\delta^i_{H_2O} = -12$ (or –16). The material-balance W/R ratios (e.g., for sample CG-C2-4H) are reduced by as much as 45% at the higher temperature (850°C) as opposed to the lower temperature. Averaged over the entire $^{18}O$-depleted zone of the stratigraphic column, these W/R ratios are overall about 30% lower at 850°C than at the lower temperatures. These oxygen W/R ratios of 0.3 to 0.6 translate into water/rock ratios by weight of about 0.16 to 0.32 (g of $H_2O$ per g of rock). This in turn implies that about 0.5 to 1.0 x $10^{17}$g of $H_2O$ exchanged with the ≈700m-thick section of tuff.

***Timescale of $^{18}O$ Depletion at Chegem-*** The caldera-fill ash-flow tuff is not appreciably mineralogically altered, and it also still contains apparently pristine (but hydrated!) volcanic glass. As discussed earlier, the $^{18}O$ depletions at Chegem were definitely not caused by an extensive long-lived hydrothermal system like the one which existed at the Lake City caldera. Furthermore, the $^{18}O$-

lowering process at Chegem must have happened on a very short timescale because of the extreme isotopic disequilibrium between groundmass and phenocrysts. A useful graphical mechanism for discussing isotopic disequilibrium is provided by δ-δ plots for coexisting quartz-feldspar or pyroxene-feldspar pairs (e.g., Gregory and Taylor, 1986). For the Chegem caldera, the $\delta_{quartz}$-$\delta_{feldspar}$ plot (Fig. 4.14a) reveals only small degrees of disequilibrium in some samples, whereas the δ-δ plot for feldspar-groundmass/glass (Fig. 4.14b) displays extreme disequilibrium. This "mineral pair" is sensitive to disequilibrium at much shorter timescales than the $\delta_{quartz}$-$\delta_{feldspar}$ mineral pair because at a given temperature, silicate glass (and very fine-grained groundmass?) exchanges oxygen isotopes with $H_2O$ much more rapidly than feldspar phenocrysts (Taylor, 1968); in turn, it has been shown in countless studies, both in nature and in the laboratory, that feldspar-$H_2O$ exchange is much more rapid than quartz-$H_2O$ exchange.

In order to quantify the necessary timescales, let us consider a particular Chegem sample, namely the one that displays the greatest degree of disequilibrium between phenocrysts and groundmass (CG-C2-4H, $\delta^{18}O_{feldspar}$ = +5.9, $\delta^{18}O_{groundmass}$ = –7.0). The kinetics of isotopic exchange greatly depend on the temperature, so here we will consider two temperature extremes: 300°C (typical hydrothermal) and 800°C (near magmatic). At either temperature, the isotope exchange process must have occurred over a long enough time scale that the glass or the groundmass could nearly fully equilibrate (>90%) with the water, but yet over a short enough timescale that the feldspars are nearly unaltered (<10%), both isotopically and mineralogically. The extent of $^{18}O$ exchange for both feldspar phenocrysts and glass are dependent on the mechanism of exchange, either surface reactions (such as dissolution and reprecipitation) or diffusion of oxygen-bearing species such as $H_2O$ (Cole et al.,

1983). Inasmuch as volume diffusion-controlled exchange is slower than exchange due to surface reactions by several orders of magnitude, this mechanism will provide a maximum estimate of the water-rock interaction time that conceivably could have elapsed without isotopically altering the feldspar.

Diffusion-controlled exchange is dependent on the diffusion coefficient for the phase of interest, the diffusion radius, the temperature, and the mole ratio of oxygen in the water to that in the rock. Typical values of hydrothermal diffusion coefficients for feldspars at 300° and 800°C are $1.4 \times 10^{-17}$ and $6.41 \times 10^{-13}$ $cm^2/sec$, respectively (Giletti et al., 1978). Assuming the feldspar is a sphere of radius 300μm and that the oxygen reservoir outside the sphere is well-mixed (i.e., that the system is fluid-buffered), the solution of Crank (1979) can be applied: 10% exchange is achieved when $Dt/a^2 \approx 0.001$ (Fig 4.15). This corresponds to timescales of approximately 2,000 yrs at 300°C and 0.04 yrs at 800°C. At temperatures of 500° to 600°C, likely temperatures for $^{18}O$ exchange at Chegem, the maximum timescale is approximately ten years (Fig. 4.15).

The isotopic composition of glass or groundmass can be used as a constraint on the minimum time necessary to create the observed isotopic systematics. We assume that the groundmass $\delta^{18}O$ value was attained before or during devitrification. Diffusion of oxygen in rhyolite glass is thought to be controlled by diffusion of water into the glass structure, and diffusion coefficients for water in glass are about 5 orders of magnitude higher than hydrothermal diffusion coefficients for oxygen in feldspar (Zhang et al., 1991). This would imply timescales of less than a year to achieve 90% exchange. Furthermore, if oxygen exchange is caused by a mechanism other than simple volume diffusion of $H_2O$ (which is especially likely for the devitrified low-$^{18}O$ groundmass), then the timescale will be even shorter.

Another approach to the timescale question is to treat the $\delta_{feldspar}$-$\delta_{glass/groundmass}$ plot as an "oxygen isotope clock," in the same way that Gregory et al. (1989) regarded the $\delta_{quartz}$-$\delta_{feldspar}$ plot for fossil hydrothermal systems in nature. We will consider our $\delta_{feldspar}$-$\delta_{glass/groundmass}$ plot to be essentially a $\delta_{feldspar}$-$\delta_{glass}$ plot. Gregory et al. (1989) pointed out that the slope of an array of data on a $\delta_{quartz}$-$\delta_{feldspar}$ plot can in principle indicate the duration of a hydrothermal system. The array moves essentially from vertical (slope = $\infty$) to 45°(slope = 1) through time as if it were the hand of an "oxygen isotope clock." In these terms, a $\delta_{feldspar}$-$\delta_{glass}$ plot is simply a clock which records much shorter timescales, because glass exchanges oxygen extremely rapidly, and (relative to coexisting glass) feldspar can be regarded as the slow-exchanging mineral.

The slope of an array of data points on a δ-δ plot is related to the kinetic rate constants (k) for the two exchanging "minerals", and to the fractional approach of that mineral-water system to equilibrium (f). The rate law used in this treatment is:

$$\frac{dR_A}{dt} = k(\alpha R_W - R_A)$$

where $R_A$ and $R_W$ are the $^{18}O/^{16}O$ ratios in the mineral and water, respectively, and α is the mineral/water equilibrium isotopic fractionation factor for the temperature of interest:

$$\alpha = \left(\frac{R_A}{R_W}\right)_{eq} \quad \text{(at equilibrium)}$$

The term f is defined as:

$$f \equiv \frac{\delta^o - \delta}{\delta^o - \delta^{eq}} = 1 - \exp(-kt)$$

where $\delta^o$ and $\delta^{eq}$ are the δ-values initially and at equilibrium, respectively. A mineral-water system is initially completely out of equilibrium with f = 0, whereas f = 1 when the system has attained equilibrium.

For buffered open-system conditions, Criss et al. (1987) showed that for spherical mineral grains, the kinetic rate constant, k, is related to the diffusion coefficient by the equations:

$$\exp(-kt) = 1 - f \approx \exp(-3.5\sqrt{Dt/a^2}) \quad \text{for } \sqrt{Dt/a^2} < 0.1$$

$$\exp(-kt) = 1 - f \approx \exp(-9.87Dt/a^2 + 0.498) \quad \text{for } \sqrt{Dt/a^2} > 0.2$$

Table 4.2 shows how these different parameters and the slopes of a data point array on a $\delta_{feldspar}$-$\delta_{glass}$ plot change with temperature, time, and grain radius. One can see immediately that glass exchanges oxygen isotopes with water extremely quickly, and for almost all of the time-temperature conditions represented in the table, the glass has completely equilibrated with the water. Even at 300°C, a sphere of 300μm will exchange ≈80% in 4 months. In contrast, a sphere of feldspar of equal size is essentially unchanged (f = 0.004) under these conditions. Therefore, the degree of attainment of isotopic equilibrium in the entire feldspar-glass-water system (and hence the slope of the $\delta_{feldspar}$-$\delta_{glass}$ plot) is controlled by the fractional approach to equilibrium of the feldspar-water system. That is, the glass-water system equilibrates so rapidly that it plays no role in defining these exchange rate systematics.

Our estimate of the grain radius for both feldspar and glass at Chegem is 300μm. For temperatures of 300°, 600° and 800°C, complete equilibrium (slope = 1) is attained after approximately 600,000 yrs, 300 yrs, and 30 yrs, respectively. The measured slope of our data array on a $\delta_{feldspar}$-$\delta_{glass/groundmass}$ plot is approximately 7 (Fig. 4.14b). For 300°, 600° and 800°C, this corresponds to approximate timescales of 3000 yrs, 3 yrs, and 0.03 yrs, similar to the timescales calculated above, because in both cases we predicted ≈10% feldspar exchange by volume diffusion in a fluid-buffered system.

*Cross-Cutting Relationships* - The low-$^{18}O$ zone is a ≈700 meter thick stratigraphic horizon located between elevations 2710 meters to 3390 meters along the sample traverses in the southern and eastern parts of the caldera. In the northeast, this horizon is apparently offset by faults which were formed during late collapse and which were reactivated when the resurgent intrusion uplifted a block of tuff. The oxygen isotopic compositions of samples from the uplifted block of tuff appear to represent a portion of the low-$^{18}O$ zone (possibly that part between 2600m to 3000m) that has been uplifted and tilted. This interpretation would suggest that a significant part of the $^{18}O$ depletion event occurred prior to the intrusion of the granodiorite. Though it is also possible that the apparent truncation of the low-$^{18}O$ zone was due to preferential fluid flow in a direction of greater permeability at that fault contact, the apparent vertical offsets between Section 1 and Section 2, which are in opposite directions for the trace-element profile and the oxygen isotope profile (as described above, Fig. 4.11), also strongly suggest that the low-$^{18}O$ zone was formed after deposition of the tuff but prior to resurgence. $^{40}Ar/^{39}Ar$ studies (Chapter 3) have constrained the resurgent intrusion to have been emplaced, crystallized, and cooled to 300°C within 50,000 years of eruption. These relationships, together with the requirement of high temperatures, suggest that the low-$^{18}O$ zone must have formed immediately after eruption of the Chegem Tuff.

Outflow-facies tuff samples are similar to the caldera fill, but they are more glass-rich and display less pronounced $^{18}O$-lowering and lesser isotopic disequilibrium effects. Inasmuch as these signatures exist up to 50 kilometers away from the caldera, and because the outflow tuff was probably everywhere less than 400m thick, it is virtually inconceivable that all of these $^{18}O$-depletions could have been caused by a single hydrothermal system. More likely alternatives are: (1) that the intracaldera tuff and the outflow tuff interacted in a

somewhat similar fashion with separate batches of meteoric waters; or (2) that the $^{18}O$-lowering occurred immediately prior to (or during) eruption, a possibility that we do not favor (see the discussion below).

The isotopic composition of the granodiorite porphyry intrusion further complicates the puzzling cross-cutting relationships. Like the outflow tuff, the granodiorite porphyry has a low-$^{18}O$ groundmass even though its phenocrysts have "normal" igneous $\delta$-values. Two pairs of samples of adjacent tuff and granodiorite, collected several meters apart across the intrusive contact (CG-C-53A,B; CG-C-58A,B), consistently indicate that the tuff is 3 to 4 per mil heavier than the nearby granodiorite. However, the quartz is isotopically identical in both the tuff and the granodiorite ($\delta^{18}O_{quartz}$ = +8.5 and +8.6), strongly suggesting that both kinds of rock initially formed from similar magmas. Three plausible explanations of this cross-cutting relationship are: (1) meteoric water interacted briefly with the granodiorite before it came into contact with the resurgent block of tuff; (2) meteoric water interacted more extensively with the granodiorite than with the tuff, either because the intrusion was hotter or more permeable, or because its groundmass was more prone to oxygen exchange (perhaps because it was still glassy, while the tuff had already been devitrified and hornfelsed by the intrusion); or (3) both samples originally suffered $^{18}O$ depletion, but a late, lower-temperature alteration event increased the $\delta^{18}O$ value of the fine-grained tuff much more than the more coarsely crystalline granodiorite.

The post-caldera andesite flows do not show any signs of interaction with meteoric water. In fact, there is an abrupt change in whole-rock $\delta^{18}O$ across the unconformity at the top of the intracaldera tuff in Section 1 (below the andesites). Because this horizon also contains glacial outwash gravels, and thus represents a significant time interval, it seems certain that whatever the process of water-

rock/glass interaction that caused the change in $\delta^{18}O$ of the tuff, it must have ceased on the surface by the time the andesites were erupted.

### 4.5.7 Possible $^{18}O$-Depletion Scenarios

The most pressing questions which remain regarding the process (or processes) of $^{18}O$ depletion that operated at Chegem are: Did this process occur before, during, or after eruption? At what temperature or temperatures did it occur? Was it a single-stage or multi-stage process? What length of time was involved? Below, we discuss and evaluate several possible $^{18}O$-depletion scenarios.

*Assimilation and/or Melting of Low-$^{18}O$ Rocks* - This process has been suggested to explain low-$^{18}O$ magmas in the Yellowstone volcanic field (Taylor, 1987), Crater Lake (Bacon et al., 1989) and the Calabozos caldera complex (Grunder, 1987). In these cases, it is proposed that either (1) a rather substantial amount of hydrothermally-altered rock foundered into the upper part of the magma chamber and exchanged with this magma or became assimilated by the magma prior to eruption; or (2) hydrothermally altered rocks were partially melted in the roof zone overlying the magma chamber. There are several problems with calling upon either of these processes to explain the $^{18}O$-depletions at Chegem: (1) The most striking $^{18}O$-depletions exist in tuff erupted right *in the middle* of the chain of eruptions which produced this complex cooling unit, so the low-$^{18}O$ effects cannot be the result of assimilation in the upper part of the magma chamber, where it is most likely. (2) In contrast to the above-described caldera complexes, there are no hydrothermally-altered country rocks in the vicinity of the Chegem caldera. There are also no pre-caldera volcanic rocks that could have been hydrothermally altered at depth. (3) There is no

compositional or mineralogical evidence for large amounts of assimilation. (4) Extremely short timescales (<<6 months) would be necessary to preserve the observed oxygen isotope disequilibrium between feldspar and coexisting silicate melt at magmatic temperatures. It is likely that at these very short timescales, such massive assimilation could not have occurred without some petrological or mineralogical evidence of assimilation being preserved.

***Direct Water-Magma Interaction*** - Direct interaction between meteoric water and magma has been proposed to explain low-$^{18}O$ magmas in southern Nevada (Lipman and Friedman,1975), Yellowstone (Hildreth et al., 1984), and southern Africa (Harris and Erlank, 1992). A criticism of this mechanism has always been that, except for possible buoyant uprise of large quantities of bubbles in a $H_2O$-saturated melt, magmas have a very low or nonexistent permeability and are under lithostatic pressures, whereas the meteoric waters in the country rocks are under much lower (hydrostatic) pressures, and are separated from the magma chamber by a zone of hot, plastic (unfractured) rock. Therefore, the direct influx of $H_2O$ into the magma will be in large part controlled by the very slow diffusion of $H_2O$ through a ductile rock or a silicate melt, and it would thus take considerable time to transport the required volumes of water into (and out of) the magma (Taylor, 1987). At Chegem, this problem is compounded by the fact that the feldspars have hardly exchanged at all with the meteoric waters. At magmatic temperatures, $^{18}O$ exchange between meteoric water and feldspars is known to be relatively rapid, occurring in days (e.g., Gregory et al., 1989).

***Water-Glass Interaction Deep in Vent System During or Just Prior to Eruption*** - At Chegem, we know that low-$^{18}O$ volcanic rocks, low-$^{18}O$ intrusive rocks, and low-$^{18}O$ glasses all exist. However, there is no proof that any of these were

actually derived from low-$^{18}O$ magmas. Nevertheless, the mere existence of the low-$^{18}O$ glasses implies that these particular materials must have been depleted in $^{18}O$ when they were either true silicate melts or super-cooled silicate melts (e.g., glasses), and, as discussed above, this must have occurred at fairly high temperatures (>250°C-350°C). One possible way that glass and water might interact at elevated temperatures is for meteoric water to infiltrate deep into the vent system of a caldera as it erupts. The extreme pressure differentials and the higher permeability provided by the interconnected fractures that develop during the cracking of the rapidly quenched glass might make large-scale fluid infiltration more plausible in this environment. For example, Sheridan et al. (1981) propose a somewhat analogous mechanism during the late stages of the AD 79 eruption of Vesuvius (Italy).

In addition, there is a possible correlation between the caldera-wide low-$^{18}O$ stratigraphic zone and the second-order fluctuations in major- and trace-element compositions, and as we suggested earlier (Gazis et al., 1992), these compositional variations may be related to eruption dynamics. Perhaps fluctuating eruption rates or eruptions from different vents disrupted the progressive downward tapping of a compositionally-zoned magma chamber. This conceivably could permit the entrainment of hot meteoric fluids into the fragmented magma or highly fractured glass deep within the vent conduit system.

The problem with this mechanism is that very large integrated fluxes of water are required by the oxygen isotope systematics, and these must be supplied over a very short period of time. That is, in days to months (?), a large volume of water similar to the volume of the $^{18}O$-depleted zone itself would need to penetrate deep into the vent system, and some efficient physical mixing process would then be needed to produce intimate exchange of oxygen between

these large volumes of materials. Furthermore, the possible tectonic offsets in Sections 1 and 2 of the trace-element trends and the oxygen isotopic trends (discussed above) are in opposite directions, which argues against the earlier suggestion of Gazis et al. (1992) that both kinds of trends were formed at the same time.

***A Short-lived, High-temperature Hydrothermal System with Good Recharge in the Upper 750 m of Caldera Fill;*** - If the caldera-wide low-$^{18}O$ zone at Chegem was formed by a flow system that developed after the tuffs were deposited, then the W/R profiles of Fig. 4.13 clearly imply that this was a very heterogeneous flow system containing horizons of variable permeability and fluid flow. In this scenario, the horizon of greatest fluid flux would be at the level of sample CG-C2-4H, which was in fact observed to be more poorly welded than the surrounding tuff. Furthermore, the $\delta^{18}O$ profile is most easily explained if the flow direction is nearly horizontal. However, it is unlikely that the flow system was perfectly horizontal, because under such conditions it is difficult to initiate convection, particularly if the isotherms are also sub-horizontal. Even a slight tilt ($\approx 5°$), either of the boundaries of the flow systems or of the isotherms, is sufficient to drive circulation (Criss and Hofmeister, 1991).

One drawback of explaining the $^{18}O$ depletions with a hydrothermal system is that one might *a priori* expect to see some indications of mineralogical alteration, especially in feldspar and biotite. Consequently, a practically unique combination of high temperatures, a very short time interval, and very high fluxes of water are required, and all of these features must occur in concert. The flow system must largely shut down before the temperatures drop into the range where hydrous alteration minerals are stable (i.e., < 400°C). Also, it is unclear why this hydrothermal system would be so short-lived and not have continued

on to produce a full range of mineralogical and isotopic alteration as is observed at many other calderas (e.g. Lake City, Valles, Long Valley). Perhaps the difference is that the Chegem hydrothermal event is related to cooling of tuffs, whereas the others are related to additional heating during emplacement of resurgent or ring intrusions.

This scenario, the existence of a short-lived hydrothermal system at Chegem immediately after eruption, depicted in Fig. 4.16, is our preferred mechanism for producing the isotopic changes in the Chegem Tuff. We propose an intense fumarolic event similar to that at the Valley of Ten Thousand Smokes (discussed below) to explain the observed oxygen isotope trends. The observations described in this paper can all be fitted into a geologic history encompassing the following sequence of events:

(1) Caldera-forming eruption and deposition of tuff (Fig. 4.16a), accompanied by slight tilting either of intracaldera stratigraphy or of isotherms (by cooling). The tuff of Section 2 may have been faulted downward ≈500 m relative to Section 1 during a late-stage intracaldera collapse.

(2) Immediately after deposition, there was vigorous hydrothermal interaction between large amounts of meteoric water and rock in the upper 750m of caldera fill while the tuff was still very hot in the center (> 500° to 600°C) but had cooled significantly in the upper 50m (Fig. 4.16b). Water circulated in convection cells, flowing into the hot ash through fractures and fissures, being heated and then being ejected upward as hot steam through fumaroles. Flow was especially intense along a zone of higher permeability about 350m below the surface. The outflow tuff probably interacted with water in a similar fashion at the same time, though with much smaller amounts and perhaps at lower temperatures (however, note that the outflow tuff is also welded and was probably very hot). This water-rock interaction was accompanied by hydration

and profound $^{18}O/^{16}O$ alteration of glasses and devitrification of the core of the caldera fill. The hydrothermal event continued for ≈10 to 25 years and abruptly ended when the upper section of tuff had been cooled enough and the tuff had devitrified (thus lowering the permeability) so that hydrothermal circulation was no longer possible.

(3) Glacial erosion occurred some time after the deposition of the tuff. The timing of this glaciation relative to the hydrothermal event and the intrusion of the granodiorite is poorly constrained. This glacier may even have melted in the hot caldera environment and fed the hydrothermal system.

(4) Resurgence of granodiorite porphyry (Fig. 4.16c), possibly accompanied by uplift of Section 2 relative to Section 1 (≈200m). The intrusion also pushed up and tilted the main resurgent block of isotopically-altered tuff. The vigorous high-temperature hydrothermal activity had largely ceased at this point but some meteoric water was still present at depth and interacted with the groundmass of the intrusion as it cooled and devitrified.

(5) Eruption of andesite flows after hydrothermal activity had ceased at the surface. The eruption of andesites could actually be synchronous with the intrusion of the granodiorite if fluid flow had ceased at the surface before it had stopped at depth.

The source of the meteoric waters and geometry of the flow system is poorly constrained by this study. Much more work will need to be done to sort out these details. Sr isotope studies (Chapter 6) indicate that the waters were fairly rich in radiogenic strontium which could only have come from the crystalline basement to the south of the caldera. However, this crystalline basement was probably also present within the intracaldera tuff sequence as megabreccias and lithic fragments, particularly along the margins of the caldera.

One possible source for the meteoric water is a lake or glacier on top or on the side of the caldera fill.

The $^{18}O/^{16}O$ systematics at Chegem, combined with laboratory data on the hydrothermal exchange rates of feldspars and silicate glass, imply a timescale for $^{18}O$ depletion of approximately 10 to 25 years, assuming that the isotopic alteration of zone B of the caldera fill occurred while the core of the mass of welded tuff was at temperatures of 500° to 600°C.

Given the large amounts of water that have to be heated to produce these $^{18}O/^{16}O$ effects, such temperatures probably could not be sustained for more than 10-25 years, because of the constraints of heat balance. The following simple heat balance calculation illustrates this point: The W/R ratio for the hydrothermally altered zone of tuff probably falls between 0.3 and 0.6 (see earlier discussion), which converts to 0.17 to 0.34 in weight units (g-$H_2O$/g-rock). The average heat capacity of water over the temperature range from 25° to 500°C is 0.75 cal/g-deg (Haar et al., 1984). Thus, the heat needed to raise the temperature of water from 25° to 500°C is 359 cal/g-$H_2O$. In addition, the water will be vaporized. The enthalpy of vaporization of water at 1 atm and the critical temperature (374°C) is 27 cal/g-$H_2O$ (Marsh, 1987), so the total heat needed to bring the water to 500°C and vaporize it is ≈386 cal/g-$H_2O$. Using the W/R ratio to convert this to rock weight, we find that the heat needed is about 65 to 131cal/g-rock. Rhyolite tuff has a heat capacity of about 0.22 cal/g (Riehle, 1973). If such a rock is cooled from 800° to 500°C, it will produce 66 cal/g of heat. Although this is not sufficient to heat and vaporize the water, an additional 30-70 cal/g of latent heat is given off as the glass crystallizes. Thus the total heat budget of the rock is 96 to 136 cal/g, very similar to the heat budget of the water. This simple calculation indicates that hot, devitrifying Chegem Tuff had just enough heat to sustain the high-temperatures and water-rock ratios in the

scenario we propose, but that after the welded tuff had devitrified (crystallized), it could no longer sustain these high temperatures.

Since we know the timescales of this hydrothermal event and the W/R ratios, we can calculate fluxes of water through the system if we assume some geometry of fluid flow. The flux of water or of an aqueous fluid (in moles per unit cross-sectional area per unit time) through an elemental volume of rock (a cube with each side length d in cm) is given by (e.g., Taylor, 1994):

$$F_{H_2O} = \frac{(\lambda / d)(m)(W / R)}{(d^2)(t)}$$

where W/R is the material-balance open-system water rock ratio, t is the duration of fluid flow in sec, $\lambda/d$ is the total flow length ($\lambda$) divided by the size of each elemental volume, and m is a factor which converts the W/R ratio to moles of $H_2O$ per unit elemental volume. If we arbitrarily choose an elemental volume of 1 $cm^3$ (d = 1cm), then m is approximately 0.076 moles. The W/R ratio for the system probably falls between 0.3 and 0.6 (see earlier discussion), and so for a length scale of 750 m (i.e., the side of an equant convection cell, defined by the thickness of the hydrothermal zone) and a timescale of 10 to 25 years we have fluxes of $2.2 \times 10^{-6}$ to $1.1 \times 10^{-5}$ $mol/cm^2$-sec.

A final question is whether this high flux of aqueous fluid is feasible. That is, can these fluxes be attained with geologically reasonable permeabilities. We can make an order of magnitude estimate of the permeability needed by using a simple version of Darcy's Law (Dullien, 1979):

$$v = \frac{-k}{\eta} \nabla P^*$$

where v is the Darcy velocity of the fluid ($cm^3/cm^2$-sec), k is the permeability in $cm^2$, $\eta$ is the fluid viscosity (poise), and P* is the piezometric pressure (dynes/$cm^2$). Thus, since the Darcy velocity is related to the flux we calculated by:

$$v = F_{H_2O} * \left( \frac{M}{\rho} \right)$$

where M is the molar weight of the aqueous fluid and ρ is its density, we can cast the permeability k in terms of these variables:

$$k = -F_{H_2O} * \left( \frac{M}{\rho} \right) * \left( \frac{\eta}{\nabla P^*} \right)$$

We must make estimates of the water density and viscosity, and the piezometric pressure gradient. At 500°C and a pressure sufficient to maintain compressed water (≈100 bars), the density of water is 0.8 g/cm$^3$ and the viscosity of water is about 1x10$^{-3}$ poise. Because this is a near-surface environment, we will assume that the water is at hydrostatic pressure in hydrothermal cells ≈750 m in diameter and that when the water rises as steam, it exerts no pressure. This is equivalent to a pressure gradient of 980 dynes/cm$^3$. These values predict permeabilities of 5.0x10$^{-11}$ to 2.5x10$^{-10}$ cm$^2$ or 5 to 25 millidarcies. Though these values are fairly high, measurements of permeabilities in ash-flow tuff from Yucca Mountain, Nevada (Nelson and Anderson, 1992) have revealed comparable values. In fact, glassy sections are commonly several orders of magnitude more permeable than devitrified tuff, with values as high as 100 millidarcies (Nelson and Anderson, 1992). Devitrification or mineralogical alteration tends to reduce the permeability of such a rock. Also, the permeabilities at Yucca Mountain were measured on borehole samples and do not reflect the bulk permeability of the rock. Any fracture permeability will increase these values, and so our estimated permeabilities for the Chegem Tuff would seem to be entirely reasonable, and well capable of allowing circulation of the required amounts of $H_2O$.

### 4.5.8 The Valley of Ten Thousand Smokes - An Historical Analogue?

In searching to understand the process which caused the extreme $^{18}O$ depletion and disequilibrium at Chegem, and in trying to develop a realistic

model of this system, we have also sought a modern analogue. We suggest that the fumarolic activity at the Valley of Ten Thousand Smokes in Alaska (Plate 3) may be just such an analogue, though at a different scale, and in a somewhat different geologic setting (namely in a much smaller eruption and in the thinner outflow-facies of a welded ash-flow sheet rather than in the thick caldera-fill facies as at Chegem).

The Valley of Ten Thousand Smokes is located at the foot of Mt. Katmai on the Alaska Peninsula. During the 1912 eruption of Novarupta caldera, ≈20 $km^3$ of air-fall tephra and 11-15 $km^3$ of ash-flow tuff were ejected, much of which filled the nearby valley with a ≈200 m thick sheet (Hildreth, 1983). This was one of the most voluminous historic eruptions, and was unique in that the pyroclastic flows came to rest on land and were subsequently welded.

The valley was discovered in 1916 by Robert F. Griggs, the head of a National Geographic Society expedition, and so named because of the many fissures and fumaroles that were vigorously emitting steam (Plate 3). In a subsequent expedition in 1917, Shipley (1920) collected gases and attempted to measure fumarole temperatures, but as he only had a mercury thermometer, he could not measure temperatures above 357°C (the boiling point of mercury). In 1919, seven years after the tuffs were deposited, Allen and Zies (1923) succeeded in measuring fumarole temperatures as high as 645°C using Hoskins thermocouples. Several other fumaroles with temperatures over 500°C were measured and several others were found which would melt lead or zinc. Allen and Zeis (1923) also determined that the gases were made up almost entirely of steam. Details of their studies of the fumarolic gases and their deposits are given in Allen and Zies (1923) and Zies (1924a,b; 1929). Griggs (1922) and Fenner (1920) also published descriptions of those early expeditions.

The hydrothermal activity at the Valley of Ten Thousand Smokes was very vigorous, but short-lived. Allen and Zies (1923) noted that in 1919 the streams draining the valley, some of which are fed by glacial meltwaters, had considerably greater volume in their upper parts than in their lower parts. They concluded that the porous pumiceous deposits had absorbed large amounts of the water from the streams. Within 15 years, the vigorous activity had ceased and the fumaroles became hot springs and mud pots before dying out (Zies, 1924b). At present, the fumaroles are cold and fumarolic alteration has ceased altogether, except in the vent region and one locality outside the vent region (Keith, 1991).

By comparison, the eruption of the Chegem caldera produced pyroclastic deposits an order of magnitude greater in volume than those at the Valley of Ten Thousand Smokes. Furthermore, the intracaldera fill is at least two kilometers thick, as opposed to the 200m thickness at the Valley of Ten Thousand Smokes. Thus, one would expect that a similar hydrothermal event at Chegem would be much more vigorous and involve larger volumes of water. This is certainly consistent with our observations, and a larger-scale Katmai would appear to fit our Chegem model beautifully. This correlation between the actual events at Katmai and our hypothetical model of the Chegem system is made even more compelling because we formulated the basic parameters of our Chegem model (i.e., temperatures of 500-600°C, a timescale of 10-25 years, and exchange with large volumes of $H_2O$) long before we realized that these same parameters are in fact part of the historical record at the Valley of Ten Thousand Smokes.

It would also be interesting to compare the discharge rates at the Valley of Ten Thousand Smokes with the calculated fluxes of water in the Chegem system. Unfortunately, no careful measurements were made of discharge rates. However, Zies (1929) did make an estimate that the total volume of steam

"exhaled" by the fumaroles was $26 \times 10^6$ liters/sec (calculated at 100°C and 1 atm). If the density of the steam is 0.00059 g/cm$^3$ and the total area through which it flows is the area of the valley (≈120 km$^2$), then this estimated discharge rate converts to a flux of $\approx 7 \times 10^{-7}$ mol/cm$^2$-sec, within an order of magnitude of our lowest calculated value. First-hand descriptions of fumaroles at the Valley of Ten Thousand Smokes also suggest that the flux of water through these permeable tuffs was in fact comparable to the calculated flux at Chegem. For example, Griggs (1918) wrote:

> Now [the valley] is traversed by hundreds of fissures extending along its margin or criss-crossing its floor. These fissures are the seat of several millions of volcanic vents of all sizes, from great volcanoes pouring forth columns of vapour more than a mile high, down to minute jets of gas which pass unnoticed amongst their greater neighbours. . . For here, continually rising quietly from the ground without explosive action of any sort, is more vapour than is given off by all the rest of the world's volcanoes put together (except during a period of dangerous eruption).

One possible shortcoming of this analogy is that the fumarolic activity at the Valley of Ten Thousand Smokes is known to have been accompanied by extensive mineralogical alteration and deposition of fumarolic minerals (e.g., Zies, 1929; Papike et al., 1991; Keith, 1991; Spilde et al., 1993). No evidence has been found for fossil fumaroles or their deposits in the Chegem intracaldera fill. However, this evidence would only be expected in the near-surface portion of the caldera fill, which has been eroded more extensively than the lower part. Also, the major fumaroles at Katmai were spaced roughly 500-1000 m apart (Zies, 1929; Fig. 4.17) and their deeper conduits might not be observed at Chegem. Moreover, fumarolic encrustations are often metastable or unstable under cooling fumarolic conditions, are soluble in water or acids formed at the surface, and/or are easily eroded (Keith et al., 1992); thus they are not likely to be preserved in a 2.8 million year old caldera system.

## 4.6 Conclusions

1. The excellent 3-dimensional exposure of the Chegem caldera has allowed us to collect 38 samples from a 1405-m section of intracaldera tuff, all part of a single cooling unit. Whole-rock oxygen isotope analyses of these samples define a striking oxygen isotope profile with "normal" igneous $\delta^{18}O$ values (+7 to +8.5) in the lower 600m, much lower $\delta^{18}O$ values (–7 to +4.3) in a 700m zone above that and a shift to high $\delta^{18}O$ values (+4.4 to +12.1) at the top of the caldera-fill exposure. Analyses of samples from two other partial stratigraphic sections indicate that these oxygen isotope trends are stratigraphically controlled and caldera-wide. The low-$^{18}O$ rocks must have been isotopically altered by interacting with meteoric waters at relatively high temperatures (>300°C), whereas the high $\delta^{18}O$ values were probably caused by low-temperature hydration (<100°C) after the top of the caldera fill sequence had cooled.

2. Mineralogically, the Chegem Tuff does not show any signs of hydrothermal alteration. Feldspars are unaltered and free of sericite; biotites are either unaltered, or have reacted to form magnetite + feldspar, without any signs of chloritization. Thus, there is no evidence for a long-lived post-caldera hydrothermal system here, as is observed in a number of other ash-flow calderas (e.g. Long Valley, Valles, Lake City).

3. There is a pronounced oxygen isotopic disequilibrium between phenocrysts and groundmass in all of the isotopically altered rocks. Almost all feldspar and quartz phenocrysts analyzed have igneous $\delta^{18}O$ values of around +7 and +8.5, respectively. A few feldspars have slightly lower $\delta^{18}O$ values (down to +5.5). In contrast, groundmass and glass $\delta^{18}O$ values range from –7.7 to +12.3. Consequently, feldspar-groundmass/glass pairs form a steep array on a $\delta_{feldspar}$-

$\delta_{groundmass/glass}$ plot. This is the first time that this sort of high-temperature phenocryst-groundmass (glass) disequilibrium has been documented. This disequilibrium indicates that the process which lowered the $\delta^{18}O$ values of these rocks occurred over a very short timescale, probably tens of years.

4. Although the effects are smaller, $^{18}O/^{16}O$ disequilibrium between groundmass and phenocrysts is also observed in samples collected from outflow tuff remnants up to 40 kilometers away from the caldera and in samples from the granodiorite porphyry which intrudes the intracaldera tuff sequence on the northeast side of the caldera. The post-caldera andesite flows which overlie the intracaldera tuff sequence have normal igneous whole-rock $\delta^{18}O$ values.

5. Major- and trace-element compositions of samples from the 1405-m section display trends of upwardly increasing $Na_2O$, CaO, $Al_2O_3$, total $Fe_2O_3$, MgO, $TiO_2$, Sr, and Zr and decreasing $SiO_2$, $K_2O$, and Rb. This mafic-upward compositional zoning is common in ash-flow tuff sequences and is usually thought to represent an inverted view of the upper part of the magma chamber from which the tuff erupted (e.g., Smith, 1979). Superimposed on this general compositional trend, there are several local fluctuations in the trend which may be due to changes in eruption dynamics.

6. In the upper dacitic tuff horizons, hydrated glassy pumices are preserved which have low $\delta^{18}O$ values (down to +1.4). The glasses must have been hydrated at temperatures above ambient temperatures but over a short enough timescale that they were not devitrified.

7. The most plausible scenario which explains the above observations is a short-lived, vigorous hydrothermal event similar to that which occurred from 1912 to 1925 at the Valley of Ten Thousand Smokes in Alaska. We propose that immediately after the caldera-forming eruption and deposition of the ash-flow tuff, a hydrothermal system was activated in the upper 750 m of intracaldera tuff. At this time, there was a temperature gradient in the caldera fill with low temperatures (<100°C) at the top of the cooling mass and much higher temperatures (500-600°C) a few hundred meters below that. In a short time interval (≈10 years), large amounts of meteoric water circulated through the upper 750 meters of caldera fill, passing in and out through fissures, joints, and fumaroles. The upper caldera fill had a high permeability because it was glassy, particularly at one horizon, where the tuff cooled slightly prior to compaction. The glassy groundmass of these deposits equilibrated $^{18}O/^{16}O$ with the water, but the feldspar phenocrysts did not. This vigorous hydrothermal activity persisted for only around 10 to 25 years, a short enough time interval that feldspar oxygen isotopic compositions were not shifted, nor were the feldspars mineralogically altered.

**Table 4.1: Oxygen Isotope Results**

| sample# | Rock type and location | | $\delta^{18}O$ wr** | qtz | feld† | other†† |
|---|---|---|---|---|---|---|
| | *Stratigraphic sections* | | | | | |
| | *Section 1 - SE side of caldera, altitude* | | | | | |
| CG-C2-4S | vitrophyre, contact w/metamorphic rocks | 2080m | 8.4 | | | |
| CG-C2-4T | vitrophyre | 2080m? | 8.6 | | | |
| CG-C2-4Q,R | vitrophyre | 2120m | 8.7 | | | 8.6(P) |
| CG-C-44A | welded rhyolitic tuff | 2180m | 7.6 | 8.5 | | |
| CG-C2-4P | white altered tuff | 2220m | 6.7,6.9 | | | |
| CG-C-44B | welded tuff | 2340m | 8.0 | | | |
| CG-C-44C | " | 2380m | 7.9 | | | |
| CG-C-44D | " | 2400m | 7.9 | | | |
| CG-C2-4O | fresh grey tuff | 2450m | 7.9 | | | |
| CG-C-44E | welded tuff | 2490m | 8.3 | 8.5 | 7.6 | 8.4(GM) |
| CG-C2-4N | partly altered tuff | 2550m | 7.8 | | | |
| CG-C2-4M | fresh red-brown tuff | 2630m | 8.0 | | | |
| CG-C-44F | " | 2680m | 7.8 | | | |
| CG-C2-4E | welded tuff | 2710m | 7.0 | | | |
| CG-C2-4D | welded tuff | 2750m | 4.0 | | | |
| CG-C2-4C | welded tuff w/pumices | 2780m | 6.1 | | | |
| CG-C2-4B | welded tuff | 2870m | 2.9 | 8.3 | 7.5 | -0.5(GM) |
| CG-C2-4A | welded tuff | 2915m | 2.2 | | | |
| CG-C2-4L | grey partly-altered tuff | 2965m | 3.0 | | | |
| CG-C2-4K | fresh grey tuff | 3050m | -1.9 | 7.9,8.1 | 5.2 | -0.4(GM) |
| CG-C2-4K2 | " | 3050m | -1.0 | | | |
| CG-C2-4J | fresh grey tuff | 3100m | 2.5 | | | |
| CG-C2-4I | fresh grey tuff | 3145m | -2.1 | | | |
| CG-C2-4H | white poorly welded tuff | 3160m | -3.9 | 7.7 | 5.9 | -7.7,-7.0(GM) |
| | | | -4.1 | 8.4 | | -4.8,-7.6(P) 6.5(LF) |
| CG-C2-4G | fresh grey tuff, bio-rich | 3165m | -0.3 | | | |
| CG-C2-4F | fresh grey tuff, bio-rich | 3225m | -0.5 | | | |
| CG-C-44G | " | 3280m | 2.7,3.0 | 7.9 | | |
| CG-C-44H | " | 3390m | 4.3 | | | |
| CG-C-44I | partial vitro. | 3400m | 7.7,8.2 | 8.2 | 8.1 | 4.5(G) |
| CG-C-44J | partial vitro. | 3410m | 4.4,4.6 | 8.5 | 7.2 | 1.4,2.5(G) 5.6(P) |
| CG-C-44K | welded tuff | 3420m | 6.5,6.5 | 8.4 | | |
| CG-C-44L | partial vitro. | 3430m | 9.5 | | | 9.3(P),7.8(G) 9.8(GM) |
| CG-C-44M | welded tuff | 3450m | 12.1 | | | 8.7(GM) |
| CG-C-44N | welded tuff | 3465m | 9.4 | 8.5 | 7.6 | 12.3(GM) 5.6 (B) |
| CG-C-44O | poorweld tuff | 3485m | 10.3 10.9 | | | |
| CG-C-44P | andesite flow | 3490m | 7.9 | | | |
| CG-C-44Q | andesite flow | 3775m | 7.5 | | 7.5 | |

*(Table 1 p.2)*

| sample# | Rock type and location | | $\delta^{18}O$ wr** | qtz | feld† | other†† |
|---|---|---|---|---|---|---|
| | *Partial stratigraphic sections* | | | | | |
| | *Section 2 - E side of caldera, altitude* | | | | | |
| KH91-2B | bio-rich tuff, local summit | 3124m | 3.0 | | | |
| KH91-3 | tuff, NW of KH91-2 | ≈3120m | 1.4 | | | |
| KH91-4 | darker tuff | 3080m | 2.5 | | | |
| KH91-9 | tuff, close to fault | 3030m | 1.7 | | | |
| CG-C2-35 | slightly altered tuff | 2900m | 7.8 | | | |
| CG-C2-34 | tuff | 2780m | 8.4 | | | |
| CG-C2-38 | tuff, saddle E of fault | 2500m | 6.8 | | | |
| CG-C2-39 | altered tuff | 2430m | 7.9 | | | |
| CG-C2-40 | tuff | 2200m | 8.0 | | | |
| CG-C2-28 | tuff, base of columnar outcrop | 1940m | 8.1 | | | |
| CG-C2-29 | tuff, 90m from contact | 1870m | 8.2 | | | |
| CG-C2-30A | tuff, 50m from contact | 1845m | 7.8 | | | |
| CG-C2-31A | vitrophyre, contact w/limestone | 1775m | 8.9 | 8.6 | | 7.5(G) |
| | *Partial stratigraphic section in dacitic tuff* | | | | | |
| | *Section 3 - SW of Kum Tyube, altitude* | | | | | |
| CG-C2-67F | poorly welded tuff | 3530m | 10.8 | | | |
| CG-C2-67E | partial vitro. | 3500m | 8.1,8.6 | 8.6 | 8.2 | 7.3(G) |
| CG-C2-67D | partial vitro. | 3495m | 5.9 | | 7.2 | 4.8(G) |
| CG-C2-67H | partial vitro. | 3425m | 5.7 | | | |
| CG-C2-67G | partial vitro. | 3415m | 8.6 | 8.5 | 7.7 | 6.8(G) |
| CG-C2-67C | welded tuff | 3390m | 4.6 | | | |
| CG-C2-67B | welded tuff | 3340m | 6.5 | | | |
| CG-C2-67A | welded tuff | 3300m | 6.6 | | | |
| | *Vitrophyres and glasses* | | | | | |
| CG-C-20 | vitrophyre, Bashil dam (south) | | 9.7 | 8.5 | | |
| CG-C2-1 | vitrophyre,same as C-20 | | | | | 9.1(G) |
| KH91-01BP | glassy pumice, same as C-20 | | 8.8 | | | |
| 90L-109 | vitrophyre, road near Bulungu | | 8.8,8.8 | 8.6,8.7 | | 8.5(G) |
| CG-C-34B | glassy pumice, dacitic, SW side of caldera | | 8.5 | | | |
| KH91-11P1 | glassy pumice, dacitic, SW side of caldera | | 8.1 | | | 6.1(B) |
| CG-C2-51 | vitrophyre,base of Kektash | | 10.1 | | | |
| CG-C2-4Q,R | vitrophyre,base of SE section | | 8.7 | | | 8.6(P) |
| CG-C2-4S | " | | 8.4 | | | |
| CG-C2-4T | vitrophyre " | | 8.6 | | | |
| CG-C2-31A | vitrophyre ,base of Section 2 | | 8.9 | 8.6 | | 7.5(G) |
| CG-C-42B | vitrophyre,Sary-su dike | | 9.2 | | | |
| CG-C-50 | vitrophyre,bottom(?) of outflow | | 6.9,6.7 | 8.7 | | 7.5(G) |

*(Table 1 p. 3)*

| sample# | Rock type and location | $\delta^{18}O$ wr** | qtz | feld† | other†† |
|---|---|---|---|---|---|
| *Welded tuff samples* | | | | | |
| CG-C-34A | welded tuff, top on west side | 8.0,7.9 | 8.5 | 7.1 | |
| CG-C-51 | welded tuff, deep interior | 5.8,6.0, 6.0 | 8.3,8.5, 8.7 | 8.1 | |
| CG-C2-24B | partial vitrophyre, E of Kyugenkaya, ≈3300m | 6.6 | | | |
| CG-C2-70C | partial vitrophyre, SW of Kum Tyube 3445m | 7.0 | | 8.5 | 6.0(G) |
| CG-C2-70B | partial vitrophyre, 3415m | 7.2 | | | |
| CG-C2-70A | welded tuff, 3370m | 6.5 | | | |
| 90L-114 | tuff w/pum., float, Dzhilgusu | 7.0 | | | 6.0(P) |
| CG-C2-74 | welded tuff, Hobetayeen block | 4.4 | | | |
| CG-C2-75 | welded tuff, Hobetayeen block | 7.1 | | | |
| KH91-10B | welded tuff, saddle S. of Likarlgi | 5.5 | | | |
| KH91-6 | fault breccia, saddle near Likarlgi | 4.9 | | | |
| KH91-5 | welded tuff, between faults | 2.8 | | | |
| CG-C2-37B | brecciated tuff near granite | 2.5 | | | |
| CG-C2-5 | welded tuff, Cheg.-Jung. 2000m | 7.2 | | | |
| CG-C2-52 | welded tuff, base of Kektosh | 8.6 | | | |
| *Welded tuff samples from block near intrusion* | | | | | |
| CG-C-53B | welded tuff, next to intrusion | 6.8 | | | |
| CG-C-58B | welded tuff, next to intrusion | 7.3,7.6, 7.7 | 8.5 | | |
| CG-C2-14 | welded tuff, 3110m | 5.9 | | | |
| CG-C2-13 | welded tuff, south of Likarilgi | 7.0 | | | |
| KH91-8 | welded tuff, contact w/granite | 4.4 | | | |
| CG-C2-15 | welded tuff, 3330m | 2.0 | | | |
| KH91-10C | welded tuff, 3030m | 5.5 | | | |
| CG-C2-12 | welded tuff, 3400m | 7.5 | | | |
| *section from* | *Likarilgi westward to saddle (fault) near Mt. Kygenkaya* | | | | |
| CG-C2-10 | welded tuff, Likarilgi, 3430m | 7.9 | | | |
| CG-C-54 | welded tuff | 6.5 | | | |
| CG-C-55 | welded tuff | 5.2 | | | |
| CG-C2-18 | welded tuff | 4.2 | | | |
| CG-C2-17A | welded tuff, 3360m | -0.3 | | | |
| CG-C2-17B | black tuff, same as C2-17A | -4.6,-4.5 | | 5.5 | -7.2,-6.9(GM) |
| CG-C2-16 | welded tuff, 3345m | 2.6 | | | |
| CG-C2-27 | welded tuff | 1.6 | | | |
| CG-C2-26 | welded tuff, 3365m | 1.9,1.5 | | | |
| CG-C2-25 | welded tuff, 3310m | 2.4 | | | |
| CG-C2-24C | welded tuff, 3200m, saddle | 1.4 | | | |
| CG-C2-24A | welded tuff, 3205m, saddle | 1.8 | | | |

*(Table 1 p.4)*

| sample# | Rock type and location | $\delta^{18}O$ wr** | qtz | feld† | other†† |
|---|---|---|---|---|---|
| *Outflow Tuff* | | | | | |
| CG-C-47A | tuff, Lechnikaya, top of exposure | 5.7 | 8.4 | 7.2 | 5.8,5.6(P) |
| CG-C-47B | tuff, 100 m below 47A | 8.2 | | | |
| CG-C-50 | vitrophyre, base of Teraklan | 6.9,6.7 | 8.7 | | 7.5(G) |
| 90L-117A | tuff, lowest-Lechnikaya | 5.5 | 8.4 | | 4.6(GM) |
| 90L-117B | tuff, Lech., 3m above A | 4.4 | 8.1 | | 3.8(GM) |
| 90L-117C | partial vit., Lech., higher up | 6.4 | 8.5 | | 6.0(GM),7.4(G) |
| 90L-127C | basalt, base(?) of outflow | 7.3 | 8.5(xeno) | | |
| 90L-119P4 | pumice, Lechnikaya | | | 6.8(S) | |
| 90L-120P7 | pumice, Lechnikaya | | | 7.8(S) | |
| 90L-119A | tuff, Lechnikaya | | | 8.1(S) | |
| CG-C-46 | tuff, Kaminka quarry | 5.3 | | | |
| *Granodiorite porphyry intrusion* | | | | | |
| CG-C-53A | granodiorite, edge of intrusion | 4.8 | | | |
| CG-C-57 | granodiorite, away from edge | 5.0 | 8.2 | 7.0 | |
| CG-C-58A | granodiorite, edge of intrusion | 3.8,3.5 | 8.6 | 6.8 | 2.7(GM) |
| CG-C2-19A | granite, border, near inclus. | 7.3 | 8.5 | 7.0 | 6.0(GM) |
| CG-C2-19C | granite, border | 6.5 | 8.3 | 7.3 | 5.9(GM) |
| CG-C2-19D | granite, 100 m from contact | 4.6 | 8.2 | 6.6 | 3.5(GM) |
| C2-19B | andesite incl., border | 5.9 | | 7.4 | |
| CG-C2-11 | granodiorite, 2960m (low) | 6.2 | | | |
| CG-C-56 | granodiorite, 3020m | 3.9 | | | |
| CG-C2-37A | granite, quenched near fault | 1.6 | | | |
| *Andesite, Diorite* | | | | | |
| KH91-16 | andesite flow, Kyugenkaya | 7.5 | | | |
| CG-C2-2 | diorite, inclusion in float | 6.6 | | | |
| CG-C-44P | andesite flow, SE section 3490m | 7.9 | | | |
| CG-C-44Q | andesite flow, SE section 3775m | 7.5 | | 7.5 | |
| CG-C2-68D | andesite, little Kum Tyube | 7.2 | | | |
| *Country Rock* | | | | | |
| CG-C-40 | granite, several km west of caldera | 8.7 | | | |
| CG-C-41 | gneiss, several km west of caldera | 8.1 | | | |
| CG-C-42D | granite, near Sary-su dike | 8.2 | | | |
| CG-C-60C | limestone, 4m from ring fault | 29.1 | | | $\delta^{13}C$=3.8 |
| CG-C-60B | limestone, 18m from ring fault | 29.4 | | | $\delta^{13}C$=3.9 |
| CG-C-60A | limestone, 30m from ring fault | 29.9 | | | $\delta^{13}C$=3.9 |
| CG-C-63B | limestone, far from fault | 28.5 | | | $\delta^{13}C$=3.7 |
| CG-C2-31B | limestone, caldera margin, fault | 27.8 | | | $\delta^{13}C$=2.7 |
| CG-C2-32 | limestone, 100m away from fault | 30.2 | | | $\delta^{13}C$=4.0 |
| CG-C2-33 | limestone,≈1km from fault | 27.4 | | | $\delta^{13}C$=3.9 |

*all $\delta^{18}O$ values are expressed as per mil differences from Standard Mean Ocean Water
**wr=whole rock; †S=sanidine; ††G=glass; GM=groundmass; P= pumice (whole, including phenocrysts); B=biotite; LF=lithic fragment; $\delta^{13}C$ expressed as per mil difference from PeeDee Belemnite (PDB) standard

**Table 4.2** Calculated values of various isotopic reaction rate parameters for feldspar-glass pairs

| | | | Feldspar | | | | Glass | | | | |
|---|---|---|---|---|---|---|---|---|---|---|---|
| | t | a(f) | k | D | f | kt | k | D | f | kt | slope |
| T = 300°C | | | | | | | | | | | |
| 0.3mm, 0.3yrs | 1.00E+08 | 0.03 | 4.365E-11 | 1.40E-17 | 0.004 | 0.004 | 4E-08 | 1.88E-12 | 0.98 | 4.01E+00 | 225.4 |
| 0.3mm, 30 yrs | 1.00E+09 | 0.03 | 1.38E-11 | 1.40E-17 | 0.014 | 0.014 | 1E-08 | 1.88E-12 | 1.00 | 1.38E+01 | 72.9 |
| 0.3mm, 300 yrs | 1.00E+10 | 0.03 | 4.365E-12 | 1.40E-17 | 0.043 | 0.044 | very fast | 1.88E-12 | 1.00 | very fast | 23.4 |
| 0.3mm, 3000yrs | 1.00E+11 | 0.03 | 1.38E-12 | 1.40E-17 | 0.129 | 0.138 | " | 1.88E-12 | 1.00 | " | 7.8 |
| 0.3mm, 30,000yrs | 1.00E+12 | 0.03 | 4.365E-13 | 1.40E-17 | 0.354 | 0.437 | " | 1.88E-12 | 1.00 | " | 2.8 |
| 0.1mm, 3000yrs | 1.00E+11 | 0.01 | 4.141E-12 | 1.40E-17 | 0.339 | 0.414 | " | 1.88E-12 | 1.00 | " | 2.9 |
| 0.6mm, 3000yrs | 1.00E+11 | 0.06 | 6.902E-13 | 1.40E-17 | 0.067 | 0.069 | " | 1.88E-12 | 1.00 | " | 15.0 |
| 1mm, 3000yrs | 1.00E+11 | 0.1 | 4.141E-13 | 1.40E-17 | 0.041 | 0.041 | " | 1.88E-12 | 1.00 | " | 24.7 |
| T = 600°C | | | | | | | | | | | |
| 0.3mm, 0.3 yrs | 1.00E+07 | 0.03 | 5.256E-09 | 2.03E-14 | 0.051 | 0.053 | very fast | 3.17E-09 | 1.00 | very fast | 19.5 |
| 0.3mm, 3 yrs | 1.00E+08 | 0.03 | 1.662E-09 | 2.03E-14 | 0.153 | 0.166 | " | 3.17E-09 | 1.00 | " | 6.5 |
| 0.3mm, 30yrs | 1.00E+09 | 0.03 | 5.256E-10 | 2.03E-14 | 0.409 | 0.526 | " | 3.17E-09 | 1.00 | " | 2.4 |
| 0.3mm, 300yrs | 1.00E+10 | 0.03 | 1.662E-10 | 2.03E-14 | 0.81 | 1.662 | " | 3.17E-09 | 1.00 | " | 1.2 |
| 0.1mm, 30yrs | 1.00E+09 | 0.01 | 1.577E-09 | 2.03E-14 | 0.793 | 1.577 | " | 3.17E-09 | 1.00 | " | 1.3 |
| 0.6mm, 30yrs | 1.00E+09 | 0.06 | 2.628E-10 | 2.03E-14 | 0.231 | 0.263 | " | 3.17E-09 | 1.00 | " | 4.3 |
| 1mm, 30yrs | 1.00E+09 | 0.1 | 1.577E-10 | 2.03E-14 | 0.146 | 0.158 | " | 3.17E-09 | 1.00 | " | 6.9 |
| T = 800°C | | | | | | | | | | | |
| 0.3mm, 0.03 yrs | 1.00E+06 | 0.03 | 6.315E-08 | 2.93E-13 | 0.061 | 0.063 | very fast | 4.46E-08 | 1.00 | very fast | 16.3 |
| 0.3mm, 0.3 yrs | 1.00E+07 | 0.03 | 1.997E-08 | 2.93E-13 | 0.181 | 0.200 | " | 4.46E-08 | 1.00 | " | 5.5 |
| 0.3mm, 3yrs | 1.00E+08 | 0.03 | 6.315E-09 | 2.93E-13 | 0.468 | 0.632 | " | 4.46E-08 | 1.00 | " | 2.1 |
| 0.3mm, 30yrs | 1.00E+09 | 0.03 | 1.997E-09 | 2.93E-13 | 0.864 | 1.997 | " | 4.46E-08 | 1.00 | " | 1.2 |
| 0.1mm, 3yrs | 1.00E+08 | 0.01 | 1.895E-08 | 2.93E-13 | 0.85 | 1.895 | " | 4.46E-08 | 1.00 | " | 1.2 |
| 0.6mm, 3yrs | 1.00E+08 | 0.06 | 3.158E-09 | 2.93E-13 | 0.271 | 0.316 | " | 4.46E-08 | 1.00 | " | 3.7 |
| 1mm, 3yrs | 1.00E+08 | 0.1 | 1.895E-09 | 2.93E-13 | 0.173 | 0.189 | " | 4.46E-08 | 1.00 | " | 5.8 |

Abbreviations: t = time (s); a = effective grain radius (cm); k = kinetic rate constant ($s^{-1}$); D = diffusion coefficient ($cm^2s^{-1}$); f = 1 – exp (–kt) (fractional approach to equilibrium; slope = $f_{glass}/f_{feld}$

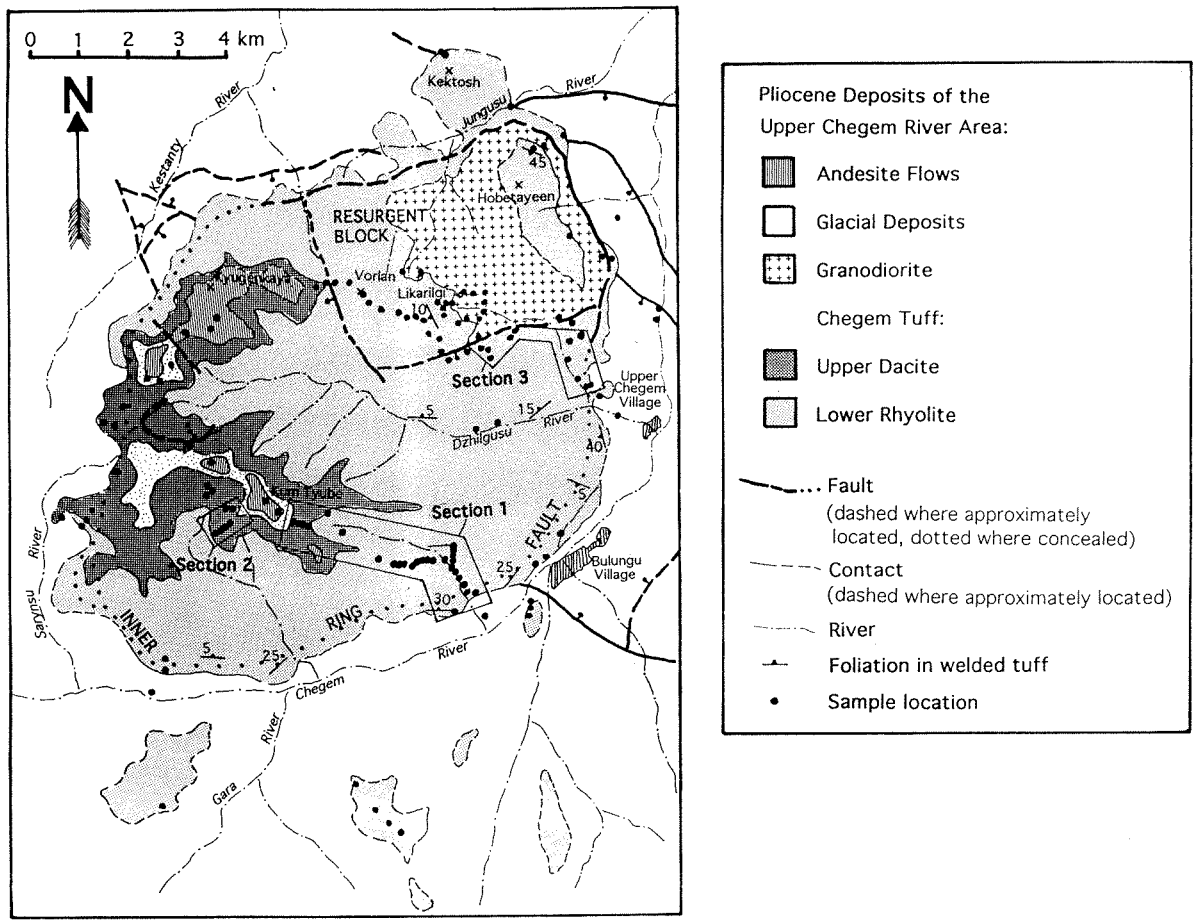


**Figure 4.1** -- Geologic map of the Chegem caldera (modified after Lipman et al., 1993). Sample locations are marked by black dots; Sections 1, 2, and 3 are stratigraphic sections which were sampled in detail, and are discussed in the text.

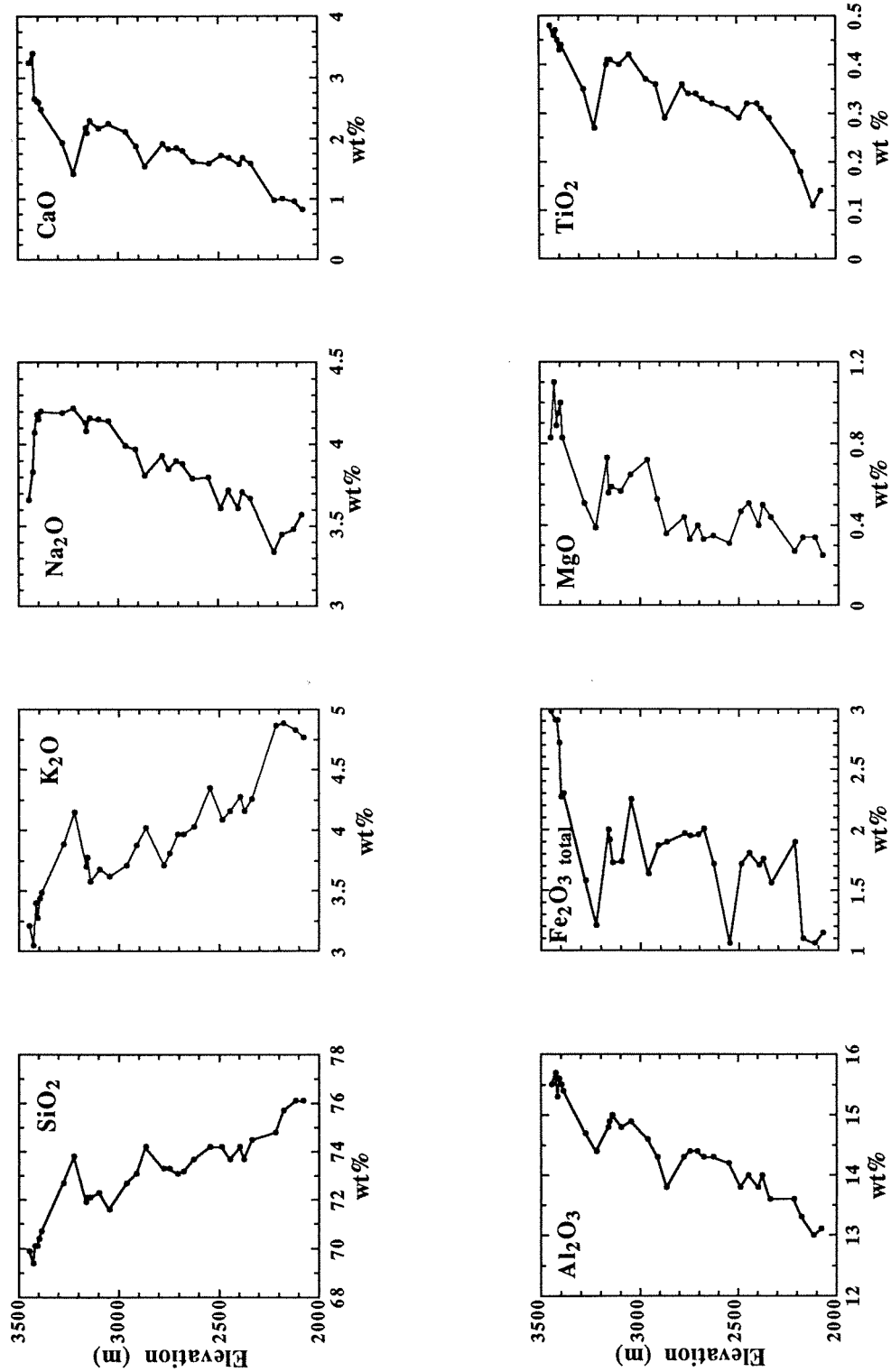


**Figure 4.2** -- Major element compositions (in wt%) of samples from Section 1 (located on Fig. 4.1).

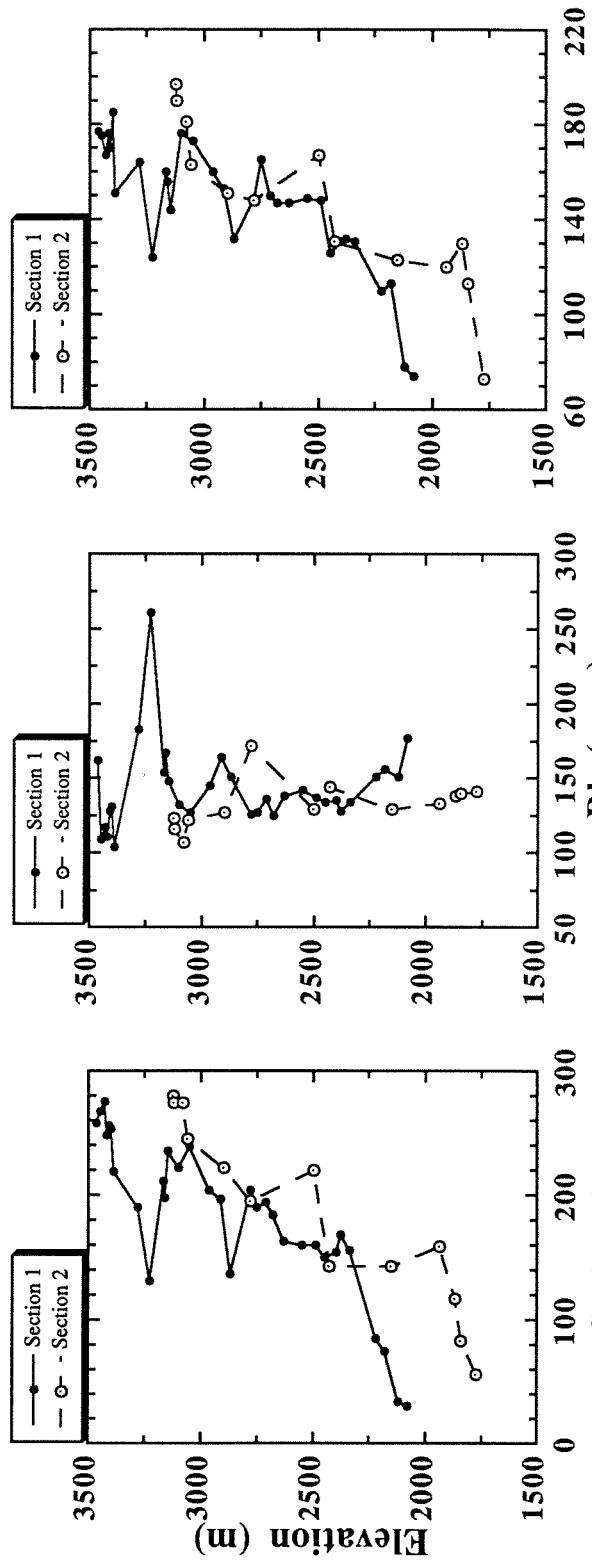


**Figure 4.3 --** Trace element compositions (in ppm) of samples from Sections 1 and 2 (located on Fig. 4.1).

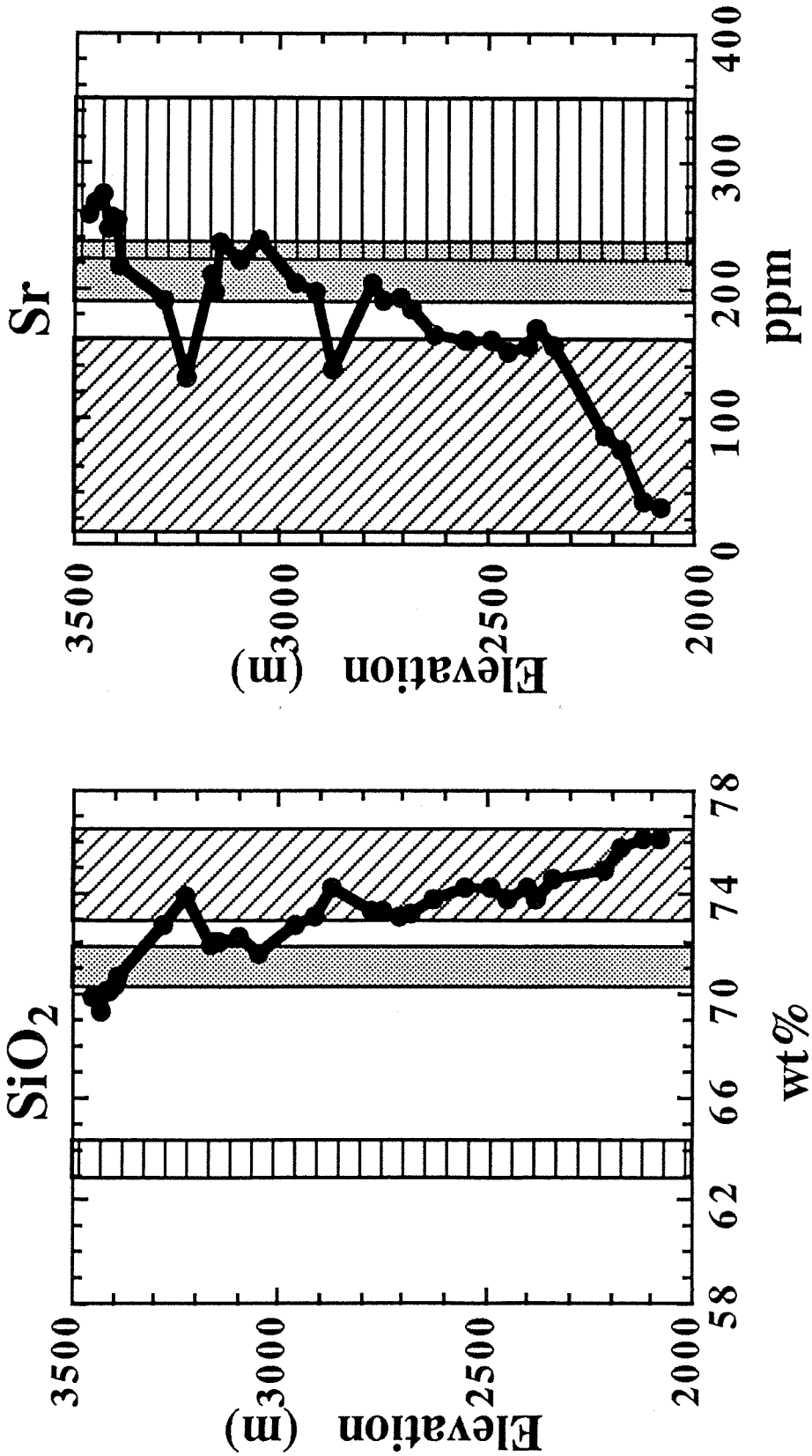


**Figure 4.4 --** Comparison of $SiO_2$ and Sr compositions in the intracaldera tuff (black dots), outflow tuff (diagonal rule), granodiorite porphyry (stippled) and andesite flows (horizontal rule). The vertical axes refer to the elevations of the intracaldera tuff samples which were taken from Stratigraphic Section 1 (located on Fig. 4.1).

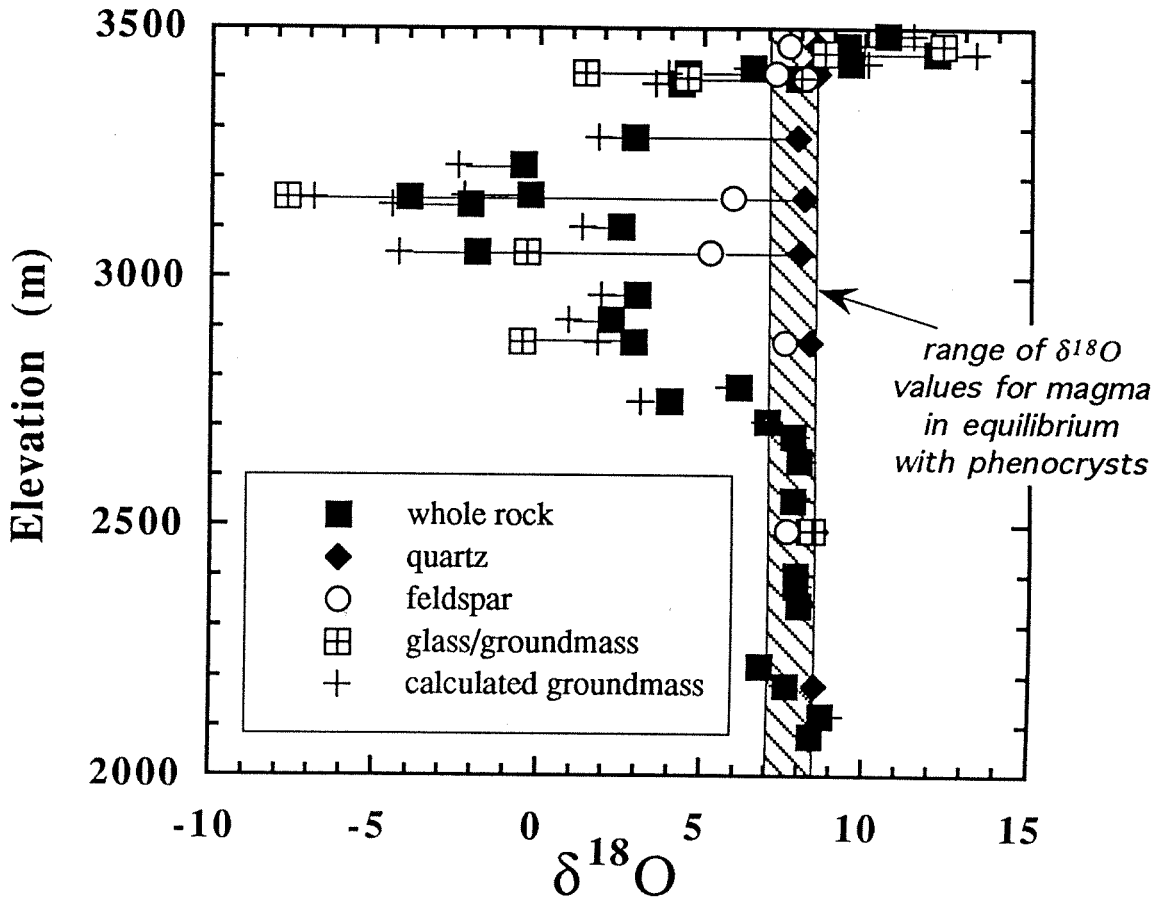


**Figure 4.5** -- Measured oxygen isotope compositions for whole rock (black squares), quartz (black diamonds), feldspar (open circle), glass/groundmass (crossed square) in Section 1. Also included are calculated material-balance groundmass $\delta^{18}O$ values based on whole rock values, assuming rock consists of 20% phenocrysts with combined $\delta^{18}O$ = +7.9 and 80% groundmass. The shaded zone is the range of calculated $\delta^{18}O$ values for magma in equilibrium with phenocrysts.

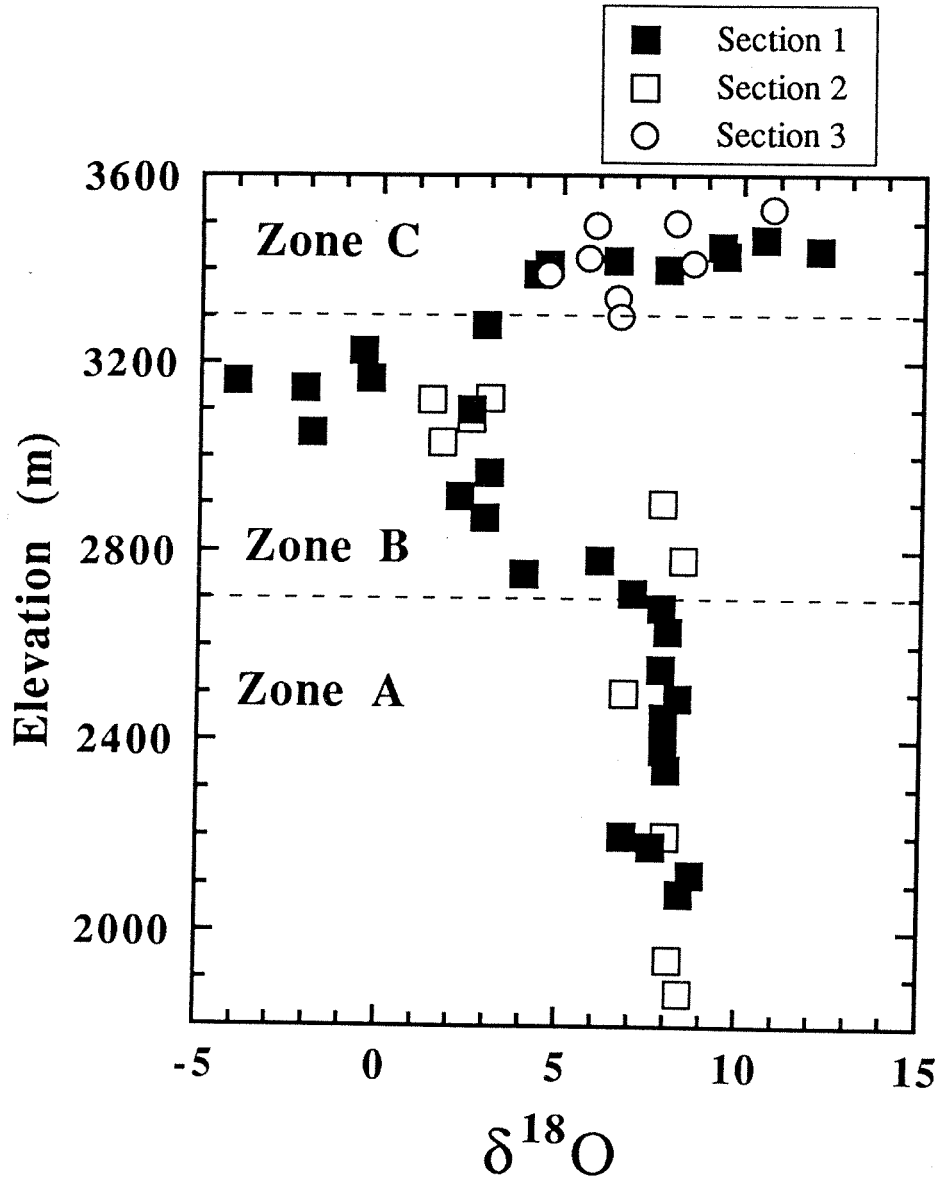


**Figure 4.6** -- Comparison of whole rock $\delta^{18}O$ values in three stratigraphic sections (Sections 1, 2, and 3; located on Fig. 4.1). Zones A, B and C are described on the text.

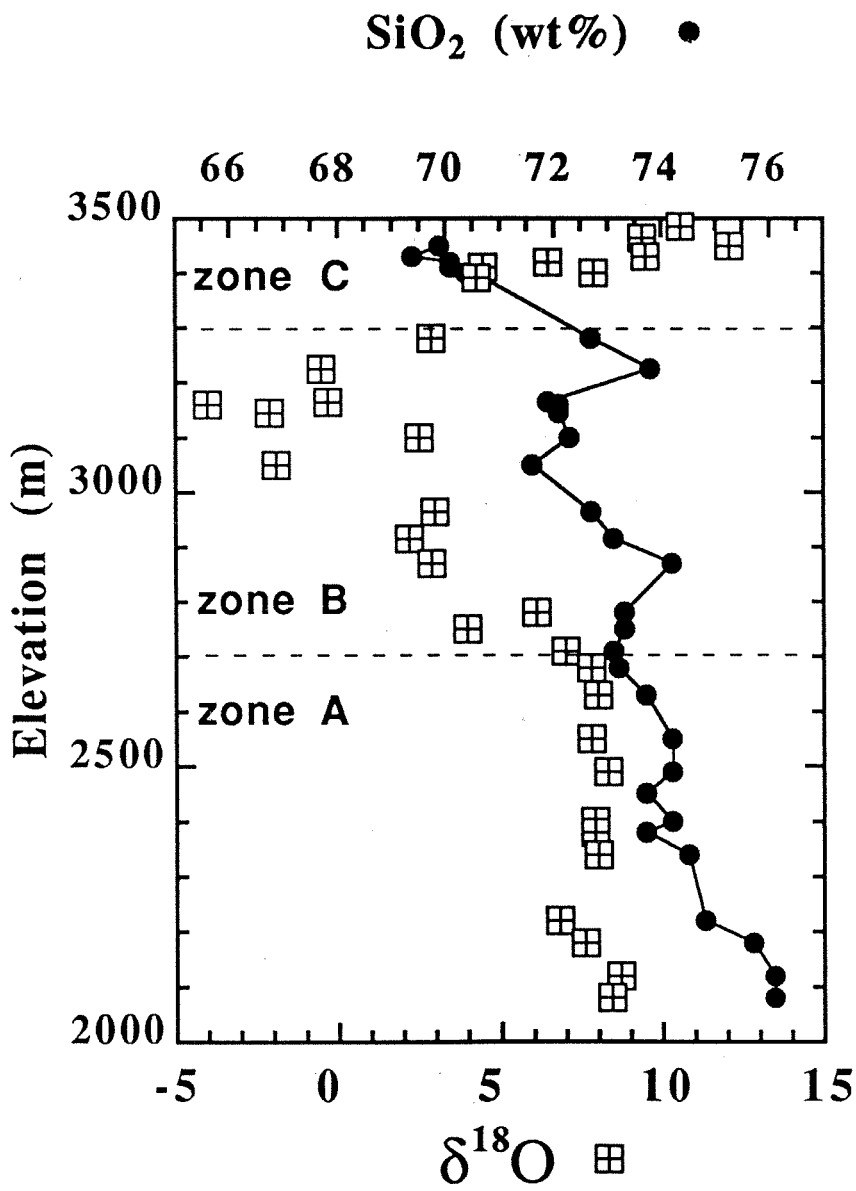


**Figure 4.7** -- Comparison of whole rock $\delta^{18}O$ values and $SiO_2$ content (wt%) for Stratigraphic Section 1. Zones A, B and C are described on the text.

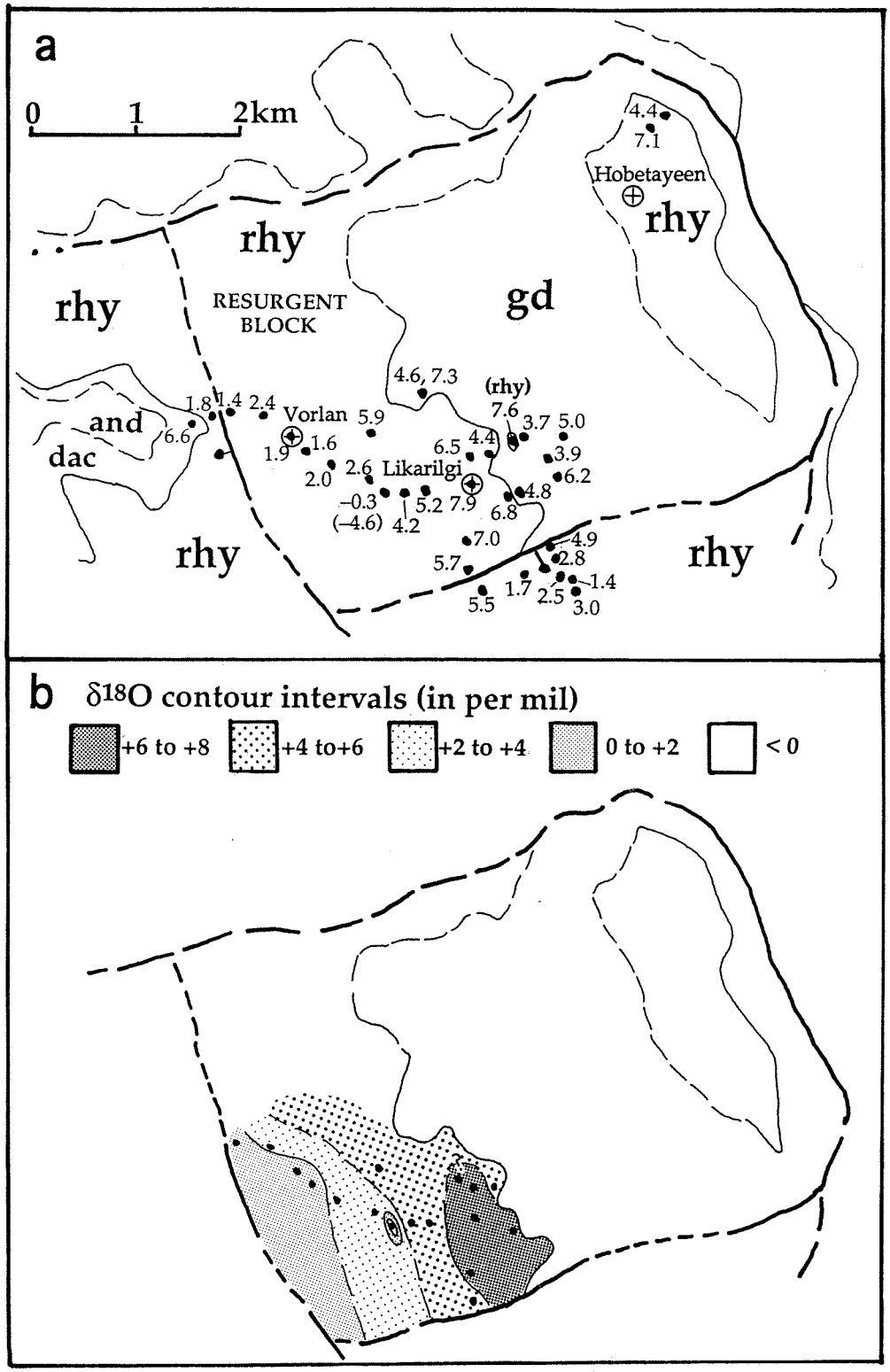


**Figure 4.8** -- (a) Whole-rock $\delta^{18}O$ values in granodiorite porphyry intrusion and resurgent block. The resurgent block is located in the northeast part of the Chegem caldera (Fig. 4.1). (b) Possible whole-rock $\delta^{18}O$ contour map of the resurgent block.

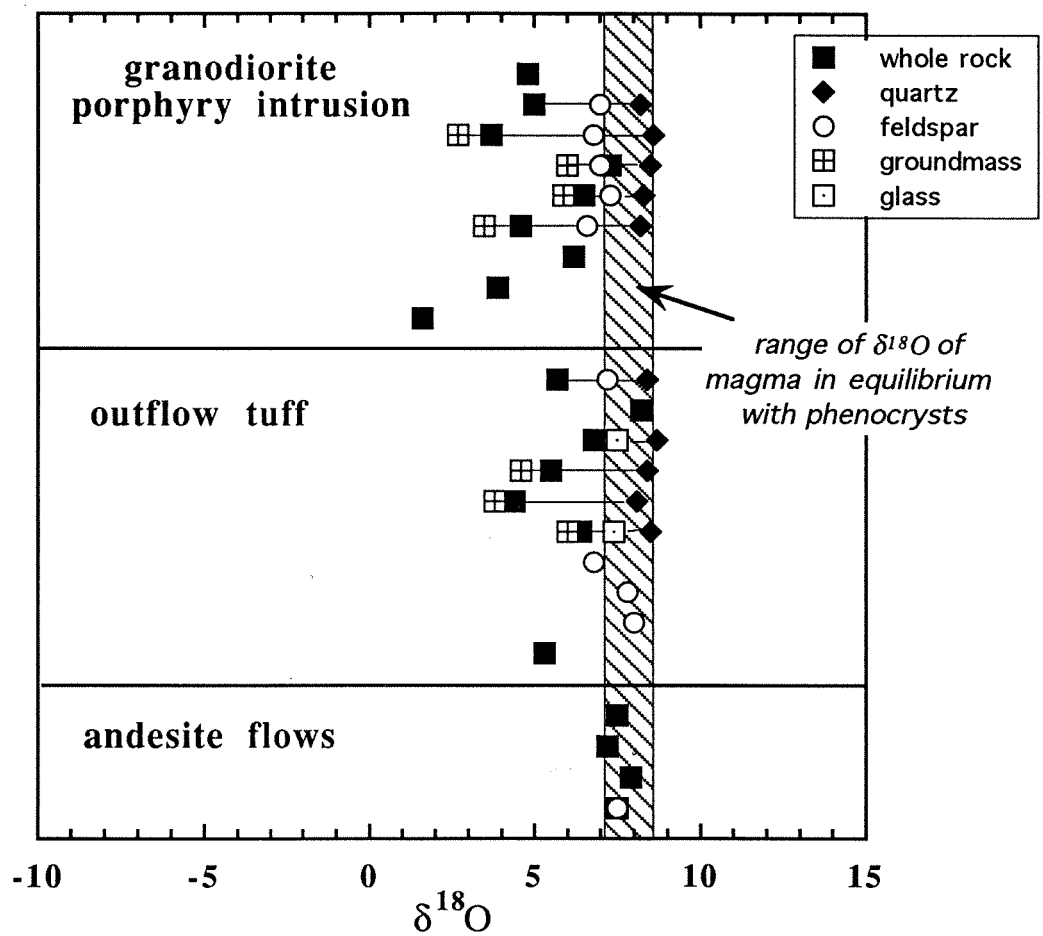


**Figure 4.9** -- Measured $\delta^{18}O$ values for whole rock (black squares), quartz (black diamonds), feldspar (open circle), and groundmass (crossed squares) in granodiorite porphyry intrusion, the outflow tuff and the andesite flows. The shaded zone represents the range of $\delta^{18}O$ values for magma in equilibrium with phenocrysts.

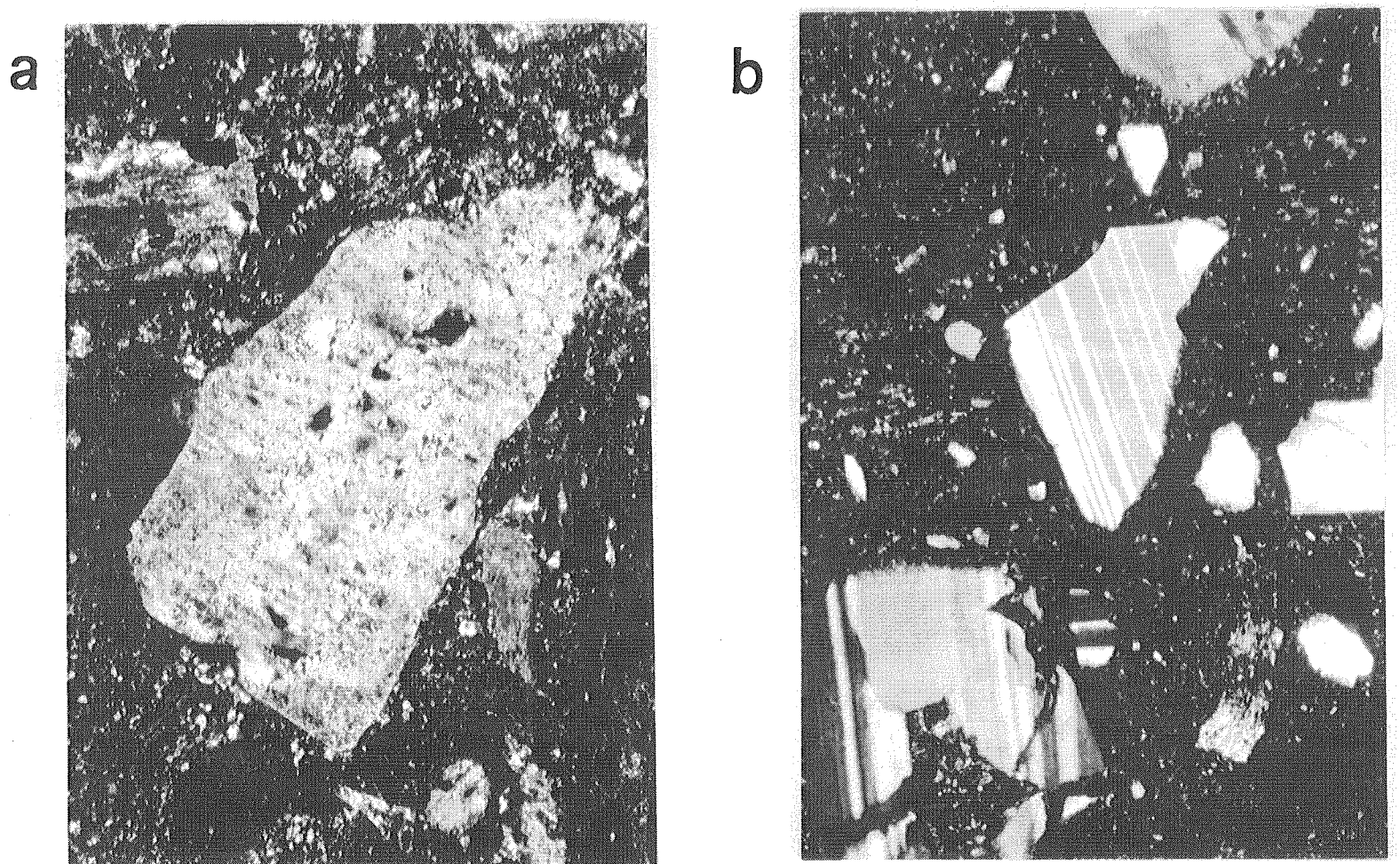


Figure 4.10 -- Photomicrographs of low-$^{18}O$ rocks from Lake City and Chegem calderas. (a) Sample SC-71 from Lake City caldera ($\delta^{18}O$ = +0.5): feldspar is altered to sericite and calcite; (b) Sample CG-C2-4H from Chegem caldera ($\delta^{18}O$ = –4.0): feldspars are entirely unaltered mineralogically.

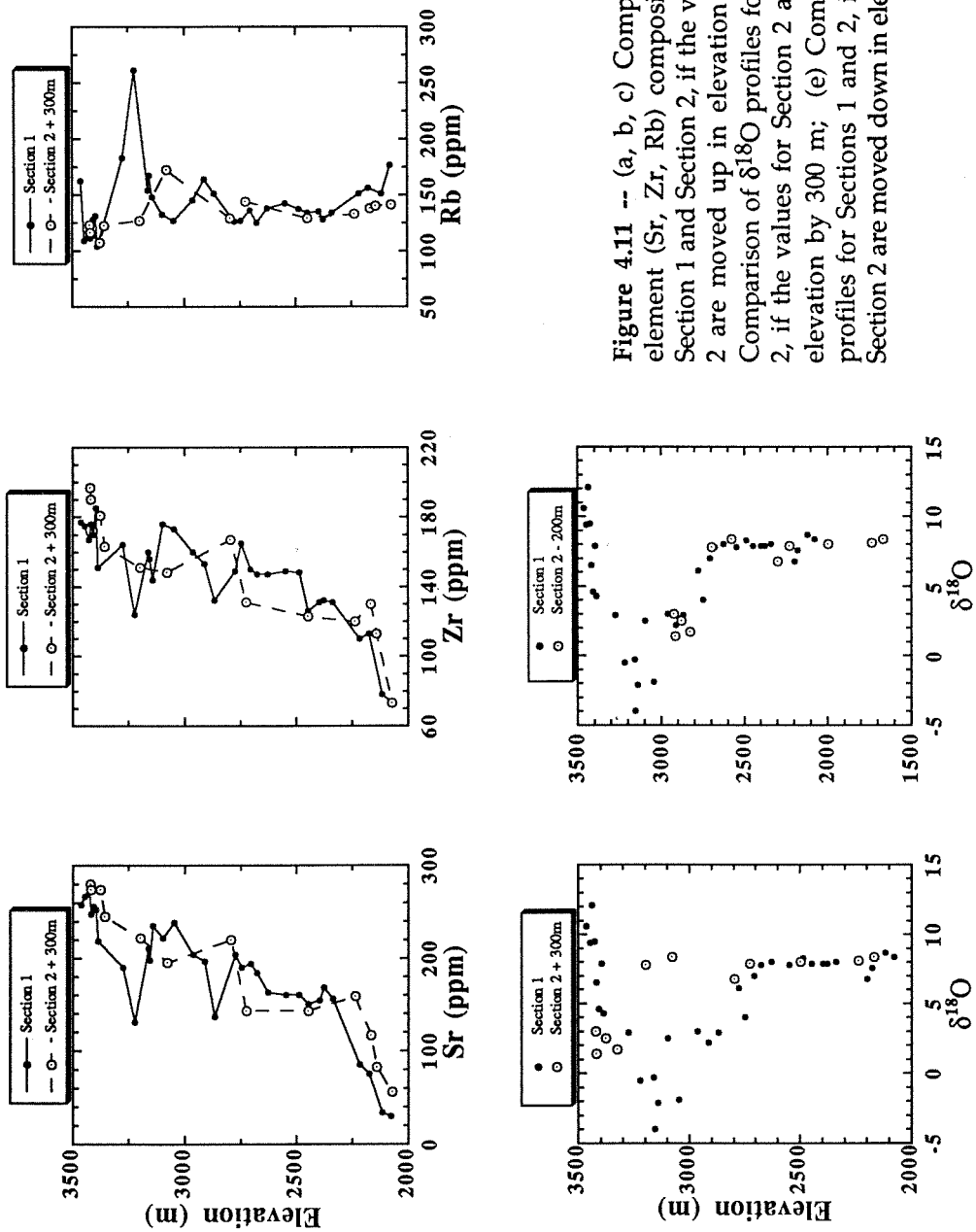


**Figure 4.11** -- (a, b, c) Comparison of trace-element (Sr, Zr, Rb) composition profiles in Section 1 and Section 2, if the values for Section 2 are moved up in elevation by 300 m; (d) Comparison of $\delta^{18}O$ profiles for Sections 1 and 2, if the values for Section 2 are moved up in elevation by 300 m; (e) Comparison of $\delta^{18}O$ profiles for Sections 1 and 2, if the values for Section 2 are moved down in elevation by 200m.

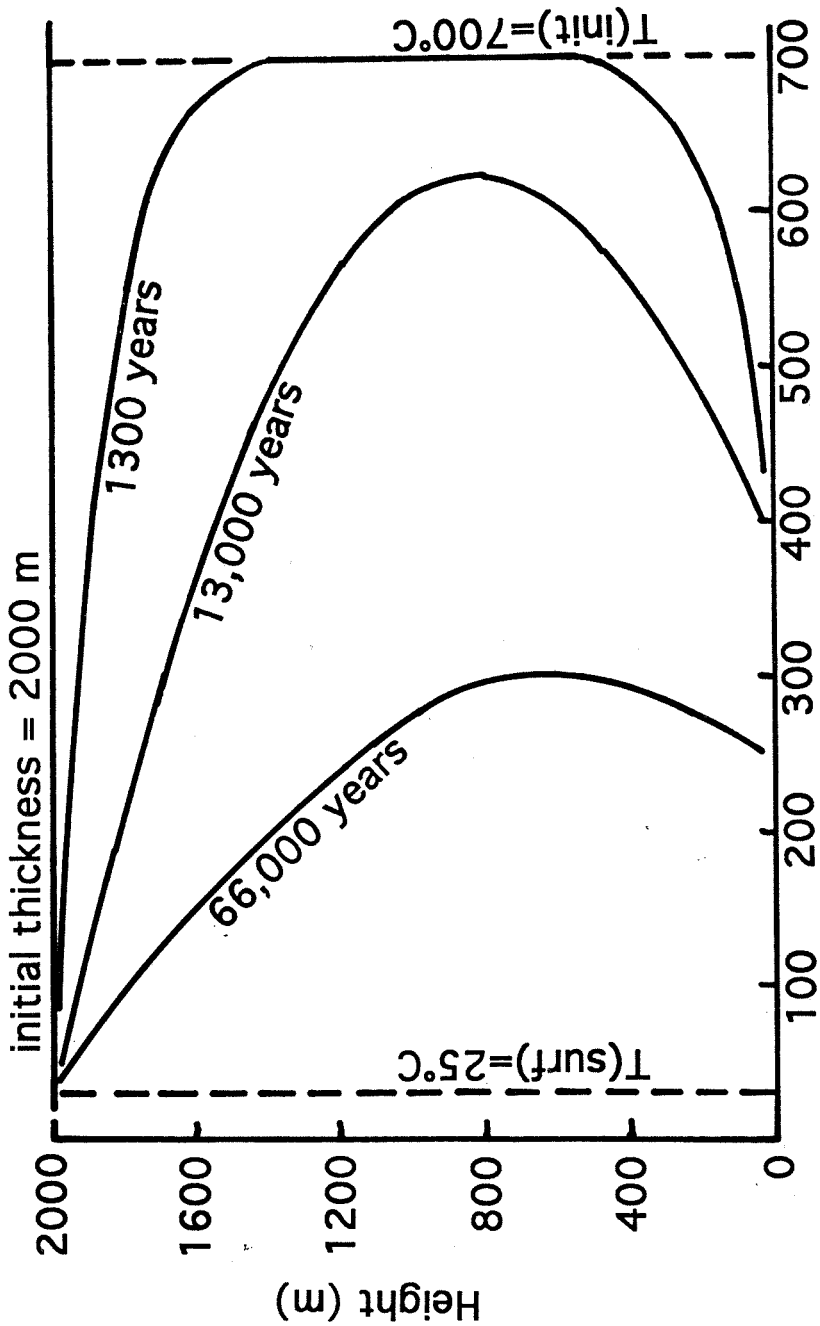


**Figure 4.12** -- Modeled cooling history of 2km thick sheet of welded tuff with intial temperature of 700°C. Modified from model by Riehle (1973). The model assumes that cooling is mainly by conduction.

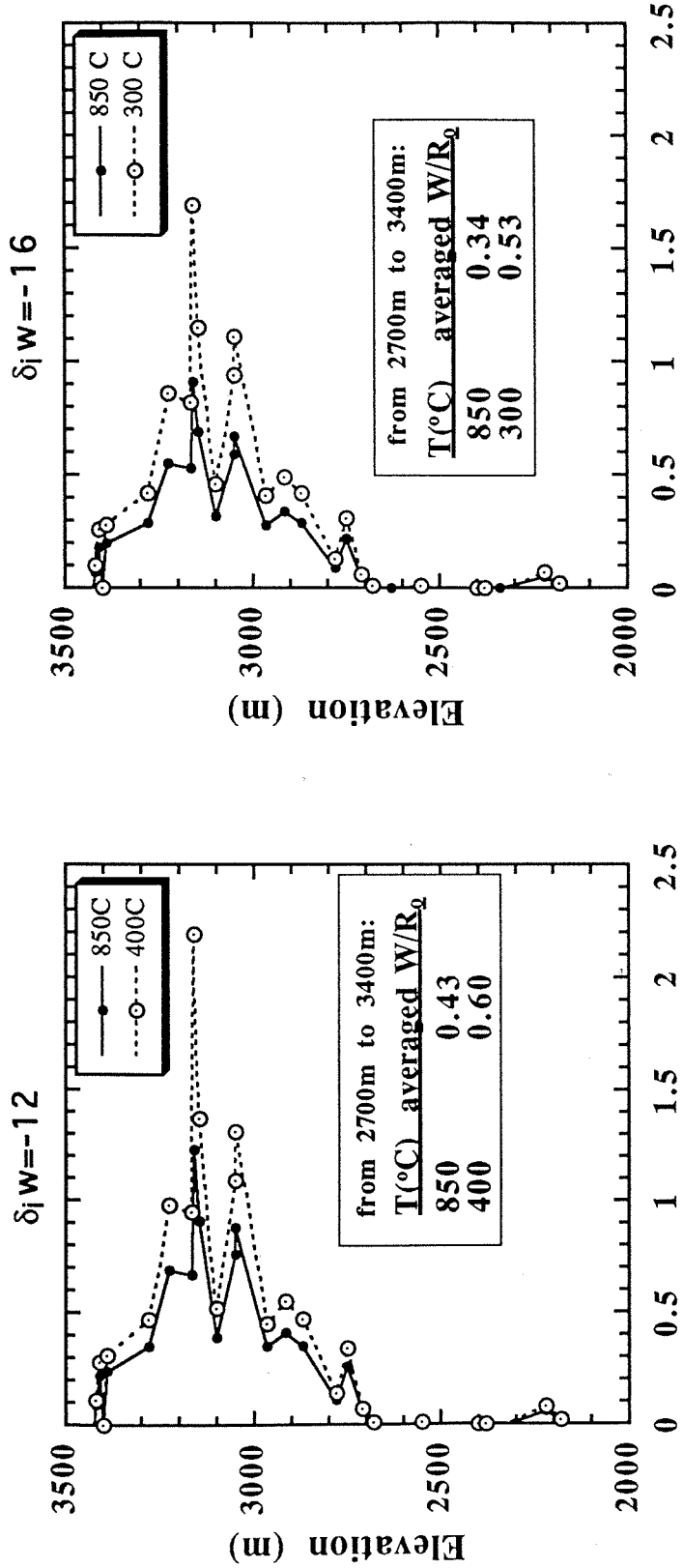


**Figure 4.13 --** Calculated open-system W/R ratios for Section 1 (Fig. 4.1). These were calculated using material-balance open system equation of Taylor (1977) for waters with initial compositions of $\delta^{18}O = -12$ (4.12a) and $\delta^{18}O = -16$ (4.12b). The fractionation factors used are averages of the fractionation factors for quartz and albite given in Clayton and Kieffer (1991). Two temperature extremes are shown for each water, T = 850°C (magmatic temperature) and T = 400°C ($\delta^{18}O = -12$) or T = 300°C ($\delta^{18}O = -16$). The averaged W/R ratios for the stratigraphic thickness from 2700m to 3400m elevation are listed.

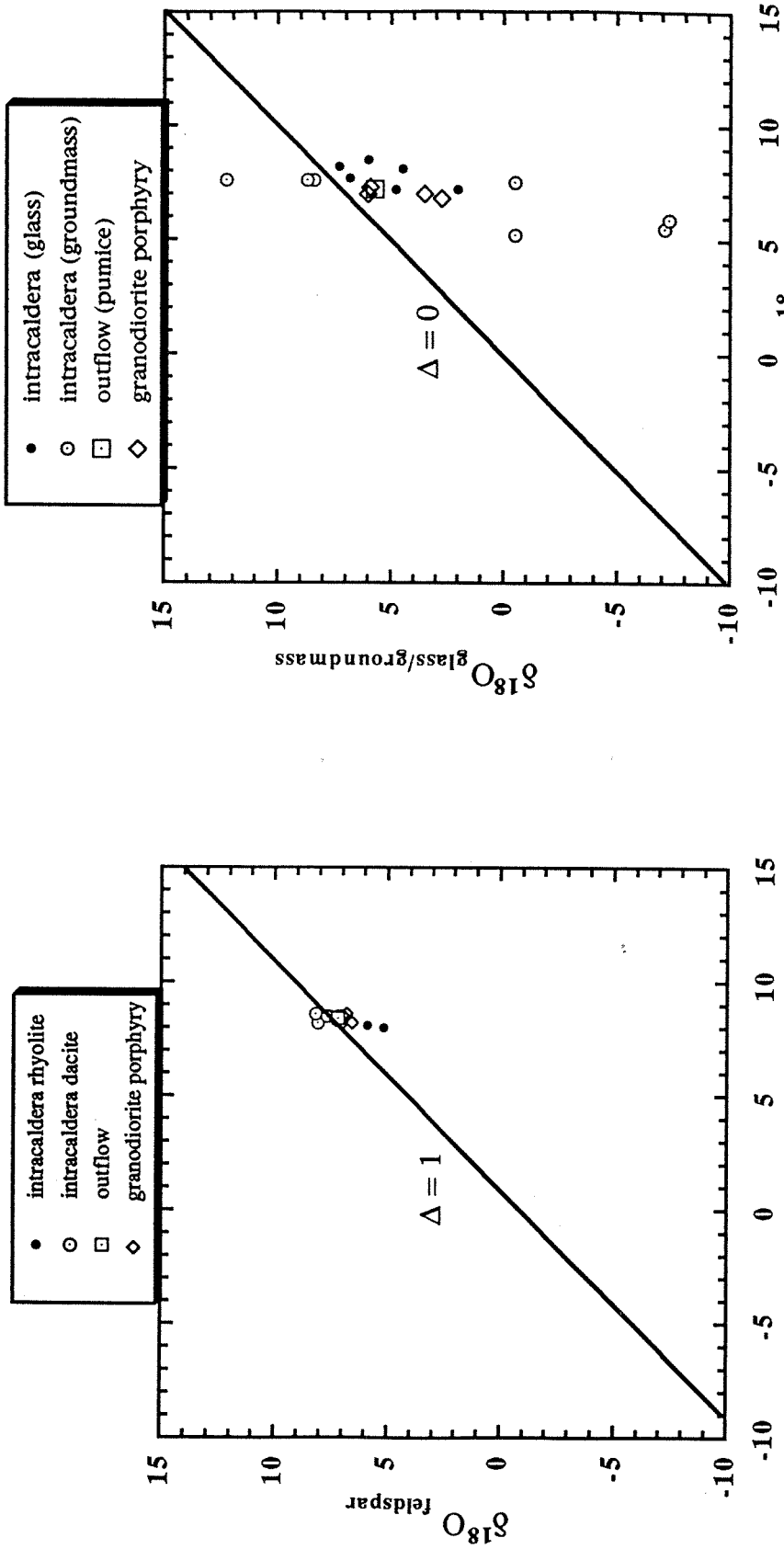


Figure 4.14 -- δ-δ plots of Chegem Tuff and granodiorite. (a) $\delta_{quartz}$-$\delta_{feldspar}$ plot; symbols: intracaldera tuff = black circles; intracaldera dacite = dotted circles; outflow tuff = dotted square; granodiorite porphyry intrusion = open diamond. (b) $\delta_{feldspar}$-$\delta_{groundmass/glass}$ plot; symbols: intracaldera tuff (glass) = black circles; intracaldera tuff (groundmass) = dotted circles; outflow tuff (pumice) = dotted squares; granodiorite porphyry intrusion (groundmass) = open diamonds.

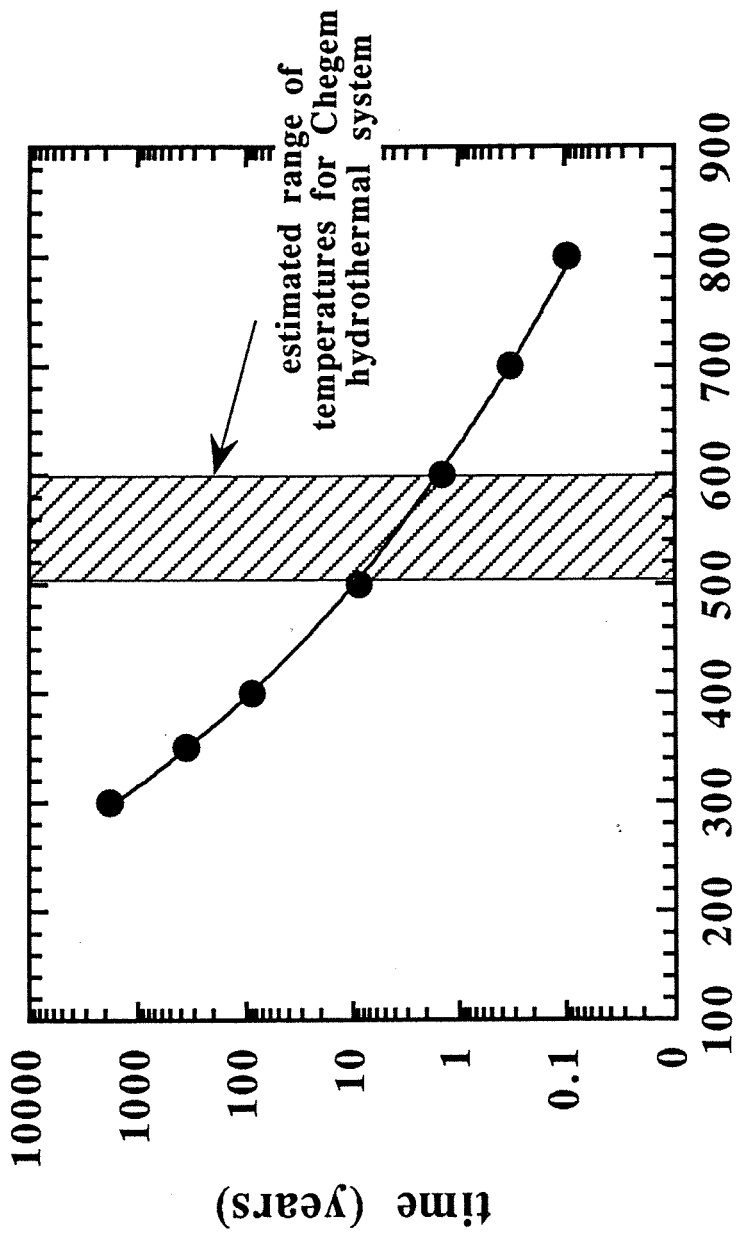


**Figure 4.15 --** Calculated time to achieve ≈10% exchange in feldspars (An35) assuming volume diffusion in a sphere of radius 300μm surrounded by a large, well-mixed reservoir of water, based on the solution of Crank (1975). The diagonally-ruled zone represents the estimated range of temperatures for the Chegem hydrothermal system (500°-600°C).

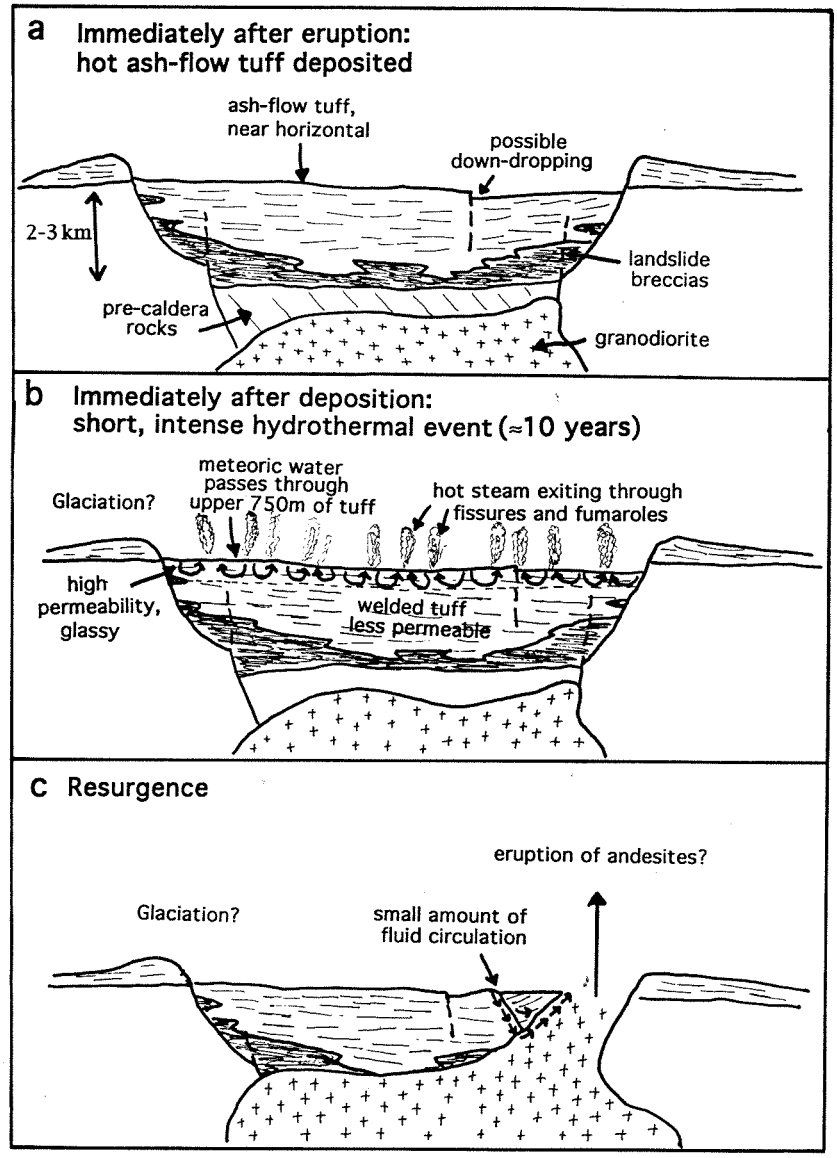


**Figure 4.16** -- Preferred $^{18}O$-depletion scenario at Chegem. (a) Immediately after eruption: Ash flow tuff was deposited near horizontal. The emplacement temperatures were approximately 600-800°C. (b) Immediately after deposition: A short-lived hydrothermal system was active in the upper 750 m of intracaldera tuff where the tuff was still glassy and very permeable. Temperatures were high (500-600°C) and hot meteoric waters circulated vigorously in small hydrothermal convection cells. This hydrothermal system was active for 10-25 years. Glaciation and erosion may have gone on at this time. (c) Resurgence: A granodiorite porphyry intruded the intracaldera tuff on the north side of the caldera along the ring fault. This pushed up and tilted a block of intracaldera tuff. Small amounts of meteoric hydrothermal waters circulted locally around the intrusion.

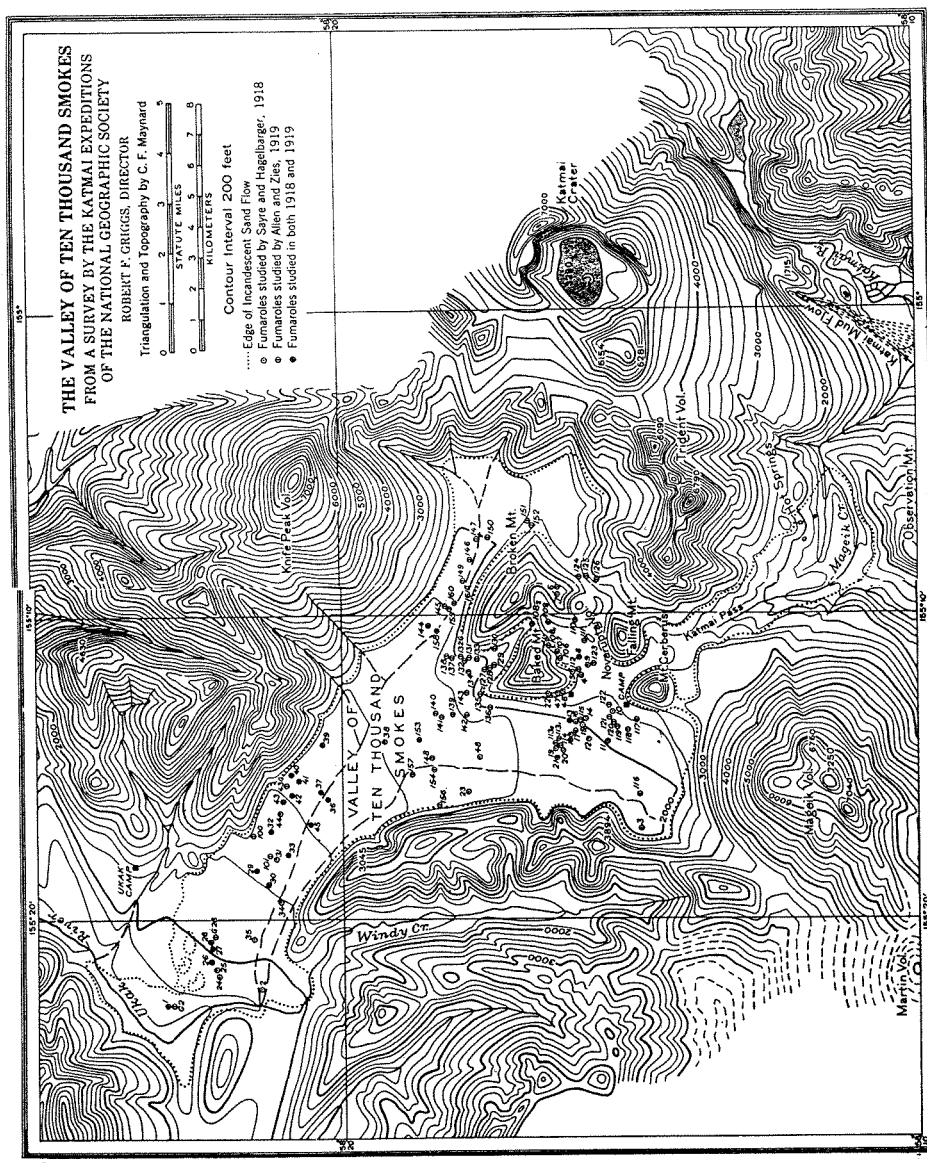


**Figure 4.17** -- Topographic map of the Valley of Ten Thousand Smokes (from Zies, 1929) showing distribution of studied fumaroles.

# Chapter 5. Stable Isotopic Compositions and $H_2O$ Concentrations of Rhyolitic Glasses from the Chegem Caldera

## 5.1 Introduction

Water and other volatiles play an important role in the evolution of volcanic magmas and rocks. The presence of water affects the physical properties of a magma (such as viscosity and crystallization temperature), the style of eruption of volcanic rocks (explosive vs. passive extrusion) and their post-eruptive alteration (including hydration and ore deposition). Studies of water contents and stable isotopic compositions of volcanic glasses can provide important clues about the eruption, degassing and hydration history of those glasses.

The solubility of water in silicate melts has been studied by many workers, using a variety of methods (e.g. Goranson, 1931; Kennedy, 1950; Yoder et al., 1956; Hamilton and Oxtoby, 1986). Among these methods, the technique of infrared spectroscopy was first used for measurement of water in silicate glasses

by Orlova (1962), who detected two species of water, molecular water and hydroxyl groups, in albitic glass. Infrared spectroscopy was not extensively used by geologists until recently, when Stolper and his coworkers began using this technique to study the solubility of water in silicate glasses of geologic interest (e.g., Stolper, 1982a, 1982b; Newman et al., 1986; Silver and Stolper, 1989).

Infrared spectroscopy has several advantages over other methods for determining the water content of a glass: (1) it is non-destructive; (2) very small spots (a few tens of microns in diameter) can be analyzed on single glass chips; (3) concentrations of hydroxyl (OH) and molecular water species can be measured as well as the total water content; (4) concentrations from a few parts per million to tens of weight per cent can be measured. With this technique, Stolper and his co-workers established that water exists both as hydroxyl (OH) and as molecular groups within the silicate framework of melts; they have had great success in determining the dependence of the concentration of molecular $H_2O$ and hydroxyl on temperature and melt composition (Stolper, 1989; Silver et al., 1990; Ihinger, 1991; Zhang et al., 1991). In addition, infrared spectroscopic studies have been performed on natural samples in order to constrain their initial volatile content and degassing histories (e.g., Newman et al., 1988; Anderson and Fink, 1989; Dixon et al., 1991).

Stable isotopes, particularly isotopes of oxygen and hydrogen, can provide essential information about interaction between water and melts or glasses. Hydrogen is present as dissolved water in the glass, and it can be extracted by heating the glass. Though the extraction of hydrogen is a relatively simple technique, hydrogen isotopic studies of continental volcanic rocks are few (e.g., Friedman and Smith, 1958; Taylor, 1968; Taylor et al., 1983; Newman et al., 1988; Anderson and Fink, 1989). One of the first isotopic studies of rhyolite glasses was by Friedman and Smith (1958), who examined the hydrated perlitic

rinds and the relatively anhydrous cores of obsidian, the so-called "perlite-obsidian pairs." They determined that variations in the D/H ratios of the perlites are correlated with the isotopic compositions of local meteoric water, whereas the D/H ratios of the obsidian cores appears to represent the original "magmatic values," although they may be effected by degassing. They found that the perlites are consistently depleted in deuterium by about 35 to 40 per mil relative to the local meteoric water. Friedman and Smith (1958) also observed that the perlites have water contents of 2 to 3.8 wt% versus the 0.1 to 0.3 wt% $H_2O$ in the obsidian.

Other hydrogen isotope studies of rhyolitic glasses (Taylor et al., 1983; Newman et al., 1988; Anderson and Fink, 1989) have examined the magmatic component of hydrogen in natural volcanic samples and explained it in terms of three degassing mechanisms for shallow intrusive environments: closed-system degassing within the magma chamber, open-system degassing during eruption and kinetically-controlled degassing after eruption. Closed- and open-system degassing will both tend to reduce both the water content and the D/H ratio of a glass, open-system degassing doing so more rapidly. Kinetically-controlled degassing has the opposite effect: $\delta D$ values increase with decreasing water content because $H_2O$ escapes more rapidly than HDO. However, these statements are only valid at very shallow depths in volcanic environments. The behavior of hydrogen isotopes in deeper-seated environments is much more complicated and still poorly understood (Taylor, 1994).

The fractionation of hydrogen isotopes between water and silicate melts as a function of temperature and melt composition is also poorly understood at present. Taylor and Westrich (1985) determined a fractionation ($\Delta D$) between vapor and natural rhyolite glass of 23.6 per mil at 950°C. Dobson et al. (1989) found that fractionation factors between vapor and dissolved water in rhyolite

glass decrease from 1.051 to 1.040 ($\Delta D$ = 50 to 39 per mil) as temperature increases from 530° to 850°C. Ihinger (1991) performed preliminary studies of hydrogen isotope fractionation in granitic melts and its relationship to speciation. His experiments were aimed at determining two fractionation factors: one between vapor and hydroxyl groups and one between vapor and molecular water. The best-fit results to this study at 850°C were fractionation factors of $1.036 \pm 0.010$ ($\Delta D$ = 35 per mil) and $1.000 \pm 0.010$ ($\Delta D$ = 0 per mil) for vapor-OH and vapor-molecular water, respectively. Thus, the hydrogen isotope fractionation between vapor and melt (total water in melt) depends on the proportions of the two dissolved species and will range from 0 to 35 per mil.

The three data sets have been reconciled by Ihinger (1991): The fractionation factor of Taylor and Westrich (1985) at 950°C is within error of the predicted value for a rhyolite with the same total water content at 850°C, based on the fractionations factors of Ihinger (1991). The fractionation factor of Dobson et al. (1989) at 850°C (1.040) is higher than that of Ihinger (1.036) for a glass with very low water content. However, when the lower temperature data of Dobson et al. (1989) are extrapolated to 850°C, the resultant fractionation factor is 1.037. Therefore, Ihinger (1991) postulates that Dobson et al. (1989) may have had experimental difficulties at 850°C because the onset of glass transition occurs near this temperature for anhydrous glass. Thus, the extrapolated value, which agrees with the value of Ihinger (1991) may be closer to the actual fractionation factor.

Unlike hydrogen, oxygen is found in both the framework structure of a silicate glass and in any dissolved water in the glass. The majority of this oxygen is in the silicate structure, and thus it can be extracted by fluorination techniques such as that of Taylor and Epstein (1962). In his reconnaissance study of the oxygen isotope geochemistry of igneous rocks, Taylor (1968) examined the D/H

and $^{18}O/^{16}O$ ratios in some obsidians and perlites from the western U.S. He found that in hydrated obsidians and perlites, both of these ratios are correlated with the isotopic compositions of local meteoric water, producing an array subparallel to the meteoric water line on a $\delta D$-$\delta^{18}O$ plot, but shifted upward by about 25 per mil in $\delta^{18}O$ and downward by about 35 per mil in $\delta D$. Oxygen isotopes are not as sensitive as hydrogen isotopes to processes such as magmatic degassing because only a small proportion of the total oxygen of the system is in the dissolved water. Therefore, the $\delta^{18}O$ of an obsidian which is not hydrated can be safely presumed to represent the original magmatic value, independent of the details of degassing. In general, glasses tend to be avoided in oxygen isotope studies, unless they were very recently erupted (e.g., unless they are only a few thousand years old). This is because they are so easily hydrated and because phenocrysts, such as quartz and pyroxene, are more likely to retain information on the primary oxygen isotope composition of a magma. Even though the Chegem caldera was formed only 2.8 million years ago, it is still much too old to *a priori* expect that the glasses preserved in these ash-flow tuffs are isotopically pristine. That can only be demonstrated by very careful and details studies of the glasses in question.

The methods outlined above, infrared spectroscopy and stable isotope studies, can be used on any preserved volcanic glass when addressing questions of initial volatile content, degassing history, and magma-water or glass-water interaction. In this chapter, I discuss the application of these techniques to glassy pumices from the Chegem caldera. Throughout most of its 2-km thickness, the densely-welded intracaldera Chegem Tuff is largely devitrified; however, some rhyolitic glasses are preserved. In particular, glassy pumices are common in the upper 100-200m of intracaldera tuff, in the dacitic part of the stratigraphic section, and in rhyolitic vitrophyres along the margins of the intracaldera tuff.

These marginal vitrophyres are preserved at the base of the exposed section, along the Chegem River on the east and south sides of the caldera.

Our oxygen isotopic studies (Chapter 4) have defined a distinct caldera-wide horizon of low-$^{18}O$ rocks, with whole-rock $\delta^{18}O$ values as low as –4. Glassy pumices from the upper part of the section have $\delta^{18}O$ as low as +1.4. As discussed in Chapter 4, these rocks must have been isotopically altered by some short-lived interaction with meteoric waters at temperatures of >250°C. We have suggested that there was a short-lived and intense hydrothermal event immediately after eruption, similar perhaps to the hydrothermal activity which occurred at the Valley of Ten Thousand Smokes, but the exact details of the water-rock interaction are poorly understood. The present D/H study was undertaken in the hope that the glasses, especially the water in the glasses, might preserve some record of the temperatures and style of interaction that produced this $^{18}O$ depletion.

This chapter presents results of infrared spectroscopic studies (water contents and speciation), oxygen isotope studies, and hydrogen isotope studies of glasses from five Chegem Tuff samples: four dacitic tuffs and one marginal vitrophyre. In addition, melt inclusions in three phenocrysts were analyzed by FTIR and the results are given. These results are discussed in terms of the magmatic water content of these glasses and their post-magmatic hydration history.

## 5.2 Analytical Methods

### *5.2.1 Sample Selection and Preparation*

Five samples with glassy pumices were selected for infrared spectroscopy and hydrogen isotope analyses based on their stratigraphic positions with respect to the oxygen isotope trends described above. Their whole rock $\delta^{18}O$

values range from +4.5 to +9.7. A tuff sample ($\delta^{18}O = -0.5$) from the low-$^{18}O$ zone of the stratigraphic sequence, where glassy pumices are not preserved, was selected for separation of phenocrysts to study melt inclusions. Fig. 5.1 shows the projected locations of all of these samples on the oxygen isotope profile of Chapter 4; Fig. 5.2a and 5.2b locate the samples on the geologic map of the caldera and on a cross section of the caldera. For convenience, I have labelled these samples A, B, C, D, I and M in this chapter. Other sample numbers, sample locations and sample descriptions are given in Table 5.1. A, B, C and D are dacitic tuffs from the upper 100m of caldera fill; M is a marginal vitrophyre from a slide block below the base of the exposed caldera fill. It is thought to represent the lowest accessible stratigraphic level within the intracaldera tuff (Lipman et al., 1993). Phenocrysts with melt inclusions were separated from the sample, labelled I, collected from the low-$^{18}O$ zone of the stratigraphic section.

The flattened glassy pumices typically have an aspect ratio of 3:1 to 5:1 and are usually ≈1cm or less in length, though some are as long as 15 cm. In thin section, perlitic cracks are visible in glass in samples A and D, especially near the edges of the pumices. Samples B, C and D display an undulose banding of clear zones and darker zones, due either to submicroscopic aligned microlites or collapsed vesicles. There are also numerous microscopic opaque microlites in these samples. Glassy pumices in sample M are remarkably pristine, with no cracks, bands or microlites.

The major element compositions of the glasses and some of the whole rock tuffs from which they come are given in Table 5.2. Though the tuffs range in composition from rhyolitic (74.4 wt% $SiO_2$) to dacitic (69.4 wt% $SiO_2$), the glasses are all rhyolitic with 73.4 to 75.5 wt% $SiO_2$.

Samples A, B, C, D and I were ground with a mortar and pestle, washed ultrasonically in acetone and dried. Glass chips and/or phenocrysts were then

hand picked from the 165-330μm or the 330-590μm fraction. Thus, the glass used for a given analysis was made up of chips from multiple glassy pumices from a single hand sample. The glassy pumices in samples A-D are small (<1cm) and have ≈10% phenocrysts, so it was difficult to obtain chips of pure glass. Nevertheless, it is estimated that all of the analyzed glasses were >95% pure. Sample M contains glassy pumices with a smaller proportion of phenocrysts (<5%). These pumices were large enough (up to 4 cm) that they could be chiseled out of the sample. Thus, a single pumice from sample M was used for infrared spectroscopy, and hydrogen and oxygen isotope analysis. A second pumice from that sample was also analyzed for $^{18}O/^{16}O$.

### *5.2.2 Infrared Spectroscopy*

For each sample, several small chips of glass approximately 500 microns in diameter were selected for spectroscopic analysis. The chips were mounted in dental resin (L. D. Caulk Co.) and polished on one side by grinding on alumina grit micropolishing paper (3M). The final polishing was performed using 0.3-1.0 micron alumina powder in distilled water on polishing cloth (3M). The singly-polished chips were then glued on glass slides with epoxy (Crystalbond 509, Aremco Products, Inc.), and samples were ground to thicknesses varying from 68 to 160 microns. Phenocrysts from samples D and I were ground to thicknesses of 14 to 29 microns in order to expose the melt inclusions. The doubly-polished sections were soaked ultrasonically in acetone to remove traces of epoxy and rinsed in toluene to remove any acetone residue. Samples were positioned over apertures of 114 microns (28 microns for sample C) in diameter for the glass chips and >11 microns for the melt inclusions. An optical microscope with a redundant aperturing system was used to position the sample. All infrared analyses were performed on a Nicolet 60SX Fourier transform infrared

spectrophotometer (FTIR) using a W tungsten source, $CaF_2$ beamsplitter, and an InSb detector with a resolution of 8 $cm^{-1}$, a mirror velocity of 1.57 cm/sec and 2048-4096 scans. A background spectrum was taken before each series of analyses and subtracted from each sample to obtain the absorption spectrum for the glass.

Concentrations of molecular water and OH were determined by measuring the absorbance at 5200 $cm^{-1}$ and 4500 $cm^{-1}$, respectively. For the melt inclusions, total water concentrations were measured at 3550 $cm^{-1}$. A given absorbance can be converted to a concentration if the molar absorptivity for the Beer-Lambert Law (Beer's Law) is known. According to Beer's Law, the amount of absorption within a matrix is proportional to the number of absorbers. The number of absorbers are given by the expression:

$$\#\ \text{of absorbers} = C^*d^*\rho$$

where C is the species concentration in the glass, d is the thickness of the glass and $\rho$ is the density of the glass. Thus, the absorbance of an infrared band (Abs) is also proportional to the concentration of the dissolved species:

$$C=Abs/(d^*\rho^*\varepsilon)$$

and $\varepsilon$ is the constant of proportionality or the molar absorptivity from Beer's Law.

Molar absorptivities, calibrated for rhyolite glasses with up to 1.8 wt% water (Newman et al., 1986) are 1.61 l/mol-cm and 1.73 l/mol-cm for 5200$cm^{-1}$ (molecular water) and 4500$cm^{-1}$ (OH), respectively. However, rhyolite glasses with higher water contents may require different calibrations (Ihinger, 1991). The variations in molar absorptivities with glass chemistry, water content and thermal history are not well known at this point, so I have chosen to use the molar absorptivities of Newman et al. (1986). The total water content was determined for melt inclusions in phenocrysts by using molar absorptivities of

89 l/mol-cm (OH) and 56 l/mol-cm for (molecular water) for the 3550cm$^{-1}$ absorption band (Dobson et al., 1989). Since the water contents in the melt inclusions were so low, we assumed that the water was made up almost entirely of OH groups and used the molar absorptivity of 89 l/mol-cm. Though absolute concentrations will change when different extinction coefficients are used, the relative concentrations should not.

### *5.2.3 Oxygen Isotopes*

For each of the oxygen isotope analyses, 9 to 25 mg of hand-picked glass was used. Extraction of oxygen was accomplished by the fluorination technique described in Taylor and Epstein (1962). Oxygen isotope ratios are reported in the familiar δ-notation relative to SMOW as described in Chapter 4. Standard deviations are less than 0.15 per mil. Details of the extraction procedure and standard analyses are reported in Appendix B. Oxygen yields (Table 5.6) for these glasses ranged from 14.4 to 15.9 μmoles $O_2$/mg (except for one sample which was probably spilled during loading).

### *5.2.4 Hydrogen Isotopes - Extraction of Water*

Usually 20 to 30 mg of glass chips, hand-picked from the 330-590μm sieve fraction of whole-rock, were used. For sample M, a large glassy pumice was ground in a mortar and pestle and glass chips >150μm were picked. For sizes smaller than 150μm, adsorbed water contributes significantly to the total gas yield (Newman et al., 1986). Water was extracted using the vacuum extraction line described in Ihinger (1991). The line consists of an input port, a copper-oxide furnace, a cryogenic trap, a uranium furnace, a manometer, a Toepler pump and an output port. The glass chips were loaded in air into a platinum crucible inside a quartz reaction vessel connected at the inlet port. After evacuation of the

reaction vessel, the glass was heated incrementally for ≈26 hours with a radio-frequency induction furnace to temperatures around 1200°C for complete extraction of all dissolved water. A typical heating schedule is given in Table 5.3. Long extraction times were necessary because shorter extraction times are known to produce bubbles which serve as a storage space for water (Ihinger, 1991). Gas in the bubbles cannot escape from the highly viscous rhyolite glass. During the heating of the sample, any reduced hydrogen or carbon was oxidized to $H_2O$ and $CO_2$ by exposure to hot (600°C) copper oxide. The water and $CO_2$ were frozen in liquid nitrogen, and then a dry ice slurry was used to separate the water from $CO_2$. The $CO_2$ was measured manometrically and discarded. The water was converted to hydrogen in a uranium furnace at 700°C (Bigeleisen et al., 1952) and passed to a manometer by means of a Toepler pump. Manometric measurements are accurate to ≈1% of the total sample. The $H_2$ gas was collected in tubes and transported to a hydrogen mass spectrometer.

The cleaning procedure between successive analyses was as follows: (1) The platinum crucible was cleaned by removing all glass fragments which were visible under a binocular microscope. Previously, platinum crucibles were soaked in HF, so that any glass fragments were dissolved. However, Ihinger (1991) observed larger blanks when this cleaning method was used and adopted the new method. Any glass fragments which remain after picking should not contain any measurable water. (2) The quartz reaction vessel was soaked overnight with dilute aqua regia, rinsed with distilled water and dried overnight in an oven at ≈100°C. (3) The reaction vessel containing the platinum crucible was re-attached to the extraction line and heated with the induction furnace to 1200°C for 2-3 hrs while under vacuum.

### *5.2.5 Hydrogen Isotopes - Mass Spectrometry*

The hydrogen mass spectrometer at Caltech is a single-focusing, double-collecting McKinney-Nier mass spectrometer (Nier, 1947; McKinney et al., 1950). The D/H ratio for each sample is compared to a reference gas of known isotopic composition and converted to the δ-notation relative to SMOW:

$$\delta D_{sample} = 1000 * \left( \frac{(D/H)_{sample} - (D/H)_{SMOW}}{(D/H)_{SMOW}} \right)$$

### *5.2.6 Hydrogen Isotopes - Uncertainty Estimates*

Reported uncertainties for this procedure, based on replicate analyses of standard waters are 1-2 per mil (Dobson et al., 1989; Ihinger, 1991). However, based on replicate analyses of glass samples (described below), our uncertainties may be as high as 5-7 per mil. There are several errors associated with the hydrogen extraction. Incomplete degassing of rhyolitic glasses because of bubble formation can prevent isotopically-fractionated water vapor from escaping from the melt. Ihinger (1991) observed that $\Delta D_{vapor\text{-}melt}$ values were up to 60 per mil lower than the presumed correct value and that these lower ΔD's could be correlated with the time the sample spent at 500°C, the temperature at which molecular water diffuses rapidly from the melt. All of our samples appeared white and frothy after the extraction procedure, suggesting that bubbles had been formed. One sample was analyzed after extraction with the FTIR and was found to contain less than 10 ppm water. However, this measurement was of the glass, not the bubbles which had formed. Nevertheless, in light of the long extraction times used, we believe that this observation implies that these samples were in fact completely degassed.

There is a measurable blank in the hydrogen extraction line, due in part to the degassing of the glasses in the line, the platinum crucible and the vacuum

grease. Table 5.4 lists some of the reported blanks on this line. As noted by Ihinger (1991), blanks run after the platinum crucible had been washed with HF tended to be higher. Unlike previous blanks which were usually only run for 4 to 14 hours, I ran three full procedural blanks, incrementally heating the empty crucible for 20 to 26 hours. All produced between 4.8 and 6.5 micromoles of water. The isotopic compositions of two of those blanks were $\delta D = -65$ and $-144$, but more typically the line blank has $\delta D = -120$ to $-130$ (Ihinger, 1991). In our results, we present both raw $\delta D$ and blank-corrected $\delta D$, where 4.9 micromoles of water with $\delta D = -130$ are removed from each gas extraction.

Another source of error in these analyses is the "memory" effect of the uranium furnace. Apparently, a small number of uranium hydride molecules are formed that retain some hydrogen and deuterium atoms from previous samples. To control this effect, one can either run samples two or more times, or flush the line out with water of a known isotopic composition between samples. I have run several of my samples two or three times and did not note any systematic difference between the first and second runs relative to the samples which were run before them. Inasmuch as all of my samples are isotopically similar, the line is essentially flushed by each sample and the "memory" effect should not be a problem.

## 5.3 Results

### *5.3.1 $H_2O$ Content and Speciation*

FTIR results for 7 glassy pumice fragments (from 5 tuff samples), and three phenocryst inclusions (from two different tuff samples) are given in Table 5.5. Total water contents range from 3.4 to 4.8 wt% for the glasses. In all glass samples except the marginal vitrophyre, the water is made up of ≈3 wt% molecular $H_2O$ and ≈0.7 wt% OH. The marginal vitrophyre contains a much

larger amount of molecular $H_2O$ (4 wt%). The melt inclusions in the phenocrysts have much lower total water contents (0.3 to 0.7 wt%).

### *5.3.2 Oxygen Isotopes*

Oxygen isotope compositions of the glassy pumices (Table 5.6) range from $\delta^{18}O$ = +1.4 to +9.1. The $\delta^{18}O$ of the glass is always lower, usually by 1 to 2 per mil, than the $\delta^{18}O$ of the whole rock, which ranges from +4.6 to +9.7. Two aliquots of glass separates from sample D, which has the lowest-$^{18}O$ glass, yielded $\delta^{18}O$ values of +1.4 and +2.5.

### *5.3.3 Hydrogen Isotopes*

Measured hydrogen isotope compositions of the five glass samples (Table 5.7) range from $\delta D$ = –100 to –126. When corrected for a 4.9 μmole blank with a $\delta D$ of –130, this range becomes –99 to –124. Three samples (M, C, and A) were analyzed two or three times. The glass fragments for M are from a single large glassy pumice, whereas for samples C and A, the glass fragments came from the same hand sample, but not the same pumice. Modern Chegem River water has a $\delta D$ of –89.

## 5.4 Discussion

### *5.4.1 Comparison of FTIR and Manometry*

In these studies we performed two independent determinations of total water content: manometric measurements following water extraction and calculated water content from FTIR absorption. Comparison of the two methods (Fig. 5.3) reveals that water extraction and manometry yielded ≈15% lower total water contents than the FTIR measurements for all samples except A, for which the two methods yielded the same water content. There are several possible

explanations for this discrepancy: (1) *impurity of glasses used for manometry* - Since the glassy pumices are very small and fairly phenocryst-rich, it is difficult to pick out fragments of pure glass. They may have contained as much as 5% phenocrysts, in addition to numerous microlites. The phenocrysts and microlites contain only trace amounts of water, so their presence will tend to reduce the total water content of the sample. (2) *incomplete extraction of water* - To check for this, we measured one sample by FTIR after water extraction and found that it did not contain measurable amounts of water. Though we did not measure the quantity of water in bubbles which were produced, we believe that the long extraction times were sufficient for water to escape from the sample. (3) *uncertain molar absorptivities* - As stated earlier, the absolute correctness of the molar absorptivities is still uncertain. I have used values of 1.61 l/mol-cm and 1.73 l/mol-cm for molecular water and OH, respectively. If molar absorptivities of 1.84 l/mol-cm (molecular water) and 1.65 l/mol-cm (OH) (Ihinger, oral communication) are used, this will decrease the FTIR measurements of total water content for these glasses, thus making them closer to the manometric measurements. However, the manometric measurement for sample A would then exceed the FTIR measurement.

### *5.4.2 Infrared Spectroscopy*

***Water Contents in Melt Inclusions*** - Melt inclusions in samples D and I both have much lower total water content than the glasses (total water = 0.3 and 0.7 wt%, respectively). Because the samples were thin, the speciation was not measurable, but the water is presumed to be almost entirely OH, as this is the normal situation in glasses with such low $H_2O$ contents (e.g., Stolper, 1982a). This should represent the water content of the magma when the phenocrysts

were formed. Thus, the much higher water concentrations in the glassy pumices must have been attained later.

*Temperatures Inferred from Speciation* - Stolper and his coworkers (Stolper, 1989; Silver et al., 1990; Zhang et al., 1991) investigated the temperature dependence of water species concentrations in hydrous glasses between 400°C and 900°C. Stolper (1989) found that the temperature dependence of water species could be described in thermodynamic terms with a regular-solution formulation for the interaction between molecular water, hydroxyl groups and oxygen in the rhyolite glass or melt. The model is based on the reaction:

$$H_2O + O <=> 2OH$$

A simplified equation which describes the regular solution model is:

$$\ln K = A + (B + C[H_2O] + D[OH])/T$$

where K (= $[OH]^2/\{[H_2O][O]\}$ at equilibrium) is the equilibrium constant; T is the temperature in K; and A, B, C and D are parameters of the regular solution model. The most recent published fit of equilibrium data to this model is that of Zhang et al. (1991), who obtain parameter values of: $A = -1.409 \pm 0.166$ ($2\sigma$ error); $B = -2816 \pm 118$; $C = -4448 \pm 2748$; and $D = -2721 \pm 3190$. The standard-state enthalpy of the reaction change is $\Delta H_r^o = -BR = -23.4 \pm 1.0$ kJ/mol where R is the gas constant.

On Fig. 5.4, our data is plotted together with speciation equilibration isotherms based on the model and data of Stolper and his coworkers. The Chegem melt inclusion data cannot be plotted precisely on the diagram because their total water content was calculated assuming a species distribution (almost entirely OH). However, a range of possible values can be plotted (Fig. 5.4). The glassy pumice data plot between the 200°C and the 300°C isotherms, with a slight trend toward higher temperature with increasing total water content. If this

water was present in the melt at magmatic temperatures (before eruption), species equilibration temperatures of 200-300°C would be difficult to explain: they require very slow cooling rates, atypical of volcanic rocks. However, it is likely that the intracaldera tuffs have been hydrated after equilibration. Hydration at low temperature adds molecular water, moving samples away from the vertical axis on this plot, toward lower apparent temperatures. Hydration of a glass with water contents similar to the melt inclusions could produce species concentrations similar to the glassy pumice data. Thus, the water speciation in the glassy pumices is almost certainly a post-magmatic phenomenon and was probably produced when the glasses were hydrated at temperatures of 300°C or less.

### *5.4.3 Stable Isotopes*

***Isotopic Composition of Local Meteoric Water*** - The Chegem River water which was analyzed was collected in the summer of 1991 from the southwest side of the Chegem caldera at an elevation of 2200m (Fig. 5.2a), several kilometers downstream from a glacier which feeds the river. Its $\delta D$ value of –89 corresponds to a $\delta^{18}O$ value of approximately –12, assuming that it lies on the meteoric water line of Craig (1961). This river water is a combination of groundwater, glacial meltwater, local precipitation and runoff from higher altitudes. If the dominant source of water is the local groundwater, then it is not likely to fluctuate much through the year, but if the local precipitation dominates, then the hydrogen isotopic composition of the river water may vary by tens of per mil (Fritz, 1981). Usually, in the summer, the $\delta D$ of the river water is heavy relative to the rest of the year because precipitation which falls during warmer periods is isotopically heavier. However, in this particular situation, a higher proportion of glacial meltwater is added to the river during the summer. The

glacial meltwater is slightly depleted in deuterium relative to the glacier ice, though this is a relatively small effect. Altitude has a more significant effect on the local precipitation, especially at Chegem, where there is considerable topographic relief. $\delta D$ of precipitation decreases with altitude, typically with gradients between 1.5 and 4 per mil/100m (Yurtsever and Gat, 1981). For 2 km of relief, this corresponds to an overall range of 30 to 80 per mil. Thus, it is possible that the local precipitation varies by as much as 100 per mil or more about the measured river water value (e.g., a range of $\delta D$ from –60 to –160). The local groundwater will tend to have a much narrower range of values because of the averaging effects of the groundwater reservoir (Gat, 1981). In the following discussion, we will assume that the local meteoric water has $\delta D$ values ranging from –70 to –110 and $\delta^{18}O$ ranging from –10 to –14.

*Sample Heterogeneity* - Multiple analyses of glasses picked from single hand samples have yielded both oxygen and hydrogen isotopic values which do not agree within the precisions of the techniques. This is most pronounced in the dacitic samples. For the marginal vitrophyre (M), three oxygen isotope values are analytically indistinguishable. The oxygen analyses were on two large pumices, one of which was used for all of the hydrogen analyses. The three hydrogen isotope values have a range of 6 per mil, only 2 per mil larger than the $2\sigma$ of Ihinger (1991). The glasses from the dacites, on the other hand, have ranges in $\delta^{18}O$ of 1.1 per mil (sample D, n=2) and in $\delta D$ of 12 and 8 per mil (sample A, n=3 and sample C, n=2, respectively), well outside of the analytical precisions of 0.15 per mil (oxygen) and 2 per mil (hydrogen). In these samples, glasses come from multiple pumices. Possible explanations for these large ranges are:
*(1) Incomplete extractions* - This does not seem likely for oxygen because all of the yields for these samples were comparable and glasses should break down very

easily with the fluorination technique used. As stated earlier, we believe that the water was fully extracted for hydrogen isotope analysis. *(2) Impurities in separated glass* - This possibility could partly explain the range in $\delta^{18}O$ observed for sample D because any phenocryst fragments attached to the glass have considerably higher isotopic values. However, even if one of the separates was only 90% pure, this would not result in the observed 1.1 per mil shift in $\delta^{18}O$. Impurities in the glass separate are less likely to effect the hydrogen isotopic values because the phenocrysts contain little, if any, water. *(3) Memory effect* - This would not explain the variability in $\delta^{18}O$, but might, as described earlier, contribute slightly to the variabilities in $\delta D$. *(4) Sample heterogeneity* - Since the glass separates from the dacites come from multiple pumices, it is possible that these pumices had different isotopic compositions. In fact, there is considerable heterogeneity in whole rock $\delta^{18}O$ on meter-scale (Chapter 4). If, as we believe, these $\delta^{18}O$ variations are due to interaction with meteoric water after deposition, one would expect a certain degree of heterogeneity caused by variabilities in permeability in the flow system. Thus, it seems likely that at least some of the observed spreads in $\delta^{18}O$ and $\delta D$ of these glasses is due to sample heterogeneity. This is supported by the observation that replicate analyses of M, from one pumice fragment, show much better reproducibility than those for samples from multiple fragments.

***Effects of Low-temperature Hydration*** - Rhyolite glasses are not stable under ambient conditions, and they will readily hydrate at low temperatures. Hydration rinds grow rapidly at rates on the order of 1-10$\mu^2$/1000yrs and their thicknesses can be used for dating of archeological artifacts (Friedman and Smith, 1960). Low temperature hydration is common in glasses older than a few

thousand years. Thus, it is not unreasonable to expect that glassy pumices from 2.8 Ma intracaldera tuff have been hydrated.

The effects of low temperature hydration on oxygen and hydrogen isotopes has been documented with the study of natural samples (Taylor, 1968; Friedman and Smith, 1958; Cerling et al., 1985). Taylor (1968) observed a correlation between the D/H and $^{18}O/^{16}O$ ratios in hydrated obsidians and perlites and in the local meteoric water. The $^{18}O$ content of the glasses were about 25 per mil higher than the local water, the result of not only hydration, but of thorough and intimate isotopic exchange between the external water reservoir and the glass. Cerling et al. (1985) also observed $^{18}O$ enrichments of at least 23 per mil relative to local meteoric water in East African glasses. Presumably this is the (metastable?) equilibrium $^{18}O/^{16}O$ fractionation between water and glass at T≈25°C. Hydrogen isotopes in hydrated glasses can also be correlated with the isotopic composition of the local meteoric water, as observed by Friedman and Smith (1958). They found that the D/H ratio of water in the perlites approximately 35 to 40 per mil lower than the local groundwater, fractionations which were later confirmed by Taylor (1968).

According to the fractionation factors of Friedman and Smith (1958) and Taylor (1968), isotopic compositions of hydrated glasses that have "equilibrated" with the meteoric water fall along a line on a $\delta^{18}O$-$\delta D$ plot which is roughly parallel to the Meteoric Water Line ($\delta D = 8\ \delta^{18}O + 10$; Craig, 1961). The equation for this line is $\delta D = 7.54\ \delta^{18}O - 210$ (Taylor, 1968; Muehlenbachs, 1987), nearly identical to the "kaolinite line" of Savin and Epstein (1970), whose equation is $\delta D = 7.6\ \delta^{18}O - 220$. If hydrated Chegem glasses "equilibrated" at about 25°C with the local meteoric water (with the range of isotopic compositions given above), they should fall near that line, with isotopic compositions of $\delta D = -105$ to $-145$ and $\delta^{18}O = +13$ to $+9$. However, if they have not thoroughly equilibrated,

their isotopic compositions should lie somewhere between their magmatic values and these hydrated values. Magmatic $\delta^{18}O$ values for these rocks are +7.0 to +8.5 (Chapter 4). The magmatic $\delta D$ value is not known, but it is expected to fall within the range of values for most igneous rocks ($\delta D = -50$ to $-95$; Taylor and Sheppard, 1986).

Fig. 5.5 is a $\delta^{18}O$-$\delta D$ plot illustrating the position of the Chegem glass data relative to the magmatic values and to the hydration values expected at Earth surface temperatures. The meteoric water line and "hydrated glass line" are also shown. The hydrogen isotope values can be explained by low-temperature hydration with either incomplete equilibration or exchange with water with a slightly different range of $\delta D$ than predicted ($\delta D = -60$ to $-90$). The oxygen data, however, cannot be entirely explained by such low-temperature hydration. The $\delta^{18}O$ values below +7 require either a higher temperature of exchange or a much lighter water ($\delta^{18}O < -23$, $\delta D < -175$). It is likely that the event which caused these low $\delta^{18}O$ values occurred before the glasses became hydrated at low temperature. This event is probably the same event which formed the low-$^{18}O$ zone in the upper part of the caldera fill (discussed in Chapter 4).

*Variation in $\delta D$ with Altitude* - The hydrogen isotope and FTIR data can be regarded in the framework of the oxygen isotope profile vs. altitude (Fig. 5.6); note that there is a rough correlation between $\delta D$ and altitude. The uppermost sample, A, which has the highest $\delta^{18}O$ value and a relatively high water content, has the lowest $\delta D(\approx -120)$. The next samples below that (B, C, D) have lower water contents and also display an intermediate isotopic composition ($\delta D \approx -115$). The marginal vitrophyre at the base of the exposed section has the highest $\delta D$ ($\approx -102$). It appears that the uppermost dacite has been hydrated more thoroughly than the other dacites, perhaps accounting for the $\delta D$ shift to a more

negative value. The difference in δD between sample A at 3430m and sample M at 2060m represents a D/H gradient of 1.5 per mil/100m, a typical gradient for precipitation with altitude. This suggests again that the glass δD values are controlled in part by the local precipitation. If the glass δD values represent full equilibration with the local meteoric precipitation, then the δD values for the precipitation would have to have been about –65 to –90, which is lower than our *a priori* estimated values.

### 5.5 Conclusion

1. Glassy pumices, collected from the upper 100m and from the lower margin of the Chegem intracaldera fill sequence, and melt inclusions in phenocrysts from two samples, collected from near the top and the middle of the sequence, were analyzed for water content and speciation by infrared spectroscopy. The total water content of the glassy pumices ranged from 3.4 to 4.8 wt%, while the melt inclusions only had 0.3 to 0.7 wt% total water. This evidence indicates that the water in the glassy pumices was not in the magma at the time that the phenocrysts were crystallized.

2. The water in the glassy pumices is made up of 2.9 to 4.0 wt% molecular water and 0.6 to 0.9 wt% hydroxyl groups (OH). This species distribution corresponds to temperatures of species equilibration between 200° and 300°C. Quenching these species equilibration temperatures would require abnormally slow cooling rates for volcanic rocks. However, the observed speciation could also be produced by low temperature hydration of $H_2O$-poor glasses, such as the glasses which formed the melt inclusions.

3. Hydrogen isotopic analyses of glassy pumices yielded δD between –99 and –124. Oxygen isotopic compositions of the same glasses range from $\delta^{18}O$ = +1.4 to +9.1. Glasses from individual hand samples appear to be fairly heterogeneous isotopically, probably due the fact that glasses from multiple pumices were analyzed. On a δD-$\delta^{18}O$ plot (Fig. 5.5), these glasses do not plot in the region predicted for glasses hydrated by Chegem meteoric water. However, the δD values do lie between the magmatic values and the predicted hydrated glass values. Some of the $\delta^{18}O$ values, on the other hand, do not fall between the magmatic values and the predicted hydrated glass values. Therefore, the hydrogen isotopic compositions of these glasses can be explained by low temperature hydration with incomplete equilibration. The oxygen isotope values are best explained by high temperature hydration during the hydrothermal event described in Chapter 4.

**Table 5.1** Glass sample descriptions

| Sample | other #'s | Elevation | Location | Rock Description | Glass Description |
|---|---|---|---|---|---|
| A | CG-C-44L<br>90L-107L | 3430m | top of caldera fill on SE side, near Mt. Kum Tyube | light brown dacitic tuff, partial vitrophyre | dark grey glassy pumices <1cm long, some perlitic cracks, esp. at edges of pumices, ≈10% phenocrysts |
| B | CG-C2-67D | 3495m | dacitic horizons, SW of Mt. Kum Tyube | grey dacitic tuff | black glassy pumices <1cm long, banded (darker zones of iron oxides?), many small, opaque microlites ≈7% phenocrysts, some spherulites at edges of pumices and near phenocrysts |
| C | CG-C2-67G | 3415m | dacitic horizons, SW of Mt. Kum Tyube | light grey dacitic tuff | black glassy pumices <2cm long, banded, many small opaque microlites 15-20% phenocrysts |
| D | CG-C-44J<br>90L-107J | 3410m | dacitic horizons, east of Mt. Kum Tyube | dark grey dacitic tuff, partial vitrophyre | dark grey glassy pumices ≈1 cm long, appear interconnected, banded, perlitic cracks, ≈10% phenocrysts some spherulites between phenocrysts, also melt inclusions in quartz |
| I | CG-C2-4F | 3225m | on ridge east of Mt. Kum Tyube | grey devitrified rhyolite tuff, no glassy pumices | glass inclusions in quartz and feldspar |
| M | CG-C2-1<br>KH91-01<br>CG-C-20<br>90L-105 | 2060m | from slide block near Chegem river on S side of caldera, below lowest intracaldera tuff exposure | black vitrophyric rhyolite tuff, lithic-rich | black glassy pumices, up to 4cm, lower compaction ratio (<2:1), <5% phenocrysts, mostly resorbed quartz, glass is very clear, no bands, cracks, or spherulites |

**Table 5.2** Major element compositions

| Sample | Elevation | $SiO_2$ | $Al_2O_3$ | $K_2O$ | $Na_2O$ | CaO | FeO | MgO | $TiO_2$ | Total |
|---|---|---|---|---|---|---|---|---|---|---|
| A-glass | 3430m | 75.0 | 12.6 | 5.1 | 3.0 | 0.7 | 0.2 | 0.04 | 0.1 | 96.7 |
| whole rock* | 3430m | 69.4 | 15.7 | 3.1 | 3.8 | 3.4 | 2.9 | 1.1 | 0.5 | 99.9 |
| B-glass | 3495m | 73.9 | 12.5 | 6.3 | 2.9 | 0.3 | 0.2 | 0.05 | 0.2 | 96.4 |
| C-glass | 3415m | 75.5 | 12.7 | 6.0 | 2.8 | 0.5 | 0.3 | 0.01 | 0.1 | 97.9 |
| D-glass | 3410m | 73.6 | 12.9 | 5.7 | 2.8 | 0.7 | 0.6 | 0.1 | 0.2 | 96.6 |
| whole rock* | 3410m | 70.1 | 15.6 | 3.3 | 4.2 | 2.6 | 2.7 | 1.0 | 0.5 | 100.0 |
| M-glass | 2060m | 73.4 | 12.5 | 4.3 | 3.5 | 0.7 | 0.6 | 0.1 | 0.2 | 95.3 |
| whole rock* | 2060m | 74.4 | 13.1 | 4.4 | 4.0 | 2.1 | 1.1 | 0.7 | 0.1 | 99.9 |

* whole rock measurements include glassy pumices, phenocrysts and devitrified groundmass

**Table 5.3** Heating schedule for water-rich rhyolite glasses used to prevent formation of bubbles at high temperature on extraction line

| ≈Temperautre | Variac Setting | | Duration |
|---|---|---|---|
| 200°C | 15 | for | 3-4 hours |
| 250°C | 16 | for | 3-4 hours |
| 350°C | 17 | for | 10-12 hours (overnight) |
| 500°C | 20 | for | 30 minutes |
| 650°C | 25 | for | 30 minutes |
| 750°C | 28 | for | 5 minutes |
| 850°C | 32 | for | 3-5 hours |
| 900°C | 35 | for | 5 minutes |
| 1000°C | 40 | for | 5 minutes |
| 1100°C | 45 | for | 5 minutes |
| 1200°C | 51 | for | 2 hours |
| Total | | | 23-29 hours |

**Table 5.4** Extraction line blanks and standard measurements

| Sample** | total time (hours) | lowT $CO_2$* (μmoles) | highT $CO_2$ (μmoles) | total $CO_2$ (μmoles) | lowT $H_2O$* (μmoles) | highT $H_2O$ (μmoles) | total $H_2O$ (μmoles) | δD ‰SMOW | HF soak? |
|---|---|---|---|---|---|---|---|---|---|
| CG-BLANK-1 | 19.8 | | | 8.26 | | | 6.54 | –64.8 | HF |
| CG-BLANK-2 | 26.3 | | | 1.52 | | | 4.95 | | no |
| CG-BLANK-3 | 22.0 | | | 1.68 | | | 4.80 | –144.3 | no |
| I-BLANK-1 | 4.4 | | | NS | 0.11 | 2.93 | 3.04 | | HF |
| I-BLANK-2 | 7.9 | 0.3 | 0.3 | 0.6 | 3.48 | 8.12 | 11.60 | | HF |
| I-BLANK-3 | 7.9 | 0.1 | 1.0 | 1.1 | 1.95 | 5.46 | 7.41 | | HF |
| I-BLANK-4 | 7.3 | | | | 0.33 | 2.74 | 3.07 | | no |
| I-BLANK-5 | 6.2 | | | NS | | | 7.10 | | HF |
| I-BLANK-6 | 10.9 | | | NS | | | 4.49 | –130.0 | no |
| I-BLANK-7 | 48.9 | | | NS | | | 6.58 | –120.0 | no |
| I-BLANK-8 | 4.6 | 0.25 | 1.70 | 1.95 | 1.13 | 2.97 | 4.10 | –111.0 | no |
| I-BLANK-9 | 32.8 | | | 1.94 | | | 8.50 | –117.2 | no |
| I-BLANK-10 | 0.8 | | | 1.07 | | | 4.68 | | no |
| D-BLANK-1 | 13.6 | | | | 0.70 | 7.10 | 7.80 | | HF |
| D-BLANK-2 | 7.7 | | | | 1.60 | 6.50 | 8.10 | | HF |
| D-BLANK-3 | 7.6 | | | | 0.80 | 4.50 | 5.30 | | HF |
| standards | | mass (g) | | | | | | | |
| CG-PYRO-1 | 2.3 | 24.6 | | 1.93 | | | 67.52 | –29.3 | no |
| CG-PYRO-2 | 3.8 | 24.4 | | 2.64 | | | 66.49 | –38.5 | no |
| CG-PYRO-3 | 4.6 | 23.0 | | 2.64 | | | 63.92 | –38.0 | no |

**CG-blanks from this study; I-blanks from Ihinger (1991); D-blanks from Dobson et al. (1989);
CG-PYRO-laboratory pyrophyllite standard
* lowT≈200° to 300°C, high T≈700° to 1200°C; lowT $CO_2$ and lowT $H_2O$ include
midT (≈300° to 700°C) $CO_2$ and midT $H_2O$ of Ihinger (1991)

**Table 5.5** Speciation of water in Chegem glasses (determined by infrared spectroscopy)

| Sample | Chip # | Thickness (microns) | Abs (5200) | Abs (4500) | Abs (3600) | $H_2O$mol (5200)* | OH (4500)* | $H_2O$total* |
|---|---|---|---|---|---|---|---|---|
| A | 1 | 115 | 0.076 | 0.0224 | | 3.15 | 0.86 | 4.0 |
| A | 2 | 110 | 0.0702 | 0.0179 | | 3.04 | 0.72 | 3.8 |
| B | 4 | 101 | 0.0588 | 0.0134 | | 2.77 | 0.59 | 3.4 |
| C | 1 | 68 | 0.0392 | 0.0096 | | 2.74 | 0.63 | 3.4 |
| C | 1 | 68 | 0.0396 | 0.0096 | | 2.77 | 0.63 | 3.4 |
| C | 1 | 68 | 0.0394 | 0.0086 | | 2.76 | 0.56 | 3.3 |
| D | 3 | 97 | 0.0591 | 0.0150 | | 2.9 | 0.69 | 3.6 |
| D | 5 | 93 | 0.058 | 0.0148 | | 2.97 | 0.71 | 3.7 |
| M | 1 | 160 | 0.1344 | 0.0284 | | 4.0 | 0.8 | 4.8 |
| D-inclusion in feldspar | | 14 | | | 0.1092 | | | 0.67 |
| I-inclusions in quartz | | 15 | | | 0.0627 | | | 0.36 |
| | | 27 | | | 0.0957 | | | 0.31 |

*molecular water and hydroxyl (OH) concentrations are calculated from the 5200cm$^{-1}$ and 4500cm$^{-1}$ absorptions, based on molar absorptivities of 1.61 $\ell$/mol-cm and 1.73 $\ell$/mol-cm, respectively. Total water concentrations for the glass chips are the sum of the molecular water and hydroxyl concentrations. For melt inclusions in phenocrysts, total water concentrations are calculated from the 3550cm$^{-1}$ absorption, using an absorption coefficient of 89 $\ell$/mol-cm for hydroxyl groups (assuming that the total water is made up almost entirely of hydroxyl groups).

**Table 5.6** Oxygen Isotope Results

| **Sample** | **$\delta^{18}O_{wr}$** | **mass glass (mg)*** | **yield glass ($\mu moles O_2/mg$)** | **$\delta^{18}O_{glass}$** |
|---|---|---|---|---|
| A | 9.5 | 10.4 (mp) | 14.5 | 7.9 |
| B | 5.9 | 18.1(mp) | 14.4 | 4.8 |
| C | 8.6 | 25.1(mp) | 15.3 | 6.8 |
| D | 4.4,4.6 | 15.6(mp) | 15.3 | 1.4 |
| | | 8.7(mp) | 15.9 | 2.5 |
| I | -0.5 | | | |
| M(CG-C2-1) | 9.7 | 22.1(sp) | 15.6 | 9.1 |
| M(KH91-01BP) | | 20.9(sp) | 12.6 (spilled?) | 9.0 |
| | | 14.7(sp) | 14.8 | 8.8 |

*mp-glass from multiple pumices; sp-glass from single pumice

**Table 5.7** Hydrogen Isotope Results

| Sample | mass (mg) | Extraction time (hrs) | $CO_2$ (μmoles) | $CO_2$(bc*) (μmoles) | $H_2O$ (μmoles) | $H_2O$(bc) (μmoles) | $H_2O$ (wt%) | $H_2O$(bc) (wt%) | δD (‰ SMOW) | δD(bc) (‰ SMOW) |
|---|---|---|---|---|---|---|---|---|---|---|
| A(1) | 18.39 | 26.1 | 5.72 | 4.04 | 44.21 | 39.34 | 4.33 | 3.85 | -124.9 | -124 |
| A(2) | 16.00 | 24.9 | 4.08 | 2.40 | 21.92 | 17.05 | 2.47 | 1.92 | -125.7 | -124 |
| A(3) | 22.34 | 24.2 | 5.75 | 4.07 | 52.58 | 47.71 | 4.24 | 3.85 | -113.8 | -112 |
| B | 26.87 | 29.2 | 5.83 | 4.15 | 45.92 | 41.05 | 3.08 | 2.75 | -109.8 | -107 |
| C(1) | 28.85 | 25.5 | 4.15 | 2.47 | 47.49 | 42.62 | 2.97 | 2.66 | -117.9 | -117 |
| C(2) | 24.58 | 26.7 | 3.53 | 1.85 | 44.53 | 39.66 | 3.26 | 2.91 | -111.7 | -109 |
| D | 21.99 | 35.0 | 3.11 | 1.43 | 41.74 | 36.87 | 3.42 | 3.02 | -117.8 | -116 |
| M(1) | 41.78 | 23.7 | 4.26 | 2.58 | 105.3 | 100.39 | 4.54 | 4.33 | -100.3 | -99 |
| M(2) | 23.64 | 23.9 | 3.19 | 1.51 | 60.5 | 55.63 | 4.61 | 4.24 | -106.6 | -105 |
| M(3) | 26.93 | 25.3 | 3.91 | 2.23 | 64.2 | 59.33 | 4.3 | 3.97 | -101.3 | -99 |
| Chegem River water | | | | | | | | | -89 | |

* bc-corrected for blank of 4.9 μmoles of $H_2O$ with δD=–130‰

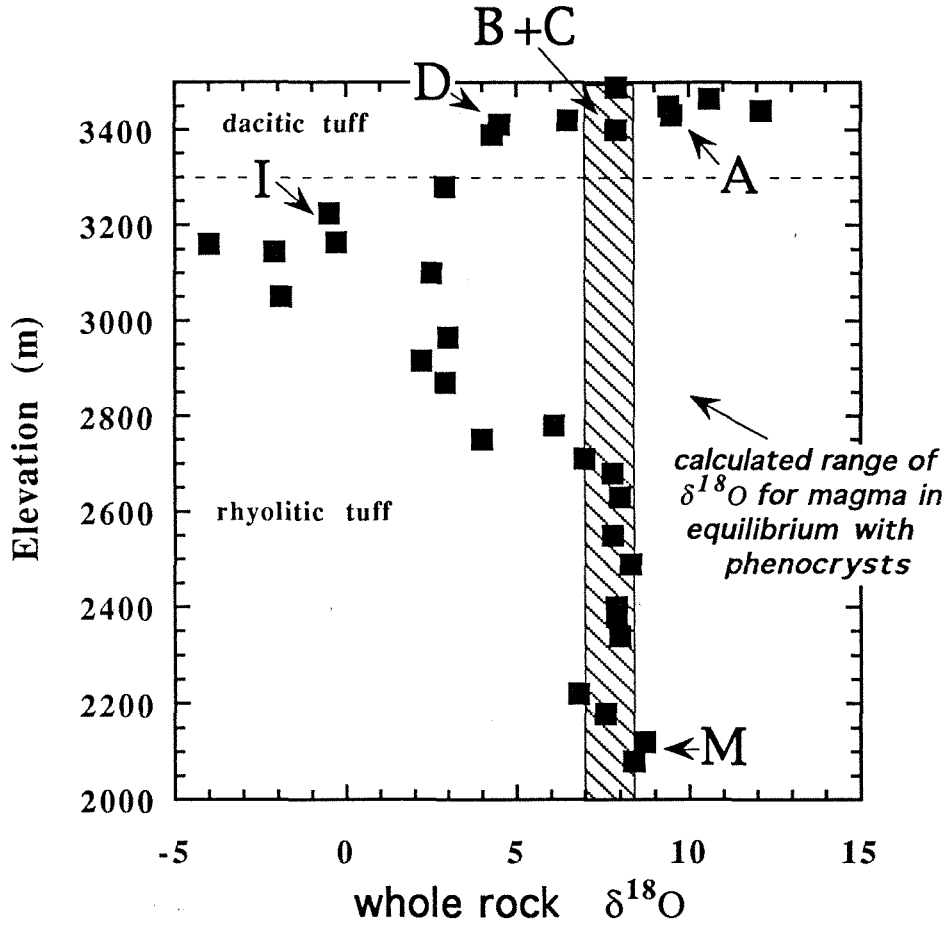


**Figure 5.1** -- Stratigraphic positions of samples studied relative to the oxygen isotope trends described in Chapter 4. Black squares - measured whole-rock oxygen isotopic compositions for samples from the stratigraphic section on the SE side of the Chegem caldera (Section 1); diagonally-ruled region - calculated range of $\delta^{18}O$ for magma in equilibrium with phenocrysts (described in Chapter 4); horizontal dashed line - gradational boundary between rhyolitic and dacitic tuffs; A, B, C, D - dacitic tuff samples with glassy pumices; I - devitrified tuff (no glassy pumices) with melt inclusions in phenocrysts; M - marginal vitrophyre with glassy pumices.

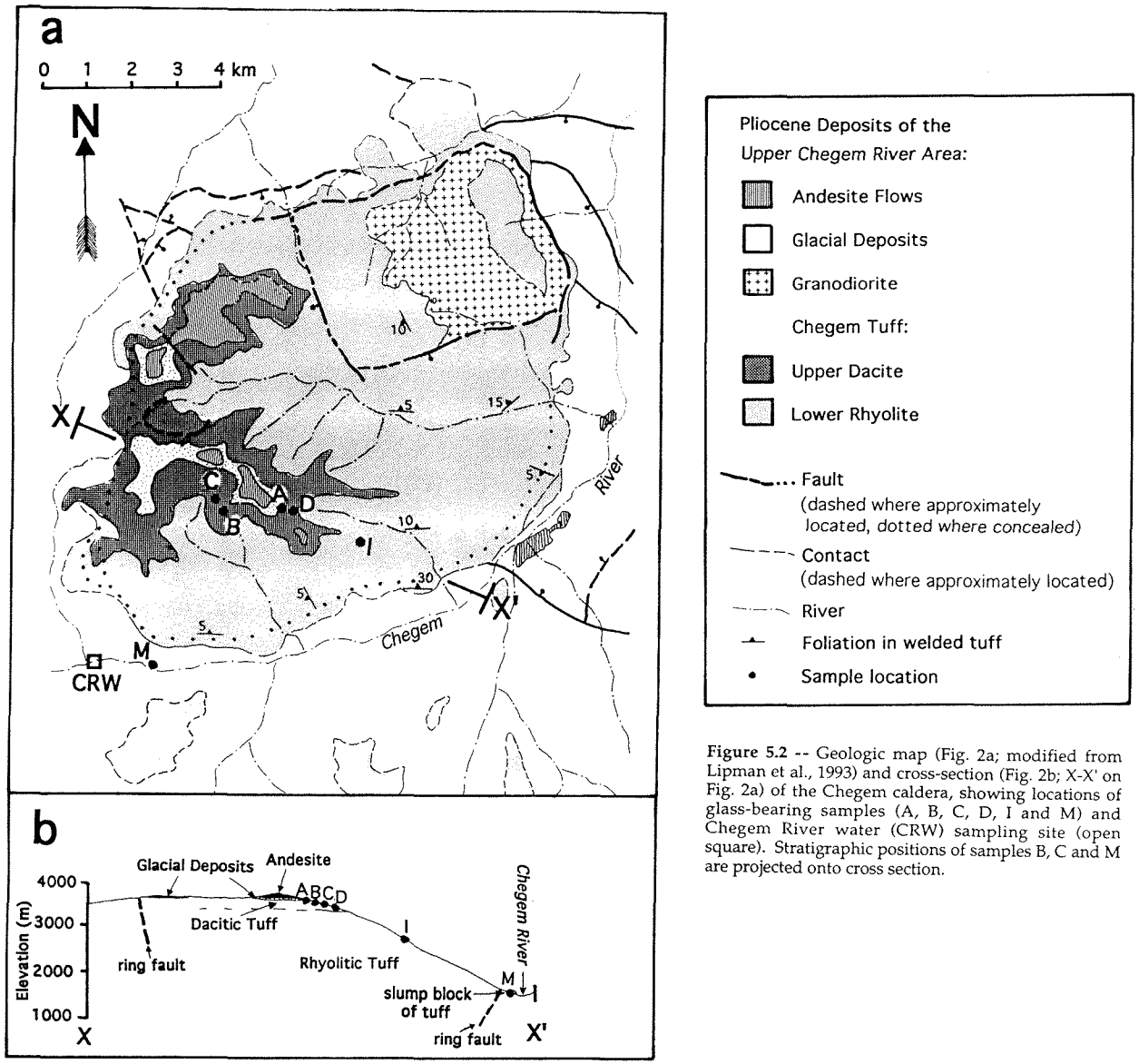


**Figure 5.2** -- Geologic map (Fig. 2a; modified from Lipman et al., 1993) and cross-section (Fig. 2b; X-X' on Fig. 2a) of the Chegem caldera, showing locations of glass-bearing samples (A, B, C, D, I and M) and Chegem River water (CRW) sampling site (open square). Stratigraphic positions of samples B, C and M are projected onto cross section.

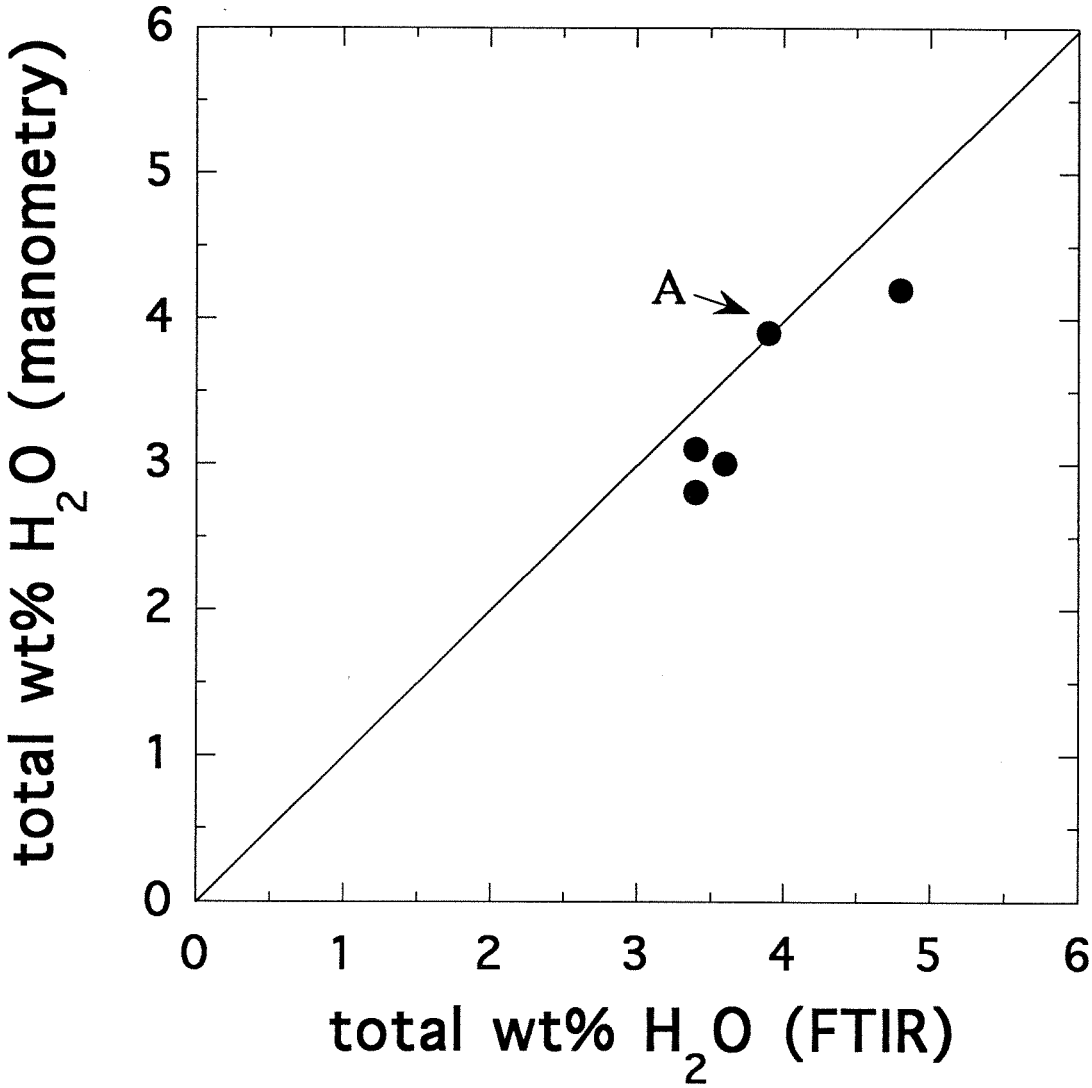


**Figure 5.3** -- Comparison of total water contents measured by vacuum extraction and manometry (vertical axis) and by infrared spectroscopy (FTIR, horizontal axis). In general, the manometric measurement is ≈15% lower than the FTIR measurement, except for sample A (labelled).

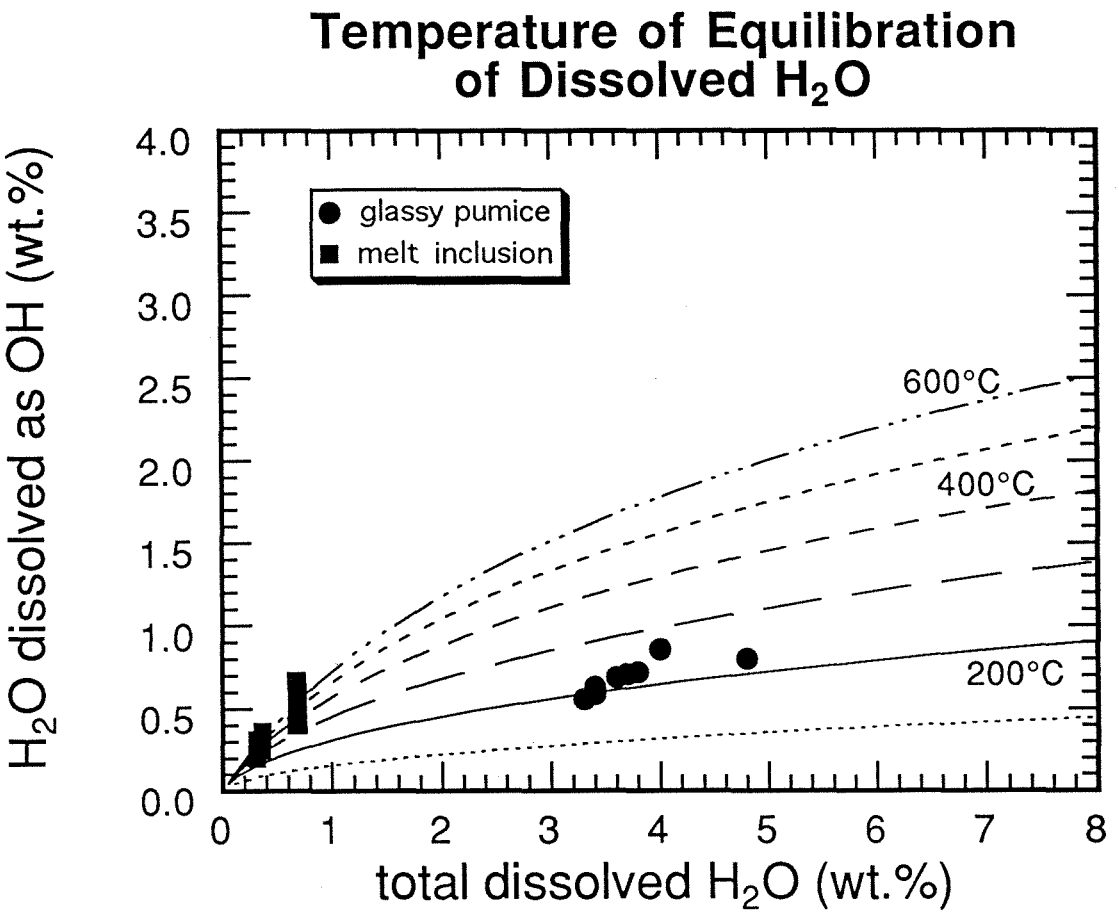


**Figure 5.4** -- The concentrations of dissolved water species in Chegem glassy pumices and melt inclusions plotted as $H_2O$ dissolved as OH vs. total dissolved $H_2O$ (determined by infrared spectroscopy). Isotherms are calculated temperatures of species equilibration based on the models of Stolper (1989) and Zhang et al. (1991), which are described in the text. Black circles - glassy pumices; black bars - melt inclusions.

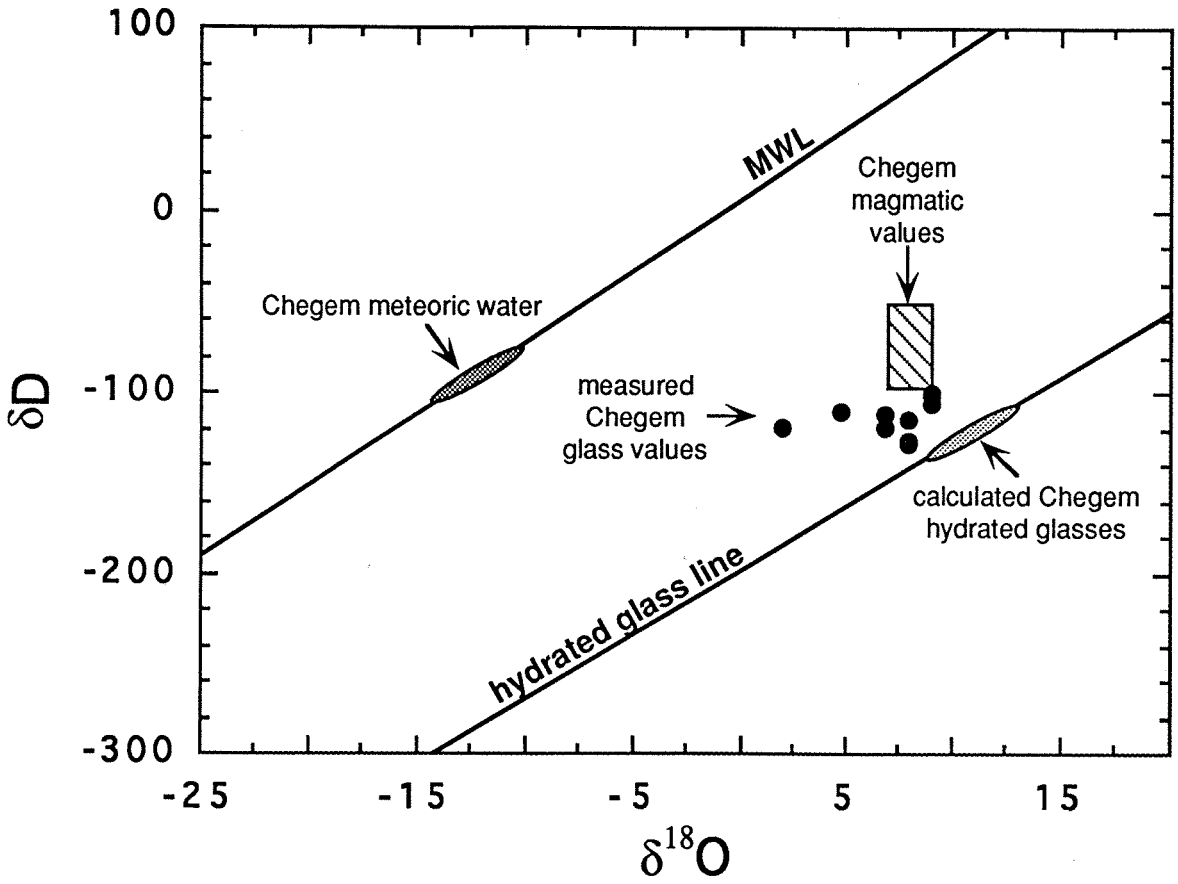


**Figure 5.5** -- $\delta D$-$\delta^{18}O$ plot showing Chegem glass data (black circles); meteoric water line (MWL, $\delta D = 8\ \delta^{18}O + 10$; Craig, 1961); "hydrated glass line" ($\delta D = 7.54\ \delta^{18}O - 210$; Taylor, 1968); estimated range of Chegem meteoric water (dark stippled zone); calculated range for Chegem glasses which have been hydrated and isotopically equilibrated at low temperature with Chegem meteoric water (dark stippled zone); and the range of Chegem magmatic values (diagonally-ruled box).

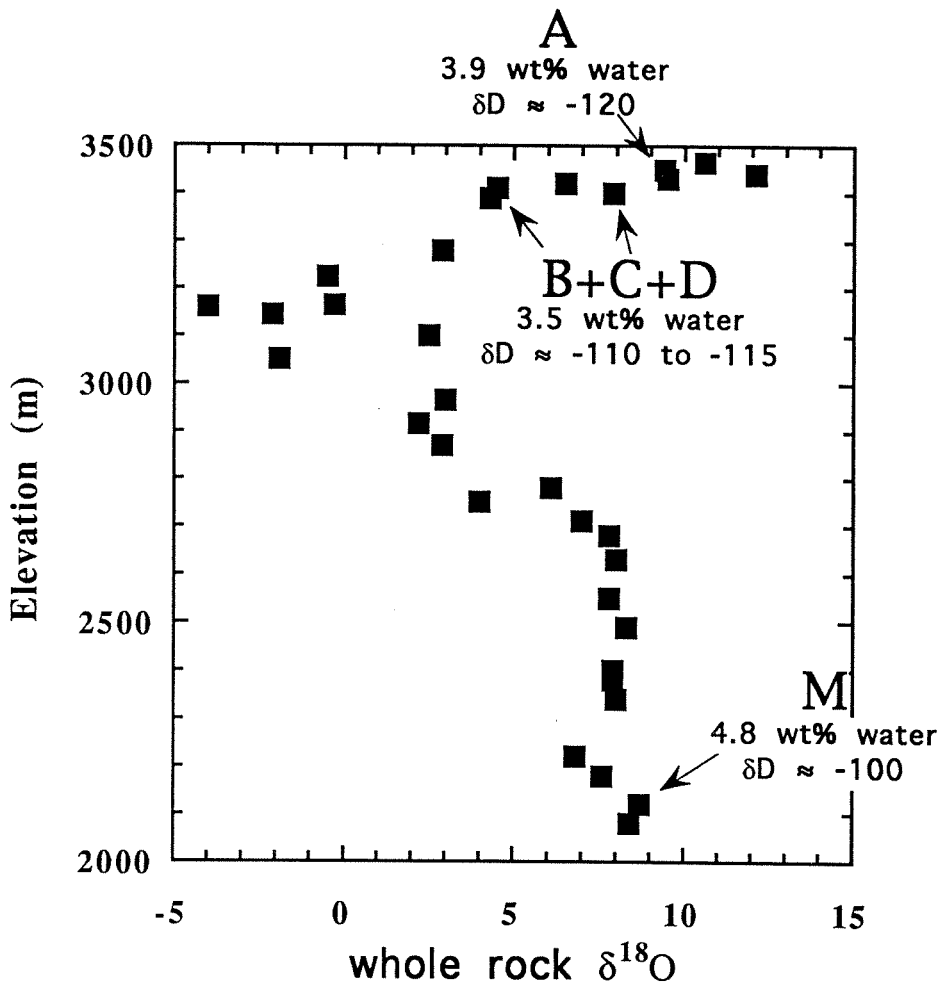


**Figure 5.6** -- Approximate total water contents and hydrogen isotopic compositions of glassy pumices shown together with stratigraphic oxygen isotope trends (whole rock) of Figure 1.

# Chapter 6. Rubidium/Strontium Isotopic Studies of the Chegem Igneous Rocks and the Eldjurta Granite: Petrogenetic and Hydrothermal Signatures

## 6.1 Introduction

The strontium isotopic compositions of volcanic rocks provide information about the sources from which the magmas originated and about the processes which modified their chemical and isotopic compositions, both before and after eruption. Because $^{87}Rb$ decays to $^{87}Sr$, different source materials can be characterized by their strontium isotopic composition if they have different Rb/Sr ratios and have existed separately for a sufficiently long period of time. Crustal rocks tend to have higher $^{87}Sr/^{86}Sr$ ratios because over geologic time rubidium has fractionated into the crust more readily than strontium. Thus, for example, if a crustal rock is melted and incorporated into a mantle-derived magma, evidence for this effect should be recorded in the strontium isotopic composition of that magma. Processes of magmatic differentiation (e.g., fractional crystallization) can also affect the Sr isotopic composition of a magma,

because Sr or Rb will be fractionated preferentially by various silicate melts and rock-forming minerals. After crystallization, the Sr isotopic composition of igneous rocks can be altered by subsolidus processes like hydrothermal activity when Sr is mobilized by fluids.

In order to constrain the isotopic history of an igneous rock, Rb/Sr isotopic studies are commonly performed in conjunction with other isotopic studies such as Sm/Nd, U/Pb, or $^{18}O/^{16}O$. These isotopic studies have been utilized in the ongoing debate over the origin of large-volume, compositionally-zoned silicic magma chambers. One of the reasons for studying pyroclastic deposits, particularly those associated with calderas, is that they "freeze" a point in time in the magma differentiation process. It is commonly accepted that an ash-flow tuff sequence represents an upside-down view of the uppermost levels of the subvolcanic magma chamber immediately prior to caldera formation (e.g., Smith, 1979; Hildreth, 1981). Zoning in major and trace elements is present in many (if not all) ash-flow tuff sequences erupted from large-volume silicic magma chambers (e.g., Yellowstone, Grizzly Peak, Questa, Long Valley, Chegem). In some cases, the major- and trace- element zoning is accompanied by zoning in strontium isotopes (e.g., Timber Mountain/Oasis Valley, Farmer et al., 1991; Grizzly Peak, Johnson and Fridrich, 1990; Superstition-Superior, Stuckless and O'Neil, 1973), oxygen isotopes (e.g., Bishop Tuff, Halliday et al., 1984) and more rarely neodymium isotopes (e.g., Timber Mountain/Oasis Valley, Farmer et al., 1991). A variety of petrogenetic histories have been proposed to explain the observed isotopic trends. Most include injection of magma from the mantle or lower crust (e.g., Noble and Hedge, 1969; Halliday et al., 1984, 1989; Mahood and Halliday, 1988; Johnson et al., 1990; Farmer et al., 1991; Christensen and DePaolo, 1993; Johnson and Fridrich, 1990; Hildreth et al., 1991), followed by either assimilation of crustal rocks (e.g., Hildreth et al., 1991), fractional

crystallization (e.g., Halliday et al., 1984, 1989) or a combination of the two processes (e.g., Mahood and Halliday, 1988; Johnson et al., 1990; Johnson and Fridrich, 1990; Farmer et al., 1991; Christensen and DePaolo, 1993). Hildreth (1981), in a paper discussing compositional gradients in silicic magma chambers, pointed out that the effectiveness of various processes that differentiate magmas is not everywhere the same. He proposed that some of the zoning in rhyolitic magmas may be produced by volatile complexing and liquid state thermodiffusion (Soret diffusion plus convective circulation).

Strontium isotopic disequilibrium among phenocrysts (usually feldspar) and groundmass is common, indicating either post-eruptive interaction with Sr-bearing meteoric waters (Halliday et al., 1984) or phenocryst growth in a magma of different isotopic composition than the magma that quenched to form the groundmass. Two proposed explanations for different magmatic isotopic compositions during phenocryst growth and during eruption are: (1) assimilation of heterogeneous crustal rocks (Duffield and Ruiz, 1991; Stuckless and O'Neil, 1973); or (2) a high Rb/Sr ratio in the residual magma remaining after the phenocrysts are crystallized (Christensen and DePaolo, 1993).

Post-eruptive interaction with hydrothermal fluids can alter both the strontium and oxygen isotopic compositions of volcanic rocks (e.g., Halliday et al., 1984; Cousens et al., 1993; McCulloch et al., 1980, 1981). Usually water-rock interaction serves to raise the $^{87}Sr/^{86}Sr$ ratio of a mantle-derived igneous rock because seawater typically has a relatively high $^{87}Sr/^{86}Sr$ ratio (0.7094 at present) and meteoric waters that leach strontium from upper crustal rocks will also have high $^{87}Sr/^{86}Sr$ ratios. Therefore, when strontium and/or oxygen isotope studies are made on volcanic rocks, the extent of post-crystallization water-rock interaction must first be ascertained before conclusions about the igneous petrogenesis are drawn.

This chapter presents a strontium isotopic study of rocks associated with the Chegem caldera and the Eldjurta Granite. Strontium and rubidium concentrations and $^{87}Sr/^{86}Sr$ ratios were measured on 29 samples: 23 whole rocks and 6 mineral separates (feldspar or biotite). The oxygen-isotopic, major- and trace-element compositions are also presented for most of these samples. The purpose of this study is twofold: (1) In Chapter 4, we identified a stratigraphic zone of low-$^{18}O$ intracaldera tuff which we argue must have been produced by high-temperature interaction with meteoric water. The first aim of this Sr study is to examine the effects of this putative water/rock interaction event on the strontium isotopic systematics. In doing so, we will gain further clues about the process which produced this low-$^{18}O$ zone, as well as gaining more information about the nature of the fluids involved. (2) The second aim is to perform a reconnaissance Sr isotope study to understand the petrogenetic history of this young silicic magma system. One particular question which is of interest is: What is the relationship between the Eldjurta Granite and the Chegem volcanic and intrusive rocks? The Eldjurta Granite is exposed ten kilometers away from the Chegem caldera, and its similarity in age and composition to the Chegem volcanic and intrusive rocks has led to the suggestion that they constitute a single physically continuous magma system at shallow depth (Lipman et al., 1993).

## 6.2 Samples Studied

The geologic setting for this study is described in Chapter 2. Samples were selected to represent the range of stratigraphic levels in the intracaldera tuff and the range of igneous lithologies present in the young igneous suite. Sample locations are shown in Fig. 6.1. Nine samples were taken from the 1405-m section of intracaldera tuff on the southeast side of the caldera (Section 1). These

samples come from the three stratigraphic zones of Chapter 4 (Fig. 6.2): four from the lowermost zone (A) of "normal" igneous $\delta^{18}O$; three from the middle zone (B) of low-$^{18}O$ rocks; and two from the upper zone (C) of dacitic tuff with a range of $\delta^{18}O$ values (Fig. 6.2).

Fourteen samples represent various igneous lithologies in the Chegem magmatic system, either map units or igneous inclusions in these units: (1) a pre-caldera basalt [B] - a flow near the outflow Chegem Tuff in the lower Chegem valley; (2) Chegem Tuff - three intracaldera [I] and two outflow [O] tuffs; (3) andesite [A] - a post-caldera flow which overlies the intracaldera tuff; (4) granodiorite [GD] - the resurgent porphyry intrusion; (5) three mafic inclusions - a basalt inclusion from the post-caldera andesite flows, and two inclusions from within the granodiorite (one andesite and one diorite); (6) Eldjurta Granite [E] - one surface sample and mineral separates from two drillhole samples.

Finally, three samples were chosen to represent the country rocks of the north-central Caucasus Mountains in the region of the Chegem caldera. Two are crystalline basement: one Hercynian(?) granite [C-GR] and one Proterozoic(?) gneiss [C-GN] collected along the Chegem river 5.5 and 6 km, respectively, west of the southwestern Chegem caldera margin. The third is a Jurassic limestone [C-L], collected ≈1 km from the eastern margin of the caldera in the Dzhilgusu drainage.

The major and trace element compositions of most of these samples have been measured (Chapter 4 and K. Hon, unpublished data) and are listed in Table 6.1. $SiO_2$ contents of intracaldera tuff samples range from 69.1 to 76.2 wt%. The intracaldera porphyry intrusion (71.6 wt% $SiO_2$) and the outflow samples (73.0-74.0 wt% $SiO_2$) are intermediate in this range. All other samples are more mafic, with 54.8-62.4 wt% $SiO_2$.

## 6.3 Previous Strontium Isotopic Studies of the Eldjurta Granite

Because of its spatial association with the Tirniauz ore deposit, the Eldjurta Granite has been the subject of numerous studies, including recent strontium isotope studies by Zhuravlev and Negrey (1993, 1994) and Kostitsyn and Kremenetskiy (1994). Zhuravlev and Negrey (1993, 1994) analyzed density separates of biotite, K-feldspar and plagioclase from the Eldjurta Granite and determined an isochron age of 1.982 ± 0.008 Ma and an initial $^{87}Sr/^{86}Sr$ ratio of 0.70685 ± 3. A similar analysis of amphibole and biotite from an ore-bearing metasomatite from the Tirniauz deposit yielded an isochron age of 1.963 ± 0.0015 Ma and $^{87}Sr/^{86}Sr_i = 0.70810 \pm 15$. Kostitsyn and Kremenetskiy (1994) performed strontium and oxygen isotopic studies on 26 samples, including samples from the 4-km deep drillhole. They observed a near constant initial $^{87}Sr/^{86}Sr$ of 0.70685 in the upper 2.5 km of the granite accompanied by a whole rock $\delta^{18}O$ which decreases smoothly towards the roof of the pluton. Below ≈1.5 km depth in the drillhole, the initial $^{87}Sr/^{86}Sr$ decreases with depth from 0.70741 to 0.70673.

## 6.4 Analytical Technique

The analytical techniques used for Sr and Rb analysis are described briefly here. More details of the procedures as well as standard measurements are given in Appendix C and references therein. Whole-rock samples were ground to powder with a mortar and pestle; mineral separates of biotite and feldspar were obtained by standard magnetic and density separation techniques. Sanidines in one vitrophyric volcanic sample (90L-109-S) were washed in dilute HF to remove any glass fragments.

Between 20 and 200 mg of each sample were weighed and spiked with $^{87}Rb$ and $^{84}Sr$ solutions of known concentration. Initial dissolution was in concentrated HF + $HNO_3$, followed by one or two dissolutions in concentrated

$HNO_3$, and finally in 1.5N HCl. The acids were evaporated between each dissolution step. Variations on this dissolution procedure are described in Appendix C. The final HCl mixture was checked for complete dissolution by centrifuging to concentrate any residues.

Rb and Sr were separated according to standard cation exchange techniques, in columns filled with AG50W-X8 resin. Maximum procedural blanks are 12 pg Rb and 220 pg Sr (Pickett, 1991).

The separated Rb (2ng) and Sr (500ng) were loaded on Re and Ta filaments, respectively, and analyzed on a VG Sector multi-collector thermal ionization mass spectrometer. Rb analyses were performed on two collectors in the static mode. Sr was run multidynamically, using four collectors, but with the 84/86 ratio collected statically in two collectors. Fractionation corrections were made to the data upon collection according to the standard ratio of $^{86}Sr/^{88}Sr = 0.1194$.

Replicate analyses of nRb(AAA) and 987 Sr standards, given in Appendix C, yielded means ($1\sigma$) of $85/87 = 2.610 \pm 0.009$ and $87/86 = 0.71024 \pm 0.00002$, respectively. The standard deviations of replicate analyses of the Rb and Sr standards give a minimum estimate of the analytical uncertainties. However, because these standards are already dissolved, these uncertainties do not account for errors due to sample heterogeneity, sample dissolution, or weighing and spiking. Replicate analyses of samples (described in Appendix C) suggest that our true analytical uncertainty for $^{87}Sr/^{86}Sr$ is $\approx 0.00005$. The isotope dilution determinations of Rb and Sr concentrations have an uncertainty of $\pm 1\%$. A comparison of the Rb and Sr concentrations in this study and those determined by XRF is given in Appendix C.

In some of the discussion which follows, the ε-notation is used for Nd and Sr. This notation is analogous to the δ-notation for oxygen:

$$\varepsilon_{Nd} = \left[ \frac{(^{143}Nd/^{144}Nd)^{T}_{init}}{(^{143}Nd/^{144}Nd)^{T}_{CHUR}} - 1 \right] \times 10^{4} \quad \text{and} \quad \varepsilon_{Sr} = \left[ \frac{(^{87}Sr/^{86}Sr)^{T}_{init}}{(^{87}Sr/^{86}Sr)^{T}_{UR}} - 1 \right] \times 10^{4}$$

where $(^{143}Nd/^{144}Nd)^{T}_{init}$ and $(^{87}Sr/^{86}Sr)^{T}_{init}$ are the measured ratios corrected for decay from the time of crystallization T and $(^{143}Nd/^{144}Nd)^{T}_{CHUR}$ and $(^{87}Sr/^{86}Sr)^{T}_{UR}$ are the ratios at time T in the standard reservoirs described by DePaolo and Wasserburg (1976).

## 6.5 Results

Measured $^{87}Sr/^{86}Sr$ ratios, and Rb and Sr concentrations, determined by isotope dilution and XRF (in parentheses), are presented in Table 6.2. Also listed are $^{87}Rb/^{86}Sr$ (based on the measured $^{87}Sr/^{86}Sr$ and the isotope dilution determinations of Rb and Sr contents), calculated initial $^{87}Sr/^{86}Sr$ ($^{87}Sr/^{86}Sr_i$, based on $^{40}Ar/^{39}Ar$ ages in Chapter 3), and whole-rock oxygen isotopic compositions (Chapter 4). Initial $^{87}Sr/^{86}Sr$ for Chegem Tuff, both intracaldera and outflow, range from 0.7055 to 0.7076. The post-caldera granodiorite porphyry intrusion and andesite flows (both with $^{87}Sr/^{86}Sr_i = 0.7056$) also falls in this range. The pre-caldera basalt flow and three mafic inclusions have $^{87}Sr/^{86}Sr_i$ from 0.7046 to 0.7051 while the initial $^{87}Sr/^{86}Sr$ ratio of the surface Eldjurta Granite sample is 0.7068. The $^{87}Sr/^{86}Sr$ ratios of the three country rocks are 0.7071, 0.7135 and 0.7320 for the limestone, granite and gneiss, respectively.

## 6.6 Discussion

### *6.6.1 Intracaldera Isotopic Trends*

***The Effects of Interaction with Meteoric Waters*** -- Before discussing the petrogenetic implications of the strontium isotopic data, it is necessary to assess the extent to which this data is affected by sub-solidus interaction with fluids. In the case of the Chegem caldera, we have established with oxygen isotopic studies (Chapter 4) that the upper ≈800m of intracaldera tuff have interacted with substantial amounts of meteoric water. How has this interaction affected the strontium isotopes? Examination of the stratigraphic section on the SE side of the caldera (Section 1) might help us answer this question.

The positions of the samples used in this study relative to the stratigraphic trends in oxygen isotopes, $SiO_2$, Sr and Rb are shown graphically in Figs. 6.2 and 6.3a-c. $^{87}Sr/^{86}Sr_i$ for these samples are plotted against elevation in Fig. 6.4, along with two other samples, a dacitic pumice from the highest point on the southwest side of the caldera (KH91-11P1; I-DP in Fig. 6.1) and sanidine from a marginal vitrophyre on the east side of the caldera (90L-109-S; I-MV in Fig. 6.1), projected onto top and bottom of the section, respectively.

Independent of the $^{18}O/^{16}O$ evidence for subsolidus meteoric-hydrothermal alteration, it would be virtually impossible in any simple eruptive scenario for the zone B or zone C samples shown on Fig. 6.4 to represent primary magmatic $^{87}Sr/^{86}Sr$ values, because there is no logical reason why the deeper parts of the magma chamber should simultaneously show both higher and more heterogeneous strontium isotope ratios than the more silicic, lowest ppm Sr magmas just beneath the roof of the magma chamber. The roof portion of the chamber would be much more likely to be contaminated by external, more radiogenic Sr than would the deeper portion.

Interaction with crustal rocks or waters will usually raise $^{87}Sr/^{86}Sr$ ratios, as is observed in zone B, the low-$^{18}O$ zone of the stratigraphic section. Three samples were analyzed from this zone. Two have major and trace element contents which are distinctly different from the overall chemical trends; they are more silicic than the rocks directly above and below them (CG-C2-4B and CG-C2-4F; Fig. 6.3a-c). Sample CG-C2-4F particularly stands out from these trends, especially in Rb content (Fig. 6.3c). The third sample, CG-C2-4H, has the lowest $\delta^{18}O$ value in the section (Fig. 6.2) and thus is probably the sample which has interacted with the greatest amount of meteoric water. The $^{87}Sr/^{86}Sr_i$ ratios of these three samples do not correlate directly with $\delta^{18}O$, but they do show a correlation with the Rb contents (measured by XRF, Fig. 6.3c). In particular, the sample with the highest Rb content, CG-C2-4F, also has the highest $^{87}Sr/^{86}Sr_i$. The other two samples have comparable Rb contents but distinctly different $\delta^{18}O$; the one with the lower $\delta^{18}O$ has the higher $^{87}Sr/^{86}Sr_i$.

These observations from zone B suggest that $^{87}Sr/^{86}Sr_i$ ratios for rocks in zone B are dependent both on the amount of water with which they have interacted and their Rb/Sr ratio. The lower the Sr concentrations in a sample, the more susceptible it is to observable $^{87}Sr/^{86}Sr$ changes, other things being equal. The question remains as to whether the Rb/Sr ratios of samples CG-C2-4B and CG-C2-4F are primary or whether they have been affected by hydrothermal activity. The fact that the reversals appear in the compositional trends of most of the major and trace elements (Chapter 4), favors a magmatic origin. Two other possibilities are that they are caused by channeling of fluids which transport Sr and other elements or that these fluctuations are caused by addition of xenocrystic or xenolithic material. However, addition of xenoliths of the measured country rocks could not explain the high Rb content of sample CG-C2-4F.

The two samples from zone C, the upper dacitic zone, have $\delta^{18}O$ values of +4.6 and +12.1. In Chapter 4, we argue that these values, particularly the higher one, were caused by low-temperature hydration; in nature, this process is commonly accompanied by devitrification, and oxygen isotope exchange. As was the case in zone B, the strontium isotopic compositions in zone C are higher than would be expected by simply projecting the (magmatic?) trend upward from zone A (Fig. 6.4). In particular, the uppermost tuff sample, which has the highest $\delta^{18}O$ value, has an $^{87}Sr/^{86}Sr_i$ of 0.7063, and the glassy dacitic pumice at a similar stratigraphic level has $^{87}Sr/^{86}Sr_i$ of 0.7055. Thus, it is logical to attribute these higher $^{87}Sr/^{86}Sr_i$ values to interaction with Sr-bearing meteoric waters.

***Primary Strontium Isotopic Trends*** -- The four rhyolite samples from the lower 700 meters of Section 1 (zone A) have "normal" igneous whole-rock $\delta^{18}O$ values between +7.0 and +8.5. These $\delta^{18}O$ values are compatible with equilibrium with the quartz and feldspar phenocrysts at magmatic temperatures; there is no indication of interaction with meteoric waters. Therefore, we would also expect these samples to have relatively unaltered strontium isotopic ratios. With the exception of the lowermost sample (CG-C2-4Q) which we will discuss below, the samples in zone A do indeed have relatively low initial $^{87}Sr/^{86}Sr$ ratios (0.7058 to 0.7060), including a sanidine separate (90L-109-S) from approximately the same stratigraphic level as CG-C2-4Q.

The unaltered samples in zone A define an apparent trend toward lower $^{87}Sr/^{86}Sr_i$ ratios with elevation (or depth in the magma chamber from which they erupted). This trend can be extended upward to the $^{87}Sr/^{86}Sr_i$ ratio of the dacitic pumice, KH91-11P1, at 3475m (Fig. 6.4). Though the dacitic pumice shows some signs of perlitization and low temperature hydration, it still has a glassy matrix and has not undergone devitrification like the other tuff samples in

zone C. In the following discussion, I will assume that the trend in $^{87}Sr/^{86}Sr_i$ projected from zone A through the value for KH91-11P1 (Fig. 6.4) represents the trend in $^{87}Sr/^{86}Sr_i$ within the upper part of the Chegem magma chamber at the time of the caldera-forming eruption. Such a magmatic trend implies either (1) that the magma assimilated some country rock, or (2) that the source rock for the magma was heterogeneous, or (3) that the magma became compositionally zoned and then resided for some time in the magma chamber. However, the difference in $^{87}Sr/^{86}Sr_i$ in this magmatic trend would imply a residence time of ≈7.5 million years.

Inasmuch as the rocks in zone B of this section have whole-rock $^{87}Sr/^{86}Sr$ ratios which have been altered by interaction with meteoric water, I analyzed feldspar phenocrysts, which are entirely unaltered in thin section, from one sample (CG-C2-4F) to see if they retained an $^{87}Sr/^{86}Sr_i$ ratio more representative of the magma from which they crystallized. Because all of the feldspar phenocrysts analyzed had near-magmatic $\delta^{18}O$ values (Chapter 4), one might expect that the feldspar $^{87}Sr/^{86}Sr_i$ ratio would be closer to the magmatic value. The feldspar $^{87}Sr/^{86}Sr_i$ ratio of sample CG-C2-4F (0.7059) is lower than the whole rock ratio (0.7063), but it is still considerably higher than the value predicted by simply extrapolating the observed trends in zone A (0.7056). However, this particular sample has an anomolously high Rb/Sr ratio for its stratigraphic level, and so it is compositionally more similar to the rhyolites lower in the stratigraphic section. Thus, the $^{87}Sr/^{86}Sr_i$ ratio of feldspar phenocrysts from sample CG-C2-4F might be consistent with the proposed magmatic trend if this anomolous sample is from a higher (more silicic) stratigraphic level in the magma chamber that the tuffs directly above and below it. Feldspar phenocrysts from other samples in Section 1, chemically more representative of their stratigraphic level, should also be analyzed to verify this trend.

### 6.6.2 *Approximate Sr Content of Meteoric Water*

An estimate of the approximate Sr content of the meteoric waters which interacted with the intracaldera Chegem Tuff can be made by using simple zero-dimensional box models. This involves using the mass balance equation (McCulloch et al., 1981):

$$\frac{W}{R}_{open} = \ln\left(\frac{\varepsilon^i_{H_2O} - \varepsilon^i_{rock}}{\varepsilon^i_{H_2O} - \varepsilon^f_{rock}}\right) \times \frac{C^i_{rock}}{C^i_{H_2O}}$$

where i = initial value, f = final value, $C^i_{H_2O}$ = concentration of Sr in meteoric water, $C^i_{rock}$ = concentration of Sr in rock and ε is defined above. This equation is exactly analogous to the mass balance equation of Taylor (1977) for oxygen isotopes which was used in Chapter 4:

$$\frac{W}{R}_{open} = \ln\left(\frac{\Delta + \delta^i_{H_2O} - \delta^i_{rock}}{\delta^i_{H_2O} - (\delta^f_{rock} - \Delta)}\right)$$

except that the oxygen isotope equation expresses the mole ratio (not a mass ratio) of oxygen in the water and rock, and it also incorporates a temperature-dependent fractionation, Δ, which is not important during strontium exchange.

To determine the approximate strontium concentrations in the meteoric-hydrothermal fluids, we must make several assumptions: (1) Sample CG-C2-4H, which has the lowest $\delta^{18}O$, will be taken to represent the model rock because it has probably had the most aqueous fluid pass through it and is thus most likely to have exchanged with a large reservoir of external strontium. The hypothetical initial $^{87}Sr/^{86}Sr$ of that rock is 0.7056 ($\varepsilon_{Sr} = 16$), based on the extrapolation from zone A (Fig. 6.4), and the final (measured) composition is 0.7061 ($\varepsilon_{Sr} = 23$). (2) We will assume that the $^{87}Sr/^{86}Sr$ of the meteoric water was either 0.7200 ($\varepsilon_{Sr} \approx 220$) or 0.7071 ($\varepsilon_{Sr} \approx 35$). These are typical values for, respectively, the crystalline rocks to the southwest of the caldera and the limestones to the northeast, estimated from our data (Table 6.2). (3) If we want to determine the Sr

content of the water, we must find the $W/R_{open}$ ratio in units of mass. This can be approximated from the $^{18}O/^{16}O$ data, as discussed in Chapter 4, by assuming a temperature of 500° to 600°C, an initial water $\delta^{18}O$ of –12, and utilizing the fact that the rock contains 15 $\mu molesO_2/mg$ while the water has 28 $\mu molesO_2/mg$. This corresponds to a $W/R_{open}$ of ≈0.85 in mass units. (4) we will assume that the initial Sr concentration of the rock is identical to its final Sr concentration. With these assumptions, we can calculate the initial Sr concentration of the water by rearranging the strontium mass balance equation:

$$C^i_{H_2O} = \ln\left(\frac{\varepsilon^i_{H_2O} - \varepsilon^i_{rock}}{\varepsilon^i_{H_2O} - \varepsilon^f_{rock}}\right) \times \frac{C^i_{rock}}{\frac{W}{R_{open}}}$$

The resulting initial Sr concentration in the water is ≈8 ppm if the strontium comes from the crystalline basement, but it would have to be as high as ≈115 ppm if the strontium comes from the limestone. Therefore, limestones, though they have high concentrations of Sr, are probably not the source of the strontium in the meteoric waters which interacted with the Chegem Tuff. Even the Sr concentration calculated for water with an isotopic composition similar to the crystalline basement rocks is high. For comparison, meteoric thermal waters from the Long Valley caldera (California) have Sr concentrations of 0.1 to 0.6 ppm (Goff et al., 1991) and a typical Sr concentration for seawater is 8 ppm (Goldberg, 1965). However, our estimate of the Sr concentration in the Chegem meteoric-hydrothermal waters is not a minimum estimate. If we do the same calculation using higher values of $\varepsilon^i_{H_2O}$ and $W/R_{open}$, the estimated Sr concentration will be lower. For example, if the $^{87}Sr/^{86}Sr$ ratio of the water is 0.7318 (the measured value for the gneiss), then this calculation yields a water Sr concentration of 5 ppm.

Surface water flowing into the intracaldera tuff from the crystalline basement could not possibly carry these high concentrations of Sr. In order to

dissolve such large amounts of Sr, these meteoric waters either had to be very hot or they had to have a high pH and/or salinity. Perhaps these waters interacted with megabreccia and lithic fragments of the crystalline basement which were incorporated into the caldera fill during eruption. If this were the case, the waters could have been very hot during this interaction. Also, we do not yet know whether this Sr isotopic shift is a caldera-wide phenomenon or whether it is a local effect on the southeast side of the caldera.

### *6.6.3 Comparison with the Samail Ophiolite*

We have shown that the strontium (Fig. 6.4) and oxygen (Fig. 6.2) isotopic profiles in Stratigraphic Section 1 of the intracaldera Chegem Tuff display distinct overprints from interactions with meteoric-hydrothermal waters. A similar situation occurs in the Samail Ophiolite, a section of oceanic crust and upper mantle which has been obducted onto the continental crust in Oman. Though this ophiolite contains entirely different rock types in a different tectonic setting, it displays a striking similarity in isotopic trends to the Chegem caldera (Fig. 6.5). McCulloch et al. (1980, 1981) performed Sm/Nd, Rb/Sr and $^{18}O/^{16}O$ isotope studies on the ophiolitic section to distinguish between the effects of seafloor hydrothermal alteration and primary magmatic isotopic variations. Their $\delta^{18}O$, $\varepsilon_{Sr}$ and $\varepsilon_{Nd}$ values from a composite profile through the Samail Ophiolite are shown in Fig. 6.5a and compared to $\delta^{18}O$ and $\varepsilon_{Sr}$ values for the vertical section of intracaldera tuff, shown in Fig. 6.5b. Though the details of the two sets of data differ, the similarity in trends is clear, perhaps reflecting the similar water-rock processes which produced the data.

The $\delta^{18}O$ and $\varepsilon_{Sr}$ trends in the Samail Ophiolite are interpreted as the results of interaction between rock and seawater in an environment of variable temperature (McCulloch et al., 1981). The fractionation of oxygen between water

and rock is highly dependent on temperature. At high temperatures, the rock will become depleted in $^{18}O$ as it is towards the bottom of the Samail Ophiolite section. At low temperature, the rock $\delta^{18}O$ will increase as it does at the top of the Samail section. An increase in $\delta^{18}O$ can also be caused by interaction with water which is isotopically heavy. Strontium isotope fractionation, on the other hand, is not dependent on temperature. Therefore, the strontium isotope profile in the Samail Ophiolite is controlled solely by the flux of water at each point and the Sr contents of the water and rock. The only way that temperature might enter the picture is in its effect on the rate of Sr exchange.

Like those of the Samail Ophiolite, the isotopic trends of the Chegem caldera were most likely caused by water-rock interaction in an environment with a temperature gradient. A qualitative comparison of the profiles in Fig. 6.5 defines differences in the two environments. For example, the shift from low $\delta^{18}O$ to high $\delta^{18}O$ in the Chegem caldera occurs over a much shorter vertical distance (400 m) than in the Samail Ophiolite (2 km). This suggests that the temperature gradient in the Chegem Tuff at the time of water-rock interaction was much greater than in the Samail Ophiolite. The $^{18}O$-lowering in the Chegem caldera is also much greater than in the Samail Ophiolite, while the $\delta^{18}O$-shift to higher values at the top of the profile is not as pronounced. This difference is explained by the different waters which interacted in the two environments: in Chegem, the waters are meteoric with a $\delta^{18}O$ of –11 to –16 (Chapter 5), whereas in the Samail Ophiolite, seawater ($\delta^{18}O = -1$) has interacted with the rocks. A third difference is that the $\varepsilon_{Sr}$ shift in the Chegem section is less than half the magnitude of the shift in the Samail Ophiolite. Three possible explanations for this observation are: (1) the difference in $^{87}Sr/^{86}Sr$ between the water and rock at Chegem was less than that at Samail; (2) relative to the Sr concentration in the rocks, the Chegem water did not transport as much Sr as the seawater which

exchanged with the Samail Ophiolite. This would either occur because the Chegem water had a lower Sr concentration relative to the concentration in the rocks, or because smaller volumes of water interacted with the rocks. In fact, the intracaldera tuffs at Chegem generally have lower Sr concentrations than the rocks in the Samail Ophiolite, so they should be more susceptible to change for a given amount of strontium; (3) the water-rock interaction responsible for the shifting $\varepsilon_{Sr}$ at Chegem took place over too short a time interval for the rocks to fully equilibrate. Incomplete equilibration might also explain the lower $\varepsilon_{Sr}$ values at the top of the section (both at Chegem and Samail) where temperatures are lower and Sr diffusion is slower.

### *6.6.4 Sample CG-C2-4Q: Evidence for Assimilation of Radiogenic Roof Rocks?*

Sample CG-C2-4Q is one of the most "evolved" intracaldera tuff samples available. It was collected at the very base of the stratigraphic section exposed on the southeast side of the caldera and probably originated near the roof of the magma chamber from which the tuff was erupted. The abnormally high $^{87}Sr/^{86}Sr_i$ ratio (0.7076) of this rock is most easily explained by assimilation of country rocks, which is thought to be common near the roofs of magma chambers (Duffield and Ruiz, 1992). Measurements of country rocks near the Chegem caldera give $^{87}Sr/^{86}Sr$ ratios of 0.7071 to 0.7320, and Sr contents at least four times higher than the most silicic rhyolites. If the average $^{87}Sr/^{86}Sr$ ratio of assimilated country rock is 0.7200, then in order to raise an $^{87}Sr/^{86}Sr$ ratio from 0.7060 to 0.7076 by simple mixing, ≈12% of the Sr in the top of the magma chamber would have to be assimilated from the roof rocks. Because of the higher Sr concentrations of the country rocks, the actual volume of assimilated rock would be less than this, only around 3-4%. The substantially lower $^{87}Sr/^{86}Sr$ of a

sanidine from a similar position in the magma chamber (90L-109-S) may indicate that assimilation occurred after the sanidine phenocrysts had formed, perhaps shortly prior to eruption. The time interval between assimilation and eruption must have been short enough that the feldspar phenocrysts had insufficient time to re-equilibrate with the coexisting magma.

Alternatively, the high $^{87}Sr/^{86}Sr$ ratio of the marginal vitrophyre (CG-C2-4Q) could be the result of xenocrystic or xenolithic contamination of the glassy groundmass. There are abundant lithic fragments in this sample, and, although I tried to select pieces of the sample which were free of such lithics fragments, if a small percentage of contaminants (again 3-4%) remained, this would raise the $^{87}Sr/^{86}Sr$ ratio of this low-Sr sample substantially.

### *6.6.4 Pre-caldera and Post-caldera Rocks*

Within the Chegem caldera, two igneous units formed after the caldera-forming eruption of Chegem Tuff: andesite flows and a granodiorite porphyry intrusion. The andesite flows overlie the Chegem Tuff in the southern and western parts of the caldera. As many as 8 separate flow units have been identified. In the south, they are separated from the underlying tuff by an erosional horizon containing glacial deposits, whereas in the west they appear to directly overlie poorly-welded tuff. The granodiorite porphyry intrudes the Chegem Tuff in the northeastern part of the caldera. Based on observations described below, Lipman et al. (1993) suggest that the granodiorite marks the core of an andesitic volcano. Though the granodiorite and the andesites differ in bulk chemistry, the $^{87}Sr/^{86}Sr_i$ of these two samples (0.7056) is identical, supporting the idea that they are comagmatic.

Within the Chegem igneous suite studied, four samples are considerably more mafic than the rest of the rocks: the pre-caldera basaltic andesite and three

mafic inclusions from the post-caldera rocks. The pre-caldera basaltic andesite, exposed as a single small flow adjacent to one of the outflow tuff remnants, is the only known precursor volcanism in the region.

One mafic inclusion, an altered basalt, was collected from the andesite flows. This might represent a more mafic parent magma from which the andesite has differentiated. The other two mafic inclusions, a diorite and an andesite, were collected from the resurgent granodiorite intrusion. The latter is one of many andesitic inclusions from within the post-caldera granodiorite intrusion. These inclusions are rounded, embayed and have finer-grained borders, suggesting that they represent a more mafic magma which was incompletely mixed with the granodiorite magma in liquid state. These observations and the similarities of the andesite inclusions to the post-caldera andesite flows led to the suggestion that the granodiorite marks the core of an andesitic volcano (Lipman et al.,1993).

These four mafic samples were analyzed for strontium isotopes because they might be closer to the magma (mantle-derived?) which initiated melting in the crust. Their $^{87}Sr/^{86}Sr_i$ ratios are in fact lower than any of the other samples, ranging from 0.7046 to 0.7051, indicating that they do in fact have a larger mantle/lower crustal component.

Interestingly, the pre-caldera basaltic andesite and the diorite inclusion from the post-caldera granodiorite have identical $^{87}Sr/^{86}Sr_i$ ratios (0.7046). These two rocks are also similar in their major- and trace-element compositions, suggesting a common origin. However, the $^{40}Ar/^{39}Ar$ age of the basaltic andesite is 3.5 Ma, and it is only exposed in the lower Chegem valley, ≈30 km from the caldera, whereas the age of the granodiorite is 2.8 Ma (Chapter 3). If the diorite inclusion is a remnant of the magma which erupted as basaltic andesite, the magma chamber must have been deep (tens of kilometers). Alternatively, the

two samples may be derived from geographically dispersed deep sources of similar composition.

The andesite inclusion in the granodiorite has a lower $^{87}Sr/^{86}Sr_i$ (0.7051) than the granodiorite and the andesite flows. It is unclear whether the inclusion comes from a separate magma chamber to that of the granodiorite or a deeper part of an isotopically-zoned magma chamber. If it is a foreign magma, then this represents one mechanism of creating isotopic heterogeneity in a magma chamber which is originally homogeneous. The altered basalt inclusion from the andesite flows has the same $^{87}Sr/^{86}Sr_i$ ratio as the andesite inclusion in the granodiorite, though it is considerably more mafic. Although this is suggestive, it does not necessarily prove that the two inclusions come from the same magma batch.

### *6.6.5 Variations of $^{87}Sr/^{86}Sr$ with Major and Trace Elements*

In the following discussion, the Chegem Tuff samples have been divided into two groups: isotopically and hydrothermally altered and unaltered, respectively, based on their whole rock $\delta^{18}O$ and $^{87}Sr/^{86}Sr_i$ (described above). Samples in zones B and C are all considered to be isotopically altered, with the exception of one glassy pumice in zone C (KH91-11P1). Among the Chegem igneous rocks, the initial $^{87}Sr/^{86}Sr$ ratio increases with $SiO_2$ content, as can be seen on Fig. 6.6. This plot reveals a linear envelope from ($^{87}Sr/^{86}Sr_i = 0.7052$, $SiO_2 = 54.8$ wt%) to ($^{87}Sr/^{86}Sr_i = 0.7060$, $SiO_2 = 75.7$ wt%) which contains "unaltered" Chegem Tuff, outflow tuff, the granodiorite porphyry intrusion, andesite flows and the basalt and andesite inclusions. The basaltic andesite flow and the diorite inclusion have $SiO_2$ contents similar to the mafic end-member of this grouping, but are less radiogenic. The altered Chegem Tuff samples that have interacted with meteoric water are more radiogenic than unaltered tuff, but

there is no correlation between their $^{87}Sr/^{86}Sr_i$ and $SiO_2$ contents. This lack of correlation further supports our conclusion that the $^{87}Sr/^{86}Sr_i$ ratios of these rocks are not magmatic. The Eldjurta Granite stands apart from the general Chegem trend as more radiogenic and will be discussed below.

A similar pattern is seen in a plot of $^{87}Sr/^{86}Sr_i$ vs. Sr content (Fig. 6.7). The Chegem volcanic and intrusive rocks, aside from the altered tuffs, define an inverse linear trend on this plot. The basaltic andesite and diorite inclusion lie slightly off the trend. The altered Chegem Tuff samples are more radiogenic and also lie well off the trend. The Eldjurta Granite sample lies outside of any of these groups of rocks. When the same plot is expanded to include the data from the analyzed country rocks (Fig. 6.8), both the Chegem igneous rocks and the Eldjurta Granite plot along a horizontal line with a broad range of Sr concentrations, but a relatively small range of $^{87}Sr/^{86}Sr_i$. These relationships indicate that only relatively small proportions (<10%) of these radiogenic country rocks could have been assimilated by these magmas.

The correlation of the strontium isotopic trends of the Chegem igneous rocks with their bulk chemistry indicates that these trends existed in the Chegem magma chamber prior to eruption. There has been much discussion about the cause of chemical and isotopic zonation in silicic magma chambers (e.g. Hildreth, 1981; Michael, 1983; Halliday et al., 1984; Johnson, 1989). The Chegem data set is too sparse at this point to settle this debate, but certain observations might be relevant: (1) This particular zoned tuff does not come from a magma system with a long history of volcanic eruptions and caldera formations. There was only a minor amount of pre-caldera volcanism in the Chegem region. These observations suggest that the Chegem magma chamber was not long-lived (i.e., >1 million years) and the isotopic zonation could not have been produced from an isotopically homogeneous magma by crystal fractionation followed by

radioactive decay in the chemically zoned magma. (2) Mafic inclusions in the post-caldera andesite and granodiorite indicate that magmas of different isotopic compositions coexisted. Thus, magma mixing may be a viable means of producing the observed isotopic heterogeneity. (3) Though there are zoning in the major- and trace-element compositions of this ash-flow tuff sequence as well as in the strontium isotopes, the oxygen isotopic compositions of phenocrysts are constant.

### *6.6.5 Eldjurta Granite*

*Relationship to Chegem Igneous Rocks* -- The Eldjurta Granite and the Chegem volcanic and intrusive rocks are close in space, age and composition and thus may constitute a single physically continuous magmatic system at shallow depth (Lipman et al., 1993). However, the two igneous suites differ in their phenocryst $\delta^{18}O$, suggesting that the magmas which formed them evolved separately for some time (Gazis et al., 1990; Chapter 3). The $^{87}Sr/^{86}Sr_i$ data presented in this chapter reinforce this conclusion. The Eldjurta Granite sample which was analyzed for whole rock $^{87}Sr/^{86}Sr$ (CG-C2-56) was collected from the Baksan River level, in the center of the surface exposure, ≈1 km below the roof. Our $^{40}Ar/^{39}Ar$ ages for the surface samples and the Rb/Sr isochron age of Zhuravlev and Negrey (1993, 1994) are both around 1.9 Ma. Assuming this age, the initial $^{87}Sr/^{86}Sr$ ratio of 0.70685 is identical to that of Zhuravlev and Negrey (1993, 1994). This is substantially higher than the initial $^{87}Sr/^{86}Sr$ ratios for all Chegem Tuff samples, except CG-C2-4Q whose isotopic signature probably reflects 3-4% assimilation of roof rocks. In addition, we have shown above that the Eldjurta sample does not fit into the Chegem trends on $^{87}Sr/^{86}Sr_i$–$SiO_2$ and $^{87}Sr/^{86}Sr_i$–Sr plots (Figs. 6.6 and 6.7). The Chegem igneous rocks and the Eldjurta Granite also have distinctly different biotite $^{40}Ar/^{39}Ar$ ages (Chapter 3). This could either be

due to different intrusion and eruption ages or to slower cooling in the Eldjurta Granite.

If the differing phenocryst $\delta^{18}O$, initial $^{87}Sr/^{86}Sr$ and chemical trends of the Eldjurta Granite and the Chegem igneous rocks are the result of their evolution as separate magma batches, it is still uncertain whether they were actually separate plutons or were at one time part of the same large magma body. The two magmas could have evolved as separate cupolas of a single magma chamber or the Eldjurta Granite could have evolved separately after the Chegem Tuff was erupted. Broadly comagmatic plutons of the Questa caldera system (New Mexico) also have variable chemical and isotopic signatures, and cooling ages, indicating that they evolved in partial isolation (Johnson et al., 1989).

Pursuing an understanding of the relationship of the Eldjurta Granite to the Chegem igneous rocks, we must ask some more questions: What differences in evolution would cause a difference in quartz $\delta^{18}O$ of 1.5 per mil (8.5 and 10 per mil) and in initial $^{87}Sr/^{86}Sr$ of 0.0009 (0.7060 and 0.7069)? Could the Eldjurta Granite represent Chegem magma which underwent late evolution after the tuff was erupted? One mechanism for altering both $\delta^{18}O$ and initial $^{87}Sr/^{86}Sr$ is assimilation, usually accompanied by fractional crystallization. The extent to which magmas are modified during ascent and emplacement, including the effects of assimilation and fractional crystallization has been discussed at length by Bowen (1928). Taylor (1980) and DePaolo (1981) have further discussed the effects of combined wallrock assimilation and fractional crystallization on isotope systematics. Taylor (1980) calculated a variety of oxygen and strontium isotope assimilation-fractional crystallization curves, concluding that these curves are markedly different from two end-member mixing curves between magma and country rock. DePaolo (1981) formulated equations to describe the evolution of

trace elements and isotopes in a magma chamber undergoing assimilation and fractional crystallization. Depending on the trace element and isotopic compositions of the country rocks, these models produce trends in $\delta^{18}O$-$^{87}Sr/^{86}Sr_i$ ratio and trace element content that could contain the values for unaltered Chegem Tuff and Eldjurta Granite. However, the data presented in this chapter is not sufficient to constrain precisely the degree of assimilation and/or fractional crystallization nor is this a unique explanation of the observed differences.

*Mineral Rb/Sr Isochron* -- Mineral separate Rb/Sr data was collected for two Eldjurta Granite samples to test the feasibility of dating these samples by means of Rb/Sr isochrons. This proved to be quite difficult: the Eldjurta Granite biotites have high Rb/Sr ratios which made it difficult to get a clean Sr separate. Any contamination of Sr with Rb will tend to raise the apparent $^{87}Sr/^{86}Sr$ ratio and increase the isochron age. However, the biotite $^{87}Sr/^{86}Sr$ data for one sample, 10-4-90, does not appear to be contaminated. Based on a decay constant of $\lambda = 1.42 \times 10^{-11}/yr$, the biotite-sanidine pair from sample 10-4-90 yields an isochron age of 2.4 Ma (Fig. 6.8). The whole-rock $^{87}Sr/^{86}Sr$ ratio for this sample has not been determined. This would provide a third point for the isochron, but it would be expected to plot very near to the sanidine. Because this isochron is defined by only two points and because of the analytical difficulties with other biotites, I regard this result as strictly preliminary and entirely uncertain pending further analyses. However, the result is encouraging in that the Rb/Sr age is comparable to the biotite (1.8 Ma) and K-feldspar (2.4 Ma) total fusion $^{40}Ar/^{39}Ar$ ages for this sample.

## 6.7 Conclusions

1. Whole-rock strontium isotopic analyses of 9 intracaldera Chegem Tuff samples from the 1405 m stratigraphic section on the southeast side of the caldera (Section 1) reveal that the same hydrothermal event which produced anomolously low to high $\delta^{18}O$ values in the upper 800m of section also raised the $^{87}Sr/^{86}Sr$ ratios of several samples in this part of the section. Mass balance calculations suggest that these meteoric waters contained 5-10 ppm Sr, and that this strontium originated in the Paleozoic and Proterozoic crystalline basement to the south and west of the caldera. Possibly, this strontium was leached at high temperature from lithic fragments and megabreccia which were incorporated into the caldera fill during eruption.

2. There is a striking similarity between overall trends of stratigraphic isotope profiles in the Samail Ophiolite (Oman) and the Chegem caldera. In both settings, the $\delta^{18}O$ shifts increases from "normal" magmatic values at the base of the section to relatively low values further up and then relatively high values at the top of the section. Simultaneously, the $\varepsilon_{Sr}$ values increase at the top of the section. They display relatively heterogeneous values in the same part of the section where the oxygen isotopic compositions are no longer "normal." Both of these isotopic patterns are interpreted to be the result of similar processes, namely interaction of the rocks with relatively low-$^{18}O$ and $^{87}Sr$-rich waters in an environment with a steep temperature gradient from about 600°C to Earth-surface temperatures. The data suggests that the waters at Chegem were isotopically lighter than the water which interacted with the Samail Ophiolite (sea water) and that the temperature gradient in the cooling Chegem Tuff was steeper than in the Samail Ophiolite.

3. Four Chegem Tuff samples from the bottom 700 m of the stratigraphic section and one glassy dacitic pumice from high in the section appear to have retained magmatic Sr isotopic compositions. Their $^{87}Sr/^{86}Sr_i$ ratios decrease upward from 0.7060 to 0.7055, indicating that the Chegem magma chamber was isotopically zoned before the caldera-forming eruption. This isotopic zonation is accompanied by a zonation of major and trace elements, a common phenomenon in ash-flow tuff sequences. The isotopically "unaltered" Chegem Tuff samples, the outflow tuffs and several other Chegem igneous lithologies (granodiorite, andesite, andesite inclusion in granodiorite and basalt inclusion in andesite), define linear trends on $^{87}Sr/^{86}Sr_i$–$SiO_2$ and $^{87}Sr/^{86}Sr_i$–Sr plots. This indicates that these samples are cogenetic and that their Sr isotopic compositions are magmatic. The zoning is thought to be the result of fractional crystallization with small amounts of assimilation, though further studies, especially of phenocrysts are necessary to verify this.

4. The lowermost sample from the stratigraphic section on the southeast side of the caldera (CG-C2-4Q) has the highest $^{87}Sr/^{86}Sr_i$ value of any Chegem Tuff (0.7076). This high value must be either due to assimilation of radiogenic roof rocks at the very top of the Chegem magma chamber or incorporation during eruption and deposition of xenocrystic/xenolithic elements in this rock.

5. A basaltic andesite flow, the only known example of pre-caldera volcanism in the region, is one of the most mafic rocks in the Chegem area. It has $^{87}Sr/^{86}Sr_i = 0.7046$, identical to a diorite inclusion from the post-caldera andesite flows. The two samples plot off of the trends of other Chegem igneous rocks on $^{87}Sr/^{86}Sr_i$-$SiO_2$ and $^{87}Sr/^{86}Sr_i$-Sr plots.

6. The Eldjurta Granite, an epizonal pluton, exposed 10 kilometers northwest of the Chegem caldera, has been considered to be part of the same magma system as the Chegem igneous rocks, based on their similar compositions and ages (Lipman et al., 1993). However, oxygen and strontium isotope studies clearly show that the Eldjurta Granite magma evolved separately from the Chegem magma for some time. These magmas could be unrelated or they might be derived from the same magma chamber. If they are derived from the same magma chamber, they either came from separate cupolas that underwent drastically different degrees of interaction with the local country rock, or they represent different stages of evolution of a large heterogeneous magma system.

**Table 6.1.** Chemical compositions of rocks used in Rb/Sr study

| sample | CG-C2-4Q rhyolite vitrophyre 2120m | CG-C-44A rhyolite tuff 2180m | CG-C-44C rhyolite tuff 2380m | CG-C-44E rhyolite tuff 2490m | CG-C2-4B rhyolite tuff 2870m | CG-C2-4H rhyolite tuff 3160m | CG-C2-4F rhyolite tuff 3225m | CG-C-44J dacite tuff 3400m | CG-C-44M dacite tuff 3440m | CG-C-44P andesite flow 3490m |
|---|---|---|---|---|---|---|---|---|---|---|
| $SiO_2$ | 76.15 | 75.69 | 73.74 | 74.18 | 74.17 | 72.06 | 73.83 | 70.07 | 69.85 | 63.41 |
| $Al_2O_3$ | 12.98 | 13.26 | 14.00 | 13.80 | 13.80 | 14.92 | 14.38 | 15.56 | 15.55 | 16.56 |
| $Fe_2O_3$ (tot) | 1.06 | 1.10 | 1.76 | 1.72 | 1.90 | 1.92 | 1.21 | 2.72 | 2.98 | 4.98 |
| MgO | 0.34 | 0.34 | 0.50 | 0.47 | 0.36 | 0.56 | 0.39 | 0.95 | 0.83 | 2.91 |
| CaO | 0.96 | 1.01 | 1.68 | 1.72 | 1.54 | 2.09 | 1.42 | 2.61 | 3.24 | 4.59 |
| $Na_2O$ | 3.48 | 3,45 | 3.71 | 3.61 | 3.81 | 4.08 | 4.22 | 4.18 | 3.66 | 4.03 |
| $K_2O$ | 4.83 | 4.89 | 4.16 | 4.09 | 4.02 | 3.78 | 4.15 | 3.28 | 3.21 | 2.41 |
| $TiO_2$ | 0.11 | 0.18 | 0.31 | 0.29 | 0.29 | 0.41 | 0.27 | 0.45 | 0.48 | 0.78 |
| $P_2O_5$ | 0.05 | 0.06 | 0.09 | 0.10 | 0.08 | 0.12 | 0.08 | 0.14 | 0.16 | 0.24 |
| MnO | 0.03 | 0.02 | 0.04 | 0.02 | 0.03 | 0.05 | 0.04 | 0.04 | 0.04 | 0.08 |
| Rb | 151 | 156 | 128 | 137 | 151 | 167 | 261 | 128 | 109 | 107 |
| Sr | 34 | 75 | 168 | 160 | 137 | 198 | 131 | 256 | 267 | 350 |
| Y | 9 | 11 | 8 | 12 | 9 | 15 | 40 | 14 | 1 | 23 |
| Zr | 78 | 113 | 132 | 148 | 132 | 156 | 124 | 170 | 175 | 218 |
| Nb | 7 | 8 | 9 | 6 | 9 | 16 | 21 | 10 | 11 | 12 |
| Ba | – | – | – | – | – | – | 453 | – | – | 439 |
| La | – | – | – | – | – | – | 35 | – | – | 40 |
| Ce | – | – | – | – | – | – | 47 | – | – | 84 |
| Nd | – | – | – | – | – | – | 28 | – | – | 18 |

| sample | 90L-109 marginal vitrophyre | KH91-11P1 dacitic pumice | 90L-120P7 outflow pumice | 90L-119A outflow tuff | CG-C-58A granodiorite porphyry | CG-C2-6 andesite inclusion | CG-C2-2 diorite inclusion | KH91-19A basalt inclusion | 90L-127C basaltic flow | 89L-208* Eldjurta Granite |
|---|---|---|---|---|---|---|---|---|---|---|
| $SiO_2$ | 76.69 | 69.10 | 73.99 | 72.97 | 71.61 | 58.34 | 55.74 | 54.77 | 56.79 | 71.39 |
| $Al_2O_3$ | 12.75 | 15.71 | 13.83 | 14.20 | 14.73 | 17.33 | 18.86 | 16.59 | 16.13 | 14.99 |
| $Fe_2O_3$ (tot) | 1.00 | 2.98 | 1.64 | 2.28 | 2.33 | 6.62 | 7.18 | 8.43 | 7.53 | 2.22 |
| MgO | 0.14 | 1.10 | 0.50 | 0.66 | 0.86 | 3.86 | 3.30 | 6.95 | 5.25 | 0.81 |
| CaO | 0.75 | 2.75 | 1.25 | 1.70 | 2.10 | 6.70 | 7.37 | 8.01 | 7.25 | 1.84 |
| $Na_2O$ | 3.60 | 4.19 | 3.33 | 3.30 | 4.06 | 4.11 | 4.11 | 2.90 | 3.90 | 3.72 |
| $K_2O$ | 4.85 | 3.47 | 5.13 | 4.39 | 3.77 | 1.52 | 1.47 | 0.78 | 1.75 | 4.45 |
| $TiO_2$ | 0.12 | 0.49 | 0.23 | 0.35 | 0.37 | 1.10 | 1.50 | 1.15 | 0.95 | 0.37 |
| $P_2O_5$ | 0.05 | 0.17 | 0.08 | 0.09 | 0.13 | 0.33 | 0.36 | 0.30 | 0.34 | 0.15 |
| MnO | 0.04 | 0.04 | 0.03 | 0.04 | 0.04 | 0.09 | 0.10 | 0.13 | 0.11 | 0.05 |
| Rb | 177 | 111 | 145 | 142 | 175 | 65 | 50 | 29 | 70 | 283 |
| Sr | 21 | 286 | 121 | 161 | 207 | 396 | 486 | 438 | 428 | 198 |
| Y | 19 | 15 | 15 | 18 | 15 | 23 | 21 | 23 | 22 | 22 |
| Zr | 76 | 225 | 132 | 132 | 141 | 229 | 174 | 158 | 133 | 168 |
| Nb | 7 | 4 | 12 | 7 | 13 | 17 | 10 | 6 | 15 | 20 |
| Ba | 118 | – | – | 687 | – | – | – | – | – | 360 |
| La | 26 | – | – | 53 | – | – | – | – | – | 35 |
| Ce | 51 | – | – | 74 | – | – | – | – | – | 77 |
| Nd | 20 | – | – | 23 | – | – | – | – | – | – |

Data from U.S. Geol. Survey labs, Denver: major oxides by XRF methods, minor elements by energy-dispersive XRF (Kevex) methods

* surface sample from a different location than CG-C2-56, data from Lipman et al. (1993)

**Table 6.2 -** Rb, Sr, and O isotope data

| Sample# | Description | Elev (m) | Sr(I) ppm | Sr(X) ppm | Rb(I) ppm | Rb(X) ppm | $^{87}Rb/^{86}Sr$ atomic | $^{87}Sr/^{86}Sr_i$* atomic | $^{87}Sr/^{86}Sr$ atomic | $\varepsilon_{Sr}$* | $\delta^{18}O$ per mil |
|---|---|---|---|---|---|---|---|---|---|---|---|
| **Section 1 (SE side of caldera)** | | | | | | | | | | | |
| CG-C2-4Q | marginal vitrophyre | 2120 | 43 | 34 | 163 | 151 | 10.847 | 0.70759 | 0.70796 | 43.9 | 8.7 |
| CG-C-44A | rhyolite tuff | 2180 | 80 | 75 | 149 | 156 | 5.319 | 0.70602 | 0.70623 | 21.6 | 7.6 |
| CG-C-44C | rhyolite tuff | 2380 | 182 | 168 | 137 | 128 | 2.166 | 0.70596 | 0.70605 | 20.8 | 7.9 |
| CG-C-44E | rhyolite tuff | 2490 | 180 | 160 | 136 | 137 | 2.182 | 0.70581 | 0.70590 | 18.6 | 8.3 |
| CG-C2-4B | rhyolite tuff | 2870 | 173 | 137 | 180 | 151 | 3.001 | 0.70577 | 0.70589 | 18.1 | 2.9 |
| CG-C2-4H | poorly welded ruff | 3160 | 241 | 198 | 165 | 167 | 1.968 | 0.70612 | 0.70626 | 23.8 | -4 |
| CG-C2-4F(1) | rhyolite tuff | 3225 | 143 | 131 | 280 | 261 | 5.632 | 0.70638 | 0.70661 | 26.8 | -0.5 |
| CG-C2-4F(2) | rhyolite tuff | 3225 | 141 | 131 | 283 | 261 | 5.763 | 0.70633 | 0.70653 | 26.0 | -0.5 |
| CG-C2-4F-F | feldspar-rhy. tuff | 3225 | 471 | | 138 | | 0.840 | 0.70594 | 0.70597 | 20.5 | |
| CG-C-44J | dacite tuff | 3410 | 286 | 256 | 126 | 128 | 1.272 | 0.70576 | 0.70581 | 17.9 | 4.6 |
| CG-C-44M | dacite tuff | 3450 | 312 | 267 | 111 | 109 | 1.026 | 0.70630 | 0.70635 | 25.6 | 12.1 |
| **andesite** | | | | | | | | | | | |
| CG-C-44P | andesite flow | 3490 | 283 | 350 | 127 | 107 | 1.291 | 0.70563 | 0.70568 | 16.1 | 7.9 |
| **intracaldera tuff** | | | | | | | | | | | |
| 90L-109-S | sanidine-marg. vit. | ≈2100 | 56 | | 159 | | 8.183 | 0.70598 | 0.70641 | 21.1 | |
| KH91-11P1 | glassy dacitic pumice | 3475 | 312 | 286 | 107 | 111 | 0.987 | 0.70554 | 0.70557 | 14.8 | 9.3 |
| CG-C-58B | tuff from resurgent block | | 222 | | 133 | | 1.719 | 0.70603 | 0.70610 | 21.8 | 7.6 |
| **granodiorite** | | | | | | | | | | | |
| CG-C-58A | granodiorite | | 230 | 207 | 173 | 175 | 2.161 | 0.70559 | 0.70567 | 15.5 | 3.7 |
| **andesite inclusion** | | | | | | | | | | | |
| CG-C2-6 | andesite inclusion in granodiorite | | 437 | 396 | 67 | 65 | 0.441 | 0.70514 | 0.70515 | 9.1 | |
| **diorite inclusion** | | | | | | | | | | | |
| CG-C2-2 | diorite inclusion in andesite flow | | 494 | 486 | 49 | 50 | 0.288 | 0.70464 | 0.70465 | 2.1 | 6.6 |

| Sample# | Description | Elev (m) | Sr(I) ppm | Sr(X) ppm | Rb(I) ppm | Rb(X) ppm | $^{87}Rb/^{86}Sr$ atomic | $^{87}Sr/^{86}Sr_i$* atomic | $^{87}Sr/^{86}Sr$ atomic | $\varepsilon_{Sr}$* | $\delta^{18}O$ per mil |
|---|---|---|---|---|---|---|---|---|---|---|---|
| **basalt inclusion** | | | | | | | | | | | |
| KH91-19A | basalt inclusion in andesite flow | | 458 | 438 | 23 | 29 | 0.051 | 0.70517 | 0.70518 | 9.6 | |
| **outflow (lower Chegem)** | | | | | | | | | | | |
| 90L-120P7 | pumice-outflow tuff | | 149 | 121 | 154 | 145 | 2.977 | 0.70575 | 0.70587 | 17.9 | 5.7 |
| 90L-120P7-S | sanidine-pumice | | 203 | | 110 | | 1.560 | 0.70586 | 0.70593 | 19.8 | 7.8 |
| 90L-119A | outflow rhyolite tuff | | 188 | 161 | 134 | 142 | 2.068 | 0.70599 | 0.70607 | 21.2 | 5.7 |
| **basaltic andesite flow (lower Chegem)** | | | | | | | | | | | |
| 90L-127C | pre-caldera basaltic andesite flow | | 466 | 428 | 61 | 70 | 0.376 | 0.70463 | 0.70464 | 1.8 | 7.3 |
| **Eldjurta granite (Baksan valley)** | | | | | | | | | | | |
| CG-C2-56 | whole rock | surface | 221 | | 205 | | 2.669 | 0.70686 | 0.70693 | 33.5* | |
| 10-4-90-S | K-feldspar | 1325d | 141 | | 529 | | 10.767 | 0.70709 | 0.70738 | 9.6 | |
| 10-4-90-B | biotite | 1325d | 6 | | 1053 | | 484.738 | 0.71043 | 0.72351 | | 5.6 |
| 17-1-90-S | K-feldspar | 1850d | 184 | | 529 | | 8.275 | | | | 9.3 |
| **country rock (upper Chegem)** | | | | | | | | | | | |
| CG-C-40 | Hercynian(?) granite | | 284 | | 136 | | 1.378 | 0.71346 | 0.71352 | 37.3 | 8.7 |
| CG-C-41 | gneiss | | 160 | | 176 | | 3.170 | 0.73185 | 0.73197 | 388.2 | 8.1 |
| CG-C2-33 | limestone | | 565 | | 12 | | 0.059 | 0.70712 | 0.70712 | 127.2 | 37.5 |

* Initial $^{87}Sr/^{86}Sr$ and $\varepsilon_{Sr}$ calculated using an age of 2.8 Ma for Chegem rocks, and 1.9 Ma for Eldjurta Granite

For Rb and Sr concentrations: I = isotope dilution; X=XRF. Estimated errors are ±1% (I) and ±5% (X).
A comparison of the two techniques is given in Appendix C

Errors for $^{87}Sr/^{86}Sr$ are better than ±0.00005

d=depth in meters of Eldjurta Granite samples in deep drillhole

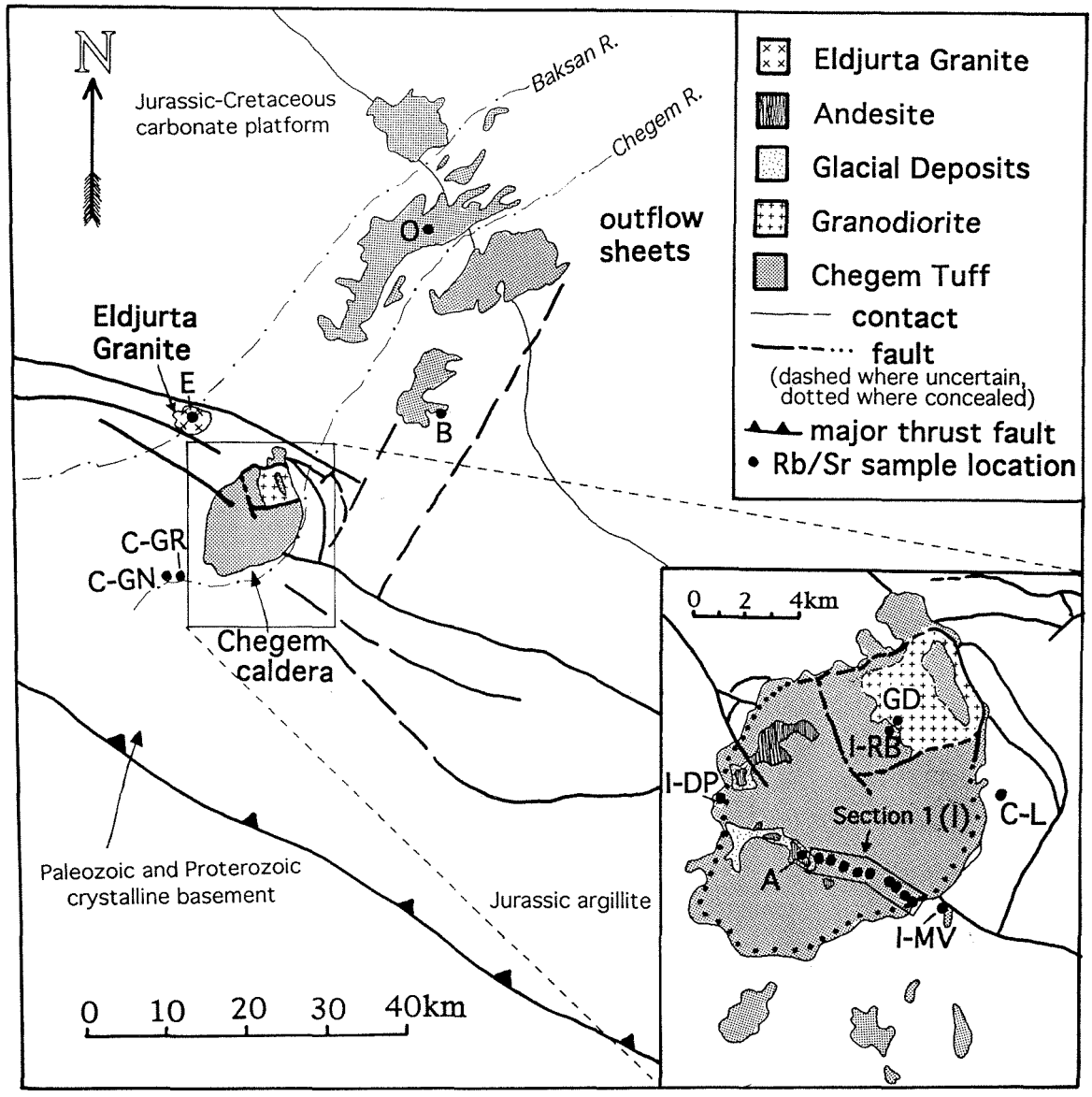


**Figure 6.1** -- Geologic map of the Chegem caldera, Eldjurta Granite and surrounding region showing the locations of samples analyzed in this Rb/Sr study. O = outflow tuff; B = basaltic andesite flow; E = Eldjurta Granite; C = country rock; GR = Hercynian (?) granite; GN = Proterozoic (?) gneiss; L = Jurassic limestone; I = intracaldera tuff; DP = dacitic pumice; MV = marginal vitrophyre; RB = tuff from resurgent block; A = andesite. Section 1 is a 1345m stratigraphic section of intracaldera tuff.

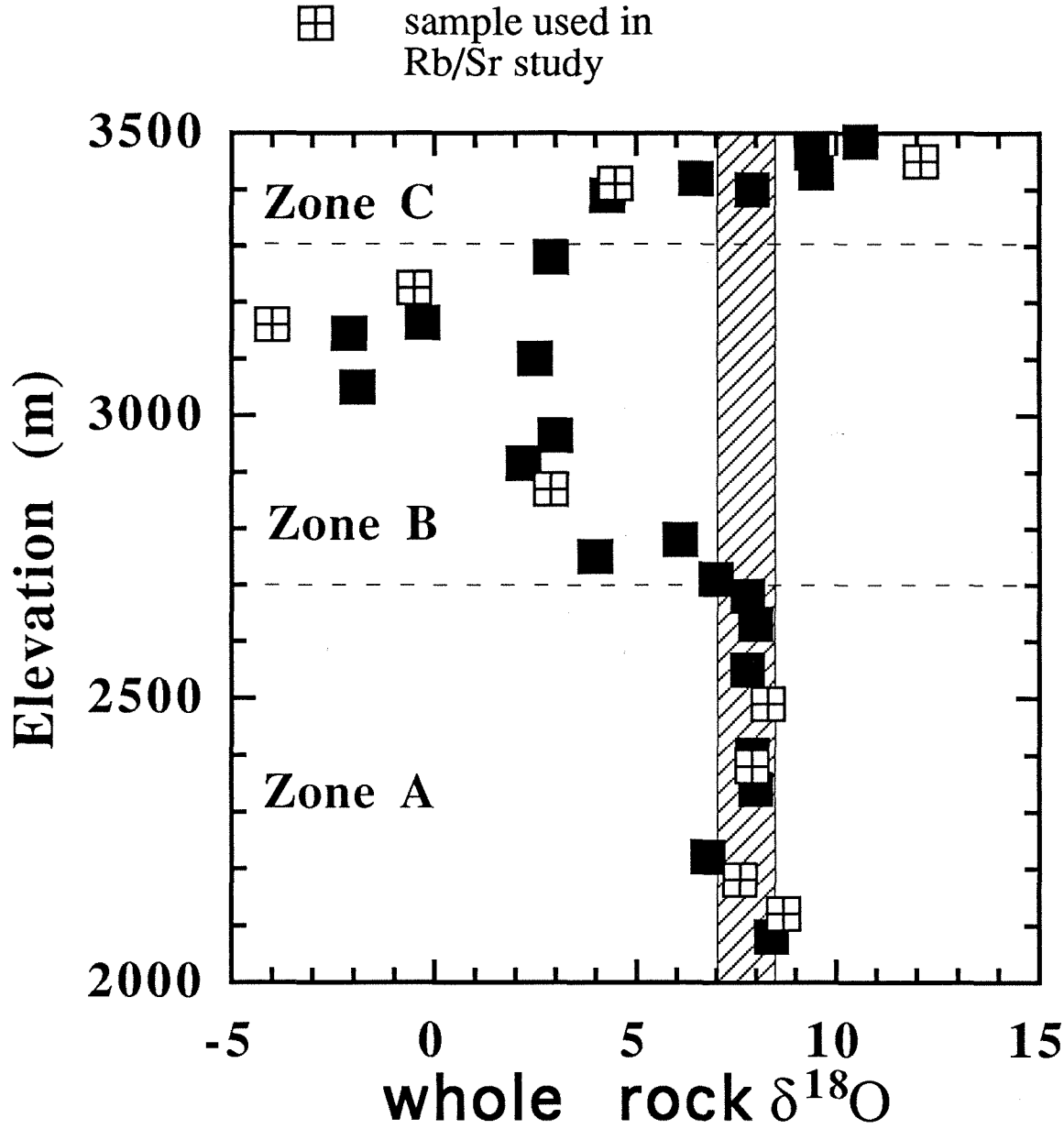


**Figure 6.2** -- Whole rock $\delta^{18}O$ of samples in Section 1 (Fig. 6.1) plotted against elevation (or stratigraphic position). Samples used in this Rb/Sr study are indicated by crossed squares. Dashed horizontal lines separate zones A, B, and C (described in Chapter 4). The diagonally-ruled area represents the range of calculated $\delta^{18}O$ values for magmas in equilibrium with the phenocrysts.

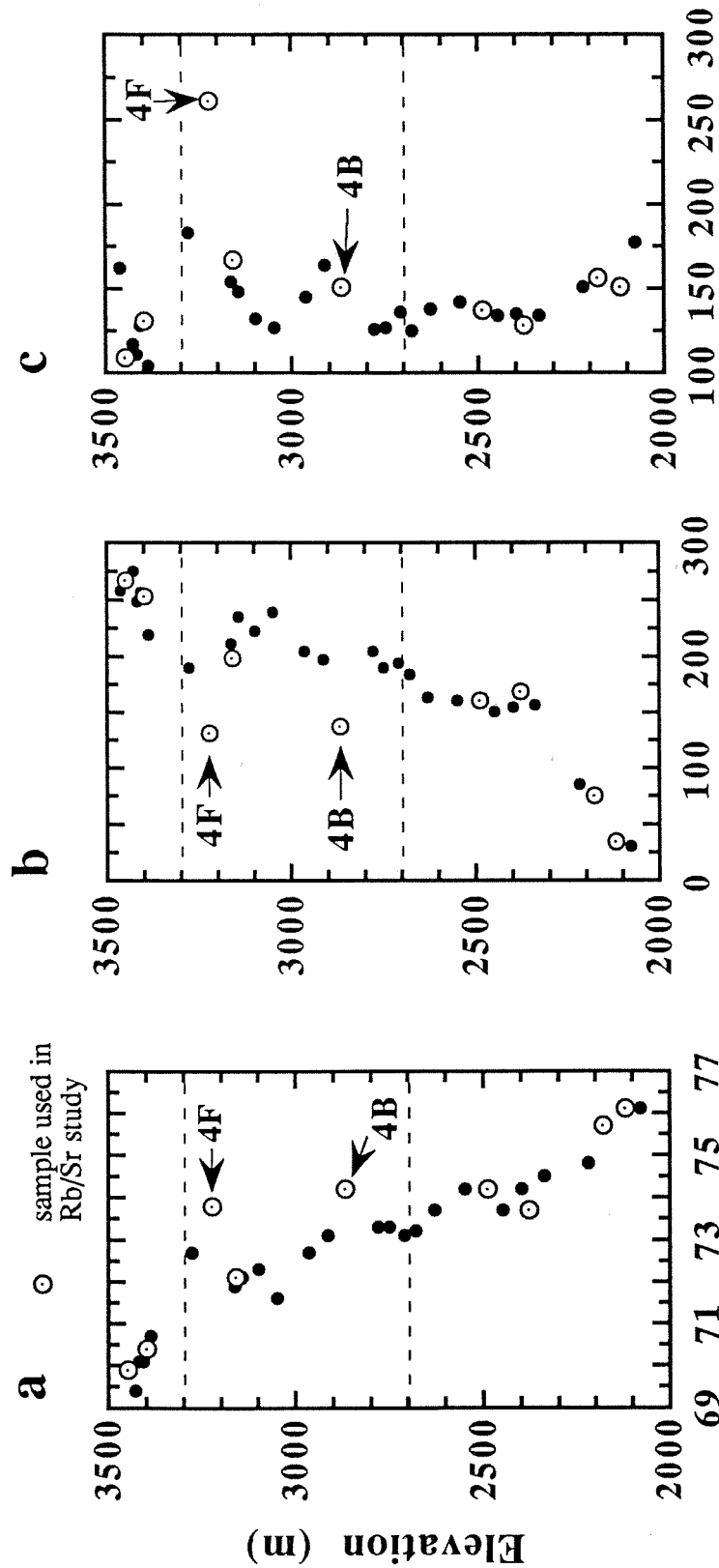


**Figure 6.3** -- Stratigraphic compositional trends in section 1 for (a) $SiO_2$, (b) Sr, and (c) Rb. Samples used in this Rb/Sr study are indicated by open dotted circle. Dashed horizontal lines separate zones A, B, and C (described in Chapter 4). 4F (CG-C2-4F) and 4B (CG-C2-4B) are two samples which plot far from the general major- and trace-element compositional trends.

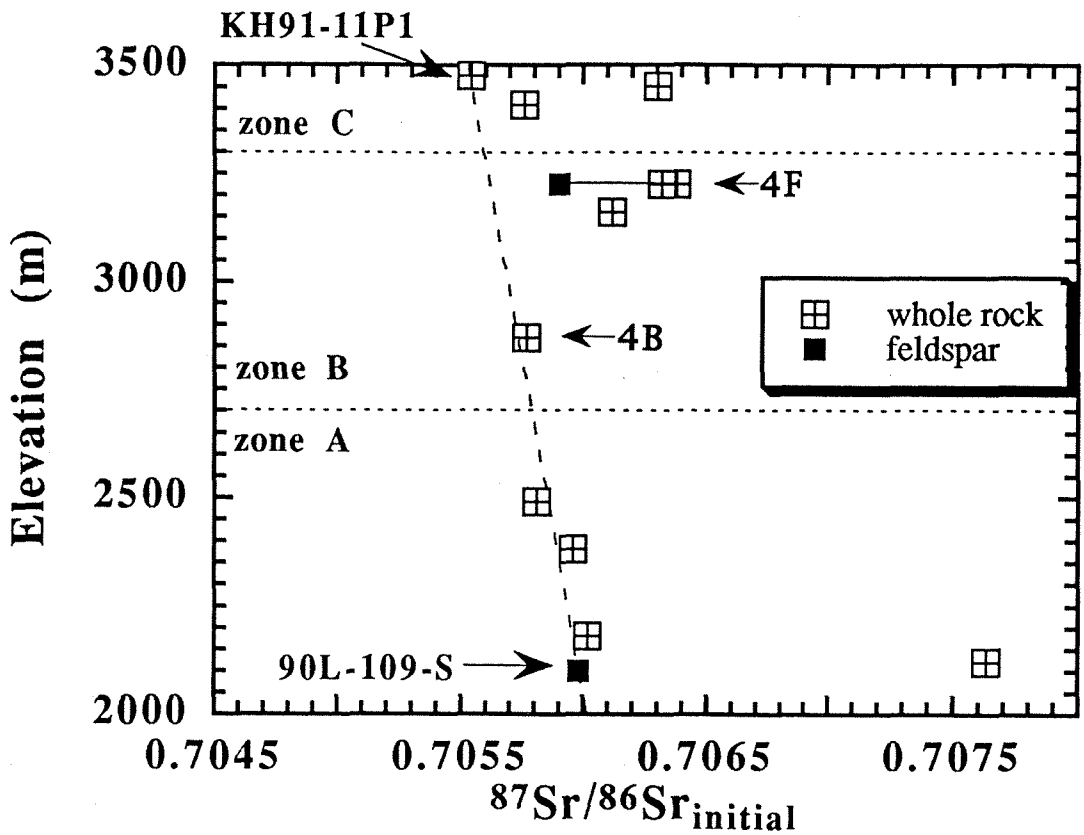


**Figure 6.4** -- Initial $^{87}Sr/^{86}Sr$ ratios vs. elevation (stratigraphic position) for nine samples from Section 1. Two additional samples, a dacitic pumice (KH91-11P1) and sanidine from a marginal vitrophyre (90L-109-S), are projected onto the top and bottom, respectively, of this section. Crossed square = whole rock $^{87}Sr/^{86}Sr_i$; filled square = feldspar $^{87}Sr/^{86}Sr_i$. Dashed lines separate zones A, B, and C (described in Chapter 4).

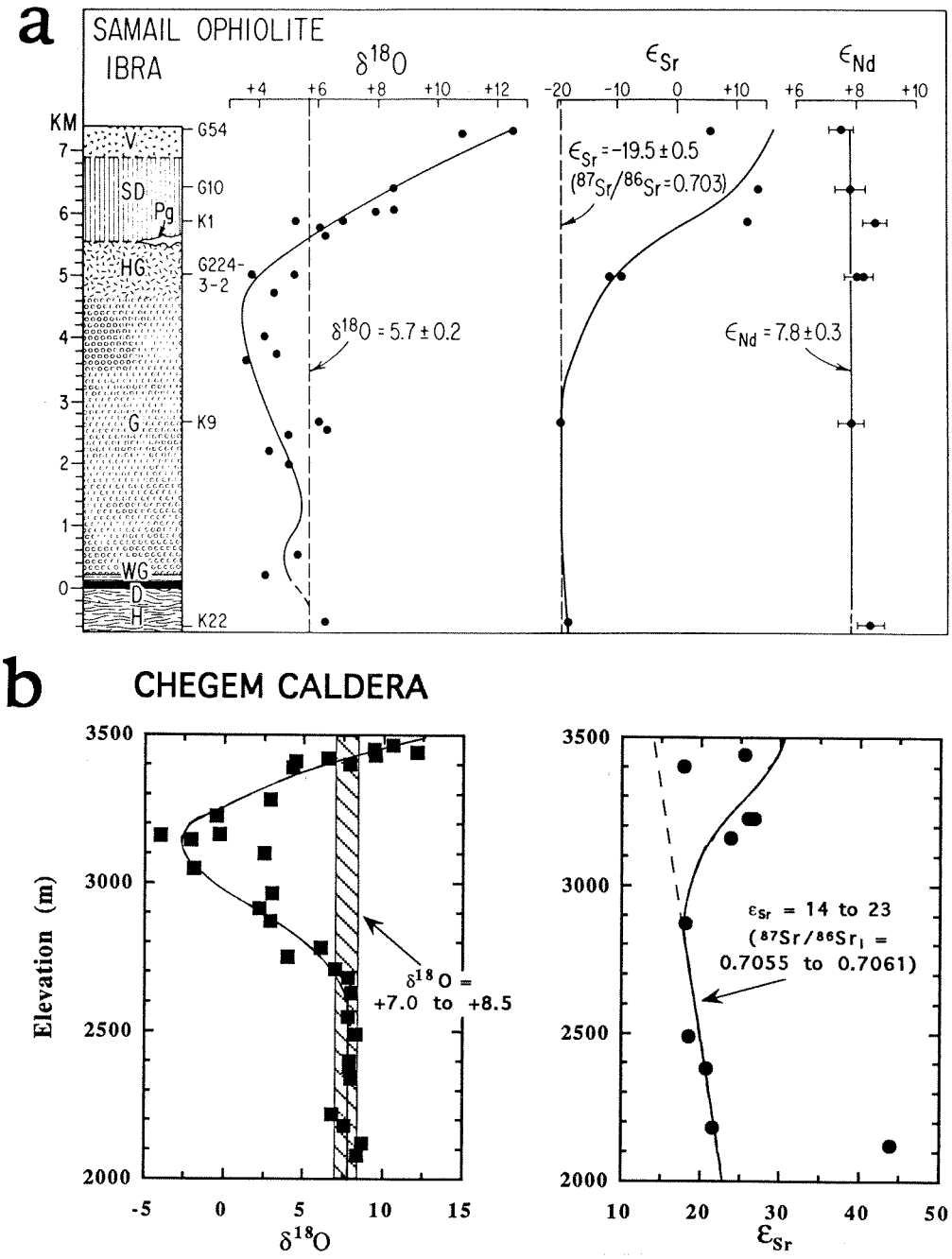


**Figure 6.5** -- Comparison of O and Sr isotopic trends in (a) the Samail ophiolite (from McCulloch et al., 1981), and (b) the Chegem caldera. Vertical dashed lines on Fig. 6.5a represent primary magmatic values. The Samail stratigraphic section is described in McCulloch et al. (1981). On Fig. 6.5b, primary magmatic values are represented by diagonally-rule zone ($\delta^{18}O$) and inclined line ($\varepsilon_{Sr}$). Both geologic settings show similar deviations from their magmatic values in $\delta^{18}O$ and $\varepsilon_{Sr}$ at the top of the section. These isotopic trends are interpreted to be the result of interaction with seawater (Samail ophiolite) and meteoric water (Chegem caldera) in an environment with a thermal gradient.

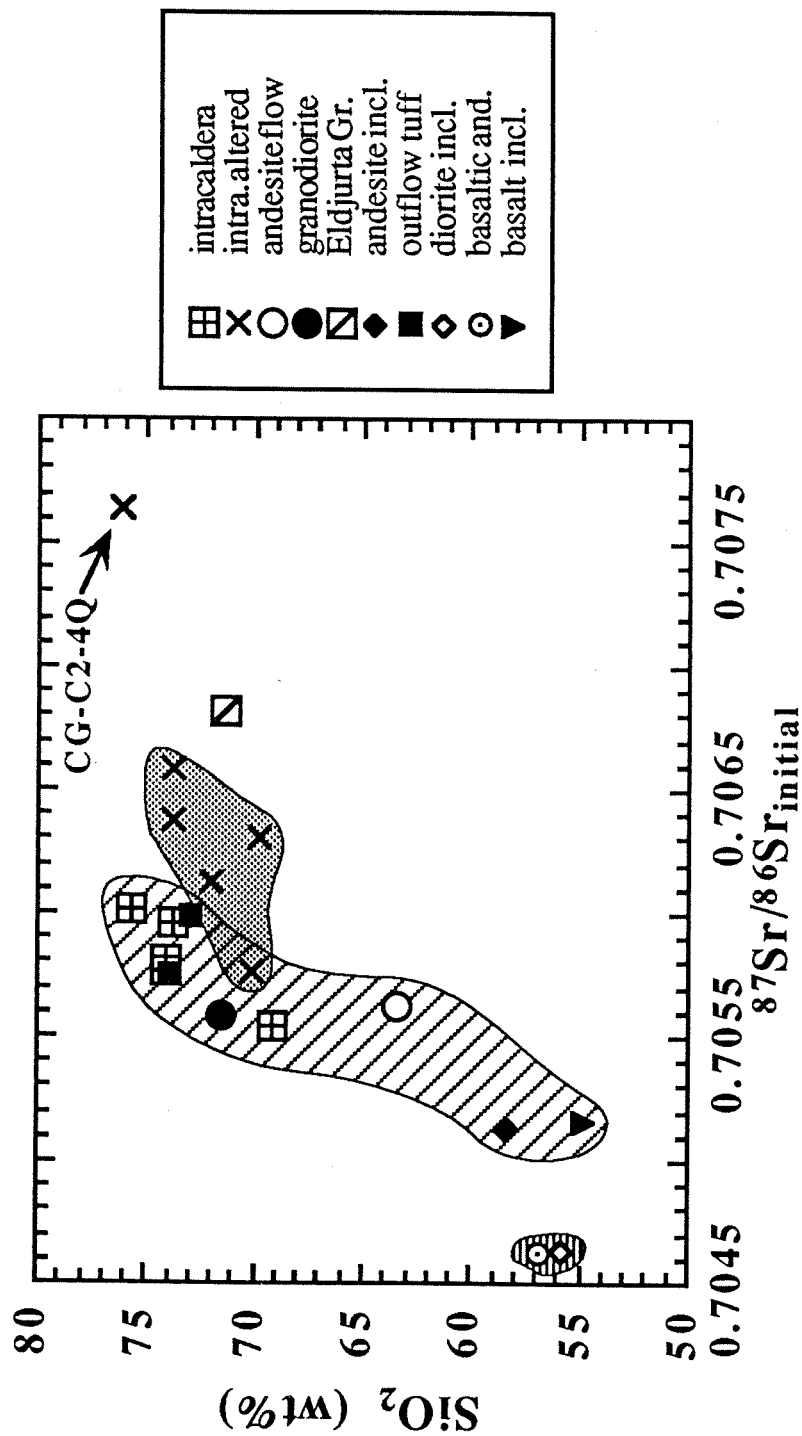


**Figure 6.6** -- $^{87}Sr/^{86}Sr_i$–$SiO_2$ plot containing data from the Eldjurta Granite and all Chegem igneous rocks. Diagonally-ruled envelope = unaltered Chegem igneous rocks; horizontally-ruled envelope = pre-caldera basaltic andesite flow and diorite inclusion from postcaldera andesite; stippled envelope = altered Chegem Tuff; sample CG-C2-4Q is discussed in the text.

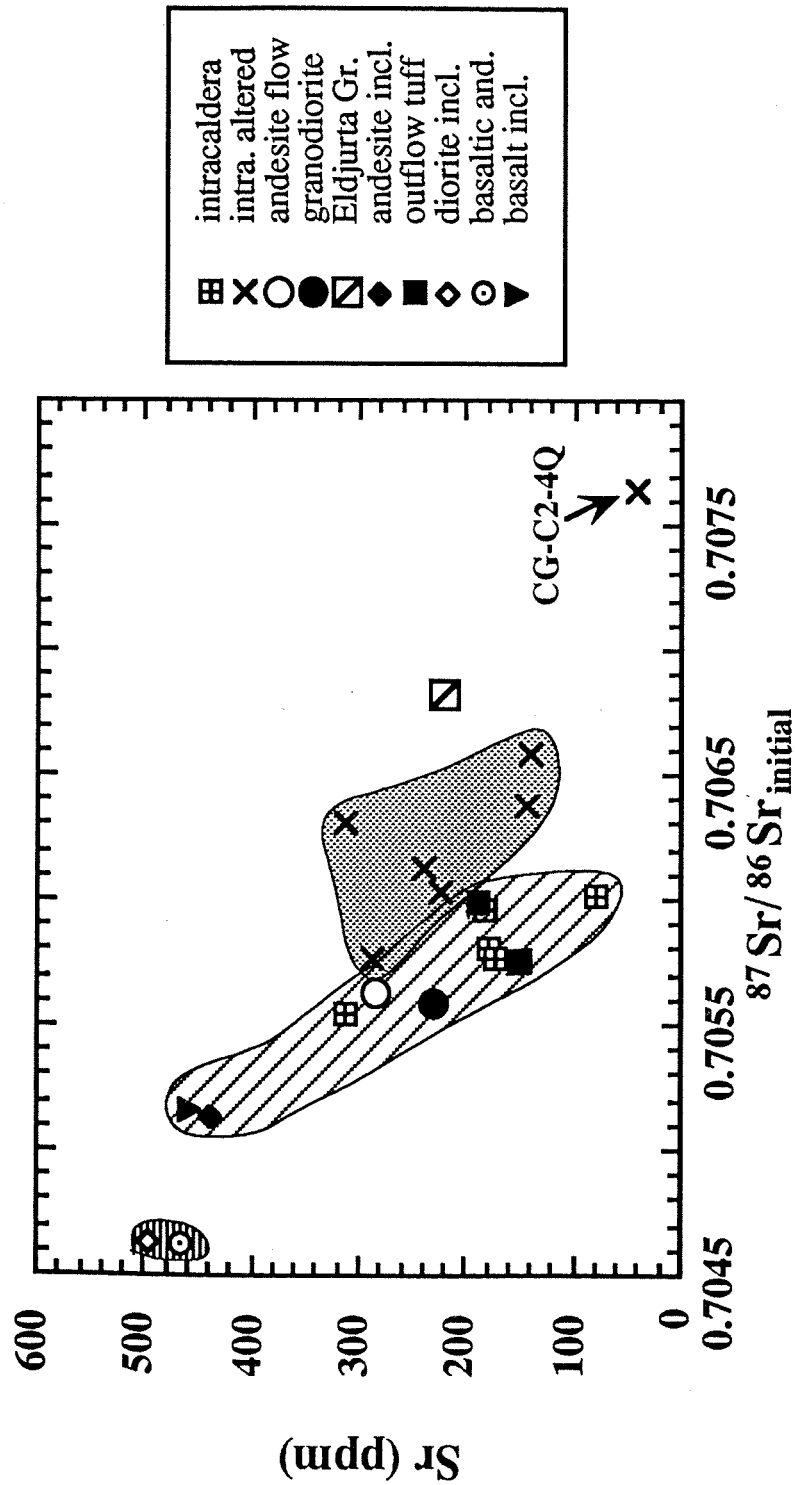


**Figure 6.7** -- $^{87}Sr/^{86}Sr_i$–Sr plot containing data from the Eldjurta Granite and all Chegem igneous rocks. Diagonally-ruled envelope = unaltered Chegem igneous rocks; horizontally-ruled envelope = pre-caldera basaltic andesite flow and diorite inclusion from post-caldera andesite; stippled envelope = altered Chegem Tuff; sample CG-C2-4Q is discussed in the text.

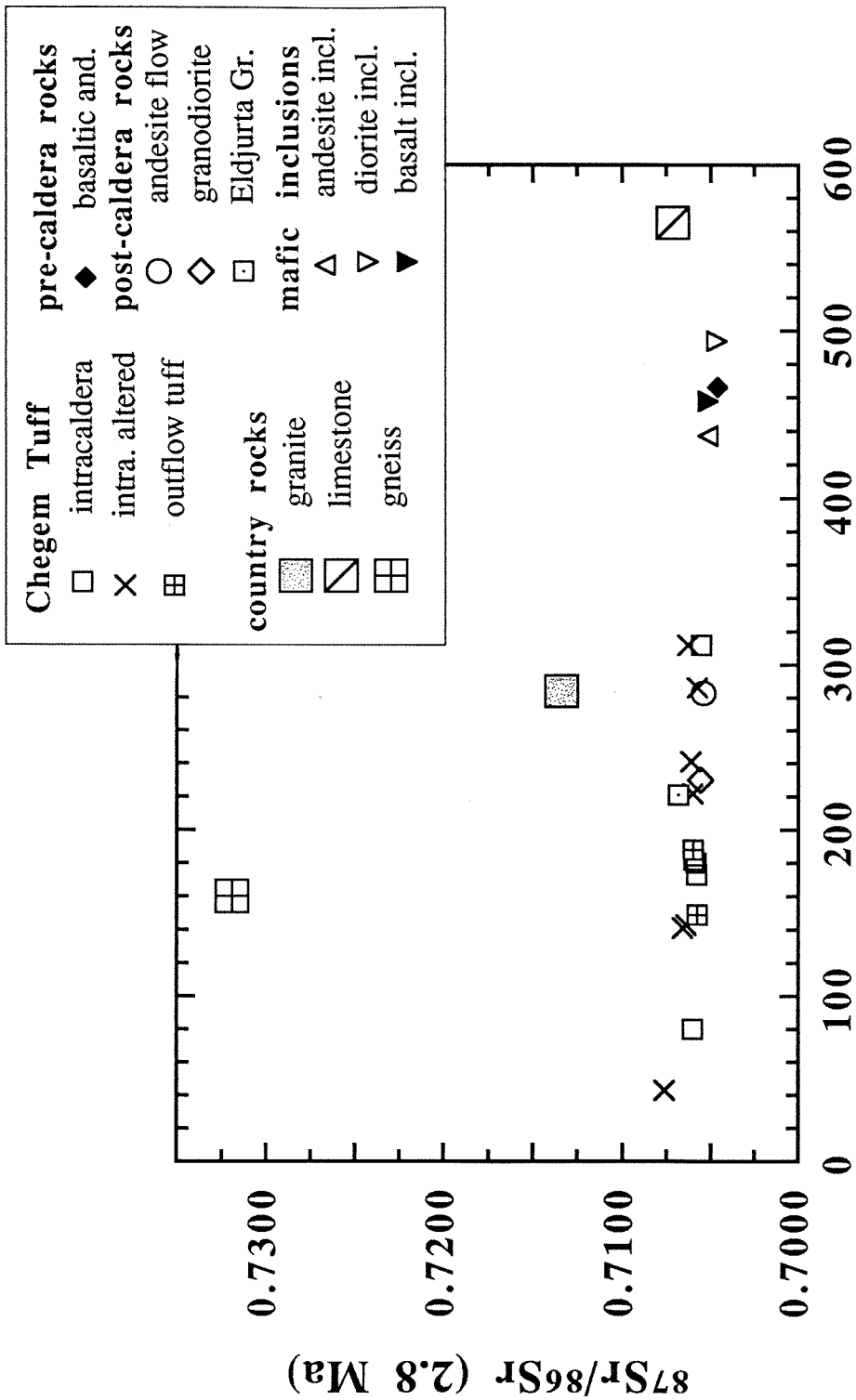


**Figure 6.8** -- $^{87}Sr/^{86}Sr_i$–Sr plot containing data from the Eldjurta Granite, all Chegem igneous rocks and three country rocks (granite, gneiss and limestone) from near the Chegem caldera.

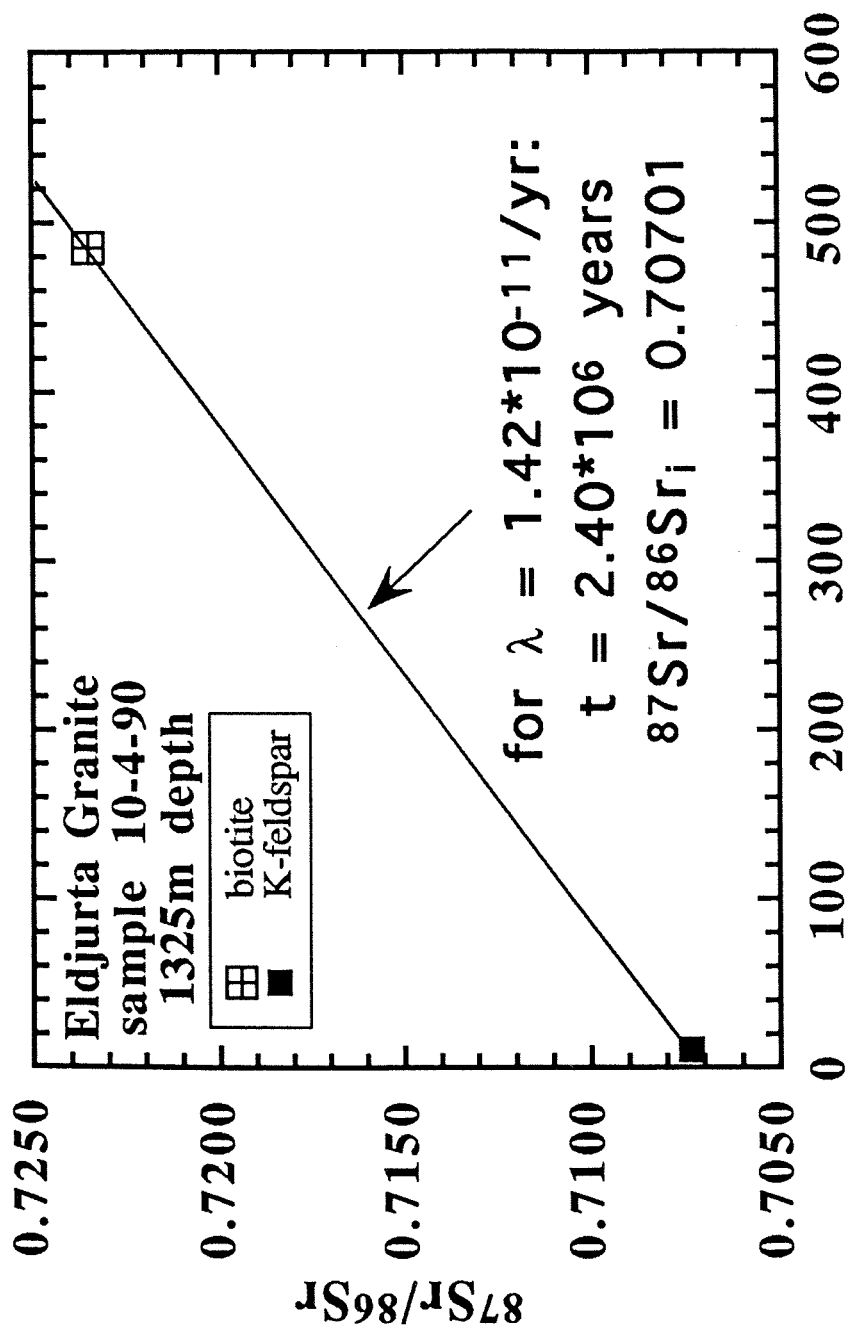


**Figure 6.9** -- Preliminary Rb/Sr isochron plot for Eldjurta Granite sample 10-4-90, collected from 1325m depth in the 4-km drillhole. Two minerals were measured: biotite (crossed square) and K-feldspar (filled square). Assuming a decay constant of 1.42x10-11/yr, a line through these points yields an isochron age of 2.4 Ma and and initial $^{87}Sr/^{86}Sr$ ratio of 0.70701.

# Chapter 7. Summary

In my thesis research, I have carried out a variety of geological and geochemical studies to try to understand the nature of the fluid flow and thermal history of the Chegem caldera and the associated silicic magma system. In this dissertation, for the sake of organization, my observations have been presented according to the analytical technique used. However, in reconstructing the fluid flow/thermal history of the Chegem caldera, it is necessary to consider the results as a whole. The purpose of this chapter is to review the conclusions of the preceding four chapters in the context of the "big picture."

## 7.1 Chegem Caldera - Comparison with Well-studied Ash-flow Calderas of the Western United States

The Chegem caldera is comparable in size to many Tertiary calderas in the western United States. The preserved core of intracaldera tuff covers an area of 11x15 km, but the original topographic size of the caldera was larger, probably

around 15x20 km. In addition, thin outflow sheets are preserved up to 50 km away. This exposure suggests an erupted volume of several hundred (500 or more?) cubic kilometers of ash-flow tuff. For comparison, estimated erupted volumes of some analogous late Tertiary to Quaternary calderas in the U.S.A. are: Lake City caldera, >300 $km^3$ (Lipman et al., 1973); Grizzly Peak caldera, >100$km^3$ (Fridrich and Mahood, 1984); Long Valley caldera, 500$km^3$ (Bailey et al., 1976); Valles caldera, >150$km^3$ (Smith and Bailey, 1966).

Compositionally, the Chegem Tuff ranges from 76 to 69 wt% $SiO_2$, also similar to many ash-flow tuffs in the western United States. Hildreth (1981) provides an informal grouping of ash-flow tuffs based on the compositional zonation of the upper parts of the magma chambers at times of major eruptions. The Chegem caldera would fall into his second group, rhyolites zoned to intermediate compositions. These eruptions are typically hundreds to thousands of cubic kilometers in volume, progressing from rhyolitic to less silicic and forming a caldera 10 to 30 kilometers in diameter (Hildreth, 1981). Examples in the western United States that formed in the last few million years include the Yellowstone caldera, the Valles caldera and the Long Valley caldera.

Despite its similarities to well-studied ash-flow calderas in the United States, the Chegem caldera exhibits certain notable differences. One important difference is that calderas in the western U.S.A. are commonly associated with abundant pre-caldera intermediate-composition volcanic rocks. In Chegem, the only known premonitory volcanism is a single basaltic andesite flow, ≈25 km northeast of the caldera. Lipman et al. (1993) point out that the lack of significant pre-caldera volcanism at Chegem may be due to the fact that the silicic crust in the region had recently been thickened by the Arabian-Eurasian collision and may have served as a density filter for intermediate composition rocks.

Another notable difference between the Chegem caldera and the calderas of the western U.S.A. is the structural simplicity of the Chegem caldera. The intracaldera tuff represents a single cooling unit, without any major erosional breaks. The intracaldera deposits generally dip 5° to 15°, except near the margins of the caldera, indicating that there has only been minor tilting since deposition. The resurgent pluton has pushed up a block of intracaldera tuff, but has not caused the larger-scale doming commonly seen in other calderas (e.g. Lake City; Lipman et al., 1973). Additionally, this thick depositional unit is strikingly coherent with well-preserved columnar joints in its interior. Aside from the faults surrounding the resurgent pluton, only a few small faults (10-50 m displacement) have been observed to cut the intracaldera tuff. This conclusion is, however, somewhat weakened by the lack of reliable stratigraphic markers and limited access to some parts of the caldera.

A third difference between the Chegem caldera and ash-flow calderas of the western U.S.A. is the lack of significant post-caldera hydrothermal activity at Chegem. Compared to many other intracaldera ash-flow tuff deposits, the intracaldera tuff at Chegem is surprisingly unaltered, with little physical evidence for hydrothermal activity. Vitrophyres are strikingly preserved along the margins of the caldera, as are glassy pumices in the upper 100 m of intracaldera tuff. Petrographically and isotopically, feldspar phenocrysts show only minor signs of alteration. The lack of any significant shift in the oxygen isotope composition of feldspar is especially noteworthy, because feldspar is known to exchange oxygen isotopes rapidly in hydrothermal environments. Biotites from the upper part of the caldera sequence are unaltered; lower in the sequence, they have been altered to magnetite, but not chlorite. There is moderate propylitic alteration (albite-epidote-chlorite±pyrite) locally near the resurgent intrusion, but this is only minor compared to the extensive propylitic

alteration seen in many calderas in the western U.S.A. (e.g., Lake City, Grizzly Peak).

Many ash-flow calderas in the U.S.A. have undergone an extended period of hydrothermal activity late in their evolution. Some of the younger calderas (Long Valley, Valles, Yellowstone) are presently in a hydrothermal stage. Two factors which may contribute to the lack of extensive hydrothermal alteration at Chegem are: (1) It is structurally simple, without many throughgoing faults for channelizing fluid flow. Also, the Chegem caldera lacks an extended history of resurgence or of ring-fault intrusions, both of which are known to have provided heat sources to drive hydrothermal circulation in other calderas. (2) The collisional tectonic setting and resultant rapid uplift in the area may have arrested the caldera evolution before significant hydrothermal activity had occurred.

## 7.2 Thermal/Fluid Flow History - Chegem Igneous Rocks

### *7.2.1 Pre-caldera (>2.8 Ma)*

The only known pre-caldera volcanic unit in the Chegem region is a single basaltic andesite flow in the lower Chegem River valley. The whole rock $^{40}Ar/^{39}Ar$ (incremental heating) age of this rock is ≈3.5 Ma. Two pieces of evidence suggest that magma resided near the future Chegem magma chamber: (1) The basaltic andesite contains quartz xenocrysts with the same oxygen isotopic composition as quartz phenocrysts in the Chegem Tuff and in the resurgent granodiorite intrusion. (2) The initial $^{87}Sr/^{86}Sr$ ratio of the basaltic andesite is identical to that of a diorite inclusion from the granodiorite which intrudes the intracaldera tuff. The two rocks also have similar major- and trace-element compositions.

### *7.2.2 Caldera-forming Eruption (2.8 Ma)*

The caldera-forming eruption emitted several hundred cubic kilometers of ash-flow material in a relatively short time (less than a year?), as evidenced by the single complex cooling unit of intracaldera tuff. Minor welding breaks in the upper dacitic horizons of tuff suggest that during the waning stages of the eruption, emission was more sporadic. The intracaldera tuff sequence is zoned in major and trace elements and strontium isotopes, indicating that the magma chamber from which these rocks came was compositionally zoned, a common phenomenon in silicic magma chambers.

During the caldera-forming eruption, a roughly circular collapse structure developed and landslide breccias slid into the edges of the resulting depression. A thick sequence of hot ash was deposited in this caldera, and ash flowed out many kilometers away to the north (and south?). The intracaldera ash-flow was quite hot at this time (≈650-800°C) and welding was quickly initiated, probably within one year of eruption. The margins of the intracaldera tuff were quenched to form vitrophyres. The uppermost dacitic horizons were also cooled fairly rapidly, allowing for the preservation of glassy pumices. As the tuff welded and cooled, the glassy groundmass began to devitrify, forming fine-grained quartz and feldspar crystals, often in spherulitic form.

### *7.2.3 High-temperature Hydrothermal Event*

Our data indicate that immediately after the caldera-forming eruption, there was a short-lived, but intense hydrothermal event involving high-temperature meteoric water. Based on the lack of mineralogical and isotopic alteration in high-temperature phenocryst minerals, in conjunction with the pronounced $^{18}O$ depletions in the intracaldera tuff, we conclude that the hydrothermal event occurred at temperatures of 500-600°C. The meteoric water

involved had a $\delta^{18}O$ similar to that of modern Chegem River water (–12). This water was rich (5-10 ppm) in radiogenic strontium, derived from the Paleozoic and Proterozoic basement rocks to the south and west of the caldera. Perhaps the strontium was leached from megabreccias and lithic fragments of that rock, which were incorporated into the hot intracaldera tuff during eruption.

Mass balance considerations imply that at least 64 $km^3$ of water passed through the intracaldera tuff sequence and became heated to 500-600°C. Water flowed along small (500-800m?), single-pass circulation cells, and was expelled as hot steam, channelized in fissures and fumaroles as it exited the tuff. Flow was localized in the upper 750 m of tuff, especially focused along a poorly-welded horizon which is presently at 3160 m elevation. Meteoric water did not penetrate below 750 m depth in any significant quantity. Two possible explanations for this are: (1) By the time the water had penetrated to this level, the groundmass had entirely crystallized and the welded tuff below that level had become considerably less permeable than the tuff above it. (2) The fluids were mainly channelized along a zone of poor welding and enhanced permeability.

While this high-temperature hydrothermal system was active , the meteoric waters exchanged oxygen and strontium isotopes with the groundmass of the tuff. At this time, there must have been a steep thermal gradient in the upper 100-200 m of intracaldera tuff. Because of the strong temperature dependence of oxygen isotope fractionations between silicates and $H_2O$, this thermal gradient also produced an upward gradient in $\delta^{18}O$ in the tuff sequence. Near the surface of the deposit, where glassy samples were being hydrated and exchanged at low temperatures, the $^{18}O/^{16}O$ ratios of the rocks increased relative to the magmatic value; whereas deeper in the section, where temperatures were still high, the $^{18}O/^{16}O$ ratios were lowered. Meanwhile, this water-rock interaction is believed to have been responsible for raising the $^{87}Sr/^{86}Sr$ ratios of

many of the rocks in the hydrothermal system, independent of depth, because the waters were more radiogenic than the rocks and strontium isotope fractionations are not dependent on temperature.

The duration of fluid flow is best constrained by the oxygen isotope systematics of the Chegem rocks. Feldspar phenocrysts, which characteristically exchange oxygen isotopes fairly rapidly, have in this case exchanged at most ≈10% of their oxygen. This limits the duration of the water-rock interaction to 10-25 years if the estimated water-rock interaction temperatures were 500-600°C.

Given the estimates of minimum fluid volume and maximum timescale and assuming flow is in 750m hydrothermal convection cells, we estimate minimum fluid fluxes of about $2.2 \times 10^{-6}$ to $1.1 \times 10^{-5}$ mol/cm$^2$-sec. Such fluxes can be achieved for the hypothesized flow geometry if the tuff has permeabilities of 5 to 25 millidarcies.

We believe that the short, very hot hydrothermal event at the Chegem caldera is comparable to the vigorous fumarolic activity which occurred at the Valley of Ten Thousand Smokes (VTTS), Alaska immediately after the 1912 eruption of Novarupta volcano. The two settings share the following characteristics: (1) Both events were short-lived, lasting less than 25 years. The high-temperature hydrothermal activity at VTTS had largely ceased after 15 years. (2) Large volumes of meteoric water passed through the upper level of a welded tuff deposit. (3) The temperatures of water-rock interaction were extremely high. At the Valley of Ten Thousand Smokes, fumarole temperatures up to 645°C were measured six years after the eruption. However, the ash-flow sheet at VTTS is an outflow facies only 200m thick, and so it is impossible for a magma chamber to have been involved in the heating process there.

There are, of course, differences between the Chegem caldera and the VTTS, most notably the size and geometry of the erupted deposit. The Chegem

caldera erupted at least 10 times more ash-flow than Novarupta and the deposits in the Chegem caldera are at least ten times thicker than those at VTTS. In addition, the hydrothermal activity at Chegem occurred within densely welded intracaldera tuff, while at VTTS it is within more poorly welded outflow tuff which fills a valley. However, these different geometries might imply that hydrothermal activity was more vigorous at Chegem than at VTTS.

### *7.2.4 Emplacement of Post-caldera Igneous Rocks*

Less than 50,000 years after the caldera-forming eruption, as the mass of intracaldera tuff continued to cool, resurgence began, focused on the northeast side of the caldera. In that region, a granodiorite porphyry intruded the caldera fill, pushing up and tilting a large block of rhyolite tuff along high-angle faults. At this point, the high-temperature hydrothermal event had largely ceased, but small amounts of meteoric water penetrated the granodiorite as the groundmass crystallized and the resultant volume change created a fracture permeability. The granodiorite may mark the core of a stratovolcano which erupted andesites flows on top of the intracaldera tuff sequence, inasmuch as its age, initial $^{87}Sr/^{86}Sr$ and feldspar $\delta^{18}O$ are indistinguishable from the andesite flows that overlie the intracaldera tuff.

The post-caldera andesite flows may have been erupted in a single event, or intermittently over a period of time. On the southeast side of the caldera, on Kum Tyube peak, they clearly overlie an erosional layer containing reworked tuff and glacial deposits. In other places on the south side of the caldera, they appear to flow into paleodrainages in the upper dacitic tuff units. Thus, a short interval of erosion and glaciation (hundreds of years?) must have preceded the eruption of these flows. On Mt. Kyugenkaya, on the east side of the caldera, the andesite flows lie directly on poorly welded tuff indicating either that erosion did not

occur at the same rate on this side of the caldera, or that these flows were deposited earlier than the flows on Mt. Kum Tyube. The whole rock $^{40}Ar/^{39}Ar$ age (incremental heating) of such an andesite is analytically indistinguishable from the age of the Chegem Tuff and the granodiorite intrusion (2.8 Ma). The andesite flows are isotopically unaltered, indicating that the meteoric-hydrothermal activity which altered the Chegem Tuff had ceased on this paleosurface at the time that the andesite flows were erupted.

## 7.3 Thermal/Fluid Flow History - Eldjurta Granite

### *7.3.1 Thermal History*

While the volcanic activity at Chegem was occurring, the magma of the Eldjurta Granite was probably collecting in a shallow magma chamber. The actual crystallization age of the Eldjurta Granite is not known, but cooling ages through the "closure temperatures" for diffusion of Ar in biotite (≈350°C) are well-documented for a 5-km vertical profile into the granite (Chapter 3; Hess et al., 1993). The upper margin of the pluton passed through the ≈350°C isotherm at approximately 2 Ma. Over the next 400,000 years, deeper levels of the pluton passed through this isotherm. The isotherm migration rate at that time was ≈13mm/yr, due to a combination of downward migration of isotherms into the cooling pluton and regional uplift and erosion. The cooling rate over this time interval was also quite high, between 200° and 500°C/Ma. After 1.4 Ma, the uplift and cooling slowed to below the net rates of <5.5mm/yr and 130°C/Ma.

By approximately 0.8 Ma, a second magma, similar in composition to the main body of Eldjurta Granite, had intruded the Eldjurta Granite ≈4.5 km below its roof. The intrusive contact at the roof of this second pluton was sheared slightly and the upper border of the younger intrusion was quenched to a finer grain size. The present day geothermal gradient in the Eldjurta granite is still

fairly high (43°C/km), possibly because heat from this magma body is still being dissipated.

### *7.3.2 Fluid Flow*

Oxygen isotope studies of minerals from eight samples collected at ≈500m intervals in a 4-km deep drillhole indicate that there has not been any extensive interaction between meteoric water and the Eldjurta Granite below 800m depth (≈1900 m below the roof of the pluton). At 800m depth, near a set of veins and dikes, the $\delta^{18}O$ values of all minerals, including quartz, have been lowered by 0.5 to 3 per mil, indicating that they have interacted with isotopically light (probably meteoric) waters at high temperatures. As the biotite $^{40}Ar/^{39}Ar$ ages of these samples have not been reset, this water-rock interaction must have occurred while the pluton was still cooling, before that particular level had cooled to ≈350°C.

In addition to the sample at 800m depth, the surface samples show some isotopic effects of water-rock interaction. The K-feldspars are markedly lower in $^{18}O$ than coexisting plagioclases, indicating that the K-feldspars exchanged $^{18}O$ in an open system down to lower temperatures. Kostitsyn and Kremenetskiy (1994) also observed a lowering of $\delta^{18}O$ toward the upper contact of the Eldjurta Granite and interpreted this to be the result of interaction with meteoric waters. More detailed isotopic studies are necessary to fully understand the extent of water-rock interaction near the roof zone of the Eldjurta Granite.

### *7.3.3 Tirniauz Ore Deposits*

The Tirniauz Mo-W deposit, the largest scheelite-molybdenite deposit in Russia, is located at the upper contact of the Eldjurta Granite, associated with a ≈2-km thick hornfels and skarn zone. Though the deposits are adjacent to the

Eldjurta Granite, the molybdenum mineralization appears to be genetically related to two small (<1 km) leucogranite bodies.

As described in Chapter 2, there has been considerable controversy over relationship of the Tirniauz deposits and the Eldjurta Granite. Many researchers have assumed the Eldjurta Granite and Tirniauz deposits are genetically related because of their close spatial association (Smirnov, 1977). A recent Rb-Sr age of an ore-bearing rock is identical to that of the Eldjurta Granite, thus supporting a genetic relationship (Zhuravlev and Negrey, 1993, 1994). However, there are several arguments against the ore body being genetically related to the Eldjurta Granite. These arguments are based on heat calculations (Liakhovich, 1953, 1976; Rodzyanko, 1969; Rodzyanko et al., 1973) and geochronological studies (Borsuk, 1979) combined with field relationships, which indicate that the ore body predates the granite.

Our $^{40}Ar/^{39}Ar$ studies (Chapter 3) reveal that the Eldjurta Granite cooled through temperatures of 200-400°C very quickly with very high isotherm migration rates. We argue that these rates were caused at least in part by downward migration of isotherms. That is, the Eldjurta Granite produced a significant thermal anomaly when it was emplaced, thus creating a conducive environment for hydrothermal convection. Our oxygen isotope studies and those of Kostitsyn and Kremenetskiy (1994) further support this idea as there are signs of high-temperature oxygen exchange with meteoric water in the upper parts of the pluton. This water did not penetrate more than 1.9 kilometers below the roof of the pluton. However, though we see evidence for hydrothermal activity at the roof of the Eldjurta Granite, that does not necessarily mean that the hydrothermal fluids were responsible for the Tirniauz deposit. More detailed isotopic studies of the uppermost kilometer of Eldjurta Granite and of the ore body itself are necessary to resolve this relationship.

## 7.4 Relationship of the Chegem Volcanics Rocks and Porphyry Intrusion to the Eldjurta Granite

The Eldjurta Granite and the Chegem granodiorite porphyry intrusion are among a regional belt of young granitic intrusions in the greater Caucasus Mountains (termed "neointrusions" by Gurbanov and Favorskaya, 1977). The location of the two intrusions along a major longitudinal fault suggests that this structure was partially responsible for the upward migration of these magmas in the crust. Based on similarities in whole-rock and mineral (biotite) chemistry, along with spatial and temporal proximity, Lipman et al. (1993) suggest that the Eldjurta Granite and the Chegem granodiorite are comagmatic and may even be physically connected in the shallow crust.

The isotopic evidence presented in this thesis argues against any direct physical connection between the bodies. The oxygen isotopic compositions of feldspar and quartz phenocrysts in the two bodies are distinctly different: all $^{18}O/^{16}O$ ratios in the Eldjurta Granite are ≈1.5 per mil higher than in the Chegem volcanic and intrusive rocks. This implies that the magmas coexisting with these phenocrysts were isotopically distinct and could not have been in physical or chemical contact for any significant amount of time just prior to emplacement. Moreover, the initial $^{87}Sr/^{86}Sr$ of the Eldjurta Granite is much higher than all Chegem igneous rocks, except for one low-Sr vitrophyre which has clearly been contaminated. There is also a broad correlation among the Chegem igneous rocks between initial $^{87}Sr/^{86}Sr$ and chemical composition, and the Eldjurta Granite does not fit into these Chegem trends.

The isotopic differences between the Eldjurta Granite and the Chegem igneous rocks imply that the two magmas must have evolved separately at some time. I suggest three possibilities: (1) The two magmas were always physically

separate but were probably formed by similar tectonic processes which account for their similar chemistries. (2) The Eldjurta Granite and the Chegem granodiorite come from two cupolas of a single magma chamber, but the isotopic composition of the Eldjurta magma was markedly changed by assimilation of higher-$^{18}O$, more radiogenic country rock. (3) The two magmas were part of the same magma chamber but were erupted and/or crystallized at different times. That is, the Chegem granodiorite intruded the caldera fill shortly after the caldera-forming eruption 2.8 Ma while the Eldjurta Granite represents the magma which remained and continued to evolve. Its different isotopic composition must be due to assimilation of higher-$^{18}O$, more radiogenic country rock after the caldera-forming eruption.

### 7.5 Concluding Questions

As is often the case when one makes a lot of new measurements and sets out to understand a part of nature, I am left with almost as many questions as I began with. Here are a few:

1. Our first summer at Chegem, we sampled only the bottom and the top of the Kum Tyube section. This was because we didn't have time to sample the intermediate stratigraphic levels, which were not exposed in the bottom of the drainage that we traversed. It later turned out that the rocks which we did not sample that first summer were in fact all very low in $^{18}O$. Was this a coincidence or is the fact that these rocks were not exposed in the drainage perhaps related to the hydrothermal event that produced their low $\delta^{18}O$ values?

2. How similar are the hydrothermal events which occurred at the Chegem caldera and at the Valley of Ten Thousand Smokes (VTTS)? What does the $\delta^{18}O$

of a stratigraphic section of the tuff in the VTTS look like? Are the rocks away from the fumaroles at VTTS mineralogically altered at any level? Data from proposed scientific drilling at VTTS may help to answer these questions.

3. What was the source of meteoric water which passed through the hot Chegem Tuff? A glacier? A lake? A river? Groundwater?

4. How common are these short-lived, intense hydrothermal events in nature? What conditions are necessary to initiate such an event? Maybe they are actually quite common, but the evidence of their existence is quickly obscured.

5. Are the pre-caldera basaltic andesite flow and the diorite inclusion in the post-caldera granodiorite from the same magma batch or are their similarities in initial $^{87}Sr/^{86}Sr$ and chemical compositions merely a coincidence?

6. The Chegem caldera is the only known ash-flow caldera in the entire Greater Caucasus Mountains, which is a cratonic collision zone. Why? Are there also calderas like this in the Himalayas?

7. How is the Eldjurta Granite related to the Chegem caldera? Is it the result of assimilation and fractional crystallization in the Chegem magma chamber after the caldera-forming eruption? Or is it from a separate magma body?

8. The Chegem caldera lies near the intersection of regional east-west structures with the transverse structures of the Trans-Caucasus Rise. The east-west structure is a regional unconformity between Paleozoic-Proterozoic basement and Jurassic-Cretaceous sedimentary deposits. How did these structural intersections influence the migration of the Chegem and Eldjurta magmas?

# Appendix A. Field Descriptions of Samples

Samples were collected during two field seasons, in the summers of 1990 and 1991. Samples beginning with the prefixes CG-C- and 90L- were collected during the summer of 1990; those which have the prefixes CG-C2- and KH91- were collected during the summer of 1991. Samples are listed below, along with a brief field description of the rock. Locations of the Chegem caldera samples are shown on Plate 2. Where a sample has two number designations, the second is given in parentheses after the first.

**Summer, 1990**

CG-C-1 -- Holocene volcanic rock from upper station on Mt. Elbrus
CG-C-2 -- vitrophyre from columnar jointed area near Mt. Elbrus- 1 1/2 km south of Azan station up Azan river
CG-C-3A -- granodiorite near contact with diorite (diorite cuts granodiorite) - same locality as CG-C-2, but west side of river
CG-C-3B -- diorite, same locality
CG-C-4 -- mica schist contains andalusite, sillimanite, collected at upper Cheget station (Mt. Elbrus), ≈300m from contact with granite. Precambrian
CG-C-5 -- same mica schist 400m lower in elevation, near 1st station on Cheget lift (Mt. Elbrus)
CG-C-6 -- gneiss, country rock of Eldjurta granite from depth 226m (≈1500m drillhole)
CG-C-7 -- Paleozoic granite from same drill hole 265m
CG-C-8A,B -- country rock - augen gneiss; 8A -- 284m; 8B -- 291m, "remobilized granite" (≈1500m drillhole)
CG-C-9 -- Eldjurta granite within 5m of country rock 316m (≈1500m drillhole)
CG-C-10 -- Eldjurta granite 803m (≈1500m drillhole)
CG-C-11 -- Eldjurta granite 1112m (≈1500m drillhole)
CG-C-12A --fine-grained inclusion in marginal Eldjurta granite ≈60m (150m?) above Baksan river
CG-C-12B -- hornfels - mafic inclusion in granite near contact, same location
CG-C-12C*(90L-100)* -- fresh Eldjurta granite at this location
CG-C-13 *(90L-101)* -- liparite dike sample, south neck (there are three necks) - collected as float ≈150m (?) above Baksan river
CG-C-14 *(90L-101)* -- liparite dike sample, middle neck - collected at same area
CG-C-15 *(90L-102)* -- obsidian from Baksanges area (Zayukovo site, lower Baksan River) source unknown, dated by K/Ar at 1.5 Ma
CG-C-16 -- welded tuff with granite inclusions collected from base of exposure ≈250m above Chegem River downstream from Bashil camp

CG-C-17 *(90L-103)* -- near basal vitrophyre, bottom level of three, downstream from Bashil camp
CG-C-18 -- granite, along steep contact with vitrophyre
CG-C-19 *(90L-104)* -- basal vitrophyre, along steep contact with granite
CG-C-20 *(90L-105)* -- vitrophyre, from west part of "Bashil dam", many lithic fragments, may represent unit below lowest exposed level, also CG-C2-1
CG-C-21A -- limestone xenolith from vitrophyre on west side of caldera (just south of Bulungu village) contact between vitrophyre and devitrified zone is shaped "like a bull"
CG-C-21B -- brown devitrified tuff from same location
CG-C-21C -- black vitrophyre, same location
CG-C-22 -- devitrified tuff from crack which looks like dike, just (50m?) south of CG-C-21
CG-C-23 *(90L-109)* -- vitrophyre along road , SW of Bulungu village, most probably out of place
CG-C-24 -- schist from Precambrian (?) basement, at top of hill above sample CG-C-23
CG-C-25A *(90L-106A)* -- devitrified tuff from summit of erosional outlier (3518m)
CG-C-25B *(90L-106B)* -- upper devitrified tuff, just downhill of CG-C-25A
CG-C-26 *(90L-106C)* --upper vitrophyre, same erosional outlier
CG-C-27A -- light, less consolidated layer above lower vitrophyre, same erosional outlier
CG-C-27B *(90L-106D)* -- lower vitrophyre, same erosional outlier
CG-C-28 -- country rock, schist, within 50m of contact
CG-C-29A,B -- small limestone clasts from megabreccia, east side of caldera, opposite Bulungu village
CG-C-30 -- unwelded tuff, has many lithic fragments, east side of caldera, opposite Bulungu village
CG-C-31 *(90L-108)* -- basal vitrophyre above limestone megabreccia, east side of caldera, opposite Bulungu village
CG-C-32 -- aplite with garnets, in Hercynian (?) country rock on southwest margin of caldera, altitude 3580m
CG-C-33 -- mica schist, ≈50m from contact with volcanics (southwest side of caldera), altitude 3700m
CG-C-34A *(90L-113A)* -- highest exposed tuff on southwest side of caldera, red, altitude 3642m
CG-C-34B *(90L-113B)* -- large glassy pumice from tuff like CG-C-34A, found in float, same location
CG-C-34C *(90L-113C)* -- similar tuff to CG-C-34A, but grey, not red, same location
CG-C-35 -- granite, ≈20m from contact with tuff, southwest side of caldera
CG-C-36 *(90L-113D)* -- welded tuff, forms cliff at 3440m, southwest side of caldera
CG-C-37 -- Hercynian (?) granite, ≈1 km from Bashil camp, down river valley to west
CG-C-38 -- Hercynian (?) granite, 1 1/2 km (?) from camp (≈4km from caldera)

CG-C-39 -- amphibolite, 2 km from camp where river begins to cut canyon
CG-C-40 -- granite, ≈1 1/2 km west of sample CG-C-39
CG-C-41 -- gneiss, 500m west of sample CG-C-40
CG-C-42 -- samples collected by P. Lipman and A. Gurbanov from Riga Sary-su dike traverse
42A *(90L-111A)* -- devitrified interior
42B *(90L-111B)* -- vitrophyric block in marginal tuff breccia
42C *(90L-111C)* -- non-welded tuff breccia within a few meters of contact
42D *(90L-111D, A. Gurbanov sample: 98/90)* -- granite, 1/2 meter from contact
42E *(90L-111E, AG 98-1/90)* -- granite, 50 m from contact
(these samples, 42A-42E are from 2960 to 2970 m altitude)
42F *(90L-111F, AG 99/90)* -- vitrophyre near bend of "dike", 3110 m
42G *(AG 99-1/90)* -- black vitrophyre breccia, 100 m above 90L-111B
42H *(AG 97-2/90)* -- very fresh vitrophyre, block from breccia
CG-C-43 -- samples collected by P. Lipman and A. Gurbanov from Riga Sary-su dike, upper part of section
43A *(90L-112A)* -- granite, 10m below contact at 3200 m
43B *(90L-112B)* -- vitrophyre, a couple of meters above contact at 3210 m
43C *(90L-112C)* -- large pumice from 3260 m
43D *(90L-112D, AG 100/90)* -- near-vitrophyric tuff, grey, 3440m
43E *(99-1/90)* -- vitrophyre, 300 m from bend, near CG-C-43A
CG-C-44 -- Chegem tuff reference section, 1600 m of section, sampled by C. Gazis, K. Hon and P. Marchev, southeast side of caldera
44A *(90L-107A)* -- light grey devitrified tuff, 2180m
44B *(90L-107B)* -- light grey devitrified tuff, 2340m
44C *(90L-107C)* -- light grey devit. tuff with pumices, 2380m
44D *(90L-107D)* -- light grey devit. tuff, ≈2400m
44E *(90L-107E)* -- light grey devit. tuff, 2490m
44F *(90L-107F)* -- medium grey devit. tuff, 2680m
44G *(90L-107G)* -- medium grey devit. tuff, 3280m
44H *(90L-107H)* -- dark grey devit. tuff, 3390m
44I *(90L-107I)* -- grey and black vitrophyre, 3400m
44J *(90L-107J)* -- grey and black vitrophyre, 3410m
44K *(90L-107K)* -- dark grey devit. tuff, 3420m
44L *(90L-107L)* -- grey and back vitrophyre, 3430m
44M *(90L-107M)* -- tan and black partial vitrophyre, 3450m
44N *(90L-107N)* -- tan, partly-welded tuff, 3465m
44O *(90L-107O)* -- non-welded tuff at top of unit, 3485m
44P *(90L-107P)* -- black, nearly vitrophyric andesite resting on tuff, 3490m
44Q *(90L-107Q)* -- light grey, partly altered andesite from top of peak, 3775m
CG-C-45 -- tuff from East Lechnikai section
45A *(90L-117A)* -- lowest exposed level, dark grey
45B *(90L-117B)* -- tuff, slightly higher than 45A, lighter grey, sharp contact between the A and B
45C *(90L-117C)* -- tuff from block from top of cliff, more crystal-rich, euhedral biotites

CG-C-46 *(90L-118)* -- tuff from Kaminka quarry, near Yaniki, rich in lithics
46B -- lithic fragment (from Main Range?)
CG-C-47A *(90L-119)* -- tuff from Lechnikai quarry, highest exposed level, has lithic fragments, large white pumices
CG-C-47B -- tuff, 50-100m lower in elevation, tuff has black, white and mixed pumices; *90L-120* -- pumices from this site
CG-C-48A *(90L-121A?)* -- tuff, collected at saddle, ≈100m from top of Taraklan hill
CG-C-48B *(90L-121B?)* -- tuff from top of Taraklan hill, grey, fairly glassy
CG-C-49 -- limestone across from bog at low flat bend in road
CG-C-50 *(90L-121C)* -- vitrophyre, collected by P. Lipman from boulder near camp, probably comes from the base of the unit sampled on Taraklan hill
CG-C-51 *(90L-115)* -- welded tuff from deep interior of caldera, collected up Dzhilgisu river by P. Lipman and A Gurbanov 390 m above Bulungu bridge
CG-C-52 *(90L-116)* -- welded tuff, deep interior, collected by P. Lipman and A Gurbanov 300 m up Dzhilgisu river from Bulungu bridge
CG-C-53A *(90L-122A?)* - granite porphyry, ≈1 m from contact with welded tuff, collected by P. Lipman (3229m), side valley of R. Dzhilgisu
CG-C-53B *(90L-122B?)* -- welded tuff, ≈1 m from contact, collected by P. Lipman, (3230 m)
CG-C-54 -- welded tuff at top of ridge, (3340m)
CG-C-55 -- welded tuff from end of ridge (away from contact with granite), propylitized (3390m)
CG-C-56 *(90L-123)* -- granite porphyry from main gully (3020m)
CG-C-57 *(90L-124)* -- granite porphyry from "Tsvetkov pass" (3100m)
CG-C-58A *(90L-125A)* -- granite porphyry, collected ≈5 m from contact with tuff where contact crosses ridge (3210m), *90L-125B,C* -- mafic inclusions in granite
CG-C-58B -- welded tuff, ≈4 m from same contact
CG-C-59 -- limestone from slumped block, ≈1 km from east border of tuff unit
CG-C-60A,B,C -- limestone, traverse into fault where road crosses river (bridge)
60A -- 30 m from fault; 60B -- 18 m from fault; 60C -- 4 m from fault
CG-C-61 -- schist, chlorite-rich, less than 1 km from fault, along road
CG-C-62 -- lower Jurassic argillite, sandstone, ≈6 km from waterfalls
CG-C-63A,B,C -- shale/limestone contact, ≈1 km from waterfall
63A -- black shale, top of shale section; 63B -- limestone, near lowest layer, ≈500 m from 63A (beds are shallowly-dipping); 63C - limestone, ≈10 m above 63B
CG-C-64 *(90L-127C)* -- basalt, collected near Taraklan hill, underlies (?) outflow tuff, outcrop is ≈20 m thick, sample collected near bottom of flow unit
*Eldjurta samples and mineral separates obtained from A. Gurbanov:*
1-1/85 -- surface sample (biotite, K-feldspar, plagioclase)
1-4/85 -- surface sample (biotite)
5-2/90 -- 800m depth (biotite, K-feldspar, plagioclase, quartz)
5-4/90 -- 800m depth (whole rock)
10-4/90 -- 1325m depth (biotite, K-feldspar, plagioclase, quartz)
10-1/90 -- 1325m depth (whole rock)
17-1/90 -- 1850m depth (biotite, K-feldspar, plagioclase, quartz)

17/90 – 1850m depth (whole rock)
26-1/90 -- 2340m depth (whole rock, biotite, K-feldspar, plagioclase, quartz)
37/90 – 2800m depth (whole rock, biotite, K-feldspar, plagioclase, quartz)
49/90 – 3300m depth (whole rock, biotite, K-feldspar, plagioclase, quartz)
59/90 – 3700m depth (whole rock, biotite, K-feldspar, plagioclase, quartz)
67/90 – 3970m depth (whole rock, biotite, K-feldspar, plagioclase, quartz)

**Summer, 1991**
CG-C2-1 *(KH91-1)* – glassy pumices collected at Bashil Dam
CG-C2-2 – diorite inclusion, float in Jungusu River, 1620m
CG-C2-3A – tuff at contact in Jungusu River, 1710m
CG-C2-3B -- schist at same locality
CG-C2-4 – Chegem Tuff reference section, collected by C. Gazis, I. Nikolaev, and K. Hon
4A -- grey tuff, 2915m
4B -- grey tuff, 2870m
4C -- tuff with pumices, 2780m
4D -- grey tuff, 2750m
4E -- grey tuff, 2710m
4F -- fresh grey tuff, biotite-rich, 3225m
4G – fresh grey tuff, biotite-rich, 3165m
4H -- white poorly-welded tuff, 3160m
4I -- fresh-grey tuff, 3145m
4J -- fresh grey tuff, 3100m
4K -- fresh grey tuff, 3050m
4L -- grey, partly altered tuff, 2965m
4M – fresh red-brown tuff, 2630m
4N -- partly altered red-grey tuff, 2550m
4O – fresh grey tuff, 2450m
4P – white altered tuff, 2220m
4Q – vitrophyre, east side of gulch at base of cliffs, 2120m
4R -- small pumice in vitrophyre, 2120m
4S -- vitrophyre on west side, in contact with metamorphics, 2080m
4U -- float of crystal-poor, quartz-bearing pumice (devitrified), 1800m
CG-C2-5 – tuff 50m above contact at Chegem-Jungusu divide, 2000m
CG-C2-6 – andesite inclusion in granodiorite in talus in slope of N. Likarilgi
CG-C2-7 – finer-grained granodiorite, near flat top contact of granodiorite and tuff, on N. peak of Likarilgi, 3300m
CG-C2-7B -- tuff from near contact with CG-C2-7A
CG-C2-8A – quartz-rich, biotite-poor tuff in ridge east of N. Likarilgi, 3330m
CG-C2-9 – grey-red, quartz-rich tuff from top of N. summit of Likarilgi, 3370m
CG-C2-10 – grey-red quartz-rich tuff from top of Likarilgi, 3430m
CG-C2-11 – granodiorite from near bottom of south gully leading up to Likarilgi, 2960m
CG-C2-12 – tuff collected 250m SSE of 3345 peak west of Likarilgi
CG-C2-13 – tuff on 3353m peak SW of Likarilgi

CG-C2-14 A, B, C -- tuff from east side of basin east of Vorlan, B and C are float samples
CG-C2-15 -- grey tuff with white pumices, from ridge, 500m east of Vorlan, 3330m
CG-C2-16 -- tuff from 1 km west of Likarilgi, 3345m
CG-C2-17A -- tuff from peak 900m west of Likarilgi, 3360m
CG-C2-17B -- black tuff, float, same location as CG-C2-17A
CG-C2-18 -- tuff from ridge 500m west of Likarilgi, 3325m
CG-C2-19A -- granite border, quartz-rich, near andesite inclusion, 15m from tuff contact
CG-C2-19B -- fine-grained andesite inclusion in granite border phase
CG-C2-19C -- quartz-rich granite border to intrusion
CG-C2-19D -- coarser-grained intrusion in float 100m from contact, still appears more granitic
CG-C2-19E -- tuff within 2 m of contact with granitic border of intrusion
CG-C2-19F -- miarolitic border of granite intrusion
CG-C2-19G -- small piece of granite with slicken slides
CG-C2-19H -- small veinlets cutting granite
CG-C2-20 -- large andesite to diorite inclusion in granodiorite in southern gully route up Likarilgi, 3075m
CG-C2-21 -- tuff from just above granodiorite in middle fork of Jungusu on west side, ≈2980m
CG-C2-22 -- altered granite porphyry near contact just below CG-C2-21, ≈2960m
CG-C2-23 -- tuff in headwall of middle Jungusu drainage just beneath 3430m summit of Likarilgi, 3200m
CG-C2-24 -- samples from saddle on ridge west of Vorlan and east of 3674 peak with layered tuffs
24A -- tuff on west side of saddle, 3205m
24B -- float of vitrophyric tuff on west side (3674m peak) of saddle, collected at 3205m, probably comes from 100-200m above
24C -- devitrified tuff with white pumices from east side of saddle
CG-C2-25 -- tuff from knob 200m east of saddle on west ridge of Mt. Vorlan, 3310m
CG-C2-26 -- tuff from summit of Mt. Vorlan, 3310m
CG-C2-27 -- tuff from top of peak 200m SE of Mt. Vorlan, 3350m
CG-C2-28 -- tuff from large columnar jointed outcrop in canyon descending from camp to Dzhilgusu River, 1940m
CG-C2-29 -- tuff 90m away from limestone contact in canyon descending to Dzhilgusu River, 1870m
CG-C2-30 -- tuff from 50m away from limestone contact, 1845m
CG-C2-31A -- vitrophyric tuff from contact with limestone, 1775m
CG-C2-31B -- limestone from breccia zone at contact, 1770m
CG-C2-32 -- limestone 100m from contact, 1720m
CG-C2-33 -- limestone from near forts along Dzhilgusu River, 1650m
CG-C2-34 -- tuff on north side of 3124m peak, 2900m
CG-C2-35 -- slightly altered tuff on N. side of 3124m peak, 2900m

CG-C2-37A -- very fine-grained granite-rhyolite porphyry quenched against faulted tuff, from 100m below saddle east of Dzhilgusu peak
CG-C2-37B -- brecciated and highly sheared tuff within 3-5m of quenched granite porphyry
CG-C2-38 -- tuff from far side of saddle east of fault zone, probably from 50m above saddle
CG-C2-39 -- altered tuff from outcrops below and east of saddle with faults, south side of ridge, 2430m
CG-C2-40 -- float of tuff, from outcrop 50m above, descending from camp to Dzhilgusu River ≈2200m
CG-C2-51 -- vitrophyre from scallop in caldera wall on back side (NW) of Kektosh, steep contact with devitrified tuff, 2495m
CG-C2-52 -- devitrified biotite-rich tuff from near CG-C2-51
CG-C2-53 -- gneiss ≈500m from contact with Eldjurta Granite, Baksan R. level
CG-C2-54A-C -- at contact between Eldjurta Gr. and upper Proterozoic schist, Baksan R. level
54A -- upper Proterozoic schist, 5m from contact
54B -- Eldjurta Gr., 5m from contact
54C -- Eldjurta Gr., 15m from contact
CG-C2-55 -- Eldjurta Gr., ≈500m from contact, ≈500m above Baksan R. level
CG-C2-56 -- fresh Eldjurta Gr., collected at site of deep drillhole (surface sample)
CG-C2-57 -- Eldjurta Gr. ≈200m from eastern contact (near Tirniauz town), 1360m
CG-C2-58 -- samples collected at upper contact near tram toward Tirniauz mine, 2180m
58A -- Eldjurta Granite, ≈5-20m from contact
58B -- Eldjurta Granite, fine-grained, 1-2m from contact
58C -- dike within Eldjurta Granite
58D -- quartz from quartz vug, stained orange
58E -- contact rock, contains country rock and vein
58F -- contact rock with molybdenum
58G -- dike in country rock
58H -- country rock, altered, 1m from contact
58I -- country rock 20m from contact, near small fault
CG-C2-59 -- Upper Proterozoic gneiss, ≈1.5 km from Eldjurta Gr.
CG-C2-60 -- aplite dike, ≈400m from Eldjurta Gr. on SW side
CG-C2-61A-D collected in Tirniauz mine near leucogranite
61A -- leucogranite -- rhyolitic, silicified by quartz veins
61B -- leucogranite with "B" vein (contains Mo)
61C -- skarnoid with molybdenite, garnet, pyroxene
61D -- marble
CG-C2-62 -- hornblende hornfels, mineralized at very low grade
CG-C2-63 -- biotite hornfels, containing quartz vein with molybdenum
CG-C2-64A-D -- at elevation of main ore body
64A -- liparite (rhyolite), middle neck, fresh
64B -- liparite, altered
64C -- contact between liparite and country rock

64D -- 20 Ma(?) aplite dike which cuts liparite
CG-C2-65A, B -- schist clasts in granodiorite porphyry collected from cobbles at place where Jungusu meets Chegem River
CG-C2-66 -- two-mica leucogranite with garnets, collected near glacier at head of Chegem River
CG-C2-67 -- samples collected from SW arm of Kum Tyube
67A -- lower cirque unit, grey devitrified tuff, 3300m
67B -- lower cirque unit, grey devitrified tuff, 3340m
67C -- lower cirque unit, grey devitrified tuff, 3390m
67D -- upper cirque unit, grey tuff with glassy pumices, 3495m
67E -- upper cirque unit, grey tuff with glassy pumices, 3500m
67F -- upper cirque unit, poorly-welded tan tuff, 3530m
67G -- middle cirque unit, grey tuff with glassy pumices, 3415m
67H -- middle cirque unit, grey tuff with glassy pumices, 3425m
CG-C2-68 -- samples collected from cliffs on edge of flat ledge about 750-1000m NW of little Kum Tyube, may be a slump block
68A -- grey nearly glassy tuff, 3410m
68B -- grey-brown, nearly glassy tuff, 3420m
68C -- tan, poorly-welded tuff, 3495m
68D -- black andesite on NW side of Little Kum Tyube
CG-C2-69 -- black, fresh andesite from base of Little Kum Tyube on south side of peak
CG-C2-70 -- section of tuffs about 500 m SE of Little Kum Tyube
70A -- grey tuff with small pumices, top of lower cirque unit, 3370m
70B -- grey tuff with glassy pumices, middle cirque unit, 3415m
70C -- grey tuff with black glassy pumices, upper cirque unit, 3445m
CG-C2-73 -- grey tuff with black glassy pumices from knob in middle of Sarynsu cirque just west of Dzhilgusu divide, probably upper cirque, 3460m
CG-C2-74 -- biotite-poor, quartz-rich tuff from within roof pendant in granodiorite on North ridge of Hobetayeen, 2595m
CG-C2-75 -- Quartz-rich tuff from summit north of Hobetayeen, 2744m
CG-C2-76 -- fine-grained granodiorite near lower contact with tuff, between ring fault and caldera wall, 2330m
CG-C2-77 -- miarolitic granodiorite near upper contact with roof pendant rocks on north ridge of Hobetayeen, 2420m
CG-C2-78 -- vitrophyric margin of tuff quenched against limestone wall of caldera, 1930m
CG-C2-79 -- granodiorite, with small schist inclusions, 2050m
CG-C2-80 -- tuff in roof pendant adjacent to contact with granodiorite, 2350m
CG-C2-81 -- float of limestone along Oru Creek from small sliver of limestone at 1980m, collected at 1700m
KH91-2A -- biotite-rich, quartz-poor tuff from summit of 3124m peak, SE of Likarilgi
KH91-2B -- slightly fresher sample, 5m below summit of 3124m peak
KH91-3 -- tuff on NW ridge from 3124m peak

KH91-4 -- darker tuff, from zone 10-20m thick on ridge NW of 3124m peak, 3080m
KH91-5 -- tuff between minor fault strands on 3030m saddle between 3124 peak and Likarilgi, 3060m
KH91-6 -- oxidized Fe-Mn coated cataclastic breccia from main fault zone on N. side of 3030m saddle between 3124m peak and Mt. Likarilgi
KH91-7 -- granite porphyry border phase just north of 3030m saddle on SE ridge from Likarilgi, 20m below contact with overlying tuff, in fault contact with tuff to the south, 3040m
KH91-8 -- tuff at contact just above granite porphyry, 3060m
KH91-9 -- small outcrops of tuff in valley south of Likarilgi that drains into Dzhilgusu, just below 3030m saddle
KH91-10A -- sample of fault material from saddle to west of 3030m saddle
KH91-10B -- tuff from saddle west of 3030m saddle, south side of fault
KH91-10C -- slabby tuff from north side of fault, same location as KH91-10B
KH91-11 -- large pumices from ≈3700m at head of Sarynsu-Dzhilgusu divide, all are crystal-rich and contain quartz and small amounts of biotite
KH91-12 -- vitrophyre from base of tuff on SE side of Mt. Gikhi above Gara branch of Chegem, 2450m
KH91-13 -- float of fresh black andesite lava at about 3500m, just beneath lower contact of lava on 3642m peak SW of Kyugenkaya
KH91-14 -- coarse cumulate nodule in andesite lava, plag + pyx intergrowth with crystals about 2-3mm, float on 3642m peak SW of Kyugenkaya
KH91-15 -- black, vesicular, near glassy andesite lava on E. side of 3642m peak SW of Kyugenkaya
KH91-16 -- black, fresh, near-glassy basal andesite flow on Kyugenkaya just NE of saddle with fault, 3430m
KH91-17A -- microdiorite inclusion in oxidized andesite
KH91-17B -- oxidized microdiorite inclusion, similar to KH91-17B
KH91-18 -- dense black, near vitric andesite mixed with red oxidized andesite from south summit of Kyugenkaya, 3740m
KH91-19A -- large microdioritic to basaltic(?) inclusion in oxidized andesite on summit of Kyugenkaya, 3700m
KH91-19B -- very large microdiorite inclusion, chilled feeder dike?, similar texture to KH91-17
KH91-19C -- smaller microdiorite inclusion, very similar to KH91-19B
KH91-20 -- fresh, black near glassy andesite from south side of 3642m peak SW of Kyugenkaya
KH91-21 -- basal vitrophyre from red tuff with abundant large glassy pumices, from center of east face of 3774m peak facing into Dzhilgusu R.

# Appendix B. Oxygen Isotope Analysis

Oxygen isotope analyses of silicates were made using the fluorination technique described in Taylor and Epstein (1962). Oxygen isotope analyses of carbonates were carried out by the $H_3PO_4$ technique described by McCrea (1950), corrected using a fractionation factor of 1.01008 (Sharma and Clayton, 1965). The purpose of this appendix is to briefly describe the procedure I used in my silicate extractions, including the modifications which I made to the extraction line and to provide a table reporting results of analyses on Rose Quartz standards (Table B.1).

## B.1 Extraction Procedure

All of my silicate extractions were carried out on the West Line in the Penthouse (Room 404 NMudd) at Caltech. The configuration of the extraction line is essentially that given in Taylor and Epstein (1962).

Prior to the first analysis and then after every ≈8 manifolds, the nickel reaction vessels were polished with sand paper and then emery paper, rinsed with water and acetone and baked out overnight with 1/3 atm of fluorine. The fluorine was removed the following morning through the waste side of the line.

Samples were weighed (usually 15-20 mg) and placed in a dry box with the evacuated reaction vessels. I generally used a dry box which uses $P_2O_5$ as a drying agent and is exposed to air during each loading. When this dry box was used, the sample was left in the dry box for at least twelve hours before loading. The humidity gauge in the dry box should read below zero when the box is sufficiently dry.

After loading the samples in the reaction vessels, the manifold was placed on the line, exposing the smallest volume of metal possible to air. This volume

was pumped out and then filled with 1/3 atm of fluorine and heated to remove any adsorbed water. The reaction vessels were then pumped for at least several hours, first to the waste pump and then to the clean pump. The samples were then exposed to 2/3 atm of fluorine, isolated and heated overnight at 550°C. Temperatures of the reaction can be measured with an external thermocouple.

The following morning, the fluorine was removed from the metal part of the line (except the reaction vessels) and cold traps were placed on either side of the clean side KBr trap, to trap fluorides on the metal side and to trap bromine on the glass side. In my extractions, I always isolated an aliquot of sample gas which I expanded back into the volume through which the sample had passed after I had converted most of the sample. This technique is meant to reduce the quantity of isotopically fractionated sample which does not get converted. My extraction procedure was as follows:

1. Sample into first fluoride trap (1 min)
2. Sample into second fluoride trap (1 min)
3. Sample into KBr trap (2 min)
4. Sample into bromine traps (1 min)
5. Expand sample into conversion chamber and aliquot volume (2-3 min)
6. Isolate aliquot, begin conversion (15-20 min) freezing sample in cold trap on conversion chamber.
7. Expand aliquot into volume and convert (5-6 min)
8. Pump remaining gas through conversion chamber with converter on (1-2 min)
9. Transfer sample to manometer and measure
10. Put dry ice slurry on manometer trap to freeze any water. Pass sample by hot mercury to collection tube

After each extraction, the reaction vessels were baked out overnight in 1/3 atm fluorine.

**B.2 Modifications to Extraction Line**

The main modification which I made to the extraction line was to change the oxygen-$CO_2$ converter. In my early extractions, I used a converter which consisted of two pointed platinum nodes. A carbon rod with two holes was placed on these nodes and a current was passed through the rod. The drawback of this style of converter is that the carbon rod frequently falls off of the nodes.

In 1991, I replaced this converter with another converter, whose design (Fig. B.1) was passed on to our laboratory by J.R. O'Neil. This converter does not pass a current directly through the carbon rod. The main advantage of this converter is that conversions are faster. I made several modifications to the design (Fig. B.2) to facilitate the welding.

This converter was originally attached to tungsten rods connected to a Variac with brass clamps. However, on heating, the different metals expanded differently and the connection would frequently heat up and at times the converter would fall off. The final modification which I made to the line was to have the platinum converter soldered to the tungsten with low-temperature silver solder.

## Table B.1 Rose Quartz Standards

| Sample # | $\delta^{18}O$* | $\delta^{13}C$* | RV** | Date extracted |
|---|---|---|---|---|
| CG-S80-1 | 8.50 | -27.64 | 11 | 6/14/93 |
| CG-S80-2 | 8.80 | -27.64 | 12 | 6/14/93 |
| CG-S80-3 | 8.58 | -27.60 | 14 | 6/14/93 |
| CG-S80-4 | 9.09 | -27.63 | 15 | 6/14/93 |
| CG-S80-5 | 8.84 | -27.65 | 16 | 6/14/93 |
| ave (S80, 1σ std dev) | 8.76 ± 0.24 | -27.63 ± 0.02 | | |
| CG-S79-1 | 8.76 | -25.86 | 25 | 6/17/93 |
| CG-S81-1 | 8.71 | -25.88 | 13 | 6/19/93 |
| CG-S82-1 | 8.47 | -25.93 | 21 | 6/21/93 |
| CG-S82-2 | 8.56 | -25.98 | 24 | 6/21/93 |
| CG-S83-1 | 8.82 | -25.85 | 12 | 6/23/93 |
| CG-S83-2 | 8.91 | -25.85 | 15 | 6/23/93 |
| CG-S84-1 | 8.77 | -25.83 | 23 | 6/25/93 |
| CG-S85-1 | 8.95 | -25.84 | 14 | 6/27/93 |
| ave (S80-S85) | 8.75 | | | |
| CG-S86-1 | 9.45 | -26.26 | 25 | 6/29/93 |
| CG-S87-1 | 9.03 | -26.14 | 15 | 7/2/93 |
| ave (S80-S87) | 8.81 | | | |
| ave (S80 -S85 and S87) | 8.77 | | | |
| CG-S88-1 | 8.97 | -26.14 | 21 | 7/9/93 |
| CG-S88-2 | 9.81 | -26.14 | 22 | 7/9/93 |
| CG-S88-3 | 8.53 | -26.13 | 23 | 7/9/93 |
| CG-S88-4 | 9.25 | -26.14 | 24 | 7/9/93 |
| CG-S88-5 | 8.63 | -26.12 | 25 | 7/9/93 |
| CG-S88-6 | 9.21 | -26.12 | 26 | 7/9/93 |
| ave (S88) | 9.07 ± 0.47 | | | |
| CG-S89-1 | 8.74 | -26.12 | 11 | 7/11/93 |
| CG-S89-2 | 8.95 | -26.15 | 12 | 7/11/93 |
| CG-S89-3 | 8.46 | -26.12 | 13 | 7/11/93 |
| CG-S89-4 | 7.87 | -26.11 | 14 | 7/11/93 |
| CG-S89-5 | 8.44 | -26.13 | 15 | 7/11/93 |
| CG-S89-6 | 10.13 | -26.14 | 16 | 7/11/93 |
| ave (S89) | 8.76 ± 0.76 | | | |
| CG-S90-1 | 8.72 | -26.11 | 21 | 7/18/93 |
| CG-S90-2 | 8.64 | -26.10 | 22 | 7/18/93 |
| CG-S90-3 | 8.43 | -26.18 | 23 | 7/19/93 |
| CG-S90-4 | 8.84 | -26.11 | 24 | 7/19/93 |
| CG-S90-5 | 8.63 | -26.12 | 25 | 7/19/93 |
| CG-S90-6 | 8.84 | -26.13 | 26 | 7/19/93 |
| ave (S90) | 8.68 ± 0.15 | | | |
| CG-S91-1 | 8.73 | -26.13 | 11 | 7/22/93 |
| CG-S91-2 | 8.74 | -26.12 | 12 | 7/22/93 |
| CG-S91-3 | 8.56 | -26.15 | 14 | 7/22/93 |
| CG-S91-4 | 9.15 | -26.10 | 16 | 7/22/93 |
| ave (S91) | 8.80 ± 0.25 | | | |

(Rose Quartz Standards, p.2)

| Sample # | $\delta^{18}O$* | $\delta^{13}C$* | RV** | Date extracted |
|---|---|---|---|---|
| CG-S92-1 | 8.52 | -26.15 | 21 | 7/27/93 |
| CG-S93-1 | 8.65 | -26.08 | 11 | 7/29/93 |
| CG-S94-1 | 8.91 | -26.07 | 15 | 8/1/93 |
| CG-S95-1 | 7.71 | -26.12 | 23 | 8/3/93 |
| CG-S96-1 | 8.94 | -26.12 | 14 | 8/5/93 |
| CG-S97-1 | 8.92 | -26.07 | 22 | 8/8/93 |
| CG-S97-2 | 8.70 | -26.34 | 26 | 8/8/93 |
| CG-S98-1 | 8.78 | -26.15 | 15 | 8/10/93 |
| CG-S99-1 | 8.66 | -26.16 | 23 | 8/12/93 |
| CG-S99-2 | 8.93 | -26.11 | 26 | 8/12/93 |
| CG-S100-1 | 8.95 | -26.14 | 16 | 8/15/93 |
| ave (S92-S100, excl. S95) | 8.79 ± 0.16 | -26.14 ± 0.08 | | |
| CG-S101-1 | 8.86 | -25.65 | 21 | 9/29/93 |
| CG-S101-2 | 8.84 | -25.65 | 22 | 9/29/93 |
| CG-S101-3 | 8.83 | -25.62 | 23 | 9/29/93 |
| CG-S101-4 | 8.82 | -25.64 | 24 | 9/29/93 |
| CG-S101-5 | 9.12 | -25.67 | 25 | 9/29/93 |
| CG-S101-6 | 9.12 | -25.66 | 26 | 9/29/93 |
| ave (S101) | 8.93 ± 0.15 | -25.65 ± 0.02 | | |
| CG-S102-1 | 9.06 | -25.70 | 21 | 10/1/93 |
| CG-S102-2 | 8.83 | -25.69 | 22 | 10/1/93 |
| CG-S102-3 | 9.08 | -25.69 | 23 | 10/1/93 |
| CG-S102-4 | 8.86 | -25.72 | 24 | 10/1/93 |
| CG-S102-5 | 8.78 | -25.69 | 26 | 10/1/93 |
| ave (S102) | 8.92 ± 0.14 | -25.70 ± 0.01 | | |
| CG-S103-1 | 8.55 | -25.68 | 11 | 10/3/93 |
| CG-S103-2 | 8.53 | -25.67 | 15 | 10/3/93 |
| CG-S103-3 | 8.76 | -25.69 | 16 | 10/3/93 |
| ave (S103) | 8.61 ± 0.12 | -25.68 ± 0.01 | | |
| CG-S104-1 | 8.59 | -26.32 | 11 | 2/2/94 |
| CG-S104-2 | 8.17 | -26.23 | 14 | 2/2/94 |
| ave (S104) | 8.38 ± 0.30 | -26.28 ± 0.06 | | |
| CG-S105-1 | 8.40 | -26.23 | 22 | 2/9/94 |
| CG-S105-2 | 8.40 | -26.24 | 23 | 2/9/94 |
| CG-S105-3 | 8.45 | -26.22 | 24 | 2/9/94 |
| CG-S105-4 | 8.49 | -26.17 | 26 | 2/9/94 |
| ave (S105) | 8.43 ± 0.05 | -26.22 ± 0.03 | | |
| CG-S106-1 | 8.47 | -26.21 | 11 | 2/11/94 |
| CG-S106-2 | 8.89 | -26.21 | 12 | 2/11/94 |
| CG-S106-3 | 8.50 | -26.21 | 13 | 2/11/94 |
| CG-S106-4 | 8.76 | -26.20 | 14 | 2/11/94 |
| CG-S106-5 | 8.62 | -26.19 | 15 | 2/11/94 |
| CG-S106-6 | 8.61 | -26.20 | 16 | 2/11/94 |
| ave (S106) | 8.64 ± 0.16 | -26.20 ± 0.01 | | |
| CG-S107-1 | 8.57 | -26.17 | 21 | 2/23/94 |
| CG-S107-2 | 8.44 | -26.20 | 25 | 2/23/94 |
| ave (S107) | 8.51 ± 0.09 | -26.19 ± 0.02 | | |

(Rose Quartz Standards, p.3)

| Sample # | $\delta^{18}O$* | $\delta^{13}C$* | RV** | Date extracted |
|---|---|---|---|---|
| CG-S108-1 | 8.72 | -26.19 | 11 | 2/26/94 |
| CG-S109-1 | 8.53 | -26.15 | 22 | 2/28/94 |
| CG-S110-1 | 8.77 | -26.15 | 12 | 3/3/94 |
| CG-S111-1 | 8.66 | -26.14 | 25 | 3/9/94 |
| CG-S112-1 | 8.71 | -26.14 | 13 | 3/12/94 |
| CG-S112-2 | 8.67 | -26.13 | 16 | 3/12/94 |
| ave (S112) | 8.69 ± 0.03 | -26.14 ± 0.01 | | |
| CG-S113-1 | 8.53 | -26.14 | 23 | 3/14/94 |
| CG-S114-1 | 8.67 | -26.12 | 14 | 3/16/94 |
| CG-S115-1 | 8.51 | -26.12 | 24 | 3/18/94 |
| CG-S116-1 | 8.53 | -26.15 | 16 | 3/20/94 |
| ave (S107-116) | 8.61 ± 0.10 | -26.15 ±0.02 | | |

* $\delta^{18}O$ and $\delta^{13}C$ expressed in per mil relative to SMOW and PDB, respectively
** first digit: 1=manifod Y, 2=manifold Z; second digit=RV number

**Figure B.1** - Oxygen-CO2 converter

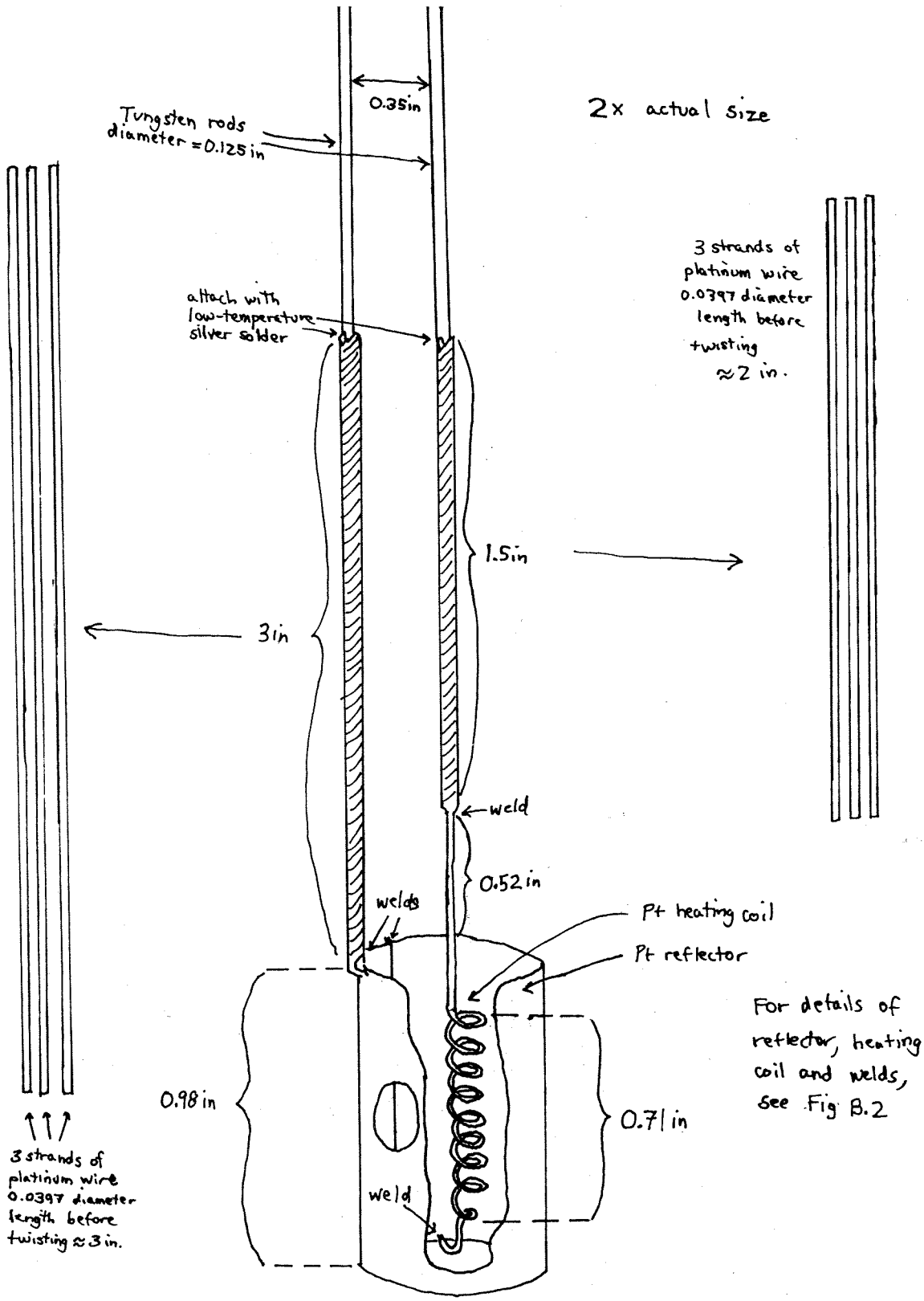

# **Figure B.2** - Details of oxygen-CO2 converter

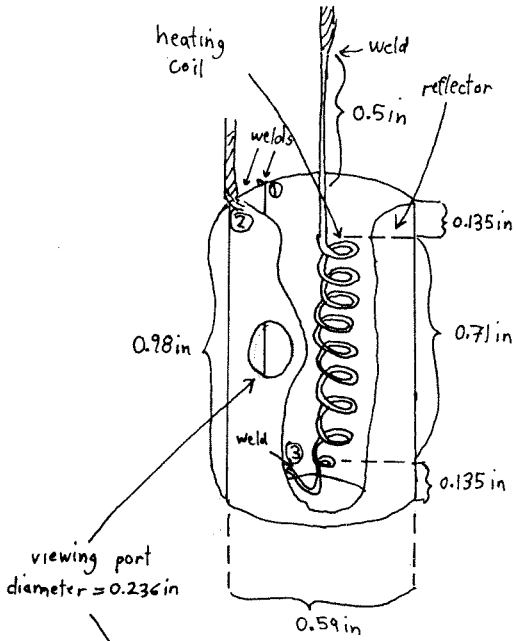


1. Inside diameter of heating coil must accomodate 0.126" diameter rod.

2. Number of coil turns is schematic.

3. All welds are platinum.

4. Coil axis is coincident with reflector axis.

5. Length of coil wire is ≈6 in., wound such that ≈0.8 in are left at each end for attachment.

6. Lowermost coil is smaller in diameter so that 0.126" diameter rod will not slip through.

7. Coil wire is 0/397 diameter platinum wire.

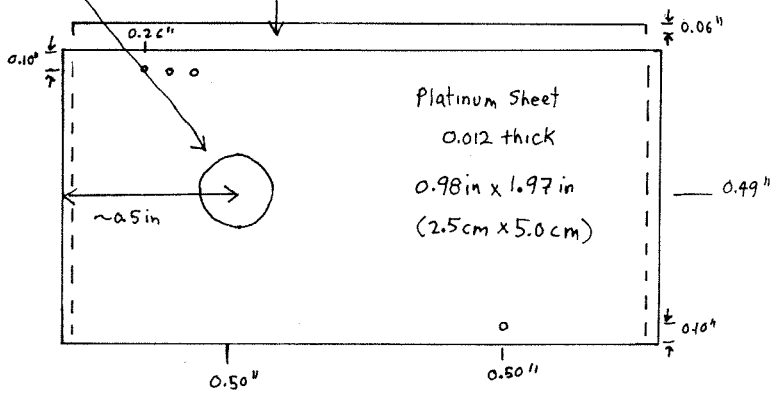


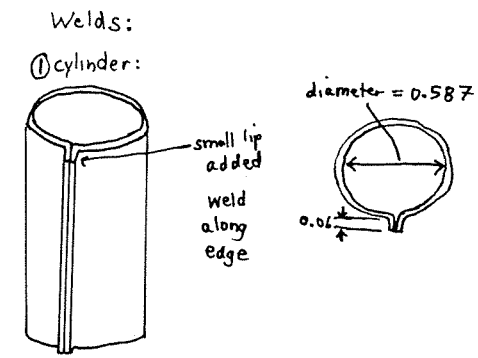


② connection of three wires to cylinder:

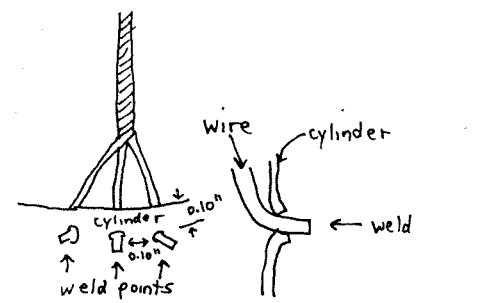


Wires pass through holes in cylinder. Holes are punched so they bevel towards outside of cylinder

③ Attachment of heating coil to cylinder:

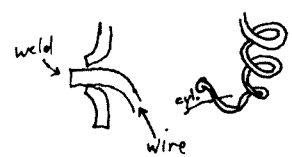


Same technique as ②: hole beveled to outside of cylinder

# Appendix C. Rb/Sr Analytical Technique

The analytical procedures for Rb/Sr and Sm/Nd analysis in the laboratory of Prof. J.B. Saleeby have been described in detail in Appendix A of D.A. Pickett's Caltech doctoral thesis (1991; Appendix A is cowritten by Pickett and D. Clemens Knott). The procedures for cleaning and preparing reagents and distilled $H_2O$ are also described there. Here, I briefly review the procedures I followed, noting any differences from those of Pickett and Clemens Knott.

## C.1 Sample Spiking and Dissolution

Between 20 and 200 mg of sample were weighed, put in a teflon beaker or screw-top vial and moistened with dilute HCl. Samples were spiked prior to dissolution. The rubidium and strontium spikes have the following concentrations:

| | | |
|---|---|---|
| sRb(1) | $^{87}Rb$ = 402.10nmol/g | 85/87=0.0089 |
| sRb(2) | $^{87}Rb$ = 220.45nmol/g | 85/87=0.0089 |
| sRb(3) | $^{87}Rb$ = 5.8218nmol/g | 85/87=0.0089 |
| sSr(1) | $^{84}Sr$ = 2.9406nmol/g | 86/84=0.000583<br>87/84=0.000090<br>88/84=0.000407 |

Sample strontium and rubidium contents were estimated. Then, spike amounts were calculated to optimize the measured ratios, according to the equations:

| | |
|---|---|
| $^{87}Rb = 18.41 \times W\ (g) \times C\ (ppm)$ | [satisfies spiked $(85/87)_M = 0.4$] |
| $^{84}Sr = 0.172 \times W\ (g) \times C\ (ppm)$ | [satisfies spiked $(88/84)_M = 40$] |

After the spikes were added, the samples were dissolved. The usual procedure was to first dissolve with ≈2ml of concentrated HF plus a long squirt of concentrated $HNO_3$. For some samples, a drop of hydrogen peroxide was added to this mixture to aid the dissolution. The mixture was placed in a screw-top vial and put on a hot plate for one day. After each dissolution step, the sample was dried in an evaporation hood. In the second dissolution step, ≈2ml of concentrated $HNO_3$ were added to the sample and the mixture was again placed on a hot plate for one or two days. After this dissolution step, the sample was dissolved in 1.25N or 1.5N HCl and centrifuged to check for solid residue. If the sample was not completely dissolved, the treatment with concentrated $HNO_3$ was repeated one or two more times. For several samples, the initial dissolution step was performed at room temperature with $HClO_4$ + HF, followed by treatment with $HNO_3$. In most cases, the sample was completely dissolved after two or three additions of acid. In several cases, some residue remained after one treatment with HF + $HNO_3$ and three treatments with $HNO_3$. In these cases, I continued the procedure without the residue, assuming that it contained negligible amounts of Sr and Rb.

## C.2 Cation Separation

Prior to cation separation, samples were dissolved in 1.25N or 1.5N HCl and centrifuged to ensure that no solid residue would enter the cation exchange columns. Elution of Rb and Sr was accomplished in cation columns containing AG50W-X4 resin using 1.0N to 4.0N HCl, according to the procedure described in Pickett (1991). During the course of my labwork, the laboratory was renovated and new cation columns were installed. These cation columns are much smaller (diameter = 7mm) than the previous columns and require less acid. For the smaller columns, the elution scheme is:

| | | |
|---|---|---|
| 1.0N HCl | Condition | 5ml |
| | Sample | 1 ml |
| | Rinse | 1 ml |
| 2.5N HCl | Wash | 8 ml |
| | Rb | 3 ml |
| | Wash | 6 ml |
| | Sr | 6 ml |
| 4.0N HCl | Wash | 5 ml |
| | REE | 10 ml |
| | Clean | 20 ml |
| | Clean | 20 ml |
| store w/distilled H2O | | 20 ml |

For several high-Rb samples, the strontium separate contained measurable Rb and was passed through the column a second time to remove that Rb.

### C.3 Filament Loading

Rubidium samples were loaded on single Re filaments. First, 2 µl of silica gel suspension were loaded on the filament. Then 2 ng of Rb were loaded, "sandwiched" between two 1 µl aliquots of 0.5N $H_3PO_4$.

For a strontium sample, 1000 ng of Sr was dried down in a snap-cap vial. Then ≈0.7 µl of $Ta_2O_5$ powder, suspended in water, was loaded onto a single Ta filament. The Sr sample was dissolved in 3 µl of 1.5N HCl and half of the sample (500 ng Sr) was loaded onto the dry $Ta_2O_5$.

### C.4 Mass Spectrometry

Samples were analyzed on an automated VG Sector multicollector thermal ionization mass spectrometer. Rb was analyzed in static mode with mass 85 in the Low 1 collector and mass 87 in the High 1 collector. The aiming intensity was usually 500 mV, normally attained with the filament at 1.2 - 1.9 A. 50 to 100 ratios were measured for each sample and the unfiltered grand mean ("before rejection") were used.

Sr was run multidynamically in four collectors (L2 to H1), but with the 84/86 ratio measured statically in the L2 and axial collectors. The aiming intensity for strontium was usually 2.5 to 2.7 V. This required filament currents of 3.2 to 3.6 A, which registered temperatures of 1600° to 1680°C on the pyrometer gauge. Normally, 150-200 cycles were run and the filtered data was used. Fractionations were made during data collection according to the standard ratio of $^{86}Sr/^{88}Sr = 0.1194$.

### C.5 Rb and Sr Standard Analyses

The results of analyses of 15 Sr standards (987 Sr) and 10 Rb standards (nRbAAA) are given in Tables C.1 and C.2. The mean (corrected, 1σ) $^{87}Sr/^{86}Sr$ and $^{84}Sr/^{86}Sr$ ratios of the 987 Sr standards measured between July 1992 and April 1993 were 0.710238 ± 0.000017 and 0.056499 ± 0.000050, respectively. These values are analytically indistinguishable from the means for 987 Sr standards analyzed between January 1988 and May 1991 ($^{87}Sr/^{86}Sr = 0.710244 \pm 0.000005$, $^{84}Sr/^{86}Sr = 0.056514 \pm 0.000010$). Two 987 Sr standards analyzed in September 1994 have slightly different values, which marginally overlap with the earlier mean when their associated errors are considered. These standards were analyzed shortly after the mass spectrometer had been repaired.

The mean (uncorrected, 1σ) $^{85}Rb/^{87}Rb$ ratio of the 10 nRb(AAA) standards measured between July 1992 and April 1993 is 2.6104 ± 0.0085, slightly lower than the mean for nRb(AAA) standards measured between May 1988 and March 1991 ($^{85}Rb/^{87}Rb = 2.6163 \pm 0.0008$). However, if one outlying standard value is not considered, the mean $^{85}Rb/^{87}Rb$ ratio is 2.6129 ± 0.0033, again agreeing well with earlier standards.

## C.5 Analytical Uncertainty of $^{87}Sr/^{86}Sr$ Ratio

The replicate 987 Sr standard analyses suggest that my precision in measuring $^{87}Sr/^{86}Sr$ ratios is 0.000017 (1σ). However, this is a minimum estimate of the analytical uncertainty since it does not account for errors due to sample heterogeneity, and sample dissolution. Three samples were analyzed two times. Two of these (CG-C2-56 and 90L-119A) were dissolved once and then passed through the cation exchange column twice; the third (CG-C2-4F) was dissolved twice. The $^{87}Sr/^{86}Sr$ ratios of these replicate analyses were:

| | |
|---|---|
| CG-C2-56: | 0.706887 ± 0.000005 |
| | 0.706890 ± 0.000006 |
| 90L-119A: | 0.706056 ± 0.000014 |
| | 0.706118 ± 0.000027 |
| CG-C2-4F: | 0.706590 ± 0.000005 |
| | 0.706517 ± 0.000008 |

These replicate analyses suggest a true analytical uncertainty for $^{87}Sr/^{86}Sr$ closer to 0.00005.

## C.6 Comparison of Sr and Rb Concentration Determinations by Isotope Dilution and X-Ray Fluorescence (XRF)

Rb and Sr concentrations have determined by the two techniques: isotope dilution (this study) and XRF (Ken Hon, unpublished data). The results of the two methods are presented in Chapter 6 and compared here in Fig. C.1. The isotope dilution technique is considered to be more precise with errors of 1% compared to the estimated errors of 5% for XRF. For both Sr (Fig. C.1a) and Rb (Fig. C.1b), the measured XRF concentrations are systematically lower (up to 10%) than those measured by isotope dilution, especially at concentrations greater than 150 ppm. However, one sample, CG-C-44P, had a much higher XRF-measured Sr concentration and the Sr content for this sample should be considered suspect.

**Table C.1** Strontium standards - 987 Sr

| date | 86/88 | %sd.err. | 87/86 | %sd.err. | 84/86 | %sd.err. |
|---|---|---|---|---|---|---|
| 7/15/92 | 0.119161 | 0.0135 | 0.710248 | 0.0006 | 0.056466 | 0.0109 |
| 10/28/92 | 0.118895 | 0.0257 | 0.710198 | 0.0012 | 0.056463 | 0.0125 |
| 11/6/92 | 0.119888 | 0.0104 | 0.710227 | 0.0021 | 0.056384 | 0.0376 |
| 11/12/92 | 0.119139 | 0.006 | 0.710242 | 0.0007 | 0.056554 | 0.0074 |
| 1/10/93 | 0.119723 | 0.0209 | 0.710225 | 0.0012 | 0.056566 | 0.0125 |
| 1/18/93 | 0.118902 | 0.0106 | 0.710252 | 0.001 | 0.056551 | 0.0103 |
| 1/22/93 | 0.119149 | 0.0172 | 0.71024 | 0.0008 | 0.056473 | 0.0087 |
| 1/29/93 | 0.119149 | 0.0172 | 0.71024 | 0.0008 | 0.056473 | 0.0087 |
| 2/4/93 | 0.11957 | 0.0199 | 0.710214 | 0.0009 | 0.056478 | 0.0109 |
| 2/16/93 | 0.119395 | 0.0137 | 0.710254 | 0.0006 | 0.056527 | 0.0082 |
| 2/18/93 | 0.11948 | 0.0128 | 0.710252 | 0.0005 | 0.056512 | 0.0074 |
| 3/22/93 | 0.11984 | 0.0059 | 0.710252 | 0.0008 | 0.056498 | 0.01 |
| 4/19/93 | 0.11966 | 0.0049 | 0.710244 | 0.0006 | 0.056547 | 0.0094 |
| | | | | | | |
| 7/92-4/93 | | | | | | |
| mean | 0.119381 | | 0.710238 | | 0.056499 | |
| std dev | 0.000340 | | 0.000017 | | 0.00005 | |
| | | | | | | |
| 9/6/94 | 0.119979 | 0.0116 | 0.7102896 | 0.0011 | 0.0555823 | 0.0224 |
| 9/22/94 | 0.1199501 | 0.0242 | 0.7102834 | 0.0015 | 0.0558715 | 0.01783 |

**Table C.2:** Rubidium standards - nRb(AAA)

| Date | 85/87 (before reject) | % std error (before reject) | 85/87 (after reject) | % std error (after reject) |
|---|---|---|---|---|
| 3/22/93 | 2.611206 | 0.0046 | 2.611306 | 0.0042 |
| 1/18/93 | 2.616962 | 0.005 | 2.616928 | 0.0049 |
| 1/17/93 | 2.617177 | 0.0023 | 2.617233 | 0.0017 |
| 10/27/92 | 2.587731 | 0.0057 | 2.587730 | 0.0055 |
| 7/20/92 | 2.613362 | 0.0026 | 2.613379 | 0.0023 |
| 1/11/93 | 2.613061 | 0.0086 | 2.613061 | 0.0086 |
| 1/12/93 | 2.607993 | 0.0073 | 2.607486 | 0.0056 |
| 2/2/93 | 2.608526 | 0.0115 | 2.607222 | 0.0061 |
| 2/8/93 | 2.615244 | 0.0049 | 2.614729 | 0.0034 |
| 4/28/93 | 2.612365 | 0.0127 | 2.612365 | 0.0127 |
| ave | 2.610363 | | 2.610144 | |
| std dev | 0.008538 | | 0.008567 | |
| w/out standard of 10/27/92 | | | | |
| ave | 2.612877 | | 2.612634 | |
| std dev | 0.003296 | | 0.003577 | |

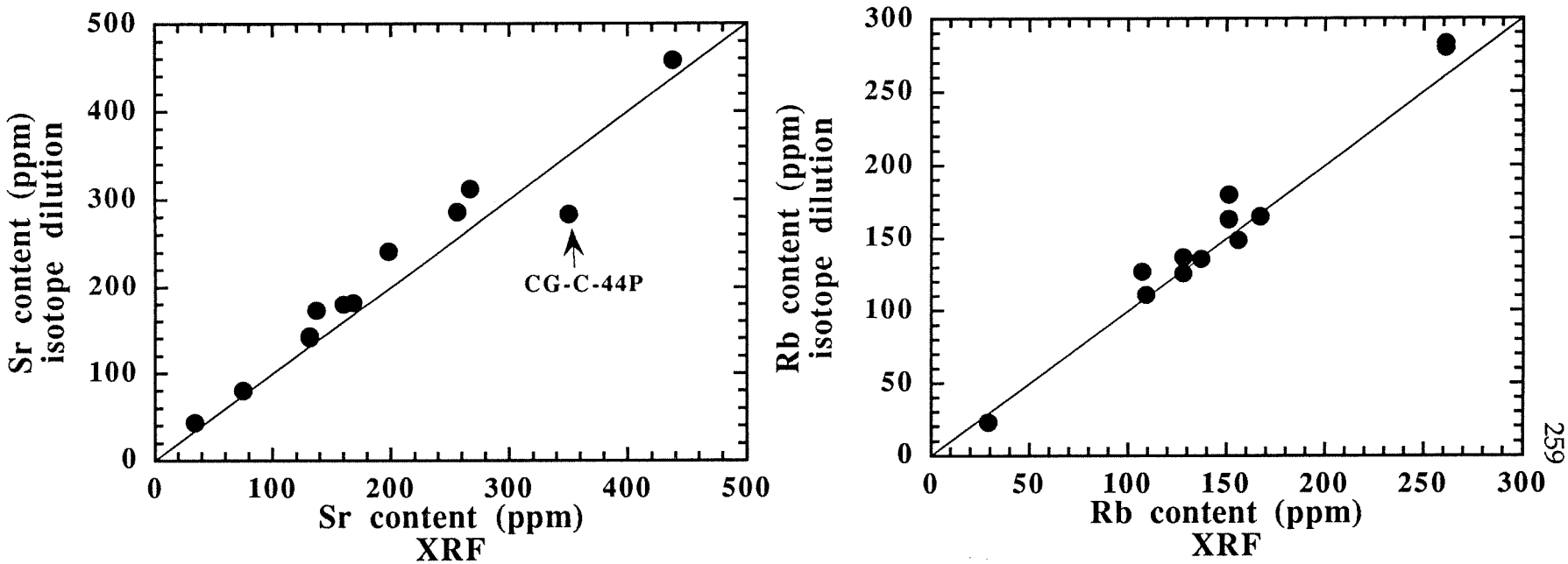


**Figure C.1** -- Comparison of (a) Sr and (b) Rb concentrations measured by X-ray fluorescence (at the U. S. Geological Survey laboratories in Denver) and isotope dilution (in the laboratory of J. Saleeby at Caltech)

# REFERENCES

Abich, H., 1874. Geologische Beobachtungen auf Reisen im Kaucasus im Jahre 1873, *Moscou Soc. Nat. Bull.* : **48**, 278-342 [in German].

Allen, E.T., and Zies, E.G., 1923. A chemical study of the fumaroles of the Katmai region, *Nat. Geogr. Soc. Contrib. Tech. Pap., Katmai Series* : **2**, 75-155.

Anderson, S.W., and Fink, J.H., 1989. Hydrogen-isotope evidence for extrusion mechanisms of the Mount St Helens lava dome, *Nature* : **341**, 521-523.

Arakelyants, M.M., Borsuk, A.M., and Gurbanov,A.G., 1988. On the thermal aureole of a granitoid intrusive, *Izv. Akad. Nauk SSR Ser. Geol.* : 124-127 [in Russian].

Bacon, C.R., 1983. Eruptive history of Mount Mazama and Crater Lake caldera, Cascade Range, U.S.A., *Journal of Volcanology and Geothermal Research* : **18**, 57-116.

Bacon, C.R., Adami, L.H., and Lanphere, M.A., 1989. Direct evidence for the origin of low-$^{18}O$ silicic magmas: quenched samples of a magma chamber's partially-fused granitoid walls, Crater Lake Oregon, *Earth and Planetary Science Letters* : **96**, 199-208.

Bailey, R.A., Dalrymple, G.B., and Lanphere, M.A., 1976. Volcanism, structure, and geochronology of Long Valley caldera, Mono County, California, *Journal of Geophysical Research:* **81**, 725-744.

Bemmelen, R.W.v., 1949. *Geology of Indonesia and adjacent archipelagos* (Government Printing Office, The Hague, Netherlands).

Berger, G.W., and York, D., 1981. Geothermometry from $^{40}Ar/^{39}Ar$ dating experiments., *Geochimica et Cosmochimica Acta* : **45**, 795-811.

Bierwirth, P.N., 1982, B.S. Hons. thesis. *Experimental welding of volcanic ash,* Monash University.

Bigeleisen, J., Perlman, M.L., and Prosser, H.C., 1952. Conversion of hydrogenic materials to hydrogen for isotopic analysis, *Analytical Chemistry* : **24**, 1356-1357.

Bogatikov, O.A., Gurbanov, A.G., Koronovsky, N.V., Kovalenko, V.I., Lipman, P.W., and Tsvetkov, A.A., 1992. 2.5 Ma ash-flow caldera at Chegem River in the northern Caucasus Mountains (USSR), contemporaneous granites and associated ore bodies, *Izv. Russian Acad. Sci. Ser. Geol. 1:5-21 [in Russian].* English transl. in *Int. Geol. Rev;* **34**: 131-147.

Bonatti, E., 1967. Palagonite, hyaloclastites and alteration of volcanic glass in the ocean, *Bulletin of Volcanology* : **28**, 1-15.

Borsuk, A.M., 1979. *Mesozoic and Cenozoic magmatic formations of the Greter Caucasus* (Nauka Press, Moscow).

Bottinga, Y., and Javoy, M., 1975. Oxygen isotope partitioning among the minerals in igneous and metamorphic rocks, *Rev. Geophys. Space Phys.* : **13**, 401-418.

Bowen, N.L., *The Evolution of Igneous Rocks.* 332 pp. (Dover, New York).

Bowman, J.R., Willett, S.D., and Cook, S.J., 1994. Oxygen isotopic transport and exchange during fluid flow: One-dimensional models and applications, *American Journal of Science* : **294**, 1-55.

Browne, P.R.L., Roedder, E., and Wodzicki, A., 1976. Comparison of past and present geothermal waters from a study of fluid inclusions, Broadlands field, New Zealand, in *Proc. Int. Symposium on Water-Rock I nteractions (WRI) 1974,* edited by J. Cadek and T. Laus (Geol. Surv. Prague) p. 140-149.

Byers, F.M., Jr., Carr, W.J., Orkild, P.P., Quinlivan, W.D. and Sargent, K.A., 1976. Volcanic suites and related cauldrons of Timber Mountain-Oasis Valley caldera complex, southern Nevada, *U.S. Geological Survey Professional Paper* : **919**, 70 pp.

Cas, R.A.F., andWright, J.V., 1988. *Volcanic succesions* (Unwin Hyman, London).

Cathles, L.M., 1981. Fluid flow and genesis of hydrothermal ore deposits, *Economic Geology* : 75th Anniv. Volume, 424-457.

Cerling, T.E., Brown, F.H., and Bowman, J.R., 1985. Low-temperature alteration of volcanic glass: Hydration, Na, K, $^{18}O$, and Ar mobility, *Chemical Geology* : **52**, 281-293 .

Christensen, J.N., and Depaolo, D.J., 1993. Time scales of large volume silicic magma systems: Sr isotopic systematics of phenocrysts and glass from the Bishop Tuff, Long Valley, California, *Contributions to Mineralogy and Petrology* : **113**, 100-114.

Christiansen, R.L. and Blank, H.R., Jr., 1972. Volcanic stratigraphy of the Quaternary rhyolite plateau in Yellowstone National Park, *U.S. Geolological Survey Professional Paper* : **729-B**, 18 pp.

Christiansen, R.L., 1984. Yellowstone magmatic evolution: Its bearing on understanding large-volume explosive volcanism, in *Explosive Volcanism: Inception, Evolution, and Hazards*, (edited by National Academy of Sciences, Washington, D.C.) pp. 84-95.

Christiansen, R.L., 1990. Quaternary and Pliocene volcanism of the Yellowstone Rhyolite Plateau region of Wyoming, Idaho, and Montana., *U.S. Geolological Survey Professional Paper* : **729-G**.

Cioni, R., Sbrana, A., and Vecci, R., 1992. Morphologic features of juvenile pyroclasts from magmatic and phreatomagmatic deposits of Vesuvius, *51* :1-27.

Clayton, R.N. and Kieffer, S.W., 1991. Oxygen isotopic thermometer calibrations, *Stable Isotope Geochemistry: A Tribute to Samuel Epstein. Geochem. Soc. Special Pub.:* **No. 3**, 3-10.

Cole, D.R., Ohmoto, H., and Lasaga, A.C., 1983. Isotopic exchange in mineral-fluid systems. I. Theoretical evaluation of oxygen isotopic exchange accompanying surface reactions and diffusion, *Geochimica et Cosmochimica Acta* : **47**, 1681-1693.

Cole, D.R., Ohmoto, H., and Jacobs, G.K., 1992. Isotopic exchange in mineral-fluid systems: III. Rates and mechanisms of oxygen isotope exchange in the system granite-$H_2O$±NaCl±KCl at hydrothermal conditions, *Geochimica et Cosmochimica Acta* : **56**, 445-466.

Condomines, M., Gronvold, K., Hooker, P.J., Muehlenbachs, K., O'Nions, R.K., Oskarsson, N. and Oxburgh, E.R., 1983. Helium, oxygen, strontium and neodymium isotopic relationships in Icelandic volcanics, *Earth and Planetary Science Letters* : **66**, 125-136.

Cousens, B.L., Spera, F.J., and Dobson, P.F., 1993. Post-eruptive alteration of silicic ignimbrites and lavas, Gran Canaria, Canary Islands: Strontium, neodymium, lead, and oxygen isotopic evidence, *Geochimica et Cosmochimica Acta* : **57**, 631-640.

Craig, H., 1961. Isotopic variations in meteoric waters, *Science* : **133**, 1702-1703.

Crank, J., 1975. *The Mathematics of Diffusion* (Clarenden Press, Oxford).

Cunningham, C G., and Steven, T.A., 1979. Mount Belknap and Red Hills calderas and associated rocks, Marysvale volcanic field, west-central Utah, *U.S. Geolological Survey Bulletin* : **1468**, 34 pp.

Dalrymple, G.B., and Lanphere, M.A., 1974. $^{40}Ar/^{39}Ar$ age spectra of some undisturbed terrestrial samples, *Geochimica et Cosmochimica Acta* : **38**, 715-738.

Dalrymple, G.B., Alexander, E.C. J., Lanphere M.A., and Kraker, G.P., 1981. Irradiation of samples for $^{40}Ar/^{39}Ar$ dating using the Geological Survey TRIGA reactor, *U.S.G.S. Professional Paper* : **1176**, 55 pp.

Dalrymple, G.B., 1989. The GLM continuous laser system for $^{40}Ar/^{39}Ar$ dating: Description and performance characteristics, *New Frontiers in Stable Isotopic Research: Laser Probes, Ion Probes and Small-Sample Analysis, U.S.G.S. Bulletin* : **1890**, 89-96.

DePaolo, D.J., and Wasserburg, G.J., 1976. Inferences about magma sources and mantle structire from variations of $^{143}Nd/^{144}Nd$, *Geophysical Research Letters* : **3**, 743-746.

DePaolo, D.J., 1981. Trace element and isotopic effects of combined wallrock assimilation and fractional crystallization, *Earth and Planetary Science Letters* : **53**, 189-202.

Dixon, J.E., Clague, D.A. and Stolper, E.M., 1991. Degassing history of water, sulfur and carbon in submarine lavas from Kilauea Volcano, Hawaii, *Journal of Geology* : **99**, 371-394.

Dobson, P.F., Epstein, S., and Stolper, E.M., 1989. Hydrogen isotope fractionation between coexisting vapor and silicate glasses and melts at low pressure, *Geochimica et Cosmochimica Acta* : **53**, 2723-2730.

Duffield, W.A., and Dalrymple, G B., 1990. The Taylor Creek Rhyolite of New Mexico: a rapidly emplaced field of lava domes and flows, *Bulletin of Volcanology* : **52**, 475-487.

Duffield, W.A., and Ruiz, J., 1992. Compositional gradients in large reservoirs of silicic magma as evidenced by ignimbrites versus Taylor Creek Rhyolite lava domes, *Contributions to Mineralogy and Petrology* : **110**, 192-210.

Dullien, F.A.L., 1979. *Porous media. Fluid transport and pore structure.* (Academic Press, New York).

Farmer, G.L., Broxton, D.E., Warren, R.G., and Pickthorn, W., 1991. Nd, Sr, and O isotopic variations in metaluminous ash-flow tuffs and related volcanic rocks at the Timber Mountain/Oasis Valley Caldera Complex, SW Nevada: implications for the origin and evolution of large-volume silicic magma bodies, *Contributions to Mineralogy and Petrology* : **109**, 53-68 .

Farquhar, J., Chacko, T., and Frost, B.R., 1993. Strategies for high temperature oxygen isotope thermometry: a worked example from the Laramie Anorthosite Complex, Wyoming, USA, *Earth and Planetary Science Letters* : **117**, 407-422.

Fenner, C. N., 1920. The Katmai region, Alaska, and the great eruption of 1912, *Journal of Geology* : **28**, 569-606.

Flexser, S., 1991. Hydrothermal alteration and past and present thermal regimes in the western moat of Long Valley caldera, *Journal of Volcanology and Geothermal Research* : **48**, 303-318.

Fridrich, C. J., and Mahood, G. A., 1984. Reverse zoning in the resurgent intrusion of the Grizzly Peak cauldron, Sawatch Range, Colorado, *Geological Society of America Bulletin* : **95**, 779-787.

Fridrich, C.J., Smith, R.P., DeWitt, E., and McKee, E.H., 1991. Structural, eruptive and intrusive evolution of the Grizzly Peak caldera, Sawatch Range, Colorado, *Geological Society of America Bulletin* : **103**, 1160-1177.

Friedman, I., and Smith, R.L., 1958. The deuterium content of water in some volcanic glasses, *Geochimica et Cosmochimica Acta* : **15**, 218-228.

Friedman, I., and Smith, R.L., 1960. A new dating method using obsidian, *Am, Antiquity* : **25**, 347-352.

Friedman, I., Smith, R.L., and Long, R.L., 1966. Hydration of natural glass and formation of perlite, *Geolocial Society of America Bulletin* : **77**, 323-328.

Fritz, P., 1981. River waters, in *Stable Isotope Hydrology. Deuterium and Oxygen-18 in the Water Cycle,* (eds. J.R. Gat and R. Gonfiantini) Technical Reports Series No. 210 (International Atomic Energy Agency, Vienna), 177-202.

Gat, J.R., 1981. Groundwater, in *Stable Isotope Hydrology. Deuterium and Oxygen-18 in the Water Cycle,* (eds. J.R. Gat and R. Gonfiantini) Technical Reports Series No. 210 (International Atomic Energy Agency, Vienna), 223-240.

Gazis, C.A., Taylor, H.P., Jr.,Tsvetkov, A.A., Gurbanov, A.G., and Lipman, P.W., 1991. An oxygen isotope study of the 2.5 Ma Chegem rhyolite ash-flow caldera, northern Caucasus Mountains, U.S.S.R. [abs.], *Geol. Soc. Amer. Abs. with Programs* : **23**, 442.

Gazis, C.A., Hon, K., Taylor, H.P., Jr., Tsvetkov, A.A., and Beus, V., 1992. Stratigraphically-controlled geochemical trends within the Chegem caldera, central Caucasus Mountains, Russia, *EOS* : **73**, 623.

Giletti, B.J., Semet, M.P., and Yund, R.A., 1978. Studies in diffusion-III. Oxygen in feldspars: and ion microprobe determination, *Geochimica et Cosmochimica Acta* : **42**, 45-57.

Giletti, B.J., 1986. Diffusion effects on oxygen isotope temperatures of slowly cooled igneous and metamorphic rocks, *Earth and Planetarry Science Letters* : **77**, 218-228.

Giletti, B.J., 1991. Rb and Sr diffusion in feldspars, with implications for cooling histories of rocks, *Geochimica et Cosmochimica Acta* : **55**, 1331-1343.

Goff, F., Wollenberg, H.A., Brookins, D.C. and Kistler, R.W., 1991. A Sr-isotopic comparison between thermal waters, rocks, and hydrothermal calcites, Long Valley caldera, California, *Journal of Volcanology and Geothermal Research* : **48**, 265-281.

Goldberg, E.D., 1965. Minor elements in sea water, in *Chemical Oceanography,* edited by J.P. Riley and G. Skirrow (Academic, New York, 1965) 162 pp.

Goranson, R.W., 1931. The solubility of water in granite magmas, *American Journal of Science* : **22**, 481-502.

Gregory, R.T., and Taylor, H.P., Jr., 1986. Non-equilibrium, metasomatic $^{18}O/^{16}O$ effects in upper mantle mineral assemblages, *Contributions to Mineralogy and Petrology* : **93**, 124-135.

Gregory, R.T., Criss, R.E., and Taylor, H.P., Jr., 1989. Oxygen isotope exchange kinetics of mineral pairs in closed and open systems: Applictions to problems of hydrothermal alteration of igneous rocks and Precambrian iron formations, *Chemical Geology* : **75**, 1-42.

Griggs, R.F., 1918. The eruption of Katmai, *Nature* : **101**, 497-499.

Griggs, R.F., 1922. *The Valley of Ten Thousand Smokes* (National Geographic Society, Washington, D.C.).

Grunder, A.L., 1987. Low $\delta^{18}O$ silicic volcanic rocks at the Calabozos Caldera Complex, Southern Andes, *Contributions to Mineralogy and Petrology*: **95**, 71-81.

Gurbanov, A.G., and Favorskaya, M.A., 1977. The problem of the neointrusions of the Caucasus, using modern data, *Sov. Geol.* **7**: 44-58 [in Russian]. English transl. in *Int. Geol. Rev.*, **20**: 495-506.

Gurbanov, A.G., Lyakhovich, T.T., Kartashova, L.F., and Korina, E.A., 1987. Contents of rare and ore elements in quartz from different age magmatic formations and metamorphic series of the Great Caucasus, *Geol. Zbornik-Geol. Carpathica Bratilava* : **38**, 387-407.

Haar, L., Gallagher, J.S., and Kell, G.S., 1984. NBS/NRC Steam Tables, (Hemisphere Press, New York).

Halliday, A.N., Fallick, A.E., Hutchinson, J., and Hildreth, W., 1984. A Nd, Sr and O isotopic investigation into the causes of chemical and isotopic zonation in the Bishop Tuff, California, *Earth and Planetary Science Letters* : **68**, 379-391.

Halliday, A.N., Mahood, G.A., Holden, P. Metz, J.M., Dempster, T.J., and Davidson, J.P., 1989. Evidence for long residence times of rhyolitic magma in the Long Valley magmatic system: The isotopic record in precaldera lavas of Glass Mountain, *Earth and Planetary Science Letters*: **94**, 274-290.

Hamilton, D.L. and Oxtoby, S., 1986. Solubility of water in albite-melt determined by the weight-loss method, *Journal of Geology* : **94**, 626-630.

Harris, C. and Erlank, A.J., 1992. The production of large-volume, low-$\delta^{18}O$ rhyolites during rifting of Africa and Antarctica: The Lebombo Monocline, southern Africa, *Geochimica et Cosmochimica Acta* : **56**, 3561-3570.

Harrison, T.M., Duncan, I. and McDougall, I., 1985. Diffusion of $^{40}Ar$ in biotite: temperature, pressure and compositional effects., *Geochimica et Cosmochimica Acta* : **49**, 2461-2468.

Harrison, T. M., and McDougall, I, 1989. *Geochronology and Thermochronology by the $^{40}Ar/^{39}Ar$ Method* (Oxford University Press, New York).

Healy, J., 1964. Volcanic mechanisms in Taupo volcanic zone, New Zealand, *New Zealand Journal of Geology and Geophysics* : **7**, 6-23

Heiken, G., 1972. Morphology and petrography of volcanic ashes, *Geological Society of America Bulletin* : **83**, 1961-1988.

Heiken, G., and Wohletz, K., 1985. *Volcanic Ash* (University of California Press, Berkeley).

Hess, J.C., Lippolt, H.J., Gurbanov, A.G. and Michalski, I., 1993. The cooling history of the late Pliocene Eldzhurtinskiy granite (Caucasus, Russia) and the thermochronological potential of grain size/age relationships, *Earth and Planetary Science Letters* : **117**, 393-406.

Hildreth, W., 1979. The Bishop Tuff: Evidence for the origin of compositional zonation in silicic magma chambers, *Geological Society of America Special Paper* : **180**, 43-75.

Hildreth, W., 1981. Gradients in silicic magma chambers: Implications for lithospheric magmatism, *Journal of Geophysical Research* : **86**, 10153-10192.

Hildreth, W., 1983. The compositionally zoned eruption of 1912 in the Valley of Ten Thousand Smokes, Katmai National Park, Alaska, *Journal of Volcanological and Geothermal Research* : **18**, 1-56.

Hildreth, W., Christiansen, R.L., and O'Neil, J.R., 1984. Catastrophic isotopic modification of rhyolitic magma at times of caldera subsidence, Yellowstone Plateau Volcanic Field, *Journal of Geophysical Research* : **89**, 8339-8369 .

Hildreth, W., Halliday, A.N., and Christiansen, R. L., 1991. Isotopic and chemical evidence concerning the genesis and contamination of basaltic and rhyolitic magma beneath the Yellowstone Plateau volcanic field, *Journal of Petrology* : **32**, 63-138.

Honnorez, J., and Kirst, P., 1975. Submarine basaltic volcanism: Morphometric parameters for discriminating hyaloclastites from hyalotuffs, *Bulletin of Volcanology* : **39**, 441-465.

Hulen, J.B., and Nielson, D.L., 1986. Hydrothermal alteration in the Baca geothermal system, Redondo dome, Valles caldera, New Mexico, *Journal of Geophysical Research* : **91**, 1867-1886.

Ihinger, P.D., 1991, Ph.D. thesis, *An experimental study of the interaction of water with granitic melt*, California Institute of Technology.

Ingebritsen, S.E., Sherrod, D.R., and Mariner, R.H., 1992. Rates and patterns of groundwater flow in the Cascade Range volcanic arc, and the effect on subsurface temperatures, *Journal of Geophysical Research* : **97**, 4599-462 .

Johnson, C.M., Czamanske, G. K. and Lipman, P. L., 1989. Geochemistry of intrusive rocks associated with the Latir volcanic field, New Mexico, and contrasts between evolution of plutonic and volcanic rocks, *Contributions to Mineralogy and Petrology* : **103**, 90-109.

Johnson, C.M., 1989. Isotopic zonations in silicic magma chambers, *Geology* : **17**, 1136-1139 .

Johnson, C.M., Lipman, P.L. and Czamanske, G.K., 1990. H, O, Sr, Nd, and Pb isotope geochemistry of the Latir volcanic field and cogenetic intrusions, New Mexico, and relations between evolution of a continental magmatic center and modifications of the lithosphere, *Contributions to Mineralogy and Petrology* : **104**, 99-124.

Johnson, C.M., and Fridrich, C.J., 1990. Non-monotonic chemical and O, Sr, Nd, and Pb isotope zonations and heterogeneity in the mafic- to silicic-composition magma chamber of the Grizzly Peak Tuff, Colorado, *Contributions to Mineralogy and Petrology* : **105**, 677-690 .

Kawada, K., 1971. Geology and petrology of the Nohi rhyolites, with special reference to those along the Hida River, *Japan Geological Survey Report* : **243**, 1-49 .

Keith, T.E.C., 1991. Fossil and active fumaroles in the 1912 eruptive deposits, Valley of Ten Thousand Smokes, Alaska, *Journal of Volcanology and Geothermal Research* : **45**, 227-254.

Keith, T.E.C., Thompson, J.M., Hutchinson, R.A., and White, L.D., 1992. Geochemistry of waters in the Valley of Ten Thousand Smokes region, Alaska, *Journal of Volcanology and Geothermal Research* : **49**, 209-231.

Kennedy, G.C., 1950. A portion of the system silica-water, *Economic Geology* : **45**, 629-653.

Kokelaar, B.P., 1983. The mechanisms of Surtseyan volcanism, *Journal of the Geological Society of London* : **139**, 21-33.

Koronovsky, N.V., 1975. Fluido-rhyolites of the Upper Chegem volcanic highland (Northern Caucasus), *Dokl. Acad. Sci. USSR* : **220**, 447-450 [in Russian].

Koronovsky, N.V., 1976a. Structure of the Upper Chegem volcanic highland (Northern Caucasus) and the problem of mobility of silicic lavas, *Vestnik Moscow State Univ., Ser. Geol.* : 16-29 [in Russian].

Koronovsky, N.V., 1976b. On the problem of ignimbrites, *Bull. MOIP* : **5**, 106-120 [in Russian].

Koronovsky, N.V., Molyavko, V.G., and Ostafiychuk, I.M., 1982. Petrochemical specialization and conditions of formation of silicic volcanic rocks of the Upper Chegem area of the Elbrus region, *Nukova Dumka, Kiev* : 150 pp. [in Russian].

Koronovsky, N.V., 1983a. Dual nature of ignimbrites, *Nature* : **183**, 12-20 in Russian].

Koronovsky, N.V., 1983b. Guide for geological excursions along the Northern Caucasus, *VIEMS, Moscow* : 95 pp.

Kostitsyn, Y.A., and Kremenetskiy, A.A., 1994. Sr and O isotopic composition in 4.7 km vertical section and petrogenesis of Eldjurta Granite (Caucasus), *ICOG-8* [abstract].

Kruschev, N.A., 1958. Tirniauz skarn tungsten-molybdenum deposit within the Northern Caucasus, *Sov. Geol.* : **2**, 51-72. [in Russian]

Lambert, S.J., and Epstein, S., 1980. Stable isotope investigations of an active geothermal system in Valles caldera, Jemez Mountains, New Mexico, *Journal of Volcanology and Geothermal Research* : **8**, 111-129.

Lanphere, M.A., and Dalrymple, G.B., 1976. Identification of excess $^{40}Ar$ by the $^{40}Ar/^{39}Ar$ age spectrum technique, *Earth and Planetary Science Letters* : **32**, 141-148.

Larson, P.B., and Taylor, H.P., Jr., 1986a. An oxygen isotope study of hydrothermal alteration in the Lake City caldera, San Juan Mountains, Colorado, *Journal of Volcanology and Geothermal Research* : **30**, 47-82 .

Larson, P.B. and Taylor, H.P., Jr., 1986b. $^{18}O/^{16}O$ ratios in ash-flow tuffs and lavas erupted from the central Nevada caldera complex and the central San Juan caldera complex, Colorado, *Contributions to Mineralogy and Petrology* : **92**, 146-156.

Levinson-Lessing, F.Y., 1913. Volcanoes and lavas of the Central Caucasus, *Izv. St. Petersburg Politech. Inst.* : 190 pp. [in Russian].

Lewis, C. J., 1993, M.S. thesis. *Transition from Subduction to Collision in the Russian Caucasus: A Reconnaissance of Differential Exhumation from Geobarometry, Ore Deposits and Fluvial Features*, University of California, Berkeley.

Liakhovich, V.V., 1953. Endomorphic alterations of young granites of Baksan in contact with limestones, *Tr. Inst. Geol. Sci. Acad. Sci. USSR* : **148**, 70-91 [in Russian].

Liakhovich, V.V., 1976. *Connection between ore mineralization and magmatism (Tirniauz)* (Nauka, Moscow) [in Russian].

Lipman, P.W., 1967. Mineral and chemical variations within an ash-flow sheet from the Aso caldera, Southwestern Japan, *Contributions to Mineralogy and Petrology* : **16**, 300-327.

Lipman, P.W., Steven, T.A., Luedke, R.G., and Burbank, W.S., 1973. Revised volcanic history of the San Juan, Uncompahgre, Silverton, and Lake City calderas in the western San Juan Mountains, Colorado, *Journal of Research of the U.S. Geological Survey* : **1**, 627-64 .

Lipman, P.W. and Friedman, I., 1975. Interaction of meteoric water with magma: An oxygen-isotope study of ash-flow sheets from southern Nevada, *Geological Society of America Bulletin* : **86**, 695-702.

Lipman, P.W., 1983. The Questa caldera, northern New Mexico - relation to batholith emplacement and associated molybdenum mineralization, in *The Genesis of Rocky Mountain Ore Deposits: Changes with Time and Tectonics*, (edited by Denver Region Exploration Geologists Society, Golden, CO).

Lipman, P.W., 1984. The roots of ash-flow calderas in western North America: Windows into the tops of granitic batholiths, *Journal of Geophysical Research* : **89**, 8801-8841.

Lipman, P.W. and Sawyer, D.A., 1985. Mesozoic ash-flow caldera fragments in southeastern Arizona and their relation to porphyry copper deposits, *Geology* : **13**, 652-656.

Lipman, P.W., 1992. Ash-flow calderas as structural controls of ore deposits: Recent work and future problems, *U.S. Geological Survey Bulletin* : **2012**, L1-L12.

Lipman, P.W., Bogatikov, O.A., Tsvetkov, A.A., Gazis, C., Gurbanov, A.G., Hon, K., Koronovsky, N.V., Kovalenko, V.I. and Marchev, P. 1993. 2.8 Ma ash-flow caldera at Chegem River in the northern Caucasus Mountains (Russia), contemporaneous granites, and associated ore deposits, *Journal of Volcanology and Geothermal Research*: **57**, 85-124.

Lofgren, G., 1970. Experimental devitrification rate of rhyolite glass, *Geological Society of America Bulletin* : **81**, 553-560.

Mahood ,G.A., and Halliday, A.N., 1988. Generation of high-silica rhyolite: A Nd, Sr and O isotopic study of Sierra La Primavera, Mexican Neovolcanic Belt, *Contributions to Mineralogy and Petrology* : **100**, 183-191.

Marsh, B.D., 1984. On the mechanisms of caldera resurgence, *Journal of Geophysical Research*: **89**, 8245-8251.

Marsh, K.N., Ed., 1987. Recommended Reference Materials for the Realization of Physicochemical Properties. (Blackewell, Oxford).

Marshall, R.R., 1961. Devitrification of natural glass, *Geological Society of Americal Bulletin* : **72**, 1493-1520.

Mastin, L G.,1991. The roles of magma and groundwater in the phreatic eruptions at Inyo craters, Long Valley caldera, California, *Bulletin of Volcanology* : **53**, 579-596 .

Masurenkov, Y.P., 1957. Specific features of evolution of Cenozoic volcanism of the Elbrus region, *Izv. Acad. Sci. USSR, Ser. Geol.* : **5**, 9-24 [in Russian].

Masurenkov, Y.P., 1961. Cenozoic volcanism of the Elbrus volcanic region, *Tr. IGEM Acad. Sci. USSR* : 130 pp. [in Russian].

McCrea, J.M., 1950. On the isotopic chemistry of carbonates and a paleotemperature scale, *Chem Physics* : **18**, 849-857.

McCulloch, M.T., Gregory, R.T., Wasserburg, G.J., and Taylor, H.P., Jr., 1981. Sm-Nd, Rb-Sr and $^{18}O/^{16}O$ isotopic systematics in an oceanic crustal section: Evidence from the Samail ophiolite, *Journal of Geophysical Research* : **86**, 2721-2735.

McCulloch, M.T., Gregory, R.T., Wasserburg G.J., and Taylor, H.P., Jr., 1980. A neodymium, strontium and oxygen study of the Cretaceous Samail ophiolite and implications for the petrogenesis and seawater-hydrothermal alteration of oceanic crust, *Earth and Planetary Science Letters* : **46**, 201-211.

McKee, E.H., 1979. Ash-flow sheets and calderas: Their genetic relationship to ore deposits, *Special Paper Geological Society of America* : **180**, 205-211.

McKinney, C.R., McCrea, J.M., Epstein, S., Allen, H.A. and Urey, H.C., 1950. Improvements in mass spectrometers for the measurement of small differences in isotope abundance ratios, *Rev. Sci. Instr.* : **21**, 724-730.

Mercali, G., and Silvestri, O. , 1891. Le eruzioni dell'isola di Vulcano, incominciate il 3 Agosto 1888 e terminate il 22 Marzo 1890, *1891 Ann. Uff. Cent. Metr. Geodin.* : **10**, 1-213.

Michael, P.J., 1983. Chemical differentiation of the Bishop Tuff and other high-silica magmas through crystallisation processes, *Geology* : **11**, 31-34.

Milanovsky, E.E., 1959. Tectonic position and some features of history of Cenozoic magmatism within the Elbrus region, *Bull. MOIP, Sec. Geol.* : **2**, 3-19 [in Russian].

Milanovsky, E.E., and Koronovsky, N.V., 1961. Tufflavas and related rocks in the central Caucasus, *Tr. Volcanol. Lab. Acad. Sci. USSR* : **20**, 72-89 [in Russian].

Milanovsky, E.E., Kaminsky, F.V. and Sedenko, S.M., 1962. Geological structure and history of formation of the Upper Chegem volcanic highland. Tr. Caucasian Expedition of VAGT and MGU (Moscow State University) for 1959-1960, in *Geology of the Central and Western Caucasus*, edited by Gostoptekhizdat, Moscow, 1962) p. 302-397 [in Russian].

Milanovsky, E.E., and Koronovsky, N.V., 1973. *Orogenic Volcanism and Tectonics of the Alpine Belt of Eurasia* (Nauka, Moscow) [in Russian].

Moore, J.G., 1975. Mechanisms of formation of pillow lavas, *Amer. Sci.* : **63**, 269-277.

Muehlenbachs, K., Anderson, A.T., Jr., and Sigvaldason, G.E., 1974. Low-$O^{18}$ basalts from Iceland, *Geochimica et Cosmochimica Acta* : **38**, 577-588.

Muehlenbachs, K., 1987. Oxygen isotope exchange during weathering and low-temperature alteration, in *Stable Isotope Geochemistry of Low Temperature Processes*, edited by T.K. Kyser (Mineralogical Society of Canada, 1987) p. 162-186.

Muffler, L.J.P., White, D.E., and Truesdell, A.H., 1971. Hydrothermal explosion craters in Yellowstone National Park, *Geological Society of Americal Bulletin*: **82**, 723-740.

Nairn, I.A., and Wirdadiradja, S., 1980. Late Quaternary hydrothermal explosion breccias at Kawerau geothermal field, New Zealand, *Bulletin of Volcanology* : **43**, 1-14.

Nelson,P.H., and Anderson, L.A., 1992. Physical properties of ash flow tuff from Yucca Mountain, Nevada, *Journal of Geophysical Research* : **97**, 6823-6841.

Newman, S., Stolper, E.M., and Epstein, S., 1986. Measurement of water in rhyolitic glasses. Calibration of an infrared spectroscopic technique, *American Mineralogist* : **71**, 1527-1541.

Newman, S., Epstein, S., and Stolper, E.M., 1988. Water, carbon dioxide, and hydrogen isotopes in glasses from the ca. 1340 A.D. eruption of Mono Craters, California: Constraints on degassing phenomena and initial volatile content, *Journal of Volcanology and Geothermal Research* : **35**, 75-96 .

Nier, A.O.C., 1947. A mass spectrometer for isotope and gas analysis, *Rev. Sci. Instr.* : **18**, 398-411.

Nier, A.O., 1950. A redetermination of the relative abundance of the isotopes of carbon, nitrogen, oxygen, argon, and potassium, *Phys. Rev.* : **77**, 789-793.

Noble, D.C., and Hedge, C.E., 1969. $Sr^{87}/Sr^{86}$ variations within individual ash-flow sheets, *U.S. Geol. Survey Professional Paper* : **650-C**, C133-C139.

Norton, D. and Knight, J., 1977. Transport phenomena in hydrothermal systems: Cooling plutons, *American Journal of Science* : **277**, 937-981.

Norton, D., and Taylor, H.P., Jr., 1979. Quantitative simulation of the hydrothermal systems of crystallizing magmas on the basis of transport theory and oxygen isotope data, *Journal of Petrology* : 20, 421-486.

Orlova, G.P., 1962. The solubility of water in albitic melts, *International Geology Review* : **6**, 254-258.

Papike, J.J., Keith, K.E.C., Spilde, M.N., Galbreath, K.C., Shearer, C.K., and Laul, J.C., 1991. Geochemistry and mineralogy of fumarolic deposits, Valley of Ten Thousand Smokes, Alaska: Bulk chemical and mineralogical evolution of dacite-rich protolith, *American Mineralogist* : **76**, 1662-1673.

Parrish, R.R., 1983. Cenozoic thermal evolution and tectonics of the Coast Mountains of British Columbia 1. Fission track dating, apparent uplift rates and patterns of uplift, *Tectonics* : **2**, 601-631 .

Parrish, R.R. 1984. Some cautions which should be exercised when interpreting fission track and other dates with regard to uplift rate calculations, *Nuclear Tracks* : **10**, 425.

Pek, A.V., 1962. Contact metamorphism associated with neogranites of the Northern Caucasus, *Tr. IGEM Acad. Sci. USSR* : **56**, 168 pp. [in Russian].

Philip, H., Cisternas, A., Gvishiani, A., and Gorshkov, A., 1989. The Caucasus: An actual example of the initial stages of continental collision, *Tectonophysics* : **161**, 1-21.

Pickett, D.A., 1991, Ph.D. thesis. An isotopic and petrologic study of an exposure of the deep Sierra Nevada batholith, Tehachapi Mountains, California, California Institute of Technology.

Rhekharskii, V.H., Gurbanov, A.G., Dikov, P., Pek, A.A., Trubkin, N.N., and Khitrov, V.G., 1987. About types of tungsten manifestations in the later Paleozoic granites of the Caucasus, *Izv. Acad. Sci. USSR, Ser. Geol.*: **7**, 127-129 [in Russian].

Riehle, J.R., 1973. Calculated compaction profiles of rhyolitic ash-flow tuffs, *Geological Society of America Bulletin* : **4**, 2193-2216.

Rodzyanko, N.G., 1969. *Distribution of chemical elements within the Tirniauz skarn ore field* (Rostov at Don, Rostov State Univ.) [in Russian].

Rodzyanko, N.G., Nefedov, V.K., and Sviridenko, A.F., 1973.*Rare-metal skarns of Tirniauz* (Nedra, Moscow) [in Russian].

Ross, C.S., and Smith, R.L., 1961. Ash-flow tuffs: Their origin, geologic relations and identification, *U.S. Geological Survey Professional Paper* : **366**, 81 pp.

Rytuba, J.J., and Glanzman, R.K., 1979. Relation of mercury, uranium, and lithium deposits to the McDermitt calder complex, Nevada-Oregon, *Nev. Bur. Mines Geol. Rep.* : **33**, 109-118.

Rytuba, J.J., 1981. Relation of calderas to ore deposits in the western United States, *Arizona Geological Society Digest* : **14**, 227-236.

Savin, S.M. and Epstein, S. 1970. The oxygen and hydrogen isotope geochemistry of ocean sediments and shales, *Geochimica et Cosmochimica Acta* : **34**, 43-63 .

Semochkin, G.A, 1969. Geological structure and specific features of exploration of the North-Western skarn of the Tirniauz deposit, *Summary of PhD Thesis, Novocherkassk* : 25 pp. [in Russian].

Sharma, T., and Clayton, R N., 1965. Measurement of $^{18}O/^{16}O$ ratios of total oxygen from carbonates, *Geochimica et Cosmochimica Acta* : **29**, 1347-1353.

Sheridan, M.F., Barberi, F., Rosi, M., and Santacroce, R., 1981. A model for Plinean eruptions of Vesuvius, *Nature* : **289**, 282-285.

Sheridan, M.F., and Wohletz, K.H., 1983. Hydrovolcanism: Basic considerations and review, *Journal of Volcanology and Geothermal Research* : **17**, 1-29.

Shipley, J.W., 1920. Some chemical observations on the volcanic emanations and incrustations in the Valley of 10,000 Smokes, Katmai, Alaska, *American Journal of Science Ser. 4* : **50**, 141-153.

Sigvaldason, G., 1968. Structure and products of subaquatic volcanoes in Iceland, *Contributions to Mineralogy and Petrology* : **18**, 1-16.

Silver, L.A., and Stolper, E.M., 1989. Water in albitic glasses, *Journal of Petrology* : **30**, 667-709.

Silver, L.A., Ihinger, P.D., and E.M. Stolper, 1990. The influence of bulk composition on the speciation of water in silicate glasses, *Contributions to Mineralogy and Petrology* : **104**, 142-162.

Smirnov, V.I. (ed.), 1977. *Ore Deposits of the USSR*, 492 pp. (Pitman Publishing).

Smith, B.M., and Suemnicht, G.A., 1991. Oxygen isotope evidence for past and present hydrothermal regimes of Long Valley caldera, California, *Journal of Volcanology and Geothermal Research* : **48**, 319-339.

Smith, R.L., 1960a. Ash flows, *Geological Society of America Bulletin* : **71**, 795-842

Smith, RL., 1960b. Zones and zonal variations in welded ash flows, *U.S.Geological Survey Professional Paper* : **354-F**, 149-159.

Smith, R.L., and Bailey, R.A., 1966. The Bandelier Tuff: A study of ash-flow eruption cycles from zoned magma chambers, *Bulletin of Volcanology* **29**, 83-104.

Smith, R.L., and Bailey, R.A., 1968. Resurgent cauldrons, *Mem. Geol. Soc. Am.* : **116**, 613-662.

Smith, R L., and Shaw, H.R., 1975. Igneous-related geothermal systems, *U.S. Geological Survey Circular* : **726**, 58-83.

Smith, R. L., 1979. Ash-flow magmatism, *Special Paper Geological Society of America* : **180**, 5-27.

Sobolev, R.N., and Kononov, O.V., 1993. New data about the Eldjurta Granite massive formation (Northern Caucasus), *Dokl. Akad. NAUK* : **330**, no. 3, 360-362 [in Russian].

Soloviev, S.P., 1938. Chegem volcanic region and area of rivers Kestanty and Sakashil (Northern Caucasus), *Tr. TSNIGRI* : **103**, 24pp. [in Russian].

Sorey, M.L., Lewis, R.E., and Olmsted, F.H., 1978. The hydrothermal system of Long Valley caldera, California, *U.S. Geological Survey Professional Paper* : **1044-A**, 1-60.

Sorey, M.L., Suemnicht, G.A., Sturchio, N.C., and Nordquist, G.A., 1991. New evidence on the hydrothermal system in Long Valley caldera, California, from wells, fluid sampling, electrical geophysics, and age determinations of hot-spring deposits, *Journal of Volcanological and Geothermal Research* : **48**, 229-263.

Sparks, R.S.J., Wilson, L., and Hulme, G., 1978. Theoretical modeling of the generation, movement, and emplacement of pyroclastic flows by column collapse, *Journal of Geophysical Research* : **83**, no. B4, 1727-1739.

Spilde, M.N., Brearley, A.J., and Papike, J.J., 1993. Alteration of plagioclase and pyroxene phenocrysts in a fissure fumarole, Valley of Ten Thousand Smokes, Alaska, *American Mineralogist* : **78**, 1066-1081.

Steven, T.A., and Ratte, J.C., 1965. Geology and structural control of ore deposition in the Creede district, San Juan Mountains, Colorado, *U.S. Geological Survey Professional Paper* : **487**, 87 pp.

Steven, T.A., Luedke, R.G., and Lipman, P.W., 1974. Relation of mineralization to calderas in the San Juan volcanic field, southwestern Colorado, *U.S. Geological Survey Journal Research*: **2**, 405-409.

Stolper, E.M., 1982a. Water in silicate glasses: An infrared spectroscopic study, *Contributions to Mineralogy and Petrology* : **81**, 1-17.

Stolper, E.M., 1982b. The speciation of water in silicate melts, *Geochimica et Cosmochimica Acta* : **46**, 2609-2620.

Stolper, E.M., 1989. Temperature dependence of the speciation of water in rhyolitic melts and glasses, *American Mineralogist* : **74**, 1247-1257.

Stuckless, J.S., and O'Neil, J.R., 1973. Petrogenesis of the Superstition-Superior volcanic area as inferred from strontium- and oxygen-isotope studies, *Geological Society of America Bulletin* : **84**, 1987-1998.

Taggart, J.E., Lindsay, J.R., Scott, B.A., Vivit, D.V., Bartel A.J.,and Stewart, K.C. 1987. Analysis of geologic materials by wavelength-dispersive X-ray flourescence spectrometry, in *Methods of Geochemical Analysis: U.S. Geological Survey Bulletin 1770*, edited by P. A. Baedecker (1987) p. E1-E19.

Taylor, B.E., Eichelberger, J.C. and Westrich, H.R., 1983. Hydrogen isotopic evidence of rhyolitic magma degassing during shallow intrusion and eruption, *Nature* : **306**, 541-545.

Taylor, B.E. and Westrich, H.R., 1985. Hydrogen isotope exchange and water solubility in experiments using natural rhyolite obsidian (abstr.), *EOS* : **66**, 387.

Taylor, H.P., Jr., 1968. The oxygen isotope geochemistry of igneous rocks, *Contributions to Mineralogy and Petrology* : **19**, 1-71.

Taylor, H.P., Jr., 1977. Water/rock interactions and the origin of $H_2O$ in granitic batholiths, *J. Geol. Soc. London* : **133**, 509-558.

Taylor, H.P., Jr., 1980. The effects of assimilation of country rocks by magma on $^{18}O/^{16}O$ and $^{87}Sr/^{86}Sr$ systematics in igneous rocks. *Earth and Planetary Science Letters* : 243-254.

Taylor, H.P., Jr., 1987. Comparison of hydrothermal systems in layered gabbros and granites, and the origin of low-$^{18}O$ magmas, in *Magmatic Processes: Physicochemical Principles*, edited by B. O. M. (ed.) (Geochem. Soc. spec. Publ. 1, 1987) p. 337-357.

Taylor, H.P., Jr., 1994. Oxygen and hydrogen isotope relationships in hydrothermal mineral deposits, Chapter in *Geochemistry of Hydrothermal Ore Deposits*, ed., H.L. Barnes (Wiley and Sons, New York) [in press].

Taylor, H.P., Jr., and Epstein, S., 1962. Relationship between $O^{18}/O^{16}$ ratios in coexisting minerals in igneous and metamorphic rocks - Part 1. Principles and experimental results, *Geological Society of America Bulletin* : **73**, 461-480.

Taylor, H.P., Jr., and Sheppard, S.M.F., 1986. Igneous Rocks: I. Processes of isotopic fractionation and isotope systematics, in *Stable Isotopes in High-Temperature Geological Processes*, eds. Valley, J.W., Taylor, H.P., Jr., and O'Neil, J.R., Mineral. Soc. Amer. *Reviews in Mineralogy* : **16**, 227-271.

Taylor, J.R., 1982.*An Introduction to Error Analysis* (University Science Books).

Truesdell, A.H., and Janik, C.J., 1986. Reservoir processes and fluid origins in the Baca geothermal system, Valles caldera, New Mexico, *Journal of Geophysical Research* : **91**, 1817-1833.

Tsvetkov, A.A., 1989. Volcanism of Transcaucasian Rise-Cenozoic rift zone in the Caucasus, USSR [abs.], *N.M. Bur. Mines, Mineral. Resource Bulletin* : **131**, 272.

Umsonst, T., 1991. Ph.D. thesis, Geochemie und Mineralogie des Eldschurtinskij-Granits im Grossen Kaukasus (UdSSR), Univ. Giessen.

Vuataz, F.D., and Goff, F., 1986. Isotope geochemistry of thermal and nonthermal waters in the Valles caldera, Jemez Mountains, northern New Mexico, *Journal of Geophysical Research* : **91**, 1835-1853.

White, A.F., 1986. Chemical and isotopic characteristics of fluids within the Baca geothermal reservoir, Valles caldera, New Mexico, *Journal of Geophysical Research* : **91**, 1855-1866.

White, A.F., and Peterson, M.L., 1991. Chemical equilibrium and mass balance relationships associated with the Long Valley hydrothermal system, California, U.S.A., *Journal of Volcanology and Geothermal Research* : **48**, 283-302.

Williams, H., 1942. The geology of Crater Lake National Park, Oregon, with a reconnaissance of the Cascade Range southward to Mount Shasta, *Carnegie Inst. Washington Publ.* : **540**, 162 pp.

Wohletz, K., 1983. Mechanisms of hydrovolcanic pyroclasts formation: grain-size, scanning electron microscopy and experimental studies, *Journal of Volcanology and Geothermal Research* : **17**, 31-63.

Wohletz, K., and Heiken, G., 1992. *Volcanology and Geothermal Energy* (University of California Press, Berkeley).

Yager, D.B., and Quick, J.E., 1992. SUPERXAP Manual: U.S. Geological Survey Open-File Report 92-13, : 45 pp. .

Yoder, H.S., Stewart, D.B., and Smith, J.R., 1956. Ternary feldspars, *Carnegie Institute of Washington Year Book* : **57**, 189-191.

Yurtsever, Y., and Gat, J.R., 1981. Atmospheric waters, in *Stable Isotope Hydrology. Deuterium and Oxygen-18 in the Water Cycle*, (eds. J.R. Gat and R. Gonfiantini) Technical Reports Series No. 210 (International Atomic Energy Agency, Vienna), 223-240.

Zeitler, P.K., and Fitz Gerald, J.D., 1986. Saddle-shaped $^{40}Ar/^{39}Ar$ age spectra from young, microstructurally complex potassium feldspars, *Geochimica et Cosmochimica Acta* : **50**, 1185-1199.

Zhang, Y., Stolper, E.M., and Wasserburg, G.J., 1991. Diffusion of water in rhyolitic glasses, *Geochimica et Cosmochimica Acta* : **55**, 441-456.

Zhuravlev, A.Z., and Negrey, E.V., 1993. Synchronous formation of the Eldzhurtinskiy Granite and an ore-bearing metasomatite from Tirniauz (northern Caucasus) by Rb-Sr dating method, *Geochimia* : **332**, 482-485.

Zhuravlev, A.Z., and Negrey, E.V., 1994. Temporal association of Tyrniauz W-Mo deposit with Eldjurta Granite: Evidence from Rb-Sr dating, *ICOG-8* : 370.

Zies, E.G., 1924a. The fumarolic incrustations of the Valley of Ten Thousand Smokes, *Nat. Geogr. Soc. Contrib. Tech. Pap., Katmai Series* : **4**, 157-179.

Zies, E.G., 1924b. Hot Springs of the Valley of Ten Thousand Smokes, *Journal of Geology* : **2**, 303-310.

Zies, E.G., 1929. The Valley of Ten Thousand Smokes: I. The fumarolic incrustations and their bearing on ore deposition. II. The acid gases contributed to the sea during volcanic activity, *Nat. Geogr. Soc. Contrib. Tech. Pap., Katmai Series* : **4**, 1-79.